

**Molecular imaging of cyclooxygenase-2 (COX-2) and autotaxin (ATX) in cancer using
positron emission tomography (PET)**

by

Marcus Elliot Litchfield

A thesis submitted in partial fulfillment of the requirements for the degree of

Master of Science

in

Cancer Studies

Department of Oncology
University of Alberta

© Marcus Elliot Litchfield, 2020

ABSTRACT

Positron emission tomography (PET) relies on the use of β^+ -emitting radionuclide-bearing molecules congregating and decaying at a specific site of interest. Use of these molecules, called radiotracers, which target common tumor characteristics has become a pillar in the diagnosis of cancer and the monitoring of treatment response. Within the last two decades, a significant appreciation for the tumorigenic and metastasis-promoting role of inflammation has emerged and biomarkers of cancer-associated inflammation have been identified. Two key players in this relationship are cyclooxygenase-2 (COX-2) and autotaxin (ATX), and their main lipid mediator products, prostaglandin E₂ (PGE₂) and lysophosphatidic acid (LPA), respectively. Having emerged as key inflammatory regulators, COX-2 and ATX have become therapeutic targets in the treatment of inflammatory diseases. Recently, our lab developed a small molecule inhibitor of COX-2, called triacoxib, using *in situ* click chemistry, a target-guided synthesis method which used the COX-2 active site to select and form its own ligand from a diverse group of building blocks. Although a relatively new effort, several inhibitors of ATX have been developed, and one has even been tested as an ATX PET imaging probe: [¹⁸F]PRIMATX. With the recognition of the role inflammatory mediators play in tumor progression, novel methods of biomarker detection and measurement are required. The focus of this work was to develop a radiochemical synthesis method for and validate novel radiotracers which target COX-2 or ATX as a step toward the clinical detection and monitoring of inflammatory biomarkers *in vivo*.

Using both nucleophilic and late-stage radiofluorination chemistry, we converted three small molecule inhibitors of COX-2 and ATX into the PET molecular imaging probes [¹⁸F]triacoxib, [¹⁸F]PRIMATX, and [¹⁸F]F-GLPG1690, derived from an ATX inhibitor nearing FDA approval.

For the [^{18}F]triacoxib project we present the radiosynthesis as well as the *in vitro* and *in vivo* validation of this radiotracer in COX-2-expressing HCA-7 human colorectal cancer cells. Radiosynthesis and purification of [^{18}F]triacoxib afforded the radiotracer in yields of $72\% \pm 6.5\%$ ($n = 7$) at molar activities exceeding $90 \text{ GBq}/\mu\text{mol}$. Baseline cellular uptake levels of [^{18}F]triacoxib could be reduced by 63% with pre-treatment using 0.1 mM of the COX-2 inhibitor celecoxib. The radiotracer showed high metabolic stability, remaining 90% intact after 60 min. PET imaging of [^{18}F]triacoxib revealed a favorable baseline uptake of $\text{SUV}_{60\text{min}} = 0.76 \pm 0.02$ ($n = 4$) that could be blocked by 20% with pre-treatment using celecoxib. Autoradiographic and immunohistochemical experiments further confirmed the COX-2-mediated uptake of [^{18}F]triacoxib *in vivo*. Despite a substantial amount of non-specific uptake *in vivo*, [^{18}F]triacoxib represents a suitable radiotracer for PET imaging of COX-2.

For the [^{18}F]PRIMATX project we present an improved radiosynthetic method and a further *in vivo* validation of the radiotracer in ATX-expressing 8305C human thyroid tumors and 4T1 murine breast tumors, where ATX is expressed in the adipose tissues rather than the tumor cells. Radiosynthesis and purification of [^{18}F]PRIMATX afforded the radiotracer in yields of $25\% \pm 6.7\%$ ($n = 9$) at molar activities exceeding $55 \text{ GBq}/\mu\text{mol}$. The radiotracer showed moderate metabolic stability, remaining $\sim 65\%$ intact after 60 min. PET imaging of [^{18}F]PRIMATX in both models revealed favorable baseline uptakes of $\text{SUV}_{60\text{min}4\text{T}1} = 0.81 \pm 0.05$ ($n = 4$) and $\text{SUV}_{60\text{min}8305\text{C}} = 0.61 \pm 0.02$ ($n = 4$). Uptake into 8305C tumors could be blocked by 12 and 8% after 30 and 60 min, respectively. Notably, brain uptake was high and could be blocked by 34%. Despite some additional work needed [^{18}F]PRIMATX appears to be a valid radiotracer for the PET imaging of ATX in multiple cells lines.

For the [¹⁸F]F-GLPG1690 project we present the radiosynthesis and *in vivo* PET imaging of the radiotracer in the 8305C human thyroid tumor model. Radiosynthesis and purification of [¹⁸F]F-GLPG1690 afforded the radiotracer in yields of 30% ± 5% (*n* = 2). PET imaging of [¹⁸F]F-GLPG1690 in the 8305C human thyroid tumor model resulted in very low baseline uptake of $SUV_{60min8305C} = 0.31 \pm 0.04$ (*n* = 3).

The results of these projects demonstrate the feasibility of using PET imaging for the *in vivo* detection of inflammatory biomarkers. Further development and implementation of these systems should allow for increased personalization of therapeutic strategies for patients with inflammatory diseases such as cancer.

PREFACE

Parts of this thesis have been submitted/ will be submitted for publication as the following:

Chapter 2 of this Master Thesis, before minor edits, has been published as **Litchfield M**, Wuest M, Glubrecht D, Wuest F. “Radiosynthesis and biological evaluation of [¹⁸F]triacoxib: a radiotracer for PET imaging of COX-2” in *Molecular pharmaceuticals*. I was the primary data collector and composed the manuscript. Wuest M assisted with data collection (particularly PET imaging), data analysis, and manuscript edits. Glubrecht D assisted with data collection and manuscript edits. Wuest F was the supervisory author and was involved in concept formation and manuscript edits. All animal experiments were performed according to guidelines from the Canadian Council on Animal Care (CCAC) and approved by the local animal care committee (Cross Cancer Institute, University of Alberta).

Chapter 3 of this Master Thesis, pending some additions, will be submitted as **Litchfield M**, Wuest M, Meng G, Briard E, Auberson YP, McMullen T, Brindley D, Wuest F. “*In vivo* imaging of autotaxin in thyroid and breast tumor models using [¹⁸F]PRIMATX” to *Molecular Imaging and Biology*. I was the primary data collector and composed the manuscript. Wuest M assisted with data collection (particularly PET imaging), data analysis, and manuscript edits. Meng G assisted with data collection (Immunohistochemistry) and contributed to the manuscript. Briard E and Auberson YP contributed by synthesizing the precursor and blocking compound and provided manuscript edits. McMullen T acquired and supplied the 8305C cell line and was involved in concept formulation. Brindley D supplied the 4T1 cell line and was involved in concept formulation. Wuest F was the supervisory author and was involved in concept formation

and manuscript edits. All animal experiments were performed according to guidelines from the Canadian Council on Animal Care (CCAC) and approved by the local animal care committee (Cross Cancer Institute, University of Alberta).

ACKNOWLEDGEMENTS

First, I would like to acknowledge and thank my supervisor, Dr Frank Wuest, for his guidance, support, and patience. His expansive knowledge, infectious motivation, and profound generosity created an atmosphere of trust and teamwork which has been invaluable in my professional and personal growth. The experiences afforded to me through his mentorship and through membership in his group have been transformative.

Next, I would like to thank the many members of my lab for their wisdom, patience, and contributions to my work and training. Particularly, I would like to mention the guidance and knowledge provided by Dr Melinda Wuest, with whom I often worked closely and who guided me through experimental planning and interpretation. Special thanks also go out to Daniel Krys, Cody Bergman, Dr. Stephanie Mattingly, Jennifer Dufour, Jenilee Way, Dr. Susan Pike, and all other members of the Wuest group for their guidance and collegiality.

I would also like to thank the members of my supervisory committee Dr. David Brindley, for always making time to speak with me and for his invaluable suggestions, and Dr. Todd McMullen, who despite his demanding schedule always conveys enthusiasm and provides encouragement.

I would like to acknowledge all the funding I have received during my graduate work. I thank the Dianne and Irving Kipnes Foundation for their generous support of the Wuest laboratory group. I also acknowledge the Alberta Cancer Foundation (ACF) Antoine Noujaim Graduate Studentship, the Faculty of Medicine and Dentistry (FoMD) 75th Anniversary Award from the University of Alberta, the Faculty of Graduate Studies and Research (FGSR) for the awarding of the Master's level Queen Elizabeth II Graduate Scholarship, and Faculty of Graduate Studies and Research & Student Aid Alberta for awarding the Alberta Graduate Student Scholarship. I would also like to acknowledge the travel funding which has been provided to me including the Mary Louise Imrie

Graduate Student Award by the Faculty of Graduate Studies and Research, and the Brian and Gail Heidecker Graduate Travel Award by the Department of Oncology; both of which allowed me to travel to and participate in 23rd International Symposium on Radiopharmaceutical Sciences in Beijing, China during May, 2019.

I would like to thank Dave Clendening and Blake Lazurko from the Edmonton PET centre for radionuclide production. I also thank Dan McGinn (Vivarium of the Cross Cancer Institute, Edmonton, Alberta, Canada) for supporting the animal work and Dr./ Hans-Soenke Jans (Department of Oncology, University of Alberta) for technical support of the preclinical PET imaging facility.

Finally, I would like to thank my wife for her unwavering support and constant encouragement, and for always listening and trying to understand. I would also like to thank my children, Lucas and Rosalind, for providing a necessary distraction and keeping me motivated and centered.

TABLE OF CONTENTS

CHAPTER 1: Introduction	1
1.1. THE ROLE OF INFLAMMATION IN CANCER.....	2
1.1.1. Hallmarks of Cancer.....	2
1.1.2. Summary of Acute Inflammation.....	3
1.1.3. Resolution of Inflammation.....	7
1.1.4. Development and Propagation of Chronic Inflammation.....	10
1.2. THE CONTRIBUTION OF INFLAMMATION TO THE ACQUISITION OF CANCER HALLMARKS.....	12
1.2.1. Sustained Proliferative Signalling.....	14
1.2.2. Activating Invasion and Metastasis.....	14
1.2.3. Inducing Angiogenesis.....	16
1.2.4. Resisting Cell Death.....	17
1.2.5. Avoiding Immune Destruction.....	17
1.2.6. Production of Reactive Oxygen and Nitrogen Species.....	20
1.3. INFLAMMATORY BIOMARKERS AS INDICATORS OF TUMOR PROMOTION AND PROGRESSION.....	22
1.3.1. The Role of Cyclooxygenase-2 in Inflammation and Cancer.....	24
1.3.2. The Role of Autotaxin in Inflammation and Cancer.....	25
1.3.3. The Relationship of Autotaxin and Cyclooxygenase-2.....	28
1.4. POSITRON EMISSION TOMOGRAPHY.....	29
1.4.1. The Imaging of Biomarkers.....	29
1.5. HYPOTHESIS AND OBJECTIVES.....	30
1.5.1. Hypothesis.....	30
1.5.2. Objectives.....	31
1.6. REFERENCES.....	32
CHAPTER 2: Radiosynthesis and biological evaluation of [¹⁸F]triacoxib: a radiotracer for PET imaging of COX-2	45
2.1. INTRODUCTION.....	49
2.2. MATERIALS AND METHODS.....	52
2.2.1. General.....	52

2.2.2.	Chemistry.....	53
2.2.3.	Radiochemistry.....	54
2.2.4.	Determination of lipophilicity.....	54
2.2.5.	<i>In vitro</i> cell uptake studies	55
2.2.6.	Animal model.....	56
2.2.7.	Radiometabolite analysis.....	56
2.2.8.	PET imaging.....	56
2.2.9.	Autoradiography.....	57
2.2.10.	Immunohistochemistry.....	58
2.2.11.	Statistical analysis.....	58
2.3.	RESULTS.....	59
2.3.1.	Chemistry.....	59
2.3.2.	Radiochemistry.....	61
2.3.3.	Lipophilicity	62
2.3.4.	Cellular uptake and inhibition studies	62
2.3.5.	Radiometabolite analysis	63
2.3.6.	PET imaging in HCA-7 tumor-bearing mice.....	64
2.3.7.	Organ distribution.....	68
2.3.8.	Autoradiography and immunohistochemistry.....	69
2.4.	DISCUSSION.....	70
2.5.	CONCLUSION.....	77
	ACKNOWLEDGEMENTS.....	77
	AUTHOR CONTRIBUTIONS.....	78
2.6.	SUPPLEMENTAL INFORMATION.....	79
2.6.1.	The determination of brown adipose tissue uptake.....	79
2.6.2.	Chemical synthesis.....	81
2.6.3.	Radiochemical synthesis – alternative routes.....	85
2.6.4.	Molar activity calculations.....	89
2.6.5.	Dynamic PET-derived biodistribution data.....	91
2.6.6.	NMR spectra.....	92
2.6.7.	HPLC traces.....	97

2.6.8.	Radio-TLC traces.....	99
2.7	REFERENCES.....	100
CHAPTER 3: <i>In vivo</i> imaging of autotaxin in thyroid and breast tumor models using		
	[¹⁸F]PRIMATX.....	110
3.1.	INTRODUCTION.....	113
3.2.	MATERIALS AND METHODS.....	115
3.2.1.	General.....	115
3.2.2.	Radiochemistry.....	116
3.2.3.	Determination of lipophilicity.....	117
3.2.4.	Animal models.....	118
3.2.5.	Immunohistochemistry.....	118
3.2.6.	Radiometabolite analysis.....	119
3.2.7.	PET imaging.....	119
3.2.8.	Statistical analysis.....	120
3.3.	RESULTS.....	121
3.3.1.	Radiochemistry.....	121
3.3.2.	Lipophilicity.....	121
3.3.3.	Radiometabolite analysis.....	121
3.3.4.	PET imaging in 4T1 murine breast tumor-bearing mice.....	123
3.3.5.	Immunohistochemical ATX staining in 8305C human thyroid cancer tissue..	124
3.3.6.	PET imaging and <i>in vivo</i> blocking in human thyroid 8305C tumor-bearing Mice.....	124
3.3.7.	Blocking effect on radiotracer brain and joint uptake and clearance profile...	127
3.4.	DISCUSSION	128
3.5.	CONCLUSION.....	132
	ACKNOWLEDGEMENTS.....	133
	AUTHOR CONTRIBUTIONS.....	133
3.6.	SUPPLEMENTAL INFORMATION.....	134
3.6.1.	Baseline PET imaging with 8305C thyroid tumors.....	134
3.6.2.	Radiotracer uptake under baseline vs two blocking conditions.....	135
3.6.3.	Molar activity calculations.....	136

3.6.4.	HPLC traces.....	137
3.6.5.	Radio-TLC traces.....	139
3.7.	REFERENCES.....	140
CHAPTER 4: <i>In vivo</i> imaging of autotaxin in a thyroid tumor model using		
	[¹⁸F]F-GLPG1690	149
4.1.	INTRODUCTION.....	150
4.2.	MATERIALS AND METHODS.....	150
4.2.1.	General.....	150
4.2.2.	Chemistry.....	151
4.2.3.	Radiochemistry.....	153
4.2.4.	Animal model.....	154
4.2.5.	PET imaging.....	154
4.2.6.	Statistical analysis.....	155
4.3.	RESULTS.....	156
4.3.1.	Chemistry.....	156
4.3.2.	Radiochemistry.....	157
4.3.3.	PET imaging in human thyroid 8305C tumor-bearing mice.....	158
4.4.	DISCUSSION.....	159
4.5.	CONCLUSION.....	161
	ACKNOWLEDGEMENTS.....	161
	AUTHOR CONTRIBUTIONS.....	162
4.6	SUPPLEMENTAL INFORMATION.....	163
4.6.1.	NMR spectra.....	163
4.6.2.	HPLC traces.....	164
4.6.3.	Radio-TLC traces.....	166
4.7	REFERENCES.....	167
CHAPTER 5: Discussion, Conclusions, and Future Directions.....		
5.1.	DISCUSSION.....	170
5.2.	CONCLUSIONS.....	177
5.3.	FUTURE DIRECTIONS.....	178
5.4.	REFERENCES.....	181

BIBLIOGRAPHY..... 187

List of Tables

Chapter 2.

Table 1. Biodistribution (static PET-derived data) for [^{18}F]triacoxib ($n=4$)

Table 2. Reaction conditions for the four triacoxib radiofluorination attempts using the trimethyl anilinium alkyne radiolabelling precursor

Table 3. [^{18}F]fluoride incorporation for the four triacoxib radiofluorination attempts using the trimethyl anilinium alkyne labelling precursor

Table 4. [^{18}F]fluoride incorporation for both triacoxib radiofluorination attempts using the nitrated triacoxib radiolabelling precursor

Table 5. Reaction conditions for the six radiofluorination attempts using the trimethyl anilinium triacoxib radiolabelling precursor

Table 6. [^{18}F]fluoride incorporation for the six radiofluorination attempts using the trimethyl anilinium triacoxib radiolabelling precursor

Table 7. Biodistribution (dynamic PET-derived data) for [^{18}F]triacoxib ($n=4$; except kidneys 8/4)

List of Figures

Chapter 1.

Figure 1. The hallmarks of cancer

Figure 2. The autotaxin (ATX)-cyclooxygenase-2 (COX-2)-inflammatory cycle

Chapter 2.

Scheme 1. Synthesis of triacoxib reference compound and radiolabelling precursor

Scheme 2. Late-stage radiofluorination of [^{18}F]triacoxib

Figure 3. [^{18}F]triacoxib uptake into HCA-7 cells *in vitro*

Figure 4. [^{18}F]triacoxib *in vivo* metabolic stability and blood distribution

Figure 5. [^{18}F]triacoxib *in vivo* PET images (mouse with colorectal tumor) with associated time activity curve

Figure 6. [^{18}F]triacoxib *in vivo* PET images under control and blocking conditions

Figure 7. [^{18}F]triacoxib autoradiography and COX-2 immunohistochemistry under control and blocking conditions

Scheme 3. The various attempted routes to producing [^{18}F]triacoxib

Graph 1. HPLC standard curve for [^{18}F]triacoxib molar activity

Figure 8. [^{18}F]triacoxib *in vivo* PET images (mouse with colorectal tumor) with delineated infrascapular brown adipose tissue

Figure 9. ^1H NMR spectrum of the boropinacol ester-triacoxib radiolabelling precursor

Figure 10. ^{13}C NMR spectrum of the Boropinacol ester-triacoxib radiolabelling precursor

Figure 11. ^1H NMR spectrum of the aminopyrazole (precursor to azide)

Figure 12. ^1H NMR spectrum of the azide (CuAAC reagent)

Figure 13. ^{13}C NMR spectrum of the azide (CuAAC reagent)

Figure 14. ^1H NMR spectrum of the nitro-triacoxib radiolabelling precursor

Figure 15. ^1H NMR spectrum of the trimethyl anilinium triacoxib radiolabelling precursor

Figure 16. ^{13}C NMR spectrum of the trimethyl anilinium triacoxib radiolabelling precursor

Figure 17. ^1H NMR spectrum of the ^{19}F triacoxib non-radioactive standard

Figure 18. ^{13}C NMR spectrum of the ^{19}F triacoxib non-radioactive standard

Figure 19. ^{19}F NMR spectrum of the ^{19}F triacoxib non-radioactive standard

Figure 20. HPLC trace of the ^{19}F triacoxib non-radioactive standard

Figure 21. HPLC trace of the ^{18}F triacoxib crude reaction mixture

Figure 22. HPLC trace of the purified ^{18}F triacoxib radiotracer

Figure 23. Radio-TLC trace of the ^{18}F triacoxib crude reaction mixture

Figure 24. Radio-TLC trace of the purified ^{18}F triacoxib radiotracer

Chapter 3.

Scheme 4. Radiofluorination of labelling precursor to produce radiotracer ^{18}F PRIMATX

Figure 25. ^{18}F PRIMATX *in vivo* metabolic stability and blood distribution

Figure 26. ^{18}F PRIMATX *in vivo* PET image (mouse with breast tumor) with associated time activity curve

Figure 27. Immunohistochemical detection of autotaxin in human thyroid tumor tissue

Figure 28. ^{18}F PRIMATX *in vivo* PET images (mouse with thyroid tumor) under control and blocking conditions with associated time activity curves

Figure 29. PET-derived time-activity curves (from mouse with thyroid tumor) showing ^{18}F PRIMATX uptake into brain, joints, and clearance organs

Figure 30. [^{18}F]PRIMATX *in vivo* PET image (mouse with thyroid tumor) with associated time activity curve

Figure 31. Time-activity curve of [^{18}F]PRIMATX radiotracer uptake in the thyroid tumor under control and 2 blocking conditions

Graph 2. HPLC standard curve for [^{18}F]PRIMATX molar activity

Figure 32. HPLC trace of the [^{19}F]PRIMATX non-radioactive standard

Figure 33. HPLC trace of the [^{18}F]PRIMATX crude reaction mixture

Figure 34. HPLC trace of the purified [^{18}F]PRIMATX radiotracer co-injected with the [^{19}F]PRIMATX non-radioactive standard

Figure 35. Radio-TLC trace of the [^{18}F]PRIMATX crude reaction mixture

Figure 36. Radio-TLC trace of the purified [^{18}F]PRIMATX radiotracer

Chapter 4.

Scheme 5. The fluorination and nosylation of GLPG1690, and the radiofluorination of nosylated GLPG1690

Figure 37. [^{18}F]GLPG1690 *in vivo* PET image (mouse with thyroid tumor) with associated time activity curve

Figure 38. ^1H NMR spectrum of the nosylated GLPG1690 radiolabelling precursor

Figure 39. ^1H NMR spectrum of the fluorinated GLPG1690 non-radioactive standard

Figure 40. HPLC trace of the [^{19}F]F-GLPG1690 non-radioactive standard

Figure 41. HPLC trace of the [^{18}F]F-GLPG1690 crude reaction mixture

Figure 42. HPLC trace of the purified [^{18}F]F-GLPG1690 radiotracer co-injected with the [^{19}F]F-GLPG1690 non-radioactive standard

Figure 43. Radio-TLC trace of the [^{18}F]F-GLPG1690 crude reaction mixture

Figure 44. Radio-TLC trace of the purified [^{18}F]F-GLPG1690 radiotracer

List of Abbreviations

%ID/g	% injected dose per gram
[¹⁸ F]FDG	2-deoxy-2-[¹⁸ F]fluoro-D-glucose
[¹⁸ F]FLT	[¹⁸ F]fluorothymidine
ACC	animal care committee
ALS	amyotrophic lateral sclerosis
ATX	autotaxin
BALBc	Bagg albino mice
BAT	brown adipose tissue
BBB	blood-brain barrier
BCA	bicinchoninic acid
C-18	carbon-18
CA	carbonic anhydrase
CCAC	canadian council on animal care
CCI	cross cancer institute
CDCl ₃	deuterated chloroform
COX	cyclooxygenase
CuAAC	copper-mediated alkyne azide cycloaddition
d	doublet
DAST	diethylamino sulfur trifluoride
DCM	dichloromethane / ethylene chloride
EDTA	ethylenediaminetetraacetic acid
ENPP2	ectonucleotide pyrophosphatase phosphodiesterase 2

EtOAc	ethyl acetate
GADD	growth-arrest DNA damage-inducible genes
GBq	gigabecquerel
GPCR	G-protein coupled receptor
HCA-7	human colon carcinoma cell line
HPLC	high performance liquid chromatography
HR-MS	high resolution mass spectrometry
i.p.	intraperitoneal
IHC	immunohistochemistry
IPF	idiopathic pulmonary fibrosis
KBq	kilobecquerel
LPA	lysophosphatidic acid
LPAR	lysophosphatidic acid receptor
LPC	lysophosphatidyl choline
m	multiplet
MAP	maximum a posteriori
MeOH	methanol
MIP	maximum intensity projection
MS	multiple sclerosis
n	neutron, as in (p,n)
n.c.a.	no carrier added
n-BuOH	n-butanol
nosylate	4-nitrobenzenesulfonate

NSAID	non-steroidal anti-inflammatory drugs
NSG	nod scid gamma mice
O.C.T.	optimal cutting temperature
OSEM	ordered subset expectation maximization
p	proton, as in (p,n)
PDK-1	phosphoinositide-dependent kinase 1
PET	positron emission tomography
PFP	polyfluorophenyl
PGE ₂	prostaglandin E ₂
PGH ₂	prostaglandin H ₂
PKB	protein kinase B
q	quartet
qd	quartet of doublets
RA	rheumatoid arthritis
Radio-TLC	radio-thin layer chromatography
R _f	retention factor
RIPA	radioimmunoprecipitation buffer
ROI	region of interest
s	singlet
SUV	standard uptake value
t	triplet
T/M	tumor-to-muscle ratio
WAT	white adipose tissue

TAC	time activity curve
TBST	Tris-buffered saline having 0.5% Tween 200
TEA	triethyl amine
TGS	target guided synthesis
TLC	thin layer chromatography

CHAPTER 1
INTRODUCTION

1.1. The Role of Inflammation in Cancer

1.1.1. Hallmarks of cancer

Tumor, a word of Latin origin meaning “to swell”, is often used to describe masses of neoplastic growth, which when malignant, are commonly called cancer. As some of the earliest recorded medical observations of cancer centered around localized tissue swelling, it is easy to see that despite lacking an in-depth molecular understanding of their interconnectivity, inflammation has an historic association with cancer.¹ In the centuries since these associations were made, especially the last two decades, a lot of information regarding the roles of inflammation in cancer has been established.

In the first of two widely influential articles on the hallmarks of cancer, Hanahan and Weinberg discuss 6 acquired capabilities which made cancer cells more able to survive *in vivo*, successfully proliferate, and to invade and colonize surrounding and distant tissues.^{2,3} These hallmarks are 1) sustaining proliferative signaling, 2) evading growth suppressors, 3) activating invasion and metastasis, 4) enabling replicative immortality, 5) inducing angiogenesis, and 6) resisting cell death. Notably, despite the historic association of inflammation and cancer, there was no hallmark dedicated to cancer-related inflammation. At that time, despite the knowledge that many tumors displayed high levels of infiltration by both adaptive and innate immune cells, the predominant explanation for their presence was still that they were completing an anti-tumoral role, and that their presence was merely a strategy by the body to fight the cancer.² Over the last two decades, however, a true appreciation for the contributions of immune cell infiltration, and subsequent inflammation, has developed. In the second of their articles on the hallmarks of cancer, Hanahan and Weinberg recognized tumor-promoting inflammation as an enabling hallmark because of how

the presence of immune cells in the tumor microenvironment directly contributes to the development of several other cancer hallmarks.

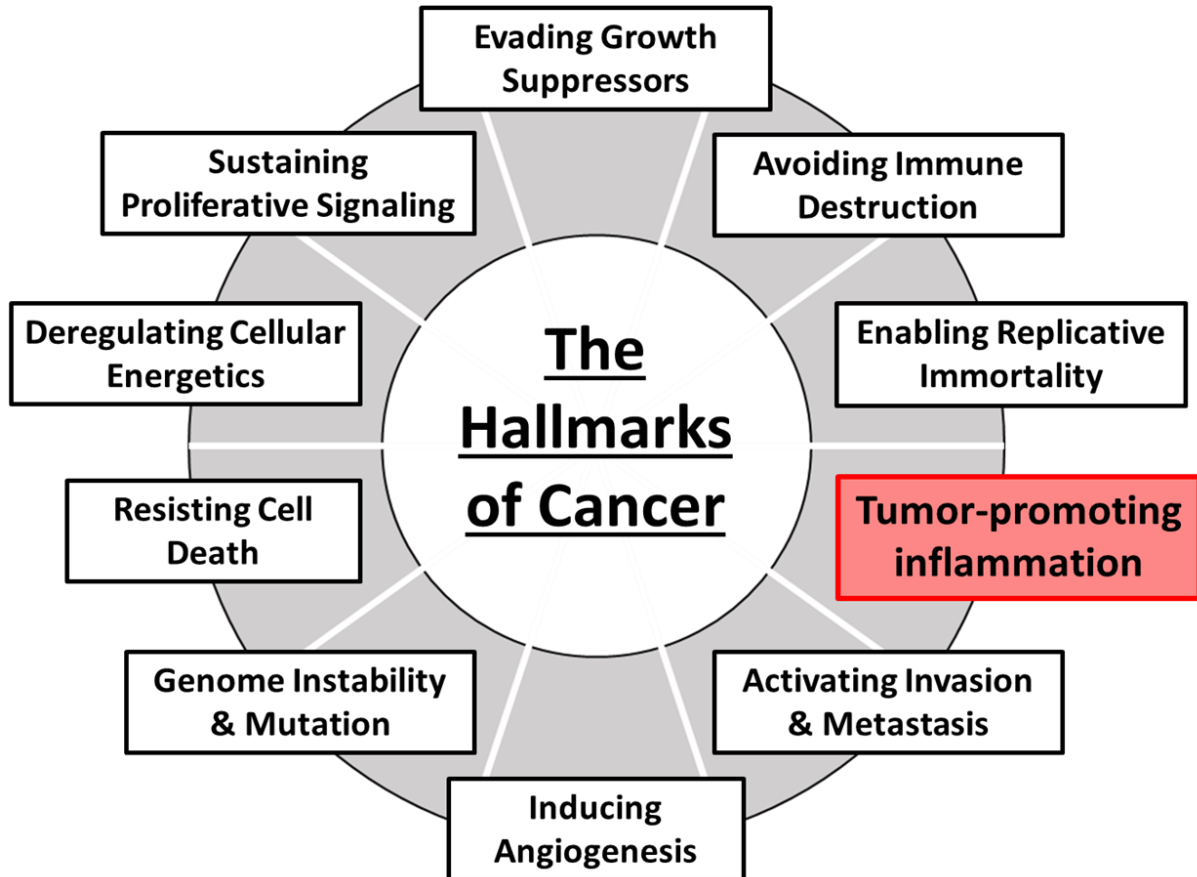


Figure 1. Tumor promoting inflammation added to the hallmarks of cancer. Adapted from Hallmarks of Cancer: The Next Generation by Hanahan and Weinberg, *Cell*, 2011.²

1.1.2. Summary of acute inflammation

When defined simply, inflammation involves the movement of fluid, proteins, and white blood cells from the blood stream to the site of tissue damage or infection, and displays the classical indicators: heat, redness, swelling, and pain.⁴

Acute inflammation is the immediate response of the innate immune system to insults such as infection, tissue damage/necrosis, the presence of foreign bodies, or self/environmental antigens.⁵ Invading microbes and dead cells release substances with recognizable molecular motifs called pathogen/associated molecular patterns (PAMPs) or damage-associated molecular patterns (DAMPs), respectively. These molecular patterns are detected by pattern recognition receptors (PRRs) such as Toll-like and NOD-like receptors (TLRs and NLRs) present on the plasma membrane, endosomal membrane, and in the cytosol of tissue-resident phagocytes, dendritic cells, mast cells, and others, including epithelial cells. The activation of NOD-like receptors by DAMPs (and some PAMPs) leads to the formation of the inflammasome protein complex, which activates caspase-I. Caspase-I cleaves pro-interleukin-1 (pro-IL-1) into IL-1 β , a secreted proinflammatory cytokine that recruits leukocytes. PRR detection of infection, tissue damage, or other insults also causes the production of tumor necrosis factor (TNF) by many cells, predominantly macrophages. PRR activation also causes the release of histamine (by mast cells) and lipid products like prostaglandins (PG; which cause pain) and leukotrienes (LT; by mast cells, leukocytes, and others). IL-1 and TNF cause the upregulation of other cytokines (like IL-6) and many chemokines by a variety of cells. Together, these cytokines, chemokines, vasoactive amines, and lipid products exert their effects on nearby vasculature to induce inflammation. Histamine, prostaglandins, and other vasoactive mediators act on vascular smooth muscle to first cause vasodilation (resultant increased blood flow is the cause of heat and redness), followed by increased permeability of the microvasculature and the movement of exudate into the extravascular tissues. The resultant loss of vascular fluid concentrates red blood cells leading to locally more viscous blood and slowed blood flow. Histamine, IL-1, and TNF cause the upregulation of P-, E-, and L-selectin on endothelial cells and leukocytes, which mediate the loose adhesion and slowing of leukocytes as they roll

along endothelium. Chemokines bound to endothelial cell proteoglycans induce leukocyte integrin activation, causing them to bind firmly to intercellular adhesion molecules (ICAMs) on the endothelia, which allows leukocytes to stop long enough to transmigrate through the vessel wall (diapedesis). Leukocytes subsequently undergo chemotactic movement toward the site of insult, attracted by bacterial products, chemokines, some components of the complement system, and lipid products like leukotrienes (especially LTB₄). Neutrophils are the most abundant leukocyte in the body and during acute inflammation they are the first to arrive and accumulate at the site of infection/injury. In general, proinflammatory cytokines and chemokines, necrotic debris, and microbial products activate leukocytes to move toward, recognize, engulf, and degrade invading microbes and necrotic cell components.⁵ IL-8, often called neutrophil chemotactic factor or CXCL8, is one of the primary chemokines responsible for chemotactic movement and activation of neutrophils (and some other leukocytes).^{4,6,7} The degradation of these components occurs in phagolysosomes of activated neutrophils and macrophages, where reactive oxygen species (ROS), reactive nitrogen species (RNS), and lysosomal enzymes can exert effects on the engulfed material without affecting the leukocytes.⁵ Additionally, phagolysosomes in neutrophils may also combine with primary or secondary granules present in the cells. Primary (azurophilic) granules are present in all polymorphonuclear (PMN) cells, or granulocytes, including neutrophils, basophils, eosinophils, and mast cells. While their contents and abundance vary by cell type, neutrophilic primary granules contain myeloperoxidase (converts H₂O₂ to OCl₂⁻), defensins (and other bactericidal factors), acid hydrolases, phospholipase A₂, elastase, collagenases, proteinase 3, cathepsin G, and other neutral proteases. Secondary granules (smaller and specific to neutrophils) contain lysozyme, lactoferrin, gelatinase, collagenase, serine proteases, histaminase, and more. Both primary and secondary granules, in addition to combining with phagolysosomes, undergo

exocytosis into the immediate environment in a process called degranulation. The release of granule enzymes into the local environment results in the degradation of many extracellular components and is an integral cause of the collateral tissue damage associated with inflammation. In order to limit that collateral damage, host cells and fluids are equipped with multiple antioxidants and antiproteases which quench free radicals or degrade granule enzymes; however, despite these protective measures, damage still occurs.

Near the start of the inflammatory response, vasodilation and increased vascular permeability result initially in edema followed by the recruitment of leukocytes.⁵ The relative abundance of neutrophils in the blood and the fact that they use cytoskeletal rearrangement to mount a rapid response means that they are the first and predominant leukocytes involved in acute inflammation. However, activated neutrophils have a relatively short lifespan of between just a few hours to about 24-48 hours before undergoing apoptosis, thus, their numbers rapidly spike at the start of inflammation, but by 24-48 hours, macrophages tend to replace them as the dominant cell type present in inflammatory exudate.^{5,8} Tissue resident macrophages are often present early on as they are located near inflammatory sites, but in general, macrophage (including monocyte derived macrophage) responses are usually slower and longer-lived because they depend on transcriptional changes in the cells.⁵ Depending on the stimuli present at the site, macrophages may be classically (M1) or alternatively (M2) activated. Classical activation of macrophages typically occurs through contact with necrotic or microbial products (also IFN- γ and colony stimulating factor-1 [CSF-1], among other things) causing PRR activation, as described above. It induces a proinflammatory phenotype resulting in macrophage production of proinflammatory cytokines, nitric oxide (NO), ROS, and lysosomal enzymes, all with the goal of destroying and clearing the offending agent. Alternative activation of macrophages results in an anti-inflammatory phenotype responsible for

anti-inflammatory cytokine production (ex. IL-10, transforming growth factor- β [TGF- β]) and various aspects of tissue repair including the secretion of growth factors responsible for promoting angiogenesis, collagen formation, and the activation of fibroblasts. Neutrophils and T lymphocytes are both able to induce an M2 phenotype in macrophages. This is achieved through the production of anti-inflammatory cytokines IL-4 and IL-13 (and several pro-resolving mediators mentioned below) and through the phagocytosis of apoptotic neutrophils.^{5,7,9} Macrophages make some crucial contributions to acute inflammation beyond cytokine production, including aiding in the clearance of damaged tissues or foreign invaders, the activation of other cells (ex. T lymphocytes through antigen displaying), and the efferocytosis of apoptotic neutrophils.⁵

In addition to the involvement of PMN leukocytes and macrophages, it appears that at least one subset of Helper T lymphocytes, T_H17 cells, are involved in acute inflammation.⁵ These proinflammatory T lymphocytes are activated by IL-1, IL-6, and PGE_2 and produce multiple cytokines, including IL-17, which acts as a promotor of neutrophil recruitment.^{5,10}

1.1.3. Resolution of inflammation

While the initiation of acute inflammation has long been recognized as the result of a series of active and necessary steps, the route by which resolution of that inflammation occurs has historically been considered a passive process.^{4,11,12} It was generally believed that the initiating chemoattractants would dissipate or become diluted to the point where their ability to cause leukocyte infiltration would disappear, leading by default to resolution. While a complete elucidation of all mechanisms within resolution is not presently available, it has been demonstrated that resolution is an active process resulting from a switch in the class of lipid mediators present at the site of inflammation.

For inflammation to be resolved several steps must occur. These steps include, but are not limited to, the cessation of PMN infiltration, the phagocytosis and removal of apoptotic PMN and other cellular debris by macrophages, reorganization of structures within the tissues and migration of new cells into this area, and an end to the cardinal signs of inflammation.⁸ The switch in lipid mediator class which brings about resolution, as mentioned above, occurs by means of proinflammatory lipid signals initiating a cascade which eventually results in the production of pro-resolving mediators.¹² It has been established that levels of several of the major lipid mediators derived from arachidonic acid, including leukotrienes, prostaglandins, and lipoxins (LX) peak at distinct times throughout the course of inflammation. High levels of leukotrienes (especially the PMN attractant LTB₄) cause increased prostaglandins (PGE₂), which are followed by high levels of lipoxins, a class of pro-resolving mediators. Specifically, it was found that treatment of PMNs with common proinflammatory prostaglandins (PGE₂ & PGD₂) leads to the upregulated transcription and processing of 15-lipoxygenase RNA – an enzyme responsible for producing lipoxins. One of the major lipoxins produced, LXA₄, acts both as a stop signal to PMN recruitment and as a stimulator of non-phlogistic phagocytosis of apoptotic neutrophils by macrophages, leading to the removal of cellular debris from the site of inflammation.¹³ In addition to lipoxins, three other classes of pro-resolving mediators (all together classified as specialized pro-resolving mediators; SPM) have been described including resolvins (resolution phase interaction products), protectins, and maresins (macrophage mediators in resolving inflammation). The exact effects exerted by SPM are not yet fully elucidated, but generally consist of resolution-directed actions including: limiting PMN infiltration, blocking LTB₄ production and receptor interactions (antagonism of pro-phlogistic receptors), inducing phagocytic cells to clear cellular debris, inducing macrophages to remove PMNs by efferocytosis, the alternate activation (M2) of

macrophages (also activated by IL-4 and IL-13), causing tissue regeneration, reducing pain, etc. Each class of SPM exerts its effects on distinct cell-surface receptors, only a few of which have been identified, resulting in cell type-specific effects. SPM are produced through multiple routes by various cells in the inflammatory exudate. Currently, they are reported to be produced through the modification of some ω -3 polyunsaturated fatty acids (PUFA) by lipoxygenase, p450, and alternative cyclooxygenase-2 (COX-2) enzymatic activity (as is seen in COX-2 acetylated by aspirin). While a perfectly detailed story of the resolution of inflammation is not yet complete, the current evidence suggests that when high enough levels of prostaglandins accumulate in the inflammatory exudate (because enough PMN have accumulated), newly arriving neutrophils are induced to prepare for resolution by beginning the production of pro-resolving mediators, an action which ultimately results in the self-limiting of inflammation.^{12,14}

Areas which undergo the initial insult go through a series of steps in order to restore homeostasis. If a wound is present, platelets aggregate and act to plug it, preventing bleeding and providing structural support to incoming inflammatory cells.⁵ During inflammation, M1 macrophages clear cellular debris while M2 macrophages (also stromal and epithelial cells) release growth factors which act on nearby cells. Damaged tissue is usually repaired through a variable mixture of two processes, regeneration and fibrosis (scar formation), the balance of which often depends on the degree of intact extracellular matrix (ECM). Both of these processes are stimulated by growth factors released by macrophages. Regeneration is characterized by the proliferation and inward migration of uninjured cells (or tissue stem cells) adjacent to the injury and is a process dependant on the proliferative abilities of the cells (ex. very successful in liver but not successful in cardiac muscle). Epidermal growth factor (among several others) stimulates epithelial cells to proliferate and migrate inward to seal off the wound.¹⁵ Fibroblast growth factors (FGF) and vascular

endothelial growth factors (VEGF) released by macrophages lead to angiogenesis by inducing the proliferation of endothelial cells and their migration to the site of damage.⁵ Platelet-derived growth factor (PDGF) aids in angiogenesis by recruiting smooth muscle cells to support new blood vessels. FGF and PDGF cause fibroblasts to migrate to the damage site where they deposit connective tissue, and TGF- β subsequently suppresses the proliferation of endothelial cells and upregulates the production and deposition of extracellular matrix (ECM) proteins. The laying down of connective tissue where cells could not fully regenerate is called fibrosis or scarring. The last step, remodeling of the wound, involves a reorganization and contraction of the collagen scar tissue to increase its strength. Taking weeks to years, this process first involves wound contraction by myofibroblasts followed by the replacement of the collagen (III) fibers for stronger, tighter linking collagen (I). Then, over a long period, matrix metalloproteinases (MMP) released by macrophages, neutrophils, fibroblasts, and epithelial cells degrade the collagen and other ECM proteins and the size of the scar is reduced.

1.1.4. Development and propagation of chronic inflammation

Chronic inflammation is a longer-lived inflammatory response characterized by ongoing recruitment of immune cells and continuing tissue damage occurring simultaneously with efforts to repair and heal the wound.⁵ Chronic inflammation usually develops when the initial insult causing inflammation is not removed. This may manifest through a persistent infection, allergies (a response to normally innocuous environmental antigens), autoimmune disorders (a response to self-antigens), or long-term toxic exposures. Additionally, in some cases, the collateral damage caused by the inflammatory response itself becomes the defining characteristic and the main reason that the disease state perpetuates.

While the dominant cells of acute inflammation tend to be neutrophils, sites of chronic inflammation are predominantly populated by macrophages, T and B lymphocytes, and plasma cells, often possessing a smaller neutrophilic component.⁵ Despite having relatively few neutrophils, many aspects of collateral damage mentioned in association with acute inflammation are continued, and even magnified, in the chronic inflammatory reaction. Much of the reason why chronic inflammation can last so long while increasing in intensity is related to how the cells involved work to activate each other. Classically activated (M1) macrophages release pro-inflammatory cytokines and mediators (IL-1, TNF, IL-12, chemokines, and lipid mediators), engage in cell-cell interactions with lymphocytes using co-stimulator molecules, and use major histocompatibility complex II (MHC class II) to perform antigen presentation, all of which activate T cells. T_H1 cells then produce cytokines, like TNF, chemokines, and interferon gamma (IFN- γ), which recruit and classically activate more macrophages.

While the classical (M1) and alternative (M2) activation of macrophages has been briefly discussed, the reality is that macrophage activation occurs on a spectrum from M1 to M2, with many potential phenotypes existing in between these two extremes. (Nielson) This means that individual macrophages can possess various M1 or M2 associated characteristics simultaneously, such as ROS production, angiogenic signaling, or mixed cytokine production. The various abilities of macrophages present in pre-malignant or malignant environments can contribute to tumorigenesis. Within these environments, macrophages approximating the M1 phenotype release pro-inflammatory cytokines and lipid mediators causing the recruitment of additional immune cells (which can cause cytotoxic and structural damage) and protect cells from apoptosis, as discussed later on. Meanwhile, M2 phenotype can release a range of pro-tumorigenic factors including VEGF, placental growth factor (PlGF), EGF, MMPs, and FGF which lead to continuous

angiogenesis and vascularization, tumor cell motility, and the recruitment of fibroblast and subsequent deposition of scar tissue, respectively. As this environment contains both pro-inflammatory and anti-inflammatory signalling and cell groups affecting aspects of both damage and repair, they often develop into sites of chronic inflammation.

In addition to the many influences of macrophages in tumorigenesis, other cells contribute to chronic inflammation, including T and B lymphocytes which are directly activated by microbes and other antigens. Activated B lymphocytes and plasma cells, sometimes present in chronic inflammation, are capable of producing antibodies against foreign-, self-, or altered self-antigens, though it is not entirely clear what level of involvement they have in chronic inflammation.

Beyond T_H1 and T_H17 proinflammatory phenotypes already discussed, an anti-inflammatory phenotype, T_H2 can be present at the site of chronic inflammation.⁵ These T cells release anti-inflammatory cytokines IL-4 and IL-13 which induce the alternative activation of macrophages along with the subsequent production of anti-inflammatory, pro-regenerative, and pro-fibrotic signalling molecules.

1.2. The contribution of inflammation to the acquisition of cancer hallmarks

A generic description of several key components of acute and chronic inflammation has been discussed above. It is the focus of this work, however, to discuss crucial aspects of chronic inflammation, not only from a generic point of view, but from a cancer-specific point of view. A consideration of cancer-specific inflammation is necessary because unique circumstances and complexity inherent to cancer complicate the influence exerted by inflammation.

The nature of cancer associated chronic inflammation involves the recruitment of immune cells, continuing tissue damage, and attempts at wound healing occurring simultaneously in and around

solid tumors.^{2,5} This occurs through the simultaneous recruitment and/or proliferation of both pro- and anti-inflammatory immune cells, as well as a range of cells with intermediate phenotypes. Many distinct signalling and effector molecules can be found within the tumor, produced by and interacting with immune cells, cancer cells, and stromal cells.^{2,16} The influence that these signals exert on other cells depends not only on their presence or absence from the tumor microenvironment (TME), but also on their concentrations and on the identity and phenotype of the effected cells. Historically, immune cells located within the tumor were thought to be playing a purely anti-tumoral role.² However, it has now been established that cells with varying identities and phenotypes play conflicting pro- and anti-tumoral roles, ultimately driving chronic inflammation and tumor progression. The ability to drive tumor progression comes from the various contributions that inflammation makes within this complex signaling environment to help tumors acquire the cancer-specific characteristics that we call the hallmarks of cancer.

There is much to be said regarding the roles that immune cells play within the TME. The complex signalling webs formed by cross-talk between immune cells and tumor cells are not only unique between tumor types, but also between individuals with the same cancers, between primary and metastatic lesions within the same individual, and between two time points within the same primary tumor. These signalling relationships seem to be constantly changing as the tumor develops. In the interest of conciseness, I will limit the discussion by giving a few salient examples of the signalling relationships which help establish each hallmark. The hallmarks we will be considering are sustained proliferative signalling, activating invasion and metastasis, inducing angiogenesis, resistance to cell death, and avoiding immune destruction. Additionally, I will discuss the secondary effects of ROS and RNS produced by immune cells, how they influence cell

signalling, and how they aid in acquiring another enabling characteristic, genome instability and mutation.

1.2.1. Sustained proliferative signalling

Several of the signalling molecules involved in the sustaining of proliferation are some of the most common cytokines found in inflammation, as discussed above.

IL-6 directly activates the Janus kinase/signal transducers and activators of transcription (JAK/STAT) factors STAT 1 and STAT3.¹⁷⁻¹⁹ Through its activation of STAT3 and subsequent activation of cell cycle regulators, IL-6 promotes cell division. IL-6 also represses P21, a cell cycle checkpoint, and upregulates cyclin D1 expression, facilitating the progression of tumor cells through cell division.

IL-10 produced by tumor-associated macrophages (TAM) has also been shown to induce tumor cell proliferation, though this occurred through c-Met/STAT3 signalling.²⁰ IL-10 induction of tumor cell proliferation seems to be an active topic of discovery.

IL-17, a pro-inflammatory cytokine produced by T_H17 cells, induces the activation of the MAPK/ERK pathway in multiple breast, skin, and gastric cancer cell lines, resulting in cellular proliferation and tumor growth.²¹

More will be said regarding the role of growth factors, especially EGF, further down.

1.2.2. Activating invasion and metastasis

A relationship was shown to exist between tumor cells and TAMs in breast cancer xenografts and metastatic breast cancer mouse models which promoted tumor cell migration and tissue invasion.²²

This relationship consists of tumor cells producing CSF-1, a stimulating factor which induces the

expression of EGF by macrophages. The EGF, normally used to stimulate cells to cover wounds, then interacts with tumor cells, causing them to proliferate and become migratory. As CSF-1 receptors are unique to macrophages, this CSF-1-EGF paracrine signalling interaction requires macrophages be present. Inhibition of these signaling molecules results in fewer circulating tumor cells. Importantly, the loss of IL-4 leads to a drastic reduction in metastatic potential, suggesting an M2-resembling macrophage phenotype is a necessary component of the relationship.^{22,23}

Another hurdle which invasive cells must jump in order to escape the tumor is a physical barrier, the ECM, which must be broken down sufficiently for cells to pass through on their way to the blood stream.²² As mentioned above, macrophages produce MMPs and proteases during activities like wound remodeling.⁵ In the context of metastasis, MMPs and proteases (cathepsins, serine proteases, etc.) degrade the ECM, allowing migratory tumor cells to leave the tumor.²²

TAMs and Myeloid-derived suppressor cells (MDSC) play a role in stimulating epithelial-to-mesenchymal transition (EMT).²⁴ TAMs and MDSCs at the primary tumor site release TGF- β and hepatocyte growth factor (HGF). Through complex signaling relationships, these growth factors induce tumor cells to undergo EMT.^{19,23,24} Notably, the participation of TGF- β in inducing EMT is a salient example of how the TME can subvert the normal functions of cytokines so that they work in the tumor's favor; in this case turning a tumor suppressing factor into a tumor promotor.^{19,24,25}

Immune cells also play a role in aiding metastatic cells of some cancer models to colonize distant sites.^{22,24,26} Bone marrow-derived myeloid progenitor cells, precursors to immune cells, are recruited to potential sites of metastasis to establish a local microenvironment which is predisposed to facilitate metastatic growth. Within the premetastatic niche, as it has been called, myeloid cells

secrete versican, an ECM proteoglycan which leads to tumor cell proliferation and mesenchymal-to-epithelial transition (MET) at the metastatic site.^{24,26}

1.2.3. Inducing angiogenesis

Macrophages play a significant role in the process of angiogenesis during tumorigenesis and later during tumor progression.²² When CSF-1 levels are curtailed, there is a significant reduction in angiogenesis and tumor growth. Conversely, when CSF-1 levels are upregulated at early stages of cancer formation there is a premature switch to accelerated vascularization and malignancy. In support of this, it has been noted that macrophage density in breast cancer correlates with microvessel density.

Hypoxia is a condition describing inadequate oxygen levels in a given tissue environment.^{27,28} This condition frequently occurs in solid tumors, as they grow so quickly and densely that vasculature, at least a first, is lacking, leading to differential oxygen perfusion throughout the tumor. In situations where hypoxia is prolonged and substantial, necrosis can and often does occur.²⁸ Macrophages tend to be more highly associated with areas of hypoxia and necrosis.²² This occurs because macrophages present in those regions produce hypoxia-inducible factor 1 alpha (HIF1 α) constitutively. HIF1 α production leads to the recruitment of more macrophages (even without CSF-1) through the induction of chemokines such as CCL-2, a monocyte chemoattractant protein. Thus, this signalling leads to an increase in the numbers of macrophages, all producing HIF1 α , at the sites of hypoxia. In addition to monocyte recruitment, HIF1 α production leads to the transcription of several genes related to angiogenesis, including VEGF. These pro-angiogenic factors then induce vascularization of necrotic regions.

Another contribution of neutrophils, macrophages, and fibroblasts to angiogenesis, in ovarian, cervical, and colorectal carcinomas, is the production of MMP9.^{22,24,29,30} In some cancers, such as these, VEGF is less readily bioavailable. Thus, through its ECM remodeling actions, MMP9 produced by immune cells causes the release of sequestered or ECM-bound VEGF from cancer cells, allowing for its participation in angiogenesis (in addition to invasion and metastasis).²²

1.2.4. Resisting cell death

TNF- α , one of the most common proinflammatory cytokines, can activate at least 4 different signalling pathways through TNF- α receptor binding.¹⁹ These pathways include both proapoptotic (through FADD and Caspase 8) and antiapoptotic (activation of cIAP-1) signalling relationships. TNF- α , expressed by both innate and adaptive immune cells, can contribute to a tumor's ability to resist cell death through NF- κ B signalling.³¹ NF- κ B, a transcription factor related to cellular proliferation, angiogenesis, and cell survival, induces the transcription of antiapoptotic proteins which actively compete against any proapoptotic factors which may be present in the cell.

Another common pro-inflammatory cytokine, IL-6, also contributes to the ability of tumor cells to resist cell death.^{17,19} As discussed above, IL-6 directly activates the JAK/STAT factors STAT 1 and STAT3. STAT3 induces the transcription of anti-apoptotic genes Bcl-x1, Bcl-2, and Mcl-1, leading to increased cell survival during adverse conditions.¹⁷

In some breast cancers, IL-4 produced by T_H2 cells confers resistance to apoptosis.³²

1.2.5. Avoiding immune destruction

Normally, natural killer (NK) cells of the innate immune system and cytotoxic T lymphocytes (CTL) of the adaptive immune system would both have anti-cancer cell cytotoxicity.³² They

directly or indirectly detect cancer cells and use granzyme B and perforin to destroy the cells, or express apoptotic ligands, ultimately triggering apoptosis within the cells.³³ NK cells target cells lacking the class I MHC, an antigen presentation complex that presents peptide fragments from within the cell for inspection by T cells, and are strongly inhibited by cells possessing MHC class I.³³ If the peptide fragments presented by the class I MHC are transformed, as may be seen in the development of tumor antigens, the T cell will be activated to kill the aberrant cell. The cytotoxic abilities of these common anti-tumor immune cells can be suppressed with assistance from immune cells. Regulatory T (T_{reg}) cells suppress the anti-tumoral activities of CTLs and NKs both indirectly, and directly. Indirectly, they increase local concentrations of immunosuppressive factors TGF- β and IL-10, which results in the inhibition of T cell proliferation and cytokine production.³⁴ Additionally, TGF- β and IL-10 can cause changes in the anti-body production by B cells, taking them from pro-inflammatory IgE to non-inflammatory IgA and IgG4. T_{reg} cells, among others, can also express cell surface ligands corresponding to cytotoxic-T-lymphocyte-associated protein 4 (CTLA-4) and programmed death – 1 (PD-1): T cell surface inhibitory receptors.^{32,33} Production of these ligands allows T_{reg} cells to prevent CTL activation, thus helping tumor cells avoid immune destruction.³² T_{reg} cells can also directly suppress CTLs and NKs through cytosolic induction of apoptosis using granzyme and perforin. In several cancers the presence of T_{reg} cells is correlated with a worse prognosis.

In normal tissues, regulatory B (B_{reg}) cells recognize antigens and regulate the presentation of antigens which allows them to help regulate the activity of cells that detect antibodies.³⁵ They also use the expression of anti-inflammatory cytokines and ligands of T cell inhibitory surface receptors (PD-L1) to suppress immune responses.

T_H cells also have pro- or anti-inflammatory effects on the tumor, depending on which subtypes are present.³² While the pro-inflammatory T_{H1} cells promote immune surveillance, T_{H2} cells release anti-inflammatory cytokines which inhibit T cell cytotoxicity, resulting in less T cell mediated cell death.

Macrophage-derived IL-10 induces PD-L1 expression in monocytes.²² PD-L1 expressing monocytes interact with CTLs, suppressing their cytotoxic responses, resulting in reduced cell killing. Alternatively, through the expression of cytokines (IL-10, TGF- β , PGE₂) and arginase-1, TAMs help to prevent T cell activation.³⁵

Myeloid-derived suppressor cells (MDSC) are perhaps one of the most important cells in the preservation of the tumor microenvironment, and are a mainstay in immunosuppression.³⁶ Originally identified for their suppression of T cell function and proliferation, these cells are a heterogeneous collection of immature myeloid cells which can be formed and recruited through the influence of PGE₂.^{22,37} MDSC themselves produce PGE₂ and together they establish a positive feedback loop upregulating MDSC function, including the production of immunosuppressive factors (IL-10, IDO, PGE₂).³⁷

Additionally, MDSCs can push macrophages toward an M2-resembling phenotype.²⁴ Together MDSCs and TAMs secrete cytokines affecting CCR5 and CCR6, resulting in the recruitment of T_{reg} cells, followed by CTL suppression. Both cell types produce NO which can inhibit T cell signalling and induce apoptosis in T cells. They also produce ROSs and RNSs which reduce the expression/cause the dissociation of the T cell activating co-receptor CD3 and prevent proper peptide-MHC class I complex formation and subsequent TCR recognition, resulting in reduced T cell activation.

MDSCs can also directly suppress activation of T cells by expressing ligands of T cell inhibitory surface receptors PD-1 or CTLA4.²⁴

Through the secretion of varying combinations of pro- and anti-inflammatory cytokines, growth factors, and lipid mediators, tumor associated immune cells are constantly contributing to cycles of wound healing and tissue destruction.² The presence of these ongoing cycles within the tumor supports the observation made by Dvorak, that cancerous tumors are “wounds that do not heal”^{35,38}. In addition to the effects described above, ROS and RNS released by immune cells have other direct and indirect effects in cancer.

1.2.6. Production of reactive oxygen and nitrogen species

While evidence for this connection has mostly accumulated over the last 2 decades, reactive oxygen species are now often described as being integral to situations of chronic inflammation leading to cancer.¹⁶ Nitric oxide (NO*) and other reactive oxygen species (ROS) (including OH*, ONOO⁻, O₂⁻, etc.) can have both direct and indirect effects on DNA and other components of the cell, as well as effects on cell signalling. Direct effects of free radicals on DNA include the oxidation of DNA groups to 8-hydroxy-deoxyguanosine (8-oxo-dG), 8-nitroguanine, thionitrites, or nitrosamines (leading to deamination) in addition to the formation of double stranded breaks (DSB).^{16,39} Free radicals have also been found to cause mutations in cancer-related genes, such as tumor suppressors or oncogenes, which then leads to the clonal expansion of mutated cells.³⁹ This signalling can then lead to the induction of angiogenesis or to the modification of genes for proteins such as DNA-repair enzymes, apoptotic modulators, and the p53 tumor suppressor, altering or eliminating their function. ROS have also been shown to influence topoisomerase II activity leading to DNA damage through double strand breaks.⁴⁰

Some of the direct effects of free radicals cause equally undesirable indirect effects. This is evident in cases of lipid peroxidation, where free radicals react with several of the polyunsaturated fatty acids, such as arachidonic acid or linoleic acid, in and around cell membranes causing oxidative damage.⁴¹ During these radical chain reactions fatty acids have electrons stolen and subsequently react with oxygen to produce peroxy fatty acid radicals which then go on to steal electrons from nearby fatty acids causing the same changes (sometimes called the arachidonic acid cascade) in them, only ending when free radicals combine with other free radicals or anti-oxidants. While this chain reaction may cause varying levels of cell membrane damage, a more serious result of lipid peroxidation is the production of malondialdehyde (MDA) and 4-hydroxynonenol (4-HNE), DNA damaging agents which generate exocyclic DNA adducts (M1G and etheno-adducts, respectively).³⁹ While the formation of DNA damaging agents in general is undesirable, 4-HNE may be especially undesirable as it has been found to preferentially cause transversions in codon 249 on the p53 tumor suppressor gene in TK6 lymphoblastoid cells.³⁹ As p53 has a regulatory role over several anti-oxidant regulating genes, its loss or malfunction may result in increased concentrations of ROS and greater levels of tumorigenesis.⁴⁰

Free radicals have been shown to activate oncogenic signalling pathways (including Src kinase, MAPK, PI3K/AKT, EGFR) leading to tumor formation, in various cells, by causing the development of invadopodia, growth factor-independent growth, anchorage-independent growth, increased tumor cell migration and colonization during metastasis, and increased growth and survival.^{16,40} While supraphysiological levels of NO are effective at destroying cells, physiological (low), and even intermediate, concentrations of NO are pro-carcinogenic, presumably because they cause enough damage to result in DNA damage, but not enough to result in death of the cell.¹⁶

ROS production in the TME has been linked with increased HIF1 α and VEGF production, recruitment of cancer associated fibroblasts (CAF), and MMP activation.¹⁶ ROS induce EMT in cancer cells, but both ROS and NO in correct relative concentrations are needed to sustain these cells in EMT. NO seems to be important in the prevention of anoikis (cell death from insufficient cell-ECM contact), an important ability for metastatic cells to gain.

It is thought that the NO and ROS production in cancer come mainly from NO synthases (NOS) and NADPH oxidases 1-5¹⁶. Current evidence suggests that the upregulation of NOS and NADPH oxidases and subsequent increased free radical production is important in the initiation and progression of tumors. Furthermore, it has been demonstrated that NOS2 is upregulated in the tumor microenvironment by several pro-inflammatory cytokines including IL-1 β , INF- γ , and TNF- α secreted from cancer cells, macrophages, tumor infiltrating lymphocytes (TIL), and CAFs.^{16,19}

The relationship between inflammation, free radical production, and cancer discussed above has measurable long-term health implications. Several chronic inflammatory diseases, such as haemochromatosis, hepatitis B/C, ulcerative colitis, inflammatory bowel disease, etc., result in greatly increased chances of developing cancer in the related organ.³⁹ These diseases, described as oxyradical overload diseases, provide evidence of the inflammation-cancer relationship with endogenous free-radical production as a link.

1.3. Inflammatory biomarkers as indicators of tumor promotion and progression

As has been discussed, a great deal of crosstalk between immune cells and tumor cells leads to the production of a range of bio-active molecules in and around tumors. Some of these bio-active molecules play pivotal roles in both acute and chronic inflammation and provide crucial signals

for tumor promotion and progression to a metastatic phenotype. Since a tumor's ability to metastasize is the primary reason for cancer associated mortality, discovering and learning to inhibit the activity of key bio-active molecules which contribute to metastasis is becoming an increasingly more attractive option for the treatment of cancer and other inflammatory diseases.^{42,43} Two bio-markers of inflammation which have emerged as key regulators of the inflammatory response and crucial participants in mediating the hallmarks of cancer are COX-2 and autotaxin (ATX).⁴³⁻⁴⁷ These enzymes are both responsible for the production of highly bio-active lipid mediators within the TME and have, thus, emerged as therapeutic targets for inhibition for the treatment of inflammatory diseases.

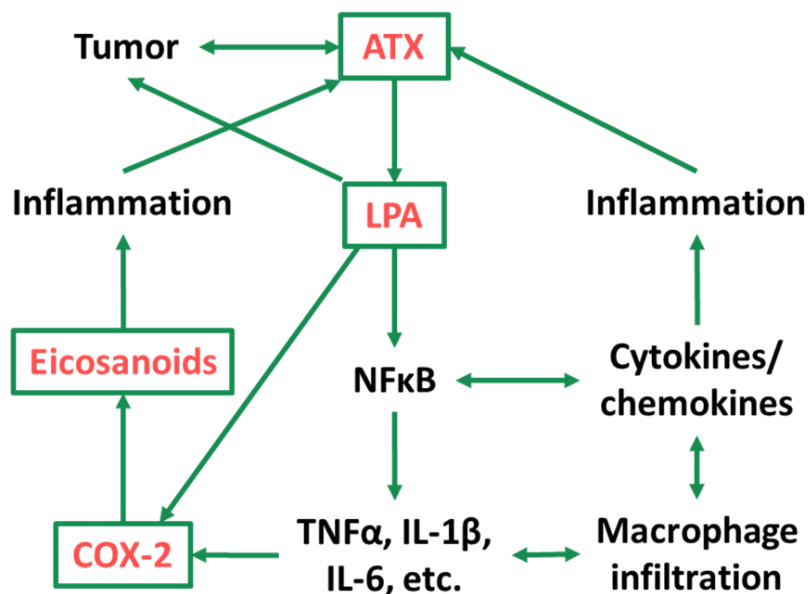


Figure 2. The autotaxin (ATX)-cyclooxygenase-2 (COX-2)-inflammatory cycle. Adapted from Signalling by lysophosphatidate and its health implications by Hemmings and Brindley, *Essays in Biochem.*, 2020.⁴⁸

1.3.1. The role of Cyclooxygenase-2 in inflammation and cancer

COX-2 (cyclooxygenase 2) is the inducible COX isoform responsible for the conversion of arachidonic acid to prostaglandin H₂ which is subsequently converted to prostacyclin, thromboxane, and various prostaglandins by several distinct synthases.⁴⁹ Two of these prostaglandins, PGE₂ and PGD₂, were mentioned above in connection with the upregulation of 15-lipoxygenase RNA leading to the resolution of acute inflammation, an idea which would later become known as the switch in lipid mediator class coming about from a change in neutrophil phenotype.^{12,50,51} Beyond this, PGE₂ has been discussed in connection with many inflammation and cancer related activities including the induction of pain (through interactions with peripheral sensory neurons), vasodilation of vascular smooth muscle in postcapillary venules (leading to increased recruitment of immune cells), suppression of T cell activation, and causing the accumulation of MDSC and T_H17 cells within the TME.^{10,35,37,49,52} PGE₂ has also been singled out as a necessary contributor to pathological angiogenesis, tumor cell intravasation, and extravasation through the lung vasculature in a triple negative breast cancer model.⁴⁴ PGE₂ is capable of promoting DNA methylation of genes for tumor suppressors and DNA repair machinery, leading to the progression of colorectal cancer through the evasion of growth suppressors and the promotion of genetic instability.⁵³

While various PGE₂-mediated relationships have been discovered, it may be argued that the practical reason that the COX-2/PGE₂ signalling axis is important is because its inhibition by non-steroidal anti-inflammatory drugs (NSAID) leads to the significant attenuation of many of the pro-inflammatory, tumorigenic, and metastasis-related effects listed above.^{10,44,53,54} The reduction in these effects can be seen in tumors of diverse origin (breast, prostate, neuroblastoma) but are especially pronounced in colorectal tumors.^{43,44,55,56} NSAIDs can be generally divided into specific

(ex. Celebrex) and non-specific (ex. aspirin, ibuprofen) classes based on whether they inhibit COX-2 significantly more than or relatively equally to COX-1, respectively.⁵⁴ While COX-2 inhibitors all contribute to the down-regulation of prostaglandin production, they do not all accomplish this by the same means. Most over the counter NSAIDs, and Celebrex, are reversible competitive inhibitors of COX-2, and their actions result in the overall inhibition of COX-2 activity.⁵⁷ This differs from the mechanism of aspirin which causes the selective acetylation of the hydroxyl group of Ser-530, which leads to the prevention of prostaglandin production, but does not prevent the processing of pro-resolving lipid mediators, such as LXA₄.^{14,58,59}

Since the level of PGE₂ expression in the TME of cancers which are commonly COX-2-positive seems to have such a strong bearing on the phenotype and capabilities of the tumor, monitoring the level of COX-2 expression within tumors has become an attractive option. From a practical point of view, a monitoring system which is minimally invasive and easy to use is much more likely to be accepted and employed by the medical field. Thus, over the last 20 years, dozens of imaging agents targeting COX-2 have been developed in an effort to create a tool which can reliably and selectively elucidate the COX-2 expression within solid tumors.⁶⁰ Discussions further on will elaborate on the design of these molecular probes; however, it is important to note that, to date, no COX-2-targeting molecular probe has provided sufficient specificity and the reliability required to become a widely used and dependable tool.

1.3.2. The role of ATX in inflammation and cancer

ATX is a secreted enzyme with ectonucleotide pyrophosphatase/phosphodiesterase (PDE) and lysophospholipase D (LysoPLD) activity responsible for the production of lysophosphatidic acid (LPA) from lysophosphatidylcholine (LPC).⁶¹ Isoforms of ATX are expressed in a range of

different tissues including the lung, kidney, pancreas, brain and spinal cord, gonads, lymph nodes, adipose, and many cancerous or chronically inflamed tissues.⁶² LPA participates in cell signalling through binding interactions with at least 6 distinct G-protein-coupled receptors, called LPAR1-6, which exert influence over multiple signalling pathways including MAPK, PI3K/Akt, JNK, Rho and more.⁶³⁻⁶⁵ During the process of wound healing, the ATX-LPA-LPAR signalling axis is involved in the induction of proliferation and migration of cells involved in tissue repair and angiogenesis, in platelet aggregation, and in temporary wound contraction.⁶⁶⁻⁶⁹ Although ATX transcription is normally suppressed by LPA, ATX is expressed and secreted in response to the expression and activity of proinflammatory cytokines TNF, IL-1, and NF- κ B.^{69,70} The LPA produced by ATX leads to further production of pro-inflammatory cytokines which leads to the production of more ATX.⁶⁷ At the resolution of inflammation, declining levels of pro-inflammatory cytokines are insufficient to induce ATX transcription and the high levels of LPA again cause its suppression.^{67,70} LPA also promotes the proliferation and migration of immune cells and fibroblasts, and the differentiation of monocytes into macrophages.^{69,71} T cells express LPA receptors and their polarization, motility, and homing to lymph nodes can be regulated by LPA production.⁷²

ATX is one of the 40 most up-regulated genes in highly metastatic cancer.⁷³ ATX was first discovered as a motility stimulating factor in melanoma cells where it could induce chemotactic or chemokinetic movement of tumor cells even at very low concentrations.⁴⁵ ATX was found to make protein-protein interactions with integrin proteins which would position the ATX near LPA receptors on the cell surface; however, even when LPA receptors were inhibited, 20% of the cell motility initially observed was still seen.⁷⁴ Due to the various pathways which can be activated by LPA signalling, ATX has come to be associated with tumorigenesis, angiogenesis, resistance to

chemotherapy and radiotherapy, and the metastatic potential of many tumor types.^{69,75,76} Along with the up-regulation of ATX in metastatic cancer, LPA receptors are also up-regulated, while lipid phosphate phosphatases, which degrade LPA, are down-regulated; these circumstances lead to greatly increased levels of LPA and a continuation of ATX expression and pro-tumorigenic influence.⁶⁹

The influence that the ATX-LPA-LPAR signalling axis exerts on events of tumor initiation, promotion, and progression has caused it to emerge as a therapeutic target, not only for cancer therapy, but for several inflammatory diseases. To date, much effort by several different groups has been directed toward the development of inhibitors of ATX.⁷⁷⁻⁷⁹ One inhibitor, GLPG1690, has recently progressed to stage III clinical trials for the treatment of idiopathic pulmonary fibrosis.⁷⁸

The presence of ATX-LPA signalling facilitates cancer growth, proliferation, survival, and metastasis in many cancers.^{69,75} Thus, ascertaining the level of ATX expression in a particular tumor, especially for individuals who have become resistant to therapy, could be useful in establishing a personalized therapeutic approach for an individual, perhaps by signalling the need for an ATX inhibitor as an adjuvant therapy. A means by which ATX levels in patient tumors may be assessed has yet to be firmly established, however, much like the COX-2 imaging discussed above, molecular imaging is a valid and ideal option. While few molecular probes for the *in vivo* detection of ATX have been reported, one of them shows promise.^{80,81}

1.3.3. The relationship of Autotaxin and Cyclooxygenase-2

It is worth noting that the two inflammation-related biomarkers discussed above are not completely independent of each other. While little focus has been placed on their interconnectivity in the

literature to date, several examples of experimental evidence have been reported which sufficiently establish their relationship.

Ye et al., 2005 first found that the presence of LPA receptor 3 (LPAR3) in the uterine epithelium is important during the egg implantation period and that when it was knocked out, COX-2 levels were significantly reduced.⁸² The subsequent reduction in levels of prostaglandins resulted in defective placental formation, embryo spacing, and fetal development, though this could only be partially rescued through treatment with prostaglandins. They later found that during activation of LPAR3 with the agonist T13, levels of PGE₂ and PGF₂α increased and could be reduced through treatment with a COX-2 inhibitor.⁸³ This demonstrates a signalling relationship with the ATX-LPA-LPAR signaling axis upstream of the COX-2 prostaglandin pathway.

The work of Nochi et al. in rheumatoid arthritic (RA) synovial fluid treated cells shows that while treatment of cells with RA synovium normally strongly induces the expression of COX-2, and subsequently PGE₂ production, treatment of those cells with the pertussis toxin, a well documented inhibitor of LPA receptors, significantly inhibited COX-2 expression.⁸⁴ They showed that two lipid mediators present in the RA synovial fluid, LPA and SIP, induced COX-2 expression in a dose-dependant and time-dependant manner, which could be inhibited, and in the case of LPA nearly prevented, by treatment with the pertussis toxin. They found that similar inhibition of COX-2 protein and mRNA expression in their RA synovial fluid model and an LPA-only treated model could be achieved through treatment with an LPA receptor antagonist. Looking closer into the composition of synovial fluid they found that all their samples contained both the autotaxin protein and its substrate LPC. This work sheds light on the relationship of ATX and COX-2 in that it shows ATX to be an upstream regulator of COX-2 expression.

1.4. Positron emission tomography

Positron emission tomography (PET) is a functional imaging modality used in both medicine and research.⁸⁵ PET imaging involves the use of short-lived positron-emitting radio-isotopes integrated into bio-active molecules, called radiotracers, which are injected into the body and circulate before being trapped by their target of interest. When these radiotracers decay, they release a positron which travels a short distance before colliding with an electron in a process called annihilation. Annihilation is a matter to energy conversion process which results in the production of two gamma photons, which exit the body at a nearly 180° angle, are detected by photo-sensors, and used to construct a 3-dimensional image.

Within the sphere of PET imaging, various positron emitters, including but not limited to ¹¹C, ¹³N, ¹⁵O, ¹⁸F, and ⁶⁸Ga, can be used depending on what application is required.⁸⁶ For example, a small molecule inhibitor which must be labeled but has no fluorine moiety may more appropriately be labeled with ¹¹C than ¹⁸F because the carbon radionuclide can replace an existing carbon, leading to the production of a radiotracer which is chemically identical to the inhibitor.

1.4.1. The imaging of biomarkers

As a functional imaging modality, PET imaging is capable of visualizing biochemical processes related to pharmacokinetics, blood flow, or other cell function within an organism.^{85,86} The ability of PET to detect physiological processes means it is often able to visualize disease-related activity before that activity causes anatomical damage, which may put it at an advantage over structural

imaging modalities, such as computed tomography (CT) or magnetic resonance imaging (MRI), in the detection of disease.

The detection of physiological processes is achieved through the use of PET radiotracers designed to associate or interact with a specific target.⁸⁵ In the case of clinical cancer imaging, the PET radiotracer 2-deoxy-2-[¹⁸F]fluoro-D-glucose, a glucose analog commonly called [¹⁸F]FDG, is the standard and is used to target locations of increased glucose metabolism. Another radiotracer, [¹⁸F]fluorothymidine or [¹⁸F]FLT, is a nucleoside analog capable of visualizing highly proliferative cells. Many PET radiotracers exist and are synthesized from a range of bioactive molecules including carbohydrates, small molecules, peptides, proteins, and any other molecules which would allow for selective association. Selectivity in associating with a target biomarker is what makes radiotracers capable of visualizing biomarker-related disease states.⁸⁵⁻⁸⁷

1.5. Hypothesis and Objectives

1.5.1. Hypothesis

The purpose of this thesis is to test two hypotheses:

1. That PET imaging using an ¹⁸F-labeled small molecule inhibitor of COX-2 will allow for its *in vivo* detection and monitoring in COX-2 expressing chronic inflammatory diseases, including cancer.
2. That PET imaging using ¹⁸F-labeled small molecule inhibitors of ATX will allow for its *in vivo* detection and monitoring in ATX-expressing chronic inflammatory diseases, including cancer.

1.5.2. Objectives

The goals of this thesis were achieved through:

1. Development of a COX-2 radiotracer synthesis using recent copper-mediated late-stage fluorination chemistry.
2. Measurement of radioactivity levels taken up into COX-2-expressing HCA7 cells *in vitro* and *in vivo* using a cellular uptake assay, dynamic PET imaging, autoradiography, immunohistochemistry, a lipophilicity assay, and a blood distribution and stability assay.
3. Modification of existing syntheses to obtain the ATX-specific radiotracers.
4. Measurement of radioactivity levels taken up in ATX-expressing tumor micro-environments using dynamic PET imaging, immunohistochemistry, a lipophilicity assay, and a blood distribution and stability assay.

1.6. REFERENCES

- (1) Chiba, T.; Marusawa, H.; Ushijima, T. Inflammation-Associated Cancer Development in Digestive Organs: Mechanisms and Roles for Genetic and Epigenetic Modulation. *Gastroenterology* **2012**, *143* (3), 550–563. <https://doi.org/10.1053/j.gastro.2012.07.009>.
- (2) Hanahan, D.; Weinberg, R. A. Hallmarks of Cancer: The next Generation. *Cell* **2011**, *144* (5), 646–674. <https://doi.org/10.1016/j.cell.2011.02.013>.
- (3) Hanahan, D.; Weinberg, R. The Hallmarks of Cancer. *Cell* **2000**, *100*, 57–70.
- (4) Serhan, C. N.; Krishnamoorthy, S.; Recchiuti, A.; Chiang, N. Novel Anti-Inflammatory-pro-Resolving Mediators and Their Receptors. *Curr. Top. Med. Chem.* **2011**, *11* (6), 629–647. <https://doi.org/10.2174/1568026611109060629>.
- (5) Robbins, S. L. *Basic Pathology*; Kumar, V., Abbas, A. K., Aster, J. C., Eds.; Elsevier, 2015.
- (6) Harada, A.; Sekido, N.; Akahoshi, T.; Wada, T.; Mukaida, N.; Matsushima, K. Essential Involvement of Interleukin-8 (IL-8) in Acute Inflammation. *J. Leukoc. Biol.* **1994**, *56* (5), 559–564. <https://doi.org/10.1002/jlb.56.5.559>.
- (7) Kumar, K. P.; Nicholls, A. J.; Wong, C. H. Y. Partners in Crime: Neutrophils and Monocytes/Macrophages in Inflammation and Disease. *Cell Tissue Res.* **2018**, *371* (3), 551–565. <https://doi.org/10.1007/s00441-017-2753-2>.
- (8) Serhan, C. N.; Chiang, N.; Dalli, J.; Levy, B. D. Lipid Mediators in the Resolution of Inflammation. *Cold Spring Harb. Perspect. Biol.* **2015**, *7* (2). <https://doi.org/10.1101/cshperspect.a016311>.
- (9) Marwick, J. A.; Mills, R.; Kay, O.; Michail, K.; Stephen, J.; Rossi, A. G.; Dransfield, I.; Hirani, N. Neutrophils Induce Macrophage Anti-Inflammatory Reprogramming by

- Suppressing NF-KB Activation Article. *Cell Death Dis.* **2018**, *9* (6).
<https://doi.org/10.1038/s41419-018-0710-y>.
- (10) Nakanishi, M.; Rosenberg, D. W. Multifaceted Roles of PGE₂ in Inflammation and Cancer. *Semin. Immunopathol.* **2013**, *35* (2), 123–137. <https://doi.org/10.1007/s00281-012-0342-8>.
- (11) Serhan, C. N. The Resolution of Inflammation: The Devil in the Flask and in the Details. *FASEB J.* **2011**, *25* (5), 1441–1448. <https://doi.org/10.1096/fj.11-0502ufm>.
- (12) Levy, B. D.; Clish, C. B.; Schmidt, B.; Gronert, K.; Serhan, C. N. Lipid Mediator Class Switching during Acute Inflammation: Signals in Resolution. *Nat. Immunol.* **2001**, *2* (7), 612–619. <https://doi.org/10.1038/89759>.
- (13) Godson, C.; Mitchell, S.; Harvey, K.; Petasis, N. A.; Hogg, N.; Brady, H. R. Cutting Edge: Lipoxins Rapidly Stimulate Nonphlogistic Phagocytosis of Apoptotic Neutrophils by Monocyte-Derived Macrophages. *J. Immunol.* **2000**, *164* (4), 1663–1667.
<https://doi.org/10.4049/jimmunol.164.4.1663>.
- (14) Serhan, C. N.; Levy, B. D. Resolvins in Inflammation: Emergence of the pro-Resolving Superfamily of Mediators Protection versus Uncontrolled Inflammation: First Responders and Resolution. *J Clin Invest* **2018**, *128* (7), 2657–2669. <https://doi.org/10.1172/JCI97943>.
- (15) Pastar, I.; Stojadinovic, O.; Yin, N. C.; Ramirez, H.; Nusbaum, A. G.; Sawaya, A.; Patel, S. B.; Khalid, L.; Isseroff, R. R.; Tomic-Canic, M. Epithelialization in Wound Healing: A Comprehensive Review. *Adv. Wound Care* **2014**, *3* (7), 445–464.
<https://doi.org/10.1089/wound.2013.0473>.
- (16) Monteiro, H. P.; Rodrigues, E. G.; Amorim Reis, A. K. C.; Longo, L. S.; Ogata, F. T.; Moretti, A. I. S.; da Costa, P. E.; Teodoro, A. C. S.; Toledo, M. S.; Stern, A. Nitric Oxide

- and Interactions with Reactive Oxygen Species in the Development of Melanoma, Breast, and Colon Cancer: A Redox Signaling Perspective. *Nitric Oxide* **2019**, *89* (October 2018), 1–13. <https://doi.org/10.1016/j.niox.2019.04.009>.
- (17) Hodge, D. R.; Hurt, E. M.; Farrar, W. L. The Role of IL-6 and STAT3 in Inflammation and Cancer. *Eur. J. Cancer* **2005**, *41* (16), 2502–2512. <https://doi.org/10.1016/j.ejca.2005.08.016>.
- (18) Fisher, D. T.; Appenheimer, M. M.; Evans, S. S. The Two Faces of IL-6 in the Tumor Microenvironment. *Semin. Immunol.* **2014**, *26* (1), 38–47. <https://doi.org/10.1038/jid.2014.371>.
- (19) Landskron, G.; De La Fuente, M.; Thuwajit, P.; Thuwajit, C.; Hermoso, M. A. Chronic Inflammation and Cytokines in the Tumor Microenvironment. *J. Immunol. Res.* **2014**, *2014*. <https://doi.org/10.1155/2014/149185>.
- (20) Chen, L.; Shi, Y.; Zhu, X.; Guo, W.; Zhang, M.; Che, Y.; Tang, L.; Yang, X.; You, Q.; Liu, Z. IL-10 Secreted by Cancer-Associated Macrophages Regulates Proliferation and Invasion in Gastric Cancer Cells via c-Met/STAT3 Signaling. *Oncol. Rep.* **2019**, *42* (2), 595–604. <https://doi.org/10.3892/or.2019.7206>.
- (21) Fabre, J.; Giustiniani, J.; Garbar, C.; Antonicelli, F.; Merrouche, Y.; Bensussan, A.; Bagot, M.; Al-Dacak, R. Targeting the Tumor Microenvironment: The Protumor Effects of IL-17 Related to Cancer Type. *Int. J. Mol. Sci.* **2016**, *17* (9). <https://doi.org/10.3390/ijms17091433>.
- (22) Qian, B. Z.; Pollard, J. W. Macrophage Diversity Enhances Tumor Progression and Metastasis. *Cell* **2010**, *141* (1), 39–51. <https://doi.org/10.1016/j.cell.2010.03.014>.
- (23) DeNardo, D. G.; Barreto, J. B.; Andreu, P.; Vasquez, L.; Tawfik, D.; Kolhatkar, N.;

- Coussens, L. M. CD4+ T Cells Regulate Pulmonary Metastasis of Mammary Carcinomas by Enhancing Protumor Properties of Macrophages. *Cancer Cell* **2009**, *16* (2), 91–102. <https://doi.org/10.1016/j.ccr.2009.06.018>.
- (24) Ugel, S.; De Sanctis, F.; Mandruzzato, S.; Bronte, V. Tumor-Induced Myeloid Deviation: When Myeloid-Derived Suppressor Cells Meet Tumor-Associated Macrophages. *J. Clin. Invest.* **2015**, *125* (9), 3365–3376. <https://doi.org/10.1172/JCI80006>.
- (25) Wendt, M. K.; Allington, T. M.; Schiemann, W. P. Mechanisms of the Epithelial-Mesenchymal Transition by TGF- β . *Futur. Oncol.* **2009**, *5* (8), 1145–1168. <https://doi.org/10.2217/fon.09.90>.
- (26) Gao, D.; Joshi, N.; Choi, H.; Ryu, S.; Hahn, M.; Catena, R.; Sadik, H.; Argani, P.; Wagner, P.; Vahdat, L. T.; Port, J. L.; Stiles, B.; Sukumar, S.; Altorki, N. K.; Raffii, S.; Mittal, V. Myeloid Progenitor Cells in the Premetastatic Lung Promote Metastases by Inducing Mesenchymal to Epithelial Transition. *Cancer Res.* **2012**, *72* (6), 1384–1394. <https://doi.org/10.1158/0008-5472.CAN-11-2905>.
- (27) Krys, D.; Hamann, I.; Wuest, M.; Wuest, F. Effect of Hypoxia on Human Equilibrative Nucleoside Transporters HENT1 and HENT2 in Breast Cancer. *FASEB J.* **2019**, *33* (12), 13837–13851. <https://doi.org/10.1096/fj.201900870RR>.
- (28) Brown, J. M. Tumor Hypoxia in Cancer Therapy. *Methods Enzymol.* **2007**, *435*. [https://doi.org/10.1016/S0076-6879\(07\)35015-5](https://doi.org/10.1016/S0076-6879(07)35015-5).
- (29) Belotti, D.; Paganoni, P.; Manenti, L.; Garofalo, A.; Marchini, S.; Taraboletti, G.; Giavazzi, R. Matrix Metalloproteinases (MMP9 and MMP2) Induce the Release of Vascular Endothelial Growth Factor (VEGF) by Ovarian Carcinoma Cells: Implications for Ascites Formation. *Cancer Res.* **2003**, *63* (17), 5224–5229.

- (30) Hawinkels, L. J. A. C.; Zuidwijk, K.; Verspaget, H. W.; de Jonge-Muller, E. S. M.; Duijn, W. van; Ferreira, V.; Fontijn, R. D.; David, G.; Hommes, D. W.; Lamers, C. B. H. W.; Sier, C. F. M. VEGF Release by MMP-9 Mediated Heparan Sulphate Cleavage Induces Colorectal Cancer Angiogenesis. *Eur. J. Cancer* **2008**, *44* (13), 1904–1913. <https://doi.org/10.1016/j.ejca.2008.06.031>.
- (31) Wang, X.; Lin, Y. Tumor Necrosis Factor and Cancer, Buddies or Foes? *Acta Pharmacol. Sin.* **2008**, *29* (11), 1275–1288. <https://doi.org/10.1111/j.1745-7254.2008.00889.x>.
- (32) DeNardo, D. G.; Andreu, P.; Coussens, L. M. Interactions between Lymphocytes and Myeloid Cells Regulate Pro-versus Anti-Tumor Immunity. *Cancer Metastasis Rev.* **2010**, *29* (2), 309–316. <https://doi.org/10.1007/s10555-010-9223-6>.
- (33) Gonzalez, H.; Hagerling, C.; Werb, Z. Roles of the Immune System in Cancer: From Tumor Initiation to Metastatic Progression. *Genes Dev.* **2018**, *32* (19–20), 1267–1284. <https://doi.org/10.1101/GAD.314617.118>.
- (34) Taylor, A.; Verhagen, J.; Blaser, K.; Akdis, M.; Akdis, C. A. Mechanisms of Immune Suppression by Interleukin-10 and Transforming Growth Factor- β : The Role of T Regulatory Cells. *Immunology* **2006**, *117* (4), 433–442. <https://doi.org/10.1111/j.1365-2567.2006.02321.x>.
- (35) Gun, S. Y.; Lee, S. W. L.; Sieow, J. L.; Wong, S. C. Targeting Immune Cells for Cancer Therapy. *Redox Biol.* **2019**, No. March, 101174. <https://doi.org/10.1016/j.redox.2019.101174>.
- (36) Tesi, R. J. MDSC; the Most Important Cell You Have Never Heard Of. *Trends Pharmacol. Sci.* **2019**, *40* (1), 4–7. <https://doi.org/10.1016/j.tips.2018.10.008>.
- (37) Ma, P.; Beatty, P. L.; McKolanis, J.; Brand, R.; Schoen, R. E.; Finn, O. J. Circulating

- Myeloid Derived Suppressor Cells (MDSC) That Accumulate in Premalignancy Share Phenotypic and Functional Characteristics with MDSC in Cancer. *Front. Immunol.* **2019**, *10* (JUN). <https://doi.org/10.3389/fimmu.2019.01401>.
- (38) Dvorak, H. Tumors: Wounds That Do Not Heal. *N. Engl. J. Med.* **1986**, *315* (26), 1650–1659.
- (39) Hussain, S. P.; Hofseth, L. J.; Harris, C. C. Radical Causes of Cancer. *Nat. Rev. Cancer* **2003**, *3* (4), 276–285. <https://doi.org/10.1038/nrc1046>.
- (40) Chio, I. I. C.; Tuveson, D. A. ROS in Cancer: The Burning Question. *Trends Mol. Med.* **2017**, *23* (5), 411–429. <https://doi.org/10.1016/j.molmed.2017.03.004>.
- (41) Ayala, A.; Munoz, M. F.; Arguelles, S. Lipid Peroxidation: Production, Metabolism, and Signaling Mechanisms of Malondialdehyde and 4-Hydroxy-2-Nonenal. *Oxid. Med. Cell. Longev.* **2014**, *2014*, 360438. https://doi.org/10.1007/978-3-211-33303-7_2.
- (42) Seyfried, T. N.; Huysentruyt, L. c. On the Origin of Cancer Metastasis. *Crit. Rev. Oncol.* **2013**, *18* (1–2), 43–73. [https://doi.org/10.1002/1097-0142\(195205\)5:3<581::AID-CNCR2820050319>3.0.CO;2-Q](https://doi.org/10.1002/1097-0142(195205)5:3<581::AID-CNCR2820050319>3.0.CO;2-Q).
- (43) Johnsen, J. I.; Lindskog, M.; Ponthan, F.; Pettersen, I.; Elfman, L.; Orrego, A.; Sveinbjornsson, B.; Kogner, P. Cyclooxygenase-2 Is Expressed in Neuroblastoma , and Nonsteroidal Anti-Inflammatory Drugs Induce Apoptosis and Inhibit Tumor Growth *in Vivo*. **2004**, 7210–7215.
- (44) Gupta, G. P.; Nguyen, D. X.; Chiang, A. C.; Bos, P. D.; Kim, J. Y.; Nadal, C.; Gomis, R. R.; Manova-Todorova, K.; Massagué, J. Mediators of Vascular Remodelling Co-Opted for Sequential Steps in Lung Metastasis. *Nature* **2007**, *446* (7137), 765–770. <https://doi.org/10.1038/nature05760>.

- (45) Stracke, M. L.; Krutzsch, H. C.; Unsworth, E. J.; Arestad, A.; Cioce, V.; Schiffmann, E.; Liotta, L. A. Identification, Purification, and Partial Sequence Analysis of Autotaxin, a Novel Motility-Stimulating Protein. *J. Biol. Chem.* **1992**, *267* (4), 2524–2529.
- (46) Benesch, M. G. K.; Tang, X.; Dewald, J.; Dong, W. F.; Mackey, J. R.; Hemmings, D. G.; McMullen, T. P. W.; Brindley, D. N. Tumor-Induced Inflammation in Mammary Adipose Tissue Stimulates a Vicious Cycle of Autotaxin Expression and Breast Cancer Progression. *FASEB J.* **2015**, *29* (9), 3990–4000. <https://doi.org/10.1096/fj.15-274480>.
- (47) Benesch, M. G. K.; Ko, Y. M.; Tang, X.; Dewald, J.; Lopez-Campistrous, A.; Zhao, Y. Y.; Lai, R.; Curtis, J. M.; Brindley, D. N.; McMullen, T. P. W. Autotaxin Is an Inflammatory Mediator and Therapeutic Target in Thyroid Cancer. *Endocr. Relat. Cancer* **2015**, *22* (4), 593–607. <https://doi.org/10.1530/ERC-15-0045>.
- (48) Hemmings, D. G.; Brindley, D. N. Signalling by Lysophosphatidate and Its Health Implications. *Essays Biochem.* **2020**, *Ahead of P* (May), 1–17.
- (49) Yang, T.; Du, Y. Distinct Roles of Central and Peripheral Prostaglandin e 2 and EP Subtypes in Blood Pressure Regulation. *Am. J. Hypertens.* **2012**, *25* (10), 1042–1049. <https://doi.org/10.1038/ajh.2012.67>.
- (50) Loynes, C. A.; Lee, J. A.; Robertson, A. L.; Steel, M. J. G.; Ellett, F.; Feng, Y.; Levy, B. D.; Whyte, M. K. B.; Renshaw, S. A. PGE₂ Production at Sites of Tissue Injury Promotes an Anti-Inflammatory Neutrophil Phenotype and Determines the Outcome of Inflammation Resolution *in Vivo*. *Sci. Adv.* **2018**, *4* (9). <https://doi.org/10.1126/sciadv.aar8320>.
- (51) Chen, C. Lipids: COX-2's New Role in Inflammation. *Nat. Chem. Biol.* **2010**, *6* (6), 401–402. <https://doi.org/10.1038/nchembio.375>.

- (52) Ricciotti, E.; A, G.; Fitzgerald. [Eicosanoid Neuroinflammation] Prostaglandins and Inflammation. *Arter. Thromb Vasc Biol.* **2011**, *31* (5), 986–1000.
<https://doi.org/10.1161/ATVBAHA.110.207449>.Prostaglandins.
- (53) Xia, D.; Wang, D.; Kim, S. H.; Katoh, H.; Dubois, R. N. Prostaglandin E 2 Promotes Intestinal Tumor Growth via DNA Methylation. *Nat. Med.* **2012**, *18* (2), 224–226.
<https://doi.org/10.1038/nm.2608>.
- (54) Dubois, R. N.; Abramson, S. B.; Crofford, L.; Gupta, R. A.; Simon, L. S.; Van De Putte, L. B.; Lipsky, P. E. Cyclooxygenase in Biology and Disease. *FASEB J.* **1998**, *12* (12), 1063–1073. <https://doi.org/9737710>.
- (55) Garg, R.; Blando, J. M.; Perez, C. J.; Lal, P.; Feldman, M. D.; Smyth, E. M.; Ricciotti, E.; Grosser, T.; Benavides, F.; Kazanietz, M. G. COX-2 Mediates pro-Tumorigenic Effects of PKC ϵ in Prostate Cancer. *Oncogene* **2018**, *37* (34), 4735–4749.
<https://doi.org/10.1038/s41388-018-0318-9>.
- (56) Ghosh, N.; Chaki, R.; Mandal, V.; Mandal, S. C. COX-2 as a Target for Cancer Chemotherapy. *Pharmacol. Reports* **2010**, *62* (2), 233–244.
[https://doi.org/10.1016/S1734-1140\(10\)70262-0](https://doi.org/10.1016/S1734-1140(10)70262-0).
- (57) Hood, W. F.; Gierse, J. K.; Isakson, P. C.; Kiefer, J. R.; Kurumbail, R. G.; Seibert, K.; Monahan, J. B. Characterization of Celecoxib and Valdecoxib Binding to Cyclooxygenase. *Mol. Pharmacol.* **2003**, *63* (4), 870–877.
<https://doi.org/10.1124/mol.63.4.870>.
- (58) Gao, Y.; Zhang, H.; Luo, L.; Lin, J.; Li, D.; Zheng, S.; Huang, H.; Yan, S.; Yang, J.; Hao, Y.; Li, H.; Gao Smith, F.; Jin, S. Resolvin D1 Improves the Resolution of Inflammation via Activating NF-KB P50/P50–Mediated Cyclooxygenase-2 Expression in Acute

- Respiratory Distress Syndrome. *J. Immunol.* **2017**, *199* (6), 2043–2054.
<https://doi.org/10.4049/jimmunol.1700315>.
- (59) Lucido, M. J.; Orlando, B. J.; Vecchio, A. J.; Malkowski, M. G. The Crystal Structure of Aspirin Acetylated Human Cyclooxygenase-2: Insight into the Formation of Products with Reversed Stereochemistry. *Biochemistry* **2016**, *55* (8), 1226–1238.
<https://doi.org/10.1021/acs.biochem.5b01378>.THE.
- (60) Laube, M.; Kniess, T.; Pietzsch, J. Radiolabeled COX-2 Inhibitors for Non-Invasive Visualization of COX-2 Expression and Activity - A Critical Update. *Molecules* **2013**, *18* (6), 6311–6355. <https://doi.org/10.3390/molecules18066311>.
- (61) Jansen, S.; Stefan, C.; Creemers, J. W. M.; Waelkens, E.; Van Eynde, A.; Stalmans, W.; Bollen, M. Proteolytic Maturation and Activation of Autotaxin (NPP2), a Secreted Metastasis-Enhancing Lysophospholipase D. *J. Cell Sci.* **2005**, *118* (14), 3081–3089.
<https://doi.org/10.1242/jcs.02438>.
- (62) Ninou, I.; Magkrioti, C.; Aidinis, V. Autotaxin in Pathophysiology and Pulmonary Fibrosis. *Front. Med.* **2018**, *5* (JUN), 1–11. <https://doi.org/10.3389/fmed.2018.00180>.
- (63) Im, D. S. Pharmacological Tools for Lysophospholipid GPCRs: Development of Agonists and Antagonists for LPA and S1P Receptors. *Acta Pharmacol. Sin.* **2010**, *31* (9), 1213–1222. <https://doi.org/10.1038/aps.2010.135>.
- (64) Ishii, I.; Fukushima, N.; Ye, X.; Chun, J. Lysophospholipid Receptors: Signaling and Biology. *Annu. Rev. Biochem.* **2004**, *73* (1), 321–354.
<https://doi.org/10.1146/annurev.biochem.73.011303.073731>.
- (65) An, S.; Bleu, T.; Hallmark, O. G.; Goetzl, E. J. Characterization of a Novel Subtype of Human G Protein-Coupled Receptor for Lysophosphatidic Acid. *J. Biol. Chem.* **1998**, *273*

- (14), 7906–7910. <https://doi.org/10.1074/jbc.273.14.7906>.
- (66) Lee, H.; Goetzl, E. J.; Songzhu, A. Lysophosphatidic Acid and Sphingosine 1-Phosphate Stimulate Endothelial Cell Wound Healing. *Am. J. Physiol. - Cell Physiol.* **2000**, *278* (3 47-3), 612–618.
- (67) Benesch, M. G. K.; Tang, X.; Brindley, D. N. Autotaxin and Breast Cancer : Towards Overcoming Treatment Barriers and Sequelae. **2020**, 1–18.
- (68) Balazs, L.; Okolicany, J.; Ferrebee, M.; Tolley, B.; Tigyi, G. Topical Application of the Phospholipid Growth Factor Lysophosphatidic Acid Promotes Wound Healing *in Vivo*. *Am. J. Physiol. - Regul. Integr. Comp. Physiol.* **2001**, *280* (2 49-2), 466–472. <https://doi.org/10.1152/ajpregu.2001.280.2.r466>.
- (69) Benesch, M. G. K.; Macintyre, I. T. K.; McMullen, T. P. W.; Brindley, D. N. Coming of Age for Autotaxin and Lysophosphatidate Signaling: Clinical Applications for Preventing, Detecting and Targeting Tumor-Promoting Inflammation. *Cancers (Basel)*. **2018**, *10* (3). <https://doi.org/10.3390/cancers10030073>.
- (70) Benesch, M. G. K.; Zhao, Y. Y.; Curtis, J. M.; McMullen, T. P. W.; Brindley, D. N. Regulation of Autotaxin Expression and Secretion by Lysophosphatidate and Sphingosine 1-Phosphate. *J. Lipid Res.* **2015**, *56* (6), 1134–1144. <https://doi.org/10.1194/jlr.M057661>.
- (71) Ray, R.; Rai, V. Lysophosphatidic Acid Converts Monocytes into Macrophages in Both Mice and Humans. *Blood* **2017**, *129* (9), 1177–1183. <https://doi.org/10.1182/blood-2016-10-743757>.
- (72) Knowlden, S.; Georas, S. The Autotaxin-LPA Axis Emerges as a Novel Regulator of Lymphocyte Homing and Inflammation. *J. Immunol.* **2014**, *192* (3), 851–857. <https://doi.org/10.1038/mp.2011.182.doi>.

- (73) Euer, N.; Schwirzke, M.; Evtimova, V.; Burtscher, H.; Jarsch, M.; Tarin, D.; Weidle, U. H. Identification of Genes Associated with Metastasis of Mammary Carcinoma in Metastatic versus Non-Metastatic Cell Lines. *Anticancer Res.* **2002**, *22* (2A), 733–740.
- (74) Wu, T.; Kooi, C. Vander; Shah, P.; Charnigo, R.; Huang, C.; Smyth, S. S.; Morris, A. J. Integrin-Mediated Cell Surface Recruitment of Autotaxin Promotes Persistent Directional Cell Migration. *FASEB J.* **2014**, *28* (2), 861–870. <https://doi.org/10.1096/fj.13-232868>.
- (75) Barbayianni, E.; Kaffe, E.; Aidinis, V.; Kokotos, G. Autotaxin, a Secreted Lysophospholipase D, as a Promising Therapeutic Target in Chronic Inflammation and Cancer. *Prog. Lipid Res.* **2015**, *58*, 76–96. <https://doi.org/10.1016/j.plipres.2015.02.001>.
- (76) Benesch, M. G. K.; Ko, Y. M.; McMullen, T. P. W.; Brindley, D. N. Autotaxin in the Crosshairs: Taking Aim at Cancer and Other Inflammatory Conditions. *FEBS Lett.* **2014**, *588* (16), 2712–2727. <https://doi.org/10.1016/j.febslet.2014.02.009>.
- (77) Auberson, Y. P.; Briard, E.; Oberhauser, B.; Legrand, D. WO 2016/116875 A1, 2016.
- (78) Desroy, N.; Housseman, C.; Bock, X.; Joncour, A.; Bienvenu, N.; Cherel, L.; Labeguere, V.; Rondet, E.; Peixoto, C.; Grassot, J. M.; Picolet, O.; Annoot, D.; Triballeau, N.; Monjardet, A.; Wakselman, E.; Roncoroni, V.; Le Tallec, S.; Blaque, R.; Cottreaux, C.; Vandervoort, N.; Christophe, T.; Mollat, P.; Lamers, M.; Auberval, M.; Hrvacic, B.; Ralic, J.; Oste, L.; Van der Aar, E.; Brys, R.; Heckmann, B. Discovery of 2-[[2-Ethyl-6-[4-[2-(3-Hydroxyazetididin-1-Yl)-2-Oxoethyl]Piperazin-1-Yl]-8-Methylimidazo[1,2-a]Pyridin-3-Yl]Methylamino]-4-(4-Fluorophenyl)Thiazole-5-Carbonitrile (GLPG1690), a First-in-Class Autotaxin Inhibitor Undergoing Clinical Evaluation. *J. Med. Chem.* **2017**, *60* (9), 3580–3590. <https://doi.org/10.1021/acs.jmedchem.7b00032>.
- (79) Shah, P.; Cheasty, A.; Foxton, C.; Raynham, T.; Farooq, M.; Gutierrez, I. F.; Lejeune, A.;

- Pritchard, M.; Turnbull, A.; Pang, L.; Owen, P.; Boyd, S.; Stowell, A.; Jordan, A.; Hamilton, N. M.; Hitchin, J. R.; Stockley, M.; MacDonald, E.; Quesada, M. J.; Trivier, E.; Skeete, J.; Ovaa, H.; Moolenaar, W. H.; Ryder, H. Discovery of Potent Inhibitors of the Lysophospholipase Autotaxin. *Bioorganic Med. Chem. Lett.* **2016**, *26* (22), 5403–5410. <https://doi.org/10.1016/j.bmcl.2016.10.036>.
- (80) Madan, D.; Ferguson, C. G.; Lee, W. Y.; Prestwich, G. D.; Testa, C. A. Non-Invasive Imaging of Tumors by Monitoring Autotaxin Activity Using an Enzyme-Activated near-Infrared Fluorogenic Substrate. *PLoS One* **2013**, *8* (11). <https://doi.org/10.1371/journal.pone.0079065>.
- (81) Briard, E.; Joshi, A. D.; Shanmukhappa, S.; Ilovich, O.; Auberson, Y. P. [¹⁸F]PRIMATX, a New Positron Emission Tomography Tracer for Imaging of Autotaxin in Lung Tissue and Tumor-bearing Mice. *ChemMedChem* **2019**, *14* (16), 1493–1502. <https://doi.org/10.1002/cmdc.201900297>.
- (82) Ye, X.; Hama, K.; Contos, J. J. A.; Anliker, B.; Inoue, A.; Skinner, M. K.; Suzuki, H.; Amane, T.; Kennedy, G.; Arai, H.; Aoki, J.; Chun, J. LPA3-Mediated Lysophosphatitic Acid Signalling in Embryo Implantation and Spacing. *Lett. to Nat.* **2005**, *435* (May), 104–108.
- (83) Aikawa, S.; Kano, K.; Inoue, A.; Wang, J.; Saigusa, D.; Nagamatsu, T.; Hirota, Y.; Fujii, T.; Tsuchiya, S.; Taketomi, Y. Autotaxin – Lysophosphatidic Acid – LPA 3 Signaling at the Embryo-Epithelial Boundary Controls Decidualization Pathways. **2017**, *36* (14), 2146–2160. <https://doi.org/10.15252/emj.201696290>.
- (84) Nochi, H.; Tomura, H.; Tobo, M.; Tanaka, N.; Sato, K.; Shinozaki, T.; Kobayashi, T.; Takagishi, K.; Ohta, H.; Okajima, F.; Tamoto, K. Stimulatory Role of Lysophosphatidic

Acid in Cyclooxygenase-2 Induction by Synovial Fluid of Patients with Rheumatoid Arthritis in Fibroblast-like Synovial Cells. *J. Immunol.* **2008**, *181* (7), 511–5119.

<https://doi.org/10.4049/jimmunol.181.7.5111>.

(85) Das, B. K. *Positron Emission Tomography*; 2015.

<https://doi.org/10.1002/9781444303254.ch133>.

(86) Bailey, D. L.; Townsend, D. W.; Valk, P. E.; Maisey, M. N. *Positron Emission Tomography Basic Sciences*; Springer-Verlag: London, 2005.

<https://doi.org/10.1016/B978-0-12-385157-4.00203-7>.

(87) Alam, I. S.; Arshad, M. A.; Nguyen, Q. D.; Aboagye, E. O. Radiopharmaceuticals as Probes to Characterize Tumour Tissue. *Eur. J. Nucl. Med. Mol. Imaging* **2015**, *42* (4), 537–561. <https://doi.org/10.1007/s00259-014-2984-3>.

CHAPTER 2

Radiosynthesis and biological evaluation of [¹⁸F]triacoxib: a radiotracer for PET imaging of COX-2

**Radiosynthesis and biological evaluation of [¹⁸F]triacoxib: a radiotracer for PET imaging
of COX-2**

Marcus Litchfield, Melinda Wuest, Darryl Glubrecht, Frank Wuest

Chapter published in Molecular Pharmaceutics

Abstract:

Inducible isozyme cyclooxygenase-2 (COX-2) is upregulated under acute and chronic inflammatory conditions, including cancer, wherein it promotes angiogenesis, tissue invasion, and resistance to apoptosis. Due to its high expression in various cancers, COX-2 has become an important biomarker for molecular imaging and therapy of cancer. Recently, our group applied *in situ* click chemistry for the identification of the highly potent and selective COX-2 inhibitor triacoxib. In this study, we present the radiosynthesis, *in vitro*, and *in vivo* radiopharmacological validation of [¹⁸F]triacoxib, a novel radiotracer for PET imaging of COX-2. Radiosynthesis of [¹⁸F]triacoxib was accomplished using copper-mediated late-stage radiofluorination chemistry. Radiosynthesis, including radio-HPLC purification, of [¹⁸F]triacoxib was accomplished within 90 min in decay-corrected radiochemical yields of 72% ± 6.5% (*n* = 7) at molar activities exceeding 90 GBq/μmol. Cellular uptake and inhibition studies with [¹⁸F]triacoxib were carried out in COX-2 expressing HCA-7 cells. Cellular uptake of [¹⁸F]triacoxib in HCA-7 cells reached 25% radioactivity/mg protein after 60 min. Cellular uptake was reduced by 63% upon pre-treatment with 0.1 mM celecoxib. 90% of the radiotracer remained intact *in vivo* after 60 min p.i. in mice. [¹⁸F]Triacoxib was further evaluated in HCA-7 tumor-bearing mice using dynamic PET imaging, radiometabolite analysis, autoradiography, and immunohistochemistry. PET imaging revealed favorable baseline radiotracer uptake in HCA-7 tumors (SUV_{60min} = 0.76 ± 0.02 (*n* = 4)), which could be blocked by 20% through i.p. pre-treatment with 2 mg of celecoxib. Autoradiography and immunohistochemistry experiments further confirmed blocking of COX-2 *in vivo*.

[¹⁸F]Triacoxib, whose non-radioactive analog was identified through *in situ* click chemistry, is a novel radiotracer for PET imaging of COX-2 in cancer. Moderately specific binding of [¹⁸F]triacoxib to COX-2 *in vivo* reinforced the feasibility of optimal structure selection by *in situ*

click chemistry. Despite a substantial amount of non-specific uptake *in vivo*, [^{18}F]triacoxib represents a suitable radiotracer for PET imaging of COX-2. It remains to be elucidated how this novel radiotracer would perform in first-in-human studies to detect COX-2 with PET.

Keywords: ^{18}F , positron emission tomography (PET), cyclooxygenase-2 (COX-2), molecular imaging

2.1 INTRODUCTION

Induction of cyclooxygenase-2 (COX-2) expression is an essential and crucial physiological response seen in inflammatory conditions. Chronic COX-2 overexpression and function associated with inflammation can also lead to the development of malignant lesions.¹ COX-2 overexpression promotes tumorigenicity, angiogenesis, metastasis, and resistance to apoptosis in a wide range of different tumor types, including brain, breast, pancreatic, leukocytic, and, perhaps most prevalently, colorectal cancers.¹⁻⁹ Thus, activation of COX-2 and COX-2 mediated downstream signaling pathways play a critical role in disease progression of colorectal cancer. Subepithelial stromal cells (especially fibroblasts) of the colon appear to be the primary source of COX-2 in early to premalignant stages of colorectal carcinogenesis.¹ While healthy gastrointestinal mucosa shows little to no COX-2 expression, human colorectal tumors display high levels of COX-2.¹⁰

The cyclooxygenase (COX) family of isozymes performs the two-step conversion of arachidonic acid to prostaglandin H₂ (PGH₂) which is subsequently converted to other eicosanoids including prostaglandins, prostacyclins, and thromboxanes.^{11,12} The most abundant of these eicosanoids, prostaglandin E₂ (PGE₂), plays various physiological, homeostatic, and pathological roles in the body.^{9,11,13,14} Three different isoforms of cyclooxygenase are expressed in humans, COX-1, COX-2, and COX-3.^{15,16} COX-1 is a constitutively expressed housekeeping enzyme associated with gastric mucosa production.^{9,11} COX-2 is inducibly expressed by various stimuli including growth factors and pro-inflammatory cytokines, and is responsible for high levels of prostaglandin production during inflammation.^{12,17,18} COX-1 and COX-2 are 60% homologous, homodimeric proteins with distinct cyclooxygenase and peroxidase active sites in the catalytic domain.^{11,18} Little more is known of COX-3 than that it is an alternative splicing variant of COX-1 found in the cerebral cortex and the heart.¹⁶

Non-steroidal anti-inflammatory drugs (NSAIDs) have been used in the treatment of inflammation and pain for more than 100 years, since the development of aspirin, an acetyl derivative of salicylic acid.¹⁹ However, because many common NSAIDs inhibit both the constitutive COX-1 isoenzyme as well as the inducible COX-2 isoenzyme, NSAID treatment resulted in gastrointestinal toxicity related to mucosa production and adverse renal effects related to blood flow.

Since the discovery of the COX-2 isoform, several selective inhibitors of COX-2 with minimal gastrointestinal side effects have been developed.^{15,18,20} While many of these inhibitors have made it to market, most of the more selective compounds have been withdrawn due to diverse renal events and severe cardiac toxicity associated with their use, the most pronounced example being rofecoxib (Vioxx).^{20,21}

Sustained treatment with COX-2 specific inhibitors significantly reduced tumorigenicity and metastasis in prostate and breast cancer and induced caspase-dependent apoptosis in neuroblastoma.^{2,22,23} Clinical trials studying combinatorial treatments using COX-2 inhibitors suggest a strong role for inhibition in the treatment of COX-2 positive tumors, especially colorectal tumors.^{7,9,24}

While invasive and labor-intensive methods for *ex vivo* assays, such as biopsy and immunostaining are available, inherent *ex vivo* instability of COX-2 mRNA and protein may prevent accurate COX-2 detection or measurement.^{25,26} Due to its expression profile in colorectal cancers, a non-invasive *in vivo* method of COX-2 detection, such as molecular imaging, could be used in diagnosis and treatment monitoring. Thus, COX-2 has become an important biomarker for the development of molecular probes. Over the past two decades there have been numerous attempts to develop a selective COX-2 molecular imaging probe for the determination of COX-2 expression *in vivo*.²⁷

These attempts have led to the development of numerous fluorescent probes,²⁸ PET,^{29–32} and SPECT radiotracers.³³ To date, many of these compounds contain structures which are based on established COX-2 inhibitors, especially celecoxib, rofecoxib, or their derivatives. While, over time, inhibitors generally became more COX-2 selective, their limited cellular uptake and specificity have, to date, been inadequate for use as COX-2 PET imaging agents.^{29–32,34–39}

Recently, our group has developed [¹⁸F]pyricoxib, a pyrimidine scaffold-based radiotracer containing a methylsulfone motif as a COX-2 pharmacophore. [¹⁸F]Pyricoxib displayed a comparable inhibitory potency to celecoxib and a good uptake profile into COX-2 expressing colorectal cancer cells and tumors *in vitro* and *in vivo*; however, the [¹⁸F]pyricoxib radiotracer still showed a very high level of non-specific uptake unrelated to COX-2 expression.²⁹

Therefore, our lab set out to develop novel COX-2 inhibitors with the most optimal structure for enzyme binding, using kinetic target-guided synthesis (TGS) or *in situ* click chemistry. In this highly innovative drug development method, the enzyme active site acts as a molecular template, selecting and positioning building blocks to construct a highly potent and selective inhibitor *in situ*. This work led to the identification of two potent triazole-based COX-2 inhibitors which had superior *in vivo* anti-inflammatory activity relative to celecoxib in a carrageenan-induced rat model.⁴⁰

The goal of the present study was to develop and validate the triazole-containing PET radiotracer [¹⁸F]triacoxib, discovered through *in situ* click chemistry, and to analyze its binding to COX-2 and its uptake *in vitro* and *in vivo* in colorectal cancer cells and tumors. Additionally, we set out to test whether this novel radiotracer could surpass the performance of [¹⁸F]pyricoxib, and other previously developed PET imaging probes, by showing less non-specific uptake and off-target

binding. This work was performed to develop a more optimal PET imaging probe for the targeting of COX-2, with potential for use in a clinical setting.

2.2 MATERIALS AND METHODS

2.2.1. General

All chemicals, reagents, and solvents for synthesis and analysis were analytical grade. Chromafix (30-PS-HCO₃, Macherey-Nagel) cartridges were purchased from ABX. All other chemicals and solvents were purchased from Sigma Aldrich. All solvents were dried and/or distilled before utilization. Reference compound 4-(4-(fluorophenyl)-1-(3-methyl-1-(4-(methylsulfonyl)phenyl)-1*H*-pyrazol-5-yl)-1*H*-1,2,3-triazole **4** was prepared according to literature.⁴⁰ Thin-layer chromatography (TLC) was carried out using HF254 silica gel. Radio-TLC analysis was performed on a Bioscan radio-TLC reader and Winscan analysis software. High-performance liquid chromatography (HPLC) purification and analysis were performed using a Luna 5 μ m polyfluorophenyl (PFP(2)) column on a Gilson 322 Pump module fitted with a 171 Diode Array and a radioactivity detector. The following elution profile was used: 0-5 min, isocratic elution with 40% CH₃CN/H₂O; 5-10 min 40% CH₃CN/H₂O to 60% CH₃CN/H₂O; 10-21 min isocratic elution with 60% CH₃CN/H₂O; 21-26 min 60% CH₃CN/H₂O to 80% CH₃CN/H₂O; 26-35 min isocratic elution with 80% CH₃CN/H₂O.

¹H-NMR and ¹³C-NMR spectra were recorded on an Agilent/Varian Inova two-channel 400 MHz spectrometer, an Agilent/Varian Inova four-channel 500 MHz spectrometer, and an Agilent/Varian VNMRS three-channel 600 MHz spectrometer. Chemical shifts are given in ppm referenced to internal standards (s = singlet, singlet, d = doublet). High-resolution mass spectrometry (HR-MS) was carried out on an Agilent Technologies 6220 oaTOF.

2.2.2. Chemistry

4-(Phenyl-boronic acid pinacol ester)-1-{1-[4-(methane-sulfonyl)phenyl]-3-methyl-1H-pyrazol-5-yl}-1H-1,2,3-triazole **3**. Labeling precursor **3** for late-stage radiofluorination reaction was prepared according to literature with some modifications which included a scaling down, a reduction in precursor reagent concentration, and the use of methanol instead of t-BuOH.⁴¹ 5-Azido-1-[4-(methanesulfonyl)-phenyl]-3-methyl-1H-pyrazole **1** (0.36 mmol)⁴⁰ and 4-ethynylphenylboronic acid pinacol ester **2** (0.36 mmol) was added to methanol (1 mL) in a reaction vial and stirred for 5 min at room temperature. 160 μ L of a 1 molar solution of sodium ascorbate (10 mol%) and 0.825 mL of de-ionized water were added to the reaction mixture.

The mixture was bubbled through with argon for 15 min followed by the addition of 16 μ L of a 1 molar solution of CuSO₄ · 5 H₂O (1 mol%) and the cap was closed tight. Reaction was stirred at room temperature for 24 hours, extracted with ethyl acetate and purified by column chromatography (EtOAc/hexane (2:3)) to give 4-(phenylboronic acid pinacol ester)-1-{1-[4-(methanesulfonyl)phenyl]-3-methyl-1H-pyrazol-5-yl}-1H-1,2,3-triazole in 74% yield as an off-white solid. ¹H-NMR (CDCl₃, 600 MHz): δ 1.37 (s, 12H, (CH₃)₄ of pinacol), 2.45 (s, 3H, CH₃), 3.04 (s, 3H, SO₂CH₃), 6.58 (s, 1H, CH of pyrazole ring), 7.40 (d, J = 9.0 Hz, 2H, Ar-H), 7.86 (d, J = 8.3 Hz, 2H, Ar-H), 7.90 (d, J = 8.7 Hz, 2H, Ar-H), 7.90 (d, J = 8.7 Hz, 2H, Ar-H), 7.95 (s, 1H, CH of triazole ring); ¹³C-NMR (CDCl₃, 150 MHz): δ 14.20 (CH₃ of pyrazole ring), 25.02 ((CH₃)₄ of pinacol), 44.64 (SO₂CH₃), 84.15 (OC(CH₃)₂C(CH₃)₂O), 106.48 (CH of pyrazole ring), 122.35 (CH of triazole ring), 123.36, 125.22, 128.98, 131.67, 134.85, 135.63, 139.50, 142.08, 148.50, 150.95; HR-MS analysis, calculated for C₂₅H₂₈BN₅NaO₄S [M + Na]⁺ m/z 528.1847, found 528.1845.

2.2.3. Radiochemistry

[¹⁸F]Fluoride was produced by the ¹⁸O(p,n)¹⁸F nuclear reaction through proton irradiation of enriched (98%) ¹⁸O water (3.0 ml, Rotem, Germany) using a TR19/9 cyclotron (Advanced Cyclotron Systems, Inc., Richmond, BC, Canada).

Synthesis of 4-[4-[¹⁸F]fluorophenyl]-1-{1-[4-(methanesulfonyl)phenyl]-3-methyl-*IH*-pyrazol-5-yl}-*IH*-1,2,3-triazole ([¹⁸F]triacoxib) was performed using a previously described method with some modifications which included the addition of a QMA washing step using n-BuOH subsequent to acetone washing, the scaling down of the reaction, and the use of n-BuOH and DMA in a 1:1 ratio.⁴² 4-(Phenylboronic acid pinacol ester)-1-{1-[4-(methanesulfonyl)phenyl]-3-methyl-*IH*-pyrazol-5-yl}-*IH*-1,2,3-triazole **3** (10 mg, 20 μmol) and Cu(OTf)₂(py)₄ (6 mg, 8.8 μmol) were dissolved in DMA (0.266 mL) in a reaction vial. Et₄NHCO₃ (1.8 mg, 9.4 μmol) was dissolved in n-BuOH (0.27 mL) and used to elute no-carrier-added [¹⁸F]fluoride from acetone and n-BuOH washed QMA cartridge directly into the DMA reaction mixture. The whole mixture was reacted at 110 °C for 20 min under atmosphere to produce the [¹⁸F]triacoxib. HPLC purification with a Luna 5 μm polyfluorophenyl (PFP(2)) column was used to isolate the radioactive compound [¹⁸F]**4** ([¹⁸F]triacoxib) eluting at a retention time of 21 min in radiochemical yields of 72 ± 6.5% (*n* = 7). The molar activity exceeded 90 GBq/μmol. Radio-TLC analysis on silica gel plates (80% EtOAc/hexane, R_f = 0.5) confirmed a radiochemical purity greater than 98%.

The HPLC solvent was removed under vacuum, and the compound was re-dissolved in a solution of 7% ethanol in saline for *in vitro* and *in vivo* studies.

2.2.4. Determination of lipophilicity

The shake-flask method was used to determine the lipophilicity of [¹⁸F]triacoxib.⁴³ The partition coefficient of [¹⁸F]triacoxib was measured using *n*-octanol as organic phase and PBS (pH 7.4) as

the aqueous phase. 500 μL of each phase were added to a LoBind Eppendorf tube, to which <1 MBq of [^{18}F]triacoxib was added, and the mixture was shaken vigorously for 5 min. The mixture was then centrifuged at 2000 rpm for 2 min to allow the layers to separate. Aliquots of 100 μL were removed from each phase, and the amount of [^{18}F]triacoxib present in each phase was measured by a Wizard gamma counter. Experiments were performed in triplicate, and $\log D_{7.4}$ values were calculated.

2.2.5. In vitro cell uptake studies

In vitro assessment of [^{18}F]triacoxib was performed using COX-2 positive human colon carcinoma HCA-7 cells (ECACC 02091238). Baseline cell uptake experiments using [^{18}F]triacoxib (~ 330 kBq/mL; molar activity >40 GBq/ μmol) were performed in triplicate using Krebs-Ringer buffer at 37°C with incubation times of 5, 15, 30, 60, and 90 min. During blocking experiments, cells were treated with a COX-2 inhibitor, celecoxib or non-radioactive triacoxib **4**, at 10 or 100 μM for 30 min as a pre-incubation before [^{18}F]triacoxib was added. Blocking experiments were performed after 60 min incubation with the radiotracer. At 60 min the buffer was removed, and cells were washed twice with ice-cold HEPES buffered (10 nM) saline solution with 1% BSA and lysed with 400 μL of radioimmunoprecipitation buffer (RIPA). 300 μL samples of cell lysate were collected and radioactivity was determined using a WIZARD2 Automatic gamma counter (Perkin Elmer; Waltham, MA, USA). Bicinchoninic acid (BCA) assay was used to determine total protein concentrations of the samples (Pierce, Thermo Scientific 23227) using bovine serum albumin (1000, 750, 500, 250, 125, 50, 25 $\mu\text{g}/\text{mL}$, blank) as the protein standard. Cell uptake data were analyzed as percent radioactivity per mg of protein (% radioactivity/mg protein).

2.2.6. Animal model

All animal experiments were performed according to guidelines from the Canadian Council on Animal Care (CCAC) and approved by the local animal care committee (Cross Cancer Institute, University of Alberta), ethics approval number AC16223.

PET experiments were performed using HCA-7 tumor-bearing NIH-III nude mice (Saint Constant, Charles River Laboratories, Quebec, Canada). Female NIH-III nude mice were housed under standard conditions with free access to standard food and tap water.

HCA-7 cells (5×10^6 cells in 100 μ L of PBS) were injected into the upper left flank of female NIH-III nude mice (20–24 g). After 14 to 21 days post-inoculation, HCA-7 tumors reached sizes of approximately 300-500 mm^3 which were suitable for all *in vivo* experiments.

2.2.7. Radiometabolite analysis

The radiotracer solution containing ~ 30 MBq [^{18}F]triacoxib in $\sim 7\%$ EtOH/saline was injected intravenously into normal female BALB/c mice under isoflurane anesthesia.

Blood samples from the tail vein (20-40 μ L) were collected at 5, 15, 30 and 60 min p.i.. Plasma was separated by centrifugation (5 min, 13,000 \times g) followed by plasma protein precipitation using methanol (two parts per one part plasma) and a second centrifugation step (5 min, 13,000 \times g). Supernatants were analyzed by radio thin-layer chromatography (radio-TLC) and radioactivity was determined using a WIZARD2 Automatic gamma counter (Perkin Elmer; Waltham, MA, USA). TLCs were developed in 80% EtOAc/hexane and analyzed using a BAS-5000 reader. [^{18}F]triacoxib had an R_f value of 0.50 in this solvent system.

2.2.8. PET imaging

HCA-7 tumor-bearing mice were immobilized in prone position into the center field of view of an Inveon® PET/CT scanner (Siemens Preclinical Solutions, Knoxville, TN, USA) with isoflurane

in 40% oxygen/ 60% nitrogen (gas flow= 1 mL/min), and. The body temperature was kept constant at 37 °C for the entire experiment. For PET experiments, 3-8 MBq of [¹⁸F]triacoxib in ~150 µL of solution (7% EtOH/saline) was administered intravenously as a bolus injection into the tail vein via a preplaced catheter. Dynamic PET data was collected over 60 min.

For the blocking experiments, COX-2 inhibitor celecoxib (2 mg per animal corresponding to 100 mg/kg dose) in 100 µL DMSO was injected intraperitoneally (i.p.) 60 min prior to radiotracer administration. Blocking experiments were performed using static data acquisition between 50 and 60 min p.i..

Mean standardized uptake values [$SUV_{\text{mean}} = (\text{activity/mL tissue})/(\text{injected activity/body weight}), \text{mL/g}$] and %ID/g (percent injected dose/gram of tissue) were calculated for each region of interest (ROI) with a threshold defined at 50% of radioactivity uptake. The time-activity curves (TACs) were generated from dynamic PET scans. All semi-quantified PET data are presented as means \pm SEM.

2.2.9. Autoradiography

For autoradiography, mice were injected with ~30 MBq of [¹⁸F]triacoxib in 7% EtOH/saline into the tail vein again. For blocking 2 mg celecoxib in 100 µL DMSO was administered intraperitoneal 60 min before radiotracer injection. A static PET scan was performed at 60 min p.i. After the PET experiment was finished, mice were euthanized, and tumor tissue was harvested.

Tumor tissue was embedded into Tissue-Tek® embedding medium for frozen tissue specimens to ensure optimal cutting temperature (O.C.T.) and frozen in liquid nitrogen. Cryoslices of 40 µm were cut using a Leica CM1850 cryostat (Leica Microsystems Inc. Concorde, Ontario, Canada). Slices were placed into a BAS Cassette (2325, Fujifilm) and exposed to a phosphor imaging plate (BAS-MS 2025, Fujifilm) for ~60 min at room temperature and analyzed using a Typhoon 9400

Variable Mode Imager from molecular dynamics (GE Amersham Pharmacia Biotech, Amersham, Great Britain).

2.2.10. Immunohistochemistry

Immunohistochemistry for detection of COX-2 on HCA-7 tumor slices was carried out on the cryo slices used for autoradiography before. Upon thawing, tissue sections were fixed with formalin for 30 min. The fixed sections were blocked overnight at 4 °C using 0.12 mg/mL unconjugated goat anti-mouse Fab fragments (115-003-007, Jackson ImmunoResearch, West Grove, PA, USA) in 0.5% fish skin gelatin (G7765, Sigma-Aldrich) pH 7.4, supplemented with 0.1% Triton X-100. The sections were rinsed 3-times with Tris-buffered saline having 0.5% Tween 200 (TBST) for 5 min each and then incubated with the goat anti-COX-2 antibody (sc-1747, Santa Cruz Biotechnology, 1:3000) overnight at 4 °C in a humidity chamber.

The samples were then treated with 3% H₂O₂ in de-ionized water for 15 min, proceeded by three 10 min washes using TBST. COX-2 was detected using the Goat-on-Rodent HRP-polymer (Biocare Medical, Concord, USA) kit.

The Goat Probe was applied for 30 min followed by three 5 min washes of TBST, and the Goat-on-Rodent HRP-polymer was applied for 1 hour followed by three 10 min washes of TBST. Both incubations were at room temperature. The samples were developed, using Dako Liquid DAB+ Substrate Chromagen System plus 1% copper sulfate and counter-stained with hematoxylin. The samples were dehydrated by reversing the re-hydration procedure and coverslipped slides.

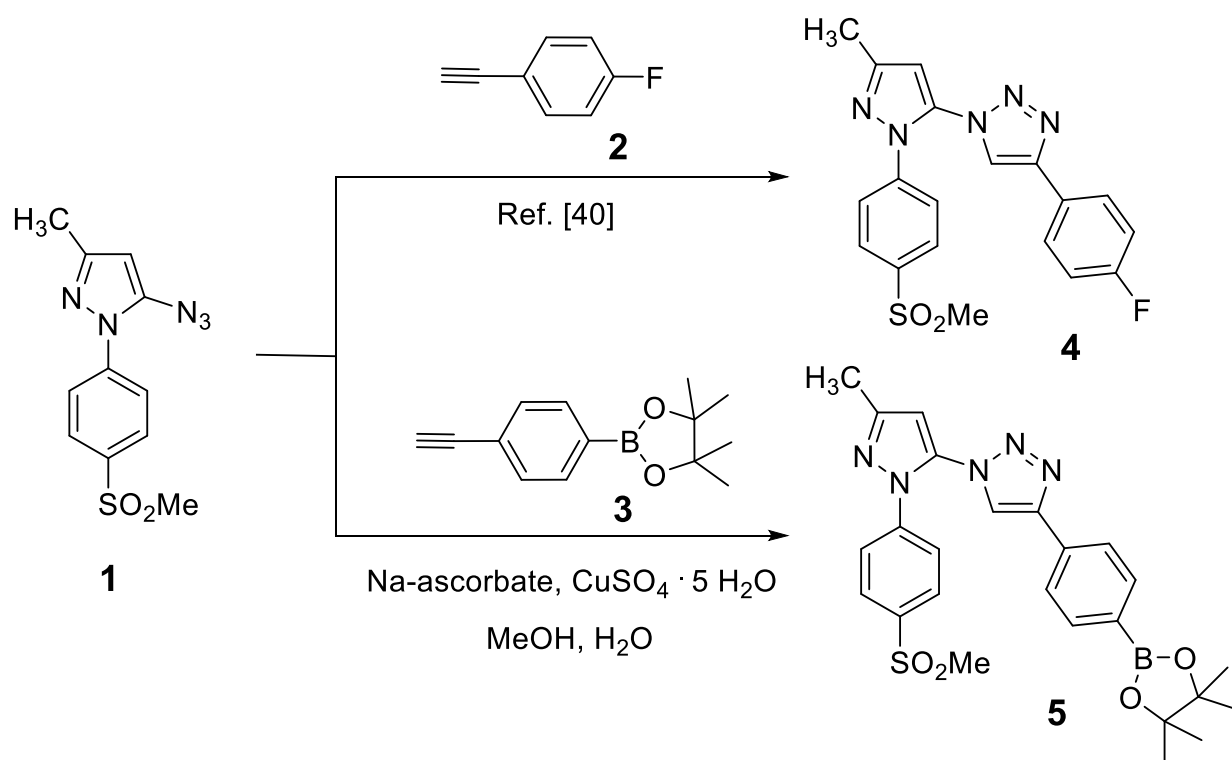
2.2.11. Statistical analysis

All *in vitro* and *in vivo* data are expressed as means ± SEM. Graphs were constructed using GraphPad Prism 5.0 (GraphPad Software). Where applicable, statistical differences were tested using unpaired Student's t-test and were considered significant for P <0.05.

2.3. RESULTS

2.3.1. Chemistry

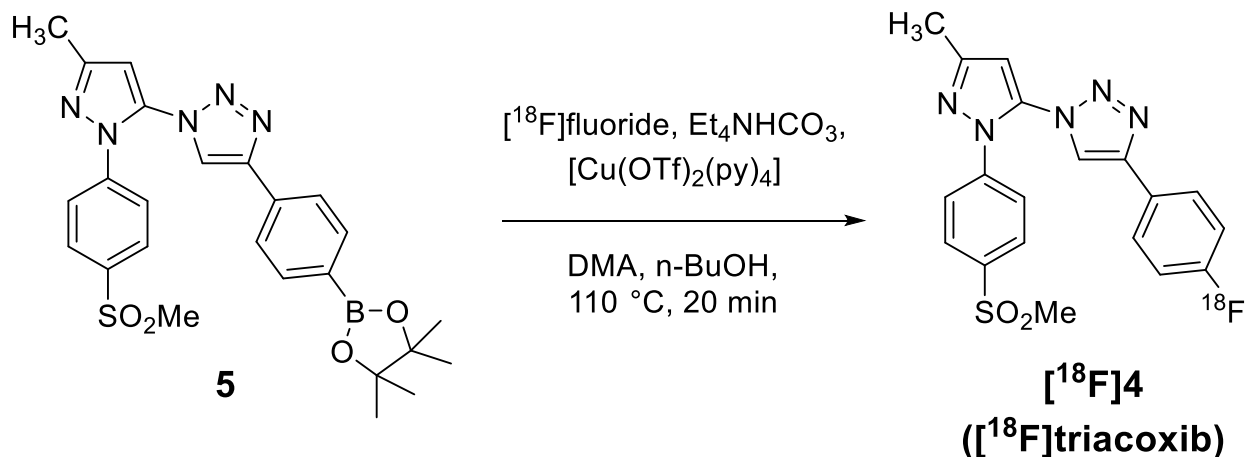
Reference compound 4-(4-(fluorophenyl)-1-(3-methyl-1-(4-(methylsulfonyl)-phenyl)-*1H*-pyrazol-5-yl)-*1H*-1,2,3-triazole **4** was prepared in 47% chemical yield starting from 5-azido-3-methyl-1-(4-(methylsulfonyl)phenyl)-*1H*-pyrazole **1** and commercially available 1-ethynyl-4-fluorobenzene **2** according to published procedures.^{40,41} Labeling precursor 4-(phenylboronic acid pinacol ester)-1-{1-[4-(methane-sulfonyl)phenyl]-3-methyl-*1H*-pyrazol-5-yl}-*1H*-1,2,3-triazole **5** was synthesized through copper-mediated alkyne-azide [3+2]-cycloaddition (CuAAC)⁴¹ between 5-azido-3-methyl-1-(4-(methyl-sulfonyl)phenyl)-*1H*-pyrazole **1**⁴⁰ and commercially available 4-ethynyl-phenylboronic acid pinacol ester **3** to form desired 1,4-disubstituted triazole **5** in 74% isolated yield. The synthesis of reference compound **4** and labeling precursor **5** is given in Scheme 1 (Details outlining the syntheses and characterizations of all chemical precursors are available in sections 1 and 5 of Supplemental Information – [¹⁸F]triacoxib, available online).



Scheme 1. Synthesis of reference compound **4** and labeling precursor **5**

2.3.2. Radiochemistry

Synthesis of 4-[4-[^{18}F]fluorophenyl]-1-{1-[4-(methanesulfonyl)phenyl]-3-methyl-*1H*-pyrazol-5-yl]-*1H*-1,2,3-triazole [^{18}F]4 ([^{18}F]triacoxib) was accomplished using Cu-mediated late-stage radiofluorination chemistry with $[\text{Cu}(\text{OTf})_2(\text{py})_4]$ as the copper source (Scheme 2).⁴²



Scheme 2. Late-stage radiofluorination of radiotracer [^{18}F]triacoxib [^{18}F]4

Reaction of no-carrier-added [^{18}F]fluoride with boronic acid ester **5** in the presence of $[\text{Cu}(\text{OTf})_2(\text{py})_4]$ in DMA and *n*-BuOH at 110 °C for 20 min afforded radiotracer [^{18}F]4 ([^{18}F]triacoxib) in radiochemical yields of $72 \pm 14\%$ ($n = 7$). The total synthesis time was 90 min, including HPLC purification, and the molar activity exceeded 90 GBq/ μmol (Figure 19-23 and Graph 1). Alternative direct radiofluorination strategies starting from corresponding *p*-nitro and *p*-trimethylanilinium precursors as well as Cu(I)-mediated click chemistry between 1-ethynyl-4-[^{18}F]fluorobenzene and azide **1** gave only highly variable radiochemical yields of less than 15% (Scheme 3 and Table 2-6 in the supplemental section).⁴⁴

2.3.3. Lipophilicity

The lipophilicity of [^{18}F]triacoxib was determined as $\text{LogD}_{7.4} = 1.70$ using the shake-flask method.⁴³

2.3.4. Cellular uptake and inhibition studies

Cellular uptake and inhibition studies in COX-2 expressing human colorectal HCA-7 cells²⁹ are shown in Figure 3.

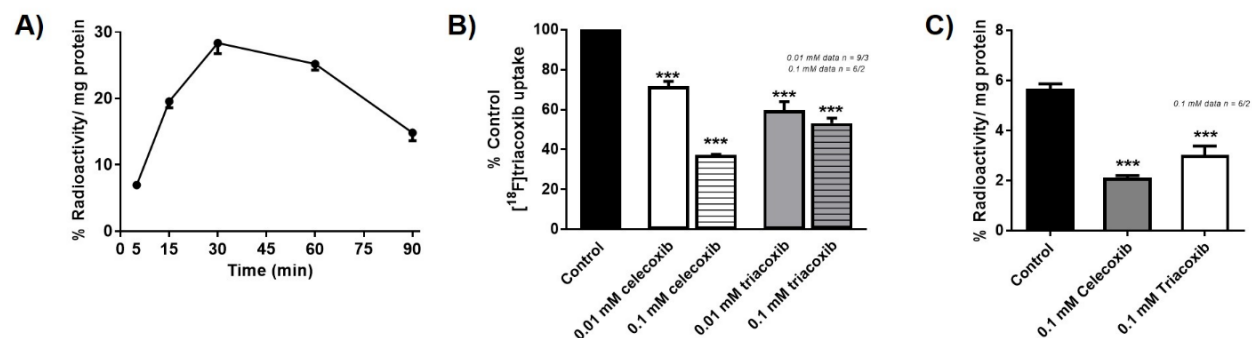


Figure 3. **A)** Uptake of radiotracer [^{18}F]triacoxib into HCA-7 cells over 90 min. Data are normalized as % radioactivity/mg protein and shown as mean \pm SEM from $n = 3$ experiments. **B)** Blocking of [^{18}F]triacoxib uptake (30-min incubation time) into HCA-7 cells using high concentrations (100 μM) of selective COX-2 inhibitor celecoxib and non-radioactive triacoxib. Data are normalized as % radioactivity/mg protein and shown as mean \pm SEM from six data points out of two experiments. **C)** Concentration-dependant inhibition of [^{18}F]triacoxib uptake (30 min incubation time) into HCA-7 cells. Data are normalized as % maximum uptake of [^{18}F]triacoxib and analyzed as mean \pm SEM from six data points out of two experiments. $*P < 0.05$; $**P < 0.01$; $***P < 0.001$

Baseline cell uptake of [¹⁸F]triacoxib showed fast initial uptake into COX-2 positive HCA-7 cells, with uptake values of 7% radioactivity/mg protein after 5 min incubation (Figure 3A). Uptake of radiotracer [¹⁸F]triacoxib over time increased reaching 28% and 25% radioactivity/mg protein at 30 min and 60 min time points, respectively, followed by a washout period to give ~15% radioactivity/mg protein at 90 min.

COX-2 specificity of [¹⁸F]triacoxib was tested using cellular uptake inhibition experiments in HCA-7 cells with COX-2 inhibitors at low (10 μM) and high (100 μM) concentrations (Figure 3B). Cells were preincubated for 30 min with respective inhibitor (celecoxib or triacoxib) before the addition of radiotracer [¹⁸F]triacoxib. Radiotracer uptake at high concentrations (100 μM) of celecoxib and triacoxib was reduced from 5.7% radioactivity/mg protein (control) to 2.1 and 3.0% radioactivity/mg protein, respectively (Figure 3C). Inhibition effects with COX-2 inhibitors were also normalized to percent uptake of the radiotracer alone. Radiotracer [¹⁸F]triacoxib uptake was reduced in a dose-dependent manner. Celecoxib treatment showed the greatest effects by inhibiting 63% of uptake at 100 μM compared to non-radioactive triacoxib which inhibited radiotracer uptake by 47% at 100 μM. Cellular uptake of triacoxib in control and pre-treated cells never exceeded 2% of administered dose. Notably, the inhibitory effects of triacoxib at 10 μM were similar to the effects seen at 100 μM. Thus, it seems that triacoxib exerted its maximum effects at or below 10 μM.

2.3.5. Radiometabolite analysis

Radiometabolite analysis of radiotracer [¹⁸F]triacoxib in blood samples from injected normal BALB/c mice showed only slow metabolism over 60 min p.i. (Figure 4). Levels of intact [¹⁸F]triacoxib decreased from >99% at 5 min p.i. to ~90% at 60 min p.i.

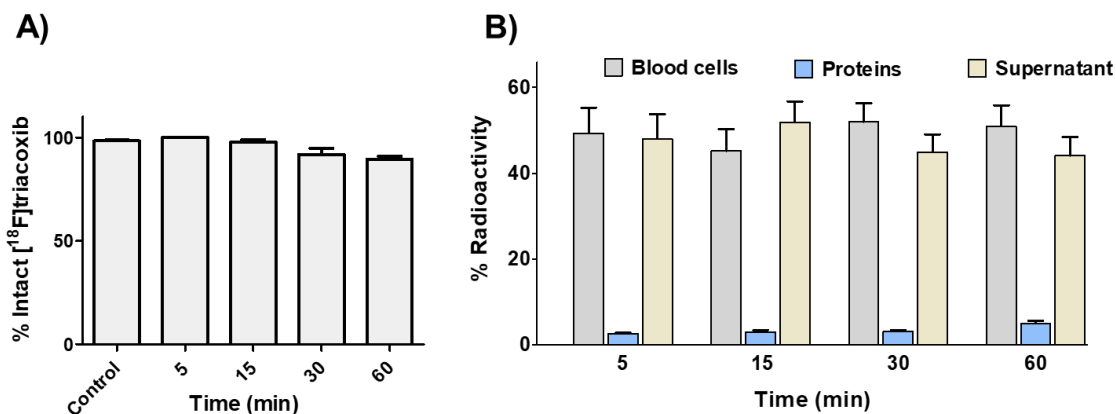


Figure 4. A) *In vivo* stability of $[^{18}\text{F}]$ triacoxib in the blood of BALB/c mice over 60 min as measured by radio-TLC. Data normalized as percent of intact radiotracer and shown as mean \pm SEM from $n = 3$ experiments. **B)** Radioactivity distribution in mouse blood over 60 min. Data normalized as percent of total radioactivity removed at each time point and shown as mean \pm SEM from $n = 3$ experiments.

Blood analysis showed relatively consistent radioactivity levels of $\sim 50\%$ in blood cells between 5 min and 60 min. Only very little radioactivity was bound to plasma proteins ($\sim 3\%$ at 5 min to $\sim 5\%$ at 60 min). Radioactivity in supernatant over time was comparable to radioactivity levels bound to blood cells (48% at 5 min to 44% at 60 min).

2.3.6. PET imaging in HCA-7 tumor-bearing mice

Representative PET images as maximum-intensity projection (MIP) as well as coronal (horizontal), sagittal and transaxial projections of HCA-7 tumor-bearing mice at 60 min p.i. of $[^{18}\text{F}]$ triacoxib and respective time-activity curves of tumor and muscle uptake over time are shown in Figure 5.

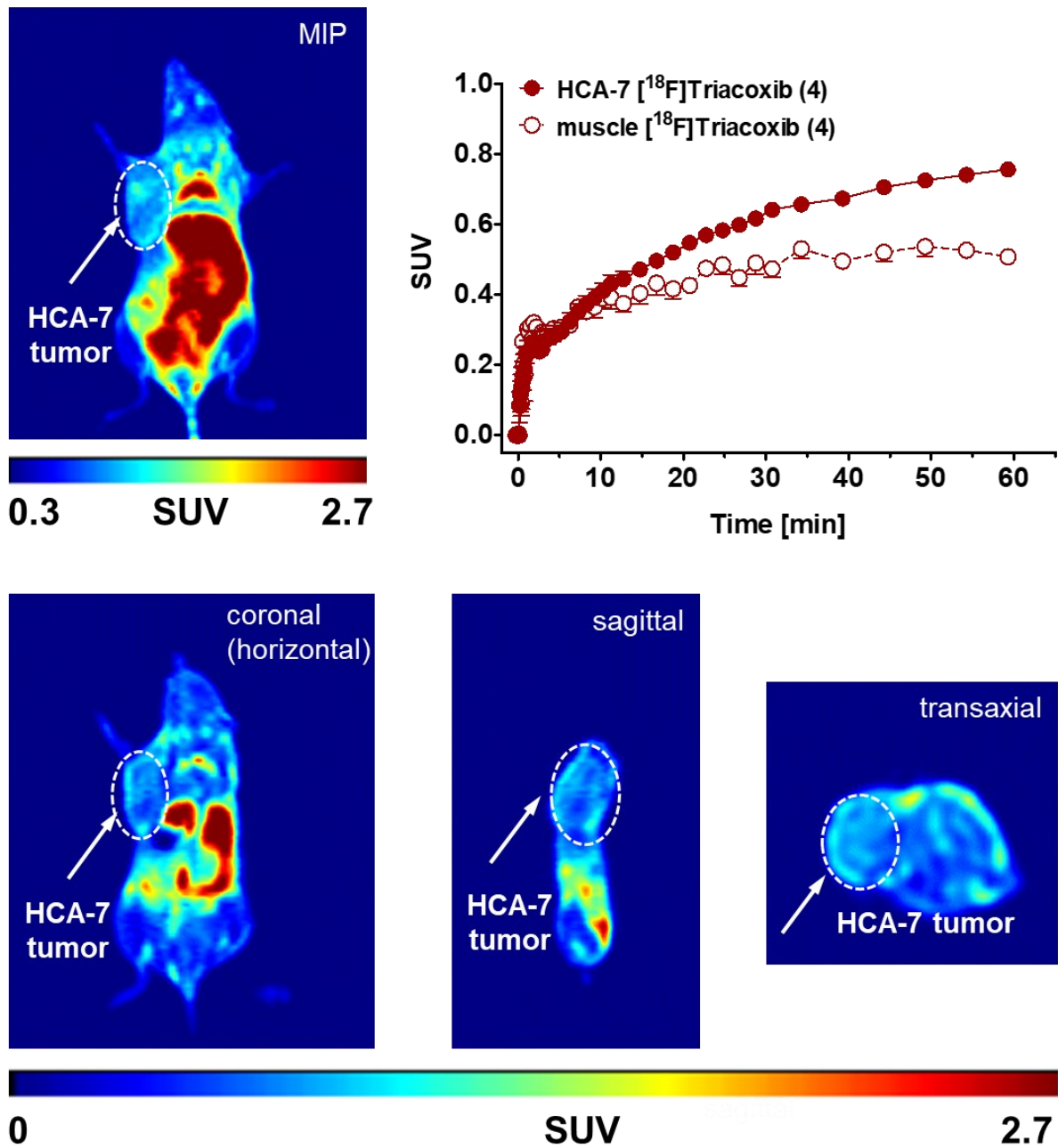


Figure 5. **Top)** PET image (MIP) and time-activity curves of an HCA-7 tumor-bearing NIH-III mouse 60 min after injection of $[^{18}\text{F}]$ triacoxib. Time-activity curves for tumor and muscle uptake of $[^{18}\text{F}]$ triacoxib over 60 min. p.i.. Data shown are mean \pm SEM from $n = 4$ dynamic PET experiments. **Bottom)** Coronal/horizontal (left) sagittal (middle) and transaxial (right) PET images after 60 min p.i.

Radiotracer uptake was analyzed in HCA-7 tumors and contralateral muscle as reference tissue. Accumulation of radiotracer [^{18}F]triacoxib in COX-2 expressing HCA-7 tumors was clearly visible. Radioactivity uptake in the tumor increased over time reaching a $\text{SUV}_{60\text{min}} = 0.76 \pm 0.02$ ($n = 4$). Muscle uptake of [^{18}F]triacoxib was also high. Radioactivity uptake in muscle increased during the first 30 min when it started to plateau to reach a $\text{SUV}_{60\text{min}} = 0.51 \pm 0.02$ ($n = 4$). High radiotracer accumulation occurred in the brown fat tissue over the imaging time course, and high initial activity levels persisted in the lungs, liver, and digestive tract (see table 2). Radiotracer [^{18}F]triacoxib mainly displayed a hepatobiliary clearance profile.

COX-2 specificity of [^{18}F]triacoxib uptake in HCA-7 tumors was demonstrated with a series of *in vivo* blocking experiments using selective COX-2 inhibitor celecoxib.

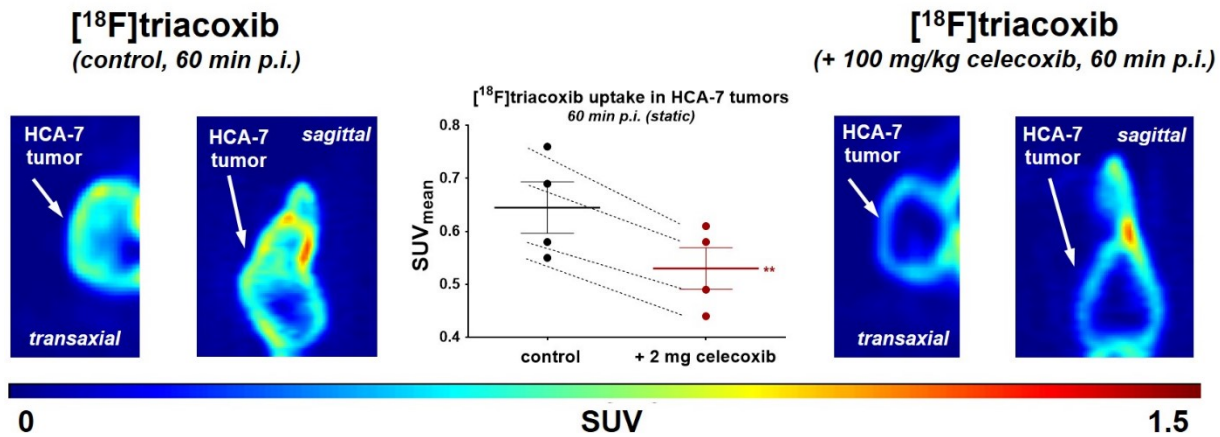


Figure 6. Transaxial and sagittal PET projection of PET images of [^{18}F]triacoxib at 60 min p.i. in the same mouse after two consecutive days under control (left) and blocking (right) conditions. Statistical analysis of the blocking effect with 2 mg celecoxib at 60 min p.i. (middle). Data are presented as individual points with mean \pm SEM from $n = 4$ dynamic PET experiments. $**P < 0.01$.

Figure 6 shows sagittal and transaxial PET images at 60 min p.i. using the same HCA-7 tumor-bearing mouse without (control) and with (blocking) celecoxib (~2 mg), administered through i.p. injection 60 min before radiotracer injection.

Distinct differences in radiotracer uptake in the tumor were measurable between control and pre-treated animals. Tumor uptake of [¹⁸F]triacoxib in pre-treated animals was significantly lower ($p < 0.01$) resulting in a $SUV_{\text{mean}} 0.53 \pm 0.04$ compared to a $SUV_{\text{mean}} 0.65 \pm 0.05$ in the control animals. This data represented a ~20% reduction of radiotracer uptake in COX-2 expressing HCA-7 tumors under blocking conditions. Each set of data points was collected from the same mice during experiments on two consecutive days.

2.3.7. Organ distribution

[¹⁸F]triacoxib radiotracer SUVs and %ID/g values derived from static PET images are shown in Table 1.

Table 1. Biodistribution (static PET-derived data) for [¹⁸F]triacoxib (n =4)

organ	SUV	SUV	%ID/g	%ID/g
	(60 min p.i.)	(60 min p.i.)	(60 min p.i.)	(60 min p.i.)
		+ 2 mg celecoxib		+ 2 mg celecoxib
lung	0.55 ± 0.03	0.83 ± 0.09	2.58 ± 0.19	3.40 ± 0.41
liver	2.68 ± 0.13	2.82 ± 0.13	12.15 ± 1.00	11.63 ± 0.63
brain	0.24 ± 0.01	0.29 ± 0.01	1.07 ± 0.04	1.20 ± 0.06
brown adipose tissue (<i>BAT</i>)	2.21 ± 0.04	3.04 ± 0.14	9.93 ± 0.23	12.61 ± 1.17
bone	0.43 ± 0.02	0.65 ± 0.05	1.93 ± 0.10	2.36 ± 0.44
tumor (<i>whole</i>)	0.72 ± 0.03	0.68 ± 0.06	3.24 ± 0.09	2.85 ± 0.38
tumor (<i>inner part</i>)	0.65 ± 0.05	0.53 ± 0.04*	2.90 ± 0.15	2.21 ± 0.29*
muscle	0.41 ± 0.03	0.45 ± 0.03	1.87 ± 0.11	1.86 ± 0.12

Baseline and blocking uptake values derived from the static PET images seen in figure 6 provide a quantification of the observed effects of celecoxib binding at 60 min p.i.. A significant reduction in uptake is seen in the inner part of the tumor between baseline (%ID/g = 2.90 ± 0.15) and blocking (%ID/g = 2.21 ± 0.29) conditions ($\Delta 24\%$; $p = 0.05$), while the reduction seen in the tumor as a whole (baseline %ID/g = 3.24 ± 0.09 and blocking %ID/g = 2.85 ± 0.38 , $\Delta 12\%$) did not reach significance. Importantly, [^{18}F]triacoxib was strongly taken up into both the brown adipose tissue (BAT) and the liver at 60 min p.i., regardless of blocking by celecoxib. Muscle and brain uptake were also detectable, but their levels couldn't be reduced through blocking.

2.3.8. Autoradiography and immunohistochemistry

COX-2 selectivity of radiotracer [^{18}F]triacoxib *in vivo* was further studied and verified through autoradiography and immunohistochemical analysis (Figure 7).

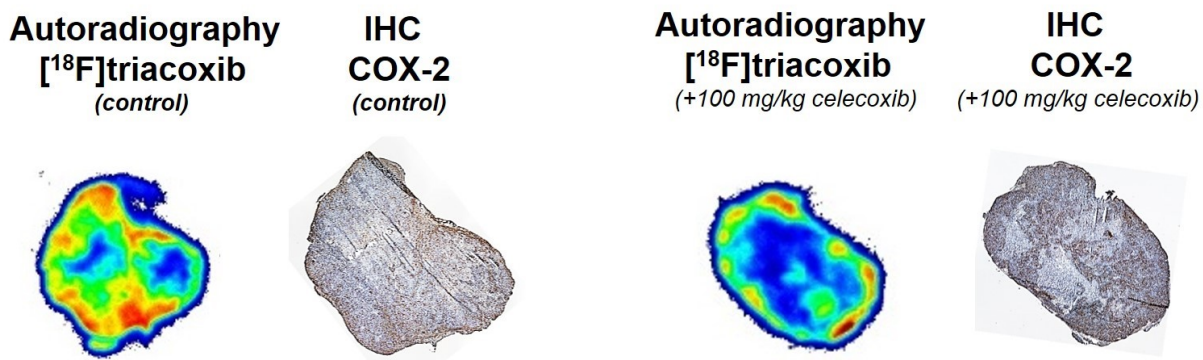


Figure 7. Autoradiography analysis and COX-2 immunohistochemistry (IHC) of excised HCA-7 tumors at 60 min. p.i. of radiotracer [^{18}F]triacoxib under control (left) and blocking conditions (right).

For autoradiography and immunohistochemistry analysis, tumors were excised and 40 μm slices were generated after 60 min p.i. of the radiotracer. Autoradiography revealed the regional distribution of radiotracer [^{18}F]triacoxib in the HCA-7 tumors with yellow and red regions highlighting areas of high and very high radioactivity accumulation, respectively. As shown in the autoradiography images, blocking with celecoxib occurred at both the margin and inside the tumor, with the most noticeable effects occurring within. For many parts of the margin, radioactivity uptake was comparable during control and blocking conditions, while for other parts it showed only mild decreases. COX-2 expression in HCA-7 tumors was also analyzed using immunohistochemistry in adjacent tumor slices after radioactive decay. More intense staining corresponded with high COX-2 expression. Regional distribution of radioactivity as detected by autoradiography matched with COX-2 distribution in the respective tumor slice as visualized through immunohistochemistry during control, but not blocking conditions. This observation further confirmed COX-2 could be visualized by radiotracer [^{18}F]triacoxib.

2.4. DISCUSSION

Over the past two decades, a variety of molecular probes have been developed to target COX-2 in inflammation and cancer.²⁷⁻³² PET imaging with COX-2 targeting radiotracers still has yet to demonstrate its feasibility for detecting COX-2 *in vivo* due to a wide range of challenges. Concerns related to low COX-2 specificity (high off-target binding), the low molar activity of the radiotracers, low inhibitory potency, high lipophilicity and thereof resulting unspecific membrane interactions, and the lack of sufficient *in vivo* metabolic stability, in some combination, have resulted in a low success rate. Hence, to date, no successful clinical translation has been presented, and a continuing need for COX-2 imaging agents with PET remains.

The focus of the present study was to develop and validate the radiotracer [^{18}F]triacoxib, whose parent compound was recently identified by *in situ* click chemistry as a highly potent and selective COX-2 inhibitor.⁴⁰ Triazole-containing COX-2 inhibitor triacoxib was generated through binding of two complementary click chemistry building blocks into the COX-2 binding pocket. *In situ* generated COX-2 inhibitor triacoxib displayed higher *in vivo* activity in an animal model of inflammation in comparison with celecoxib. Therefore, we envisioned the synthesis of an ^{18}F -labeled version of novel COX-2 inhibitor triacoxib and its evaluation in the established COX-2 expressing HCA-7 colorectal cancer model.²⁹ The [^{18}F]triacoxib radiotracer contains a methylsulfone COX-2 pharmacophore in addition to a triazole ring as a result of the copper-mediated [3+2]-cycloaddition (CuAAC) reaction used for its formation. During early drug development projects for the preparation of selective COX-2 inhibitors, both the sulfonamide (present in celecoxib) and the methyl sulfone (present in rofecoxib) COX-2 pharmacophores were identified as critical molecular motifs facilitating tight binding to amino acid residues present in the COX-2 binding site. However, the sulfonamide COX-2 pharmacophore is also used in drugs that bind to other drug targets like carbonic anhydrases.^{45,46} Therefore, sulfonamide COX-2 pharmacophore was not used in the design of triacoxib to avoid off-target binding.⁴⁰

To achieve optimal ^{18}F -labeling of triacoxib, Cu-mediated late-stage radiofluorination chemistry was selected after several conventional radiofluorination methods based on direct nucleophilic aromatic substitution with respective *p*-nitro and *p*-trimethylanilinium compounds as labeling precursors failed to produce sufficient amounts of the [^{18}F]triacoxib radiotracer (see supplemental information Scheme 3 for more details).

Over the last decade, several significant advancements have been made in the development of elegant and versatile late-stage radiofluorinations which allow for the efficient preparation of

radiopharmaceuticals containing structural motif which typically eluded conventional radiofluorination chemistry.⁴⁷ Many of the novel late-stage radiofluorination strategies utilize polar aprotic organic reaction solvents, and the presence of protic solvents, such as water or alcohols, is usually detrimental to the conventional S_NAr reactions which use direct radiofluorination chemistry. Recent Cu-mediated radiofluorination chemistry strategies utilize primary or secondary alcohols as co-solvents to radiolabel various phenylboronic acids and pinacol ester compounds with no-carrier-added (n.c.a.) [¹⁸F]fluoride. This chemistry represents a highly versatile and high yield alternative for the ¹⁸F-labeling of aromatic rings, including electron-rich aromatic compounds, under mild conditions.⁴²

Therefore, we selected Cu-mediated late-stage radiofluorination chemistry with boronic acid pinacol ester containing compound **5** as the labeling precursor for the incorporation of n.c.a. [¹⁸F]fluoride. The [¹⁸F]triacoxib radiotracer (**[¹⁸F]4**) was prepared in average decay-corrected radiochemical yields of 72% confirming the versatile and highly flexible nature of late-stage radiofluorination chemistry.

[¹⁸F]Triacoxib displayed high metabolic stability *in vivo*, with ~90% of [¹⁸F]triacoxib remaining intact after 60 min p.i. This makes [¹⁸F]triacoxib metabolically more stable than the recently developed COX-2 radiotracer [¹⁸F]pyricoxib, which was found to be 75% intact after 60 min p.i..²⁹ In vitro COX-1 and COX-2 inhibition data of triacoxib revealed high inhibitory potency and selectivity towards COX-2 (COX-2: IC₅₀ = 90 nM; COX-1: IC₅₀ >100 μM), comparable to that of celecoxib (COX-2: IC₅₀ = 70 nM; COX-1: IC₅₀ >100 μM) in the same binding assay.⁴⁰

The high metabolic stability, inhibitory potency, and relative selectivity towards COX-2 along with the convenient preparation using late-stage radiofluorination chemistry make [¹⁸F]triacoxib an interesting and suitable radiotracer candidate for PET imaging of COX-2 *in vivo*.

Uptake of [¹⁸F]triacoxib in COX-2 expressing HCA-7 cells was highest at 30 min to 60 min p.i.. HCA-7 cells pre-treated with COX-2 inhibitors at different concentrations showed a concentration-dependent reduction in [¹⁸F]triacoxib cellular uptake and retention. Reduction of radiotracer uptake confirmed specific binding of [¹⁸F]triacoxib to COX-2. However, radiotracer uptake could not be reduced by greater than 50% at high (100 μM) concentrations of non-radioactive triacoxib even after several washing steps with BSA to remove unbound [¹⁸F]triacoxib. This finding suggests the occurrence of several unidentified, nonspecific cellular uptake and retention processes of radiotracer [¹⁸F]triacoxib in HCA-7 cells. Some of the observed nonspecific binding can likely be attributed to the moderately lipophilic nature of the radiotracer (LogD_{7.4} = 1.70). However, neither the present *in vitro* blocking experiments nor previously reported data with [¹⁸F]pyricoxib showed complete inhibition of radiotracer uptake.²⁹ Incomplete inhibition of cellular uptake of radiolabeled COX-2 inhibitors seems to be a common challenge, as all COX-2 radiotracers studied displayed varying levels of nonspecific cellular uptake and retention. On that note, both COX-2 specific and non-specific NSAIDs have been shown to exert COX-2 dependent and independent mechanisms of influencing cancer, particularly colon cancers, through multiple means such as the induction of apoptosis and the inhibition of cell cycle progression.⁴⁸⁻⁵¹ The ability to affect COX-independent physiological pathways suggests the existence of several off-target binding mechanisms by COX-2 specific and non-specific NSAIDs, a position supported by reports of varying clinical responses after treatment with celecoxib versus rofecoxib.⁴⁶ Celecoxib as a COX-2 selective inhibitor containing a sulfonamide pharmacophore also inhibits carbonic anhydrase (CA II), a family of metalloenzymes responsible for pH balance in the cell through the interconversion of water and carbon dioxide. Celecoxib has also been reported to inhibit protein

kinase B (PKB/Akt) or phosphoinositide-dependent kinase 1 (PDK-1) due to its 4-methylphenyl moiety, a variety of CDK-cyclin complexes, ornithine decarboxylase,⁵¹ and cadherin-11.⁵²

The methylsulfone pharmacophore-containing COX-2 inhibitor, rofecoxib, while having little effect on cell proliferation, was shown to decrease cyclin D1 expression and increase expression of P21, P33 and growth-arrest DNA damage-inducible genes (GADD)34 and GADD45.⁵¹ Thus, while these NSAIDs selectively inhibit COX-2 relative to COX-1, they are far from entirely selective.

Triacoxib consists of a heterocyclic core of 5- and 6-member rings including the 4-fluorophenyl moiety. Apart from direct evaluation with COX-2 inhibitors, tests using compounds containing 4-fluorophenyl groups attached to 5- and 6-member heterocyclic rings showed inhibition of P38 MAP kinase at the ATP binding site.⁵³ This fact may indicate additional non-specific binding of triacoxib, which needs to be tested but was beyond the scope of the present study. Neither the data collected in this work nor data from any previous work explain the origin of the non-specific binding, though similarities in pharmacophores and overall structure suggest the possibility that triacoxib also experiences off-target binding similar to that of celecoxib and rofecoxib.

Pre-clinical *in vivo* PET imaging of COX-2 in HCA-7 tumors suggests that at least 20% of [¹⁸F]triacoxib uptake is COX-2 mediated. [¹⁸F]Triacoxib was readily taken up into HCA-7 tumors over a time course of 60 min with no washout. Lower radiotracer uptake was detected in muscle as reference tissue. SUV values demonstrated a distinct tumor versus muscle uptake difference of about 33% corresponding to a tumor-to-muscle (T/M) ratio of ~1.49 after 60 min p.i. which is in a similar range to that of the [¹⁸F]pyricoxib radiotracer (T/M 1.47).²⁹ *In vivo* blocking experiments confirmed COX-2 specific uptake. Pre-treatment of HCA-7 tumor-bearing mice with 2 mg of celecoxib 60 min before administration of the radiotracer reduced [¹⁸F]triacoxib tumor uptake by

~20% at 60 min p.i. (SUV) which was also in a similar range as observed for [¹⁸F]pyricoxib (Δ24%)²⁹ as determined in the same animal model under similar experimental conditions. The remaining ~80% of radiotracer uptake and retention in HCA-7 tumors, as exemplified by continued uptake in the tumor margin, must be justified by non-specific mechanisms, including lipophilicity, lysosomal trapping, and off-target binding not related to COX-2.⁵⁴ Reports of celecoxib's non-COX-2 mediated effects in cancer suggest much greater inhibitor concentrations are needed to inhibit these alternative pathways, thus, pointing to lower binding affinities against other cellular targets.^{48,50,51}

The presented autoradiography and immunohistochemical analysis further confirmed the COX-2-visualization capabilities of [¹⁸F]triacoxib. HCA-7 tumor tissue slices under baseline conditions, confirmed by PET imaging to have [¹⁸F]triacoxib uptake, showed a radiotracer distribution profile by autoradiography in regions corresponding to COX-2 protein expression detected by IHC. Treatment with celecoxib reduced overall radiotracer uptake into the tumor through blocking of COX-2 binding sites. The uptake pattern seen by autoradiography after blocking no longer matches the IHC staining pattern, confirming the occurrence of COX-2-specific interactions with [¹⁸F]triacoxib taking place within the tumor.

It is important to mention that muscle uptake of [¹⁸F]triacoxib was higher than expected, given that COX-2 usually is not expressed in healthy muscle tissue.¹² Very high uptake was also seen in brown adipose tissue (BAT), and blocking with celecoxib failed to reduce the uptake into both BAT and muscle. While this may be caused in part by off-target binding, it is more likely that the lipophilicity of the radiotracer (LogD_{7.4} = 1.70), as measured by the shake-flask method, is contributing to its pharmacokinetic profile, resulting in slow muscle and fat clearance due to its interaction with lipids found in the cell membranes. This explanation is also supported by the

observation of radiotracer uptake in the brain, as transport across the blood-brain barrier (BBB) traditionally requires moderate lipophilicity.⁵⁵

To date, while some attempts at developing COX-2 specific PET radiotracers have shown moderate COX-2 selective uptake in preclinical models of inflammation, none of the reported radiotracers have shown successful clinical translation for cancer imaging.^{29,32,56} These radiotracers share several pharmacological and physico-chemical properties such as high muscle uptake and retention, high lipophilicity, and a lack of a distinct COX-2 specificity.⁵⁶ As celecoxib is the only clinically approved COX-2 inhibitor, numerous previous attempts to image COX-2 have relied on celecoxib-based imaging probes.^{32,57} The celecoxib-derived compounds have shown some moderate success in preclinical imaging of COX-2. They are, however, disadvantaged, since their similarities to celecoxib make them prone to similar off-target binding effects while their structural differences from celecoxib cause them to suffer from reduced COX-2 affinity. More recently, valdecoxib-derived PET radiotracers targeting COX-2 in the brain have been developed, though these compounds also demonstrated non-specific uptake and poor retention, and underwent rapid metabolism and radiodefluorination in blood plasma.^{56,58} While other COX-2 inhibitor-based probes such as [¹⁸F]pyricoxib have shown some selective COX-2 uptake into cancer cells *in vivo*,²⁹ the existence of off-target binding sites and high lipophilicity still represent a significant challenge for further clinical development.

As a COX-2 selective inhibitor generated through *in situ* click chemistry within the COX-2 active site, the [¹⁸F]triacoxib radiotracer was envisioned to be a more suitable candidate for PET imaging of COX-2. Nevertheless, [¹⁸F]triacoxib still displays high non-specific binding which influences its pharmacokinetic profile *in vivo*. Thus, it remains to be seen whether [¹⁸F]triacoxib is a suitable radiotracer for PET imaging of COX-2 in patients with inflammatory conditions such as cancer,

and perhaps additional work in another model may be a useful step in determining if [¹⁸F]triacoxib is ready to be used in clinical studies.

2.5. CONCLUSION

We have reported the development and validation of radiotracer [¹⁸F]triacoxib for PET imaging of COX-2 *in vivo*. This compound was discovered through *in situ* click chemistry as it was generated in the active site of COX-2. Radiotracer [¹⁸F]triacoxib performed similarly to [¹⁸F]pyricoxib *in vitro* and *in vivo*, as analyzed in the same preclinical colorectal cancer models with high COX-2 baseline expression. Despite the target-directed generation of highly potent and selective COX-2 inhibitor triacoxib, the respective radiotracer [¹⁸F]triacoxib still displayed substantial off-target binding resulting in unspecific uptake and retention of the radiotracer *in vitro* and *in vivo*. The non-specific interactions, which presumably are caused by [¹⁸F]triacoxib's lipophilicity and off-target binding, still represent a significant challenge for its use as a COX-2 imaging agent with PET. Despite the difficulties, [¹⁸F]triacoxib represents one of the most promising radiotracers for PET imaging of COX-2. Only additional preclinical, followed by clinical analyses will answer remaining important questions regarding the usefulness of [¹⁸F]triacoxib for the detection of COX-2 in patients with inflammatory conditions, including cancer.

Acknowledgements

The authors would like to thank Dave Clendening and Blake Lazurko from the Edmonton PET centre for radionuclide production. Furthermore, the authors thank other members of the Wuest research lab including Jennifer Dufour for helping with the cell culture, Cody Bergman for helping with the establishment of HPLC purification conditions, and Daniel Krysz for assistance and training in data processing and figure preparation. The authors also want to thank Dr. Ingrid

Hamann (former member of the Wuest research lab) for helping with the autoradiography experiment. The authors also thank Dan McGinn (Vivarium of the Cross Cancer Institute, Edmonton, Alberta, Canada) for supporting the animal work and Dr./ Hans-Soenke Jans (Department of Oncology, University of Alberta) for technical support of the preclinical PET imaging facility.

Author Contributions

Experimental planning: ML, MW, and FW. Radiosynthesis: ML, *In vitro* cell experiments: ML. Animal experiments including imaging and image data analysis: MW. Ex vivo autoradiography and immunohistochemistry: MW, DG. Figures preparation ML and MW. Manuscript writing: ML, MW, and FW.

2.6. SUPPLEMENTAL INFORMATION

2.6.1. The determination of brown adipose tissue uptake

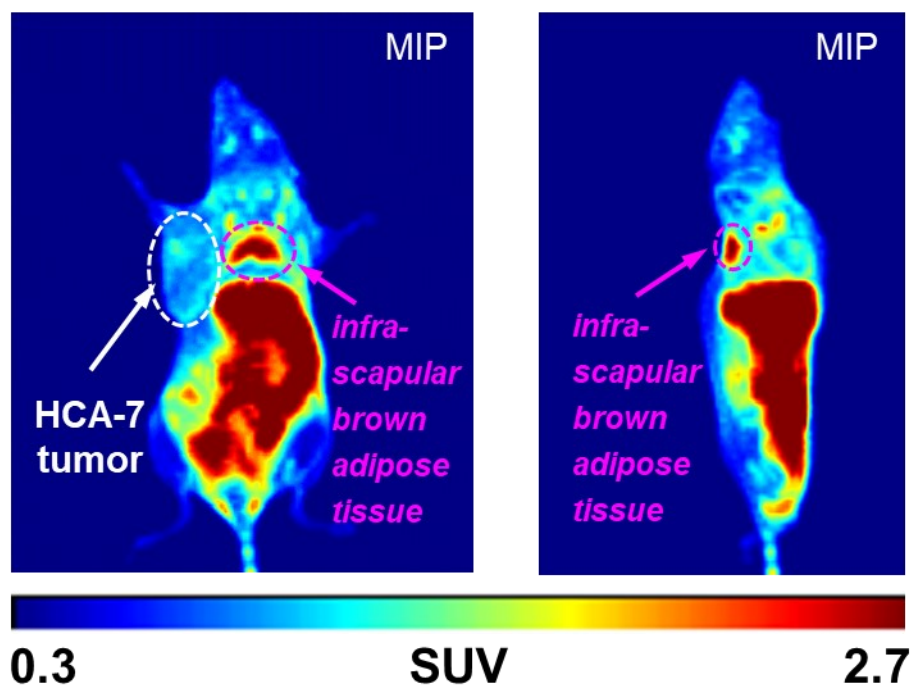
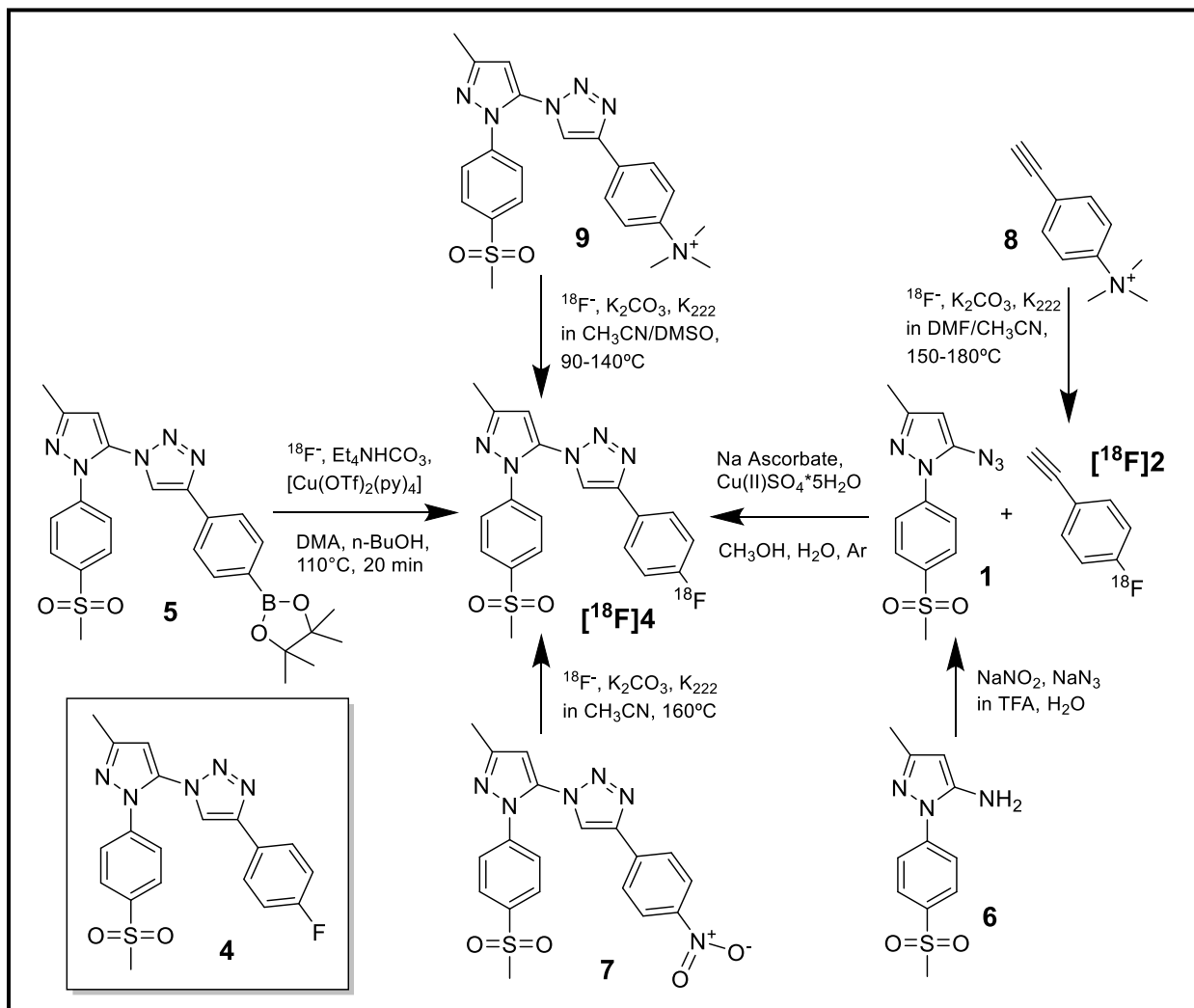


Figure 8. PET image (MIP) of an HCA-7 tumor-bearing NIH-III mouse 60 min after injection of [^{18}F]triacoxib including left) coronal and right) sagittal views. Infrascapular brown adipose tissue delineated in purple.

The static PET-derived biodistribution data displayed in table 1 states that [^{18}F]triacoxib radiotracer uptake into brown adipose tissue, or BAT, occurs but makes no mention of its uptake into white adipose tissue, or WAT. Our interpretation of BAT uptake was driven by the observation of uptake into classical BAT infrascapular fat deposits and a lack of salient visible uptake into classical WAT deposits, such as inguinal WAT (or iWAT) or suprascapular WAT.⁵⁹ At this time, the exact reason for the selectivity of [^{18}F]triacoxib for BAT over WAT is not entirely clear. It may have to do with the general level of lipophilicity in the white adipose cells. WAT stores fat as triacylglycerols in a single, large droplet within the cell, whereas BAT stores lipids in small

droplets throughout the cell where they can be quickly consumed by mitochondria.⁶⁰ The general presence of more triacylglycerides, which have lipophilicity values in the range of 10-25, in WAT may cause those tissues to be more lipophilic in nature than BAT, and too lipophilic to allow association with [¹⁸F]triacoxib.⁶¹ Additionally, it was found that brown adipocytes and muscle cells have a common origin, both come from the dermomyotome, whereas white adipocytes have a distinct origin, suggesting there may be some similarities between BAT and muscle tissue which may affect uptake.⁶⁰ Importantly, we also saw radiotracer uptake that was not reduced by inhibition in muscle tissue. Lastly, BAT is more heavily vascularized, since the heat it produces must be effectively distributed to the rest of the body, than is WAT.⁶² It may be the case that vascularization differences make [¹⁸F]triacoxib more able to perfuse through BAT than through WAT, leading to more opportunity for uptake.

2.6.2. Chemical synthesis



Scheme 3. The various attempted routes to producing [^{18}F]triacoxib.

Synthesis of the aminopyrazole 6. 2-(4-methane-sulfonyl-phenyl)-5-methyl-2H-pyrazol-3-ylamine **6** was prepared using a modification to the literature which included a scaling down.⁶³ 1-[4-(methylsulfonyl)phenyl]hydrazine hydrochloride (6.76 mmol) and 3-Aminocrotonitrile (6.76 mmol) were refluxed in 20 mL of ethanol at 100°C for 8 hours, washed with NaHCO₃, and purified by flash chromatography (Hex 30%: EtOAc 70%). (251.3 g/mol, average yield = 82%) as a yellow solid. ¹H NMR (DMSO, 600 MHz): δ 2.08 (s, 3H, CH₃), 3.23 (s, 3H, SO₂CH₃), 5.38 (s, 1H, CH of pyrazole ring), 5.53 (s, 2H, NH₂), 7.89 (d, J = 9.0 Hz, 2H, Ar-H), 7.96 (d, J = 9.0 Hz, 2H, Ar-H).

Synthesis of the azide 1. 5-azido-1-[4-(methanesulfonyl)phenyl]-3-methyl-1H-pyrazole **1** was prepared using a modification to Bhardwaj et al., 2017.⁴⁰ 2-(4-methane-sulfonyl-phenyl)-5-methyl-2H-pyrazol-3-ylamine **6** (2 mmol) was dissolved in TFA (5 mL) at 0 °C. NaNO₂ (10 mmol) in H₂O (1 mL) was added dropwise and the mixture was allowed to stir for 15 minutes. NaN₃ (21 mmol) in H₂O (5 mL) was added dropwise and the reaction was allowed to reach RT over 2 hours. Reaction was diluted with 50 mL of saturated NaHCO₃, extracted with 40 mL EtOAc, and purified by flash chromatography (Hex 50%: EtOAc 50%). (277.3 g/mol, average yield = 92%) as an orange solid. ¹H NMR (CDCl₃, 600 MHz): δ 2.31 (s, 3H, CH₃), 3.07 (s, 3H, SO₂CH₃), 6.08 (s, 1H, CH of pyrazole ring), 7.93 (d, J = 9.0 Hz, 2H, Ar-H), 7.99 (d, J = 9.0 Hz, 2H, Ar-H); ¹³C NMR (CDCl₃, 150 MHz): δ 14.31 (CH₃), 44.79 (SO₂CH₃), 97.36 (CH of pyrazole ring), 122.43, 128.60, 137.96, 139.02, 142.74, 151.16.

Synthesis of the *para*-nitrophenyl compound 7. 5-azido-1-[4-(methanesulfonyl)phenyl]-3-methyl-1H-pyrazole **1** (0.3 mmol) was dissolved in 2 mL of acetonitrile and added to 1.6 mL of 1:1 EtOH:H₂O in a 25 mL round bottom flask with a stir bar. 1-ethynyl-4-nitrobenzene (0.3 mmol) was added to 8.4 mL of 1:1 EtOH:H₂O in a 25 mL round bottom flask with a stir bar. Both solutions

were stirred 15 minutes before being combined and stirred for an additional 12 hours at 60 °C. The reaction was extracted with ethyl acetate and purified by column chromatography (EtOAc 2:3 Hexane) to yield 1-[1-(4-methanesulfonyl)-3-methyl-1H-pyrazol-5-yl]-4-(4-nitrophenyl)-1H-1,2,3-triazole **7**. (424.1 g/mol, average yield = 31%) as a yellow solid. ¹H NMR (CDCl₃, 600 MHz): δ 2.46 (s, 3H, CH₃), 3.04 (s, 3H, SO₂CH₃), 6.60 (s, 1H, CH of pyrazole ring), 7.40 (d, J = 9.0 Hz, 2H, Ar-H), 7.91 (d, J = 9.0 Hz, 2H, Ar-H), 8.03 (d, J = 9.0 Hz, 2H, Ar-H), 8.04 (s, 1H, CH of triazole ring), 8.33 (d, J = 8.7 Hz, 2H, Ar-H).

Synthesis of the *para*-trimethylanilinium compound **9.** The same procedure used to produce the boropinacol ester radiochemical precursor was used to produce the *para*-trimethylanilinium radiochemical precursor. 5-azido-1-[4-(methanesulfonyl)phenyl]-3-methyl-1H-pyrazole **1** (0.36 mmol) and 4-ethynyl-*N,N,N*-trimethylanilinium triflate **8** (0.29 mmol) are added to Methanol (1 mL) in a reaction vial and stirred 5 min at room temperature. 160 μL of a 1 molar solution of Na Ascorbate (10 mol%) and 0.824 mL of de-ionized water were added to the reaction mixture. Mixture was bubbled through with argon for 15 min followed by the addition of 16 μL of a 1 molar solution of Cu(II)SO₄*5H₂O (1 mol%) and the cap was closed tight. The reaction was stirred at room temperature for 24 hours, extracted with ethyl acetate and purified by column chromatography (EtOAc 2:3 Hexane) to yield 4-{1-[1-(4-methanesulfonyl)phenyl]-3-methyl-1H-pyrazol-5-yl]-1H-1,2,3-triazol-4-yl}-*N,N,N*-trimethylanilinium triflate **9**. (586.61 g/mol, average yield = 12%) as a yellow solid. ¹H NMR (CDCl₃, 600 MHz): δ 2.44 (s, 3H, CH₃), 3.12 (s, 3H, SO₂CH₃), 3.71 (s, 9H, N[CH₃]₃), 6.80 (s, 1H, CH of pyrazole ring), 7.45 (d, J = 9.0 Hz, 2H, Ar-H), 7.96 (d, J = 8.7 Hz, 2H, Ar-H), 8.02 (d, J = 9 Hz, 2H, Ar-H), 8.16 (d, J = 9 Hz, 2H, Ar-H), 8.84 (s, 1H, CH of triazole ring). ¹³C NMR (CDCl₃, 150 MHz): δ 13.88 (CH₃), 44.16 (SO₂CH₃), 57.71,

107.01 (CH of pyrazole ring), 122.04 (CH of triazole ring), 125.03, 126.07, 128.62, 129.89, 133.27, 136.39, 141.39, 143.24, 147.13, 148.29, 152.33.

Synthesis of reference compound 4. The same procedure used to produce the boropinacol ester radiochemical precursor was used to produce non-radioactive triacoxib. 5-azido-1-[4-(methanesulfonyl)phenyl]-3-methyl-1H-pyrazole **1** (0.36 mmol) and 1-ethynyl-4-fluorobenzene **2** (0.36 mmol) are added to Methanol (1 mL) in a reaction vial and stirred 5 min at room temperature. 160 μ L of a 1 molar solution of Na Ascorbate (10 mol%) and 0.824 mL of de-ionized water were added to the reaction mixture. Mixture was bubbled through with argon for 15 min followed by the addition of 16 μ L of a 1 molar solution of Cu(II)SO₄*5H₂O (1 mol%) and the cap was closed tight. The reaction was stirred at room temperature for 24 hours, extracted with ethyl acetate and purified by column chromatography (EtOAc 2:3 Hexane) to yield 4-(4-fluorophenyl)-1-{1-[4-(methanesulfonyl)phenyl]-3-methyl-1H-pyrazol-5-yl}-1H-1,2,3-triazole **4**. (397.1 g/mol, average yield = 28%) as an off-white solid. ¹H NMR (CDCl₃, 600 MHz): δ 2.45 (s, 3H, CH₃), 3.04 (s, 3H, SO₂CH₃), 6.58 (s, 1H, CH of pyrazole ring), 7.16 (d, J = 9.0 Hz, 2H, Ar-H), 7.39 (d, J = 4.3 Hz, 2H, Ar-H), 7.83 (d, J = 8.3 Hz, 2H, Ar-H), 7.85 (s, 1H, CH of triazole ring), 7.90 (d, J = 4.4 Hz, 2H, Ar-H); ¹³C NMR (CDCl₃, 150 MHz): δ 14.19 (CH₃), 44.62 (SO₂CH₃), 106.51 (CH of pyrazole ring), 116.29 (d, J_{CCF} = 21.0 Hz), 121.67 (CH of triazole ring), 123.34, 125.46, 127.93 (d, J_{CCCF} = 7.74 Hz), 128.97, 134.81, 139.51, 142.06, 147.76, 150.98, 163.26 (d, J_{CF} = 249 Hz); ¹⁹F NMR (CDCl₃, 564.8 MHz): δ -111.89 (m); Identified by HR-MS analysis, calculated for C₁₉H₁₆FN₅NaO₂S [M + Na]⁺ m/z 420.0901, found 420.0899.

2.6.3. Radiochemical synthesis – alternative routes

In an effort to prepare [^{18}F]triacoxib ($[^{18}\text{F}]\mathbf{4}$), various radiochemical precursors were used with the notion that click chemistry may be performed before or after radiolabeling. These precursors included 4-ethynyl-N,N,N-trimethylanilinium triflate **8**, 1-[1-(4-methanesulfonyl)-3-methyl-1H-pyrazol-5-yl]-4-(4-nitrophenyl)-1H-1,2,3-triazole **7**, and 4-{1-[1-(4-methanesulfonylphenyl)-3-methyl-1H-pyrazol-5-yl]-1H-1,2,3-triazol-4-yl}-N,N,N-trimethylanilinium triflate **9**.

The radio-fluorination of **4-ethynyl-N,N,N-trimethylanilinium triflate 8** to produce 1-ethynyl-4- $[^{18}\text{F}]$ fluorobenzene $[^{18}\text{F}]\mathbf{2}$ was performed in varying conditions throughout 4 attempts in order to ascertain the viability of the precursor for radiolabeling. As the product would need to be sufficiently present that it may be used in a subsequent CuAAC reaction, the radiolabeling would need to be maximally efficient. Conditions for each of the 4 trials can be found in supplemental Table 2, below, but in summary, reaction mass was varied from 5 to 10 mg of precursor in ~0.5 mL DMF or acetonitrile, reacted at either 150 °C or 180 °C for 5 to 60 minutes.

Table 2. Reaction conditions for the four radiofluorination attempts using the trimethyl anilinium alkyne radiolabelling precursor **8**.

Reaction Conditions				
Entry	Mass of precursor (mg)	Solvent used	Temperature (°C)	Time (min)
1	5	DMF	150	5, 15, 30, 60
2	10	DMF	150	5, 15, 30, 60
3	5	Acetonitrile	150	5, 15, 30, 60
4	7	DMF	180	10, 15, 20, 30

Table 3, below, shows the [¹⁸F]fluoride incorporation results of the 4 trials as measured by radio-TLC analysis. Our results suggest that the most favorable reaction conditions were DMF, 150 °C, 5-10 mg of precursor, and a reaction time of 15-30 minutes, with which the reaction reached incorporation values of ~15%, a yield far too little to be of use in subsequent CuAAC reactions.

Table 3. [¹⁸F]fluoride incorporation for the four radiofluorination attempts using the trimethyl anilinium alkyne labelling precursor **8**.

	Entry			
	1	2	3	4
Reaction time (min)	% Radiochemical yield by radio-TLC			
5	2.2	4.3	2.05	
10				0.88
15	14.7	12.6	8.72	10.44
20				1.58
30	6.2	15.6	13.56	2.06
60	11.9	13.26	9.84	

The radio-fluorination of 1-[1-(4-methanesulfonyl)-3-methyl-1H-pyrazol-5-yl]-4-(4-nitrophenyl)-1H-1,2,3-triazole 7 to produce [¹⁸F]4 was performed twice, using 5 mg and 10 mg, respectively. Precursor was dissolved in ~0.5 mL DMSO containing dried [¹⁸F]fluoride and heated to 160 °C for between 0 and 45 minutes. Supplementary Table 4, below, shows the [¹⁸F]fluoride incorporation results of both trials as measured by radio-TLC analysis. Our results suggest that neither set of conditions using this precursor were particularly effective.

Table 4. [¹⁸F]fluoride incorporation for both radiofluorination attempts using the nitrated triacoxib radiolabelling precursor 7.

	Entry	
	1	2
Reaction time (min)	% Radiochemical yield by Radio-TLC	
0	0	0
10	2.2	1.5
20	4.8	2.6
30	6.1	2.5
40		2.4
45	7.26	

The radiofluorination of 4-{1-[1-(4-methanesulfonylphenyl)-3-methyl-1H-pyrazol-5-yl]-1H-1,2,3-triazol-4-yl}-N,N,N-trimethylanilinium triflate **9** to produce [¹⁸F]**4** was performed in varying conditions throughout 6 attempts. Conditions for each of the 6 trials can be found in supplementary Table 5, below, but in summary, reaction mass was varied from 4.5 to 6.1 mg of precursor, in ~0.5 mL acetonitrile or DMSO, reacted at temperatures between 90 °C and 140 °C for 10 to 40 minutes.

Table 5. Reaction conditions for the six radiofluorination attempts using the trimethyl anilinium triacoxib radiolabelling precursor **9**.

Reaction Conditions				
Entry	Mass of precursor (mg)	Solvent	Temperature (°C)	Time (min)
1	5.4	Acetonitrile	120	10, 20, 30, 40
2	4.7	Acetonitrile	120	15
3	5.4	Acetonitrile	140	20
4	4.5	DMSO	140	20
5	6.1	Acetonitrile	90	20
6	4.6	Acetonitrile	90	20

Table 6 shows the [¹⁸F]fluoride incorporation results of the 6 trials as measured by radio-TLC analysis. Our results suggest that none of the various reaction conditions were successful in producing appreciable amounts of [¹⁸F]4.

Table 6. [¹⁸F]fluoride incorporation for the six radiofluorination attempts using the trimethyl anilinium triacoxib radiolabelling precursor **9**.

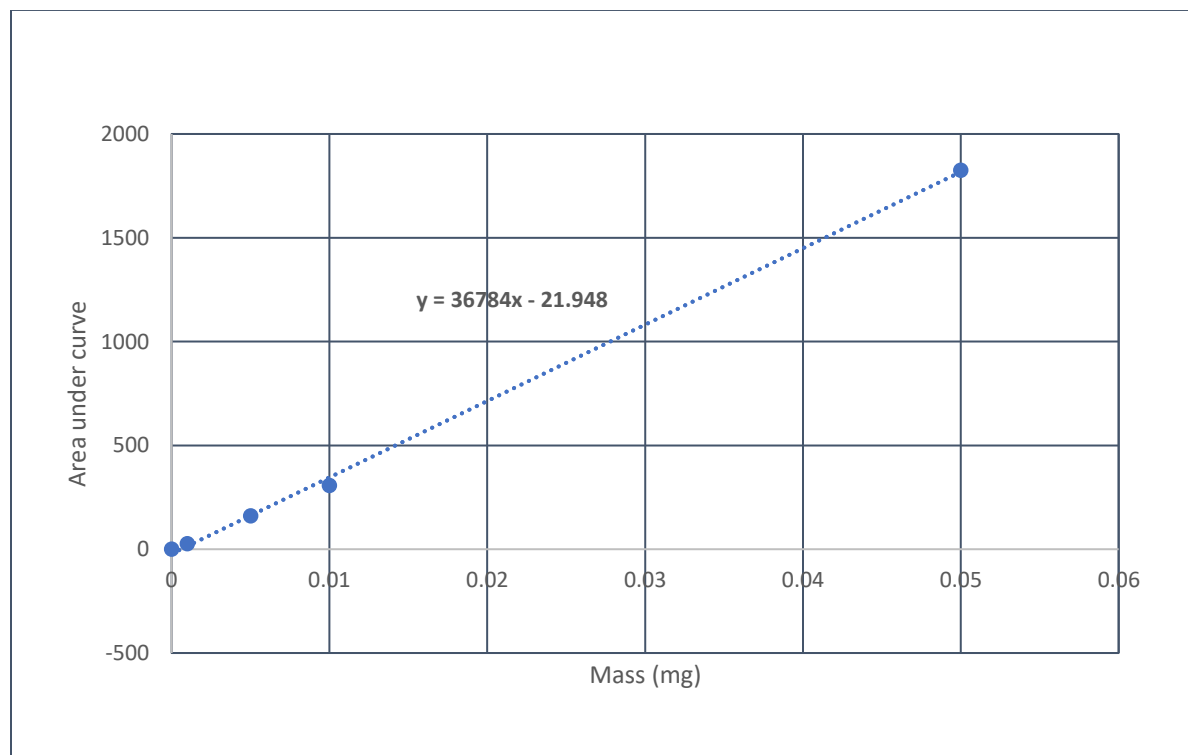
	Entry					
	1	2	3	4	5	6
Reaction time (min)	% Radiochemical yield by Radio-TLC					
10	0					
15		0				
20	1.2		0	0	0	0
30	0					
40	0.5					

2.6.4. Molar activity calculations

Molar activity was assessed through the establishment of an HPLC standard curve using varying masses of non-radioactive triacoxib. For each HPLC run using varying masses of [¹⁹F]triacoxib, corresponding areas under the UV elution peak were recorded. Plotting these data on a graph produced a line equation unique to triacoxib. During [¹⁸F]triacoxib HPLC purifications where radioactive mass could not be directly measured, the value of the area under the UV elution peak

corresponding to $[^{18}\text{F}]$ triacoxib was recorded and inserted as the y-component into the $[^{19}\text{F}]$ triacoxib line equation. The resultant x-value gave the mass of $[^{18}\text{F}]$ triacoxib present in the elution peak. Thus, dividing the eluted activity by the moles of $[^{18}\text{F}]$ triacoxib present in the peak gave the molar activity of $[^{18}\text{F}]$ triacoxib. Supplementary graph 1, below, shows the plotted values of the area under the UV peaks versus the mass of non-radioactive triacoxib injected in the HPLC. Thus, with the line equation $y = 36784x - 21.948$ and a UV peak integration value of 0.3002 for a peak where 0.1412 GBq were collected, the molar activity of $[^{18}\text{F}]$ triacoxib in our runs reached 92.5 GBq/ μmol .

Graph 1. Area under the UV peak versus mass injected to establish an HPLC standard curve.



2.6.5. Dynamic PET-derived biodistribution data

Table 7. Biodistribution (dynamic PET-derived data) for [¹⁸F]triacoxib (n=4; except kidneys 8/4)

organ	SUV (5 min p.i.)	SUV (60 min p.i.)	%ID/g (5 min p.i.)	%ID/g (60 min p.i.)
heart (=blood pool)	2.26 ± 0.57	1.27 ± 0.26	10.64 ± 2.39	8.27 ± 1.50
lung	3.61 ± 0.35	2.02 ± 0.20	17.35 ± 1.89	13.47 ± 1.76
liver	4.61 ± 0.26	3.28 ± 0.22	22.20 ± 1.53	21.77 ± 1.43
brain	0.53 ± 0.03	0.32 ± 0.01	2.57 ± 0.19	2.10 ± 0.10
brown adipose tissue (BAT)	0.57 ± 0.04	1.45 ± 0.06	2.75 ± 0.20	9.64 ± 0.56
kidneys	2.32 ± 0.08	1.35 ± 0.04	15.30 ± 0.50	8.88 ± 0.17
bone	0.26 ± 0.03	0.62 ± 0.03	1.24 ± 0.20	4.13 ± 0.32
tumor	0.29 ± 0.03	0.76 ± 0.02	1.41 ± 0.13	5.02 ± 0.25
muscle	0.31 ± 0.02	0.51 ± 0.02	1.48 ± 0.11	3.37 ± 0.17
tumor / muscle	0.94 ± 0.02	1.49 ± 0.02	0.95 ± 0.12	1.49 ± 0.21

2.6.6. NMR spectra

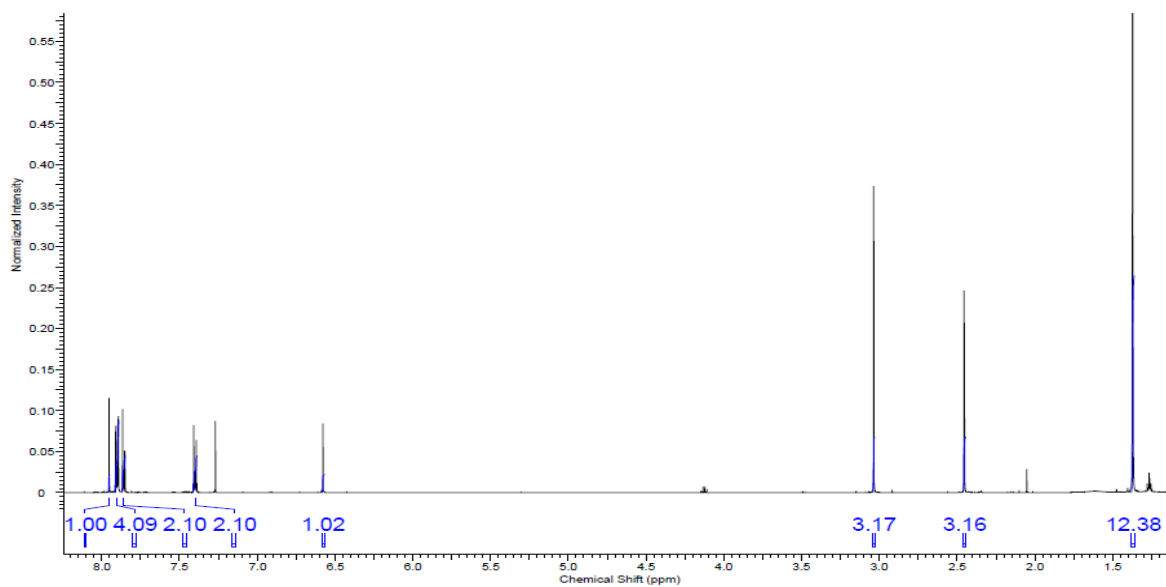


Figure 9. ¹H NMR spectrum of the boropinacol ester-triacoxib radiolabelling precursor **5**.

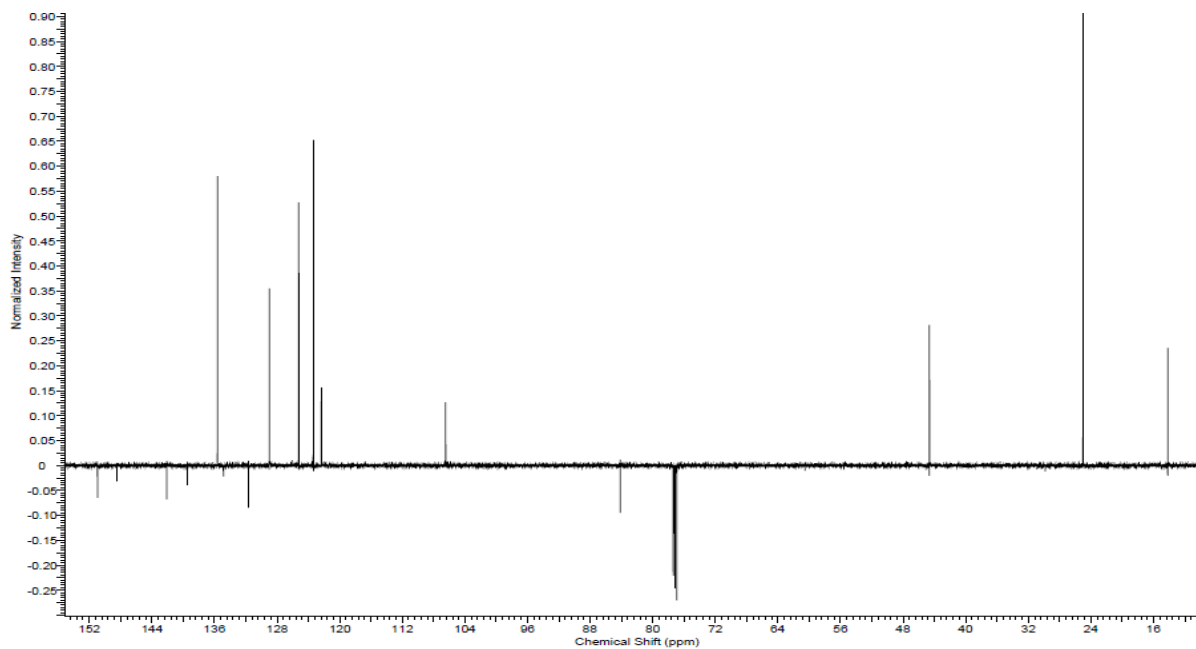


Figure 10. ¹³C NMR spectrum of the Boropinacol ester-triacoxib radiolabelling precursor **5**.

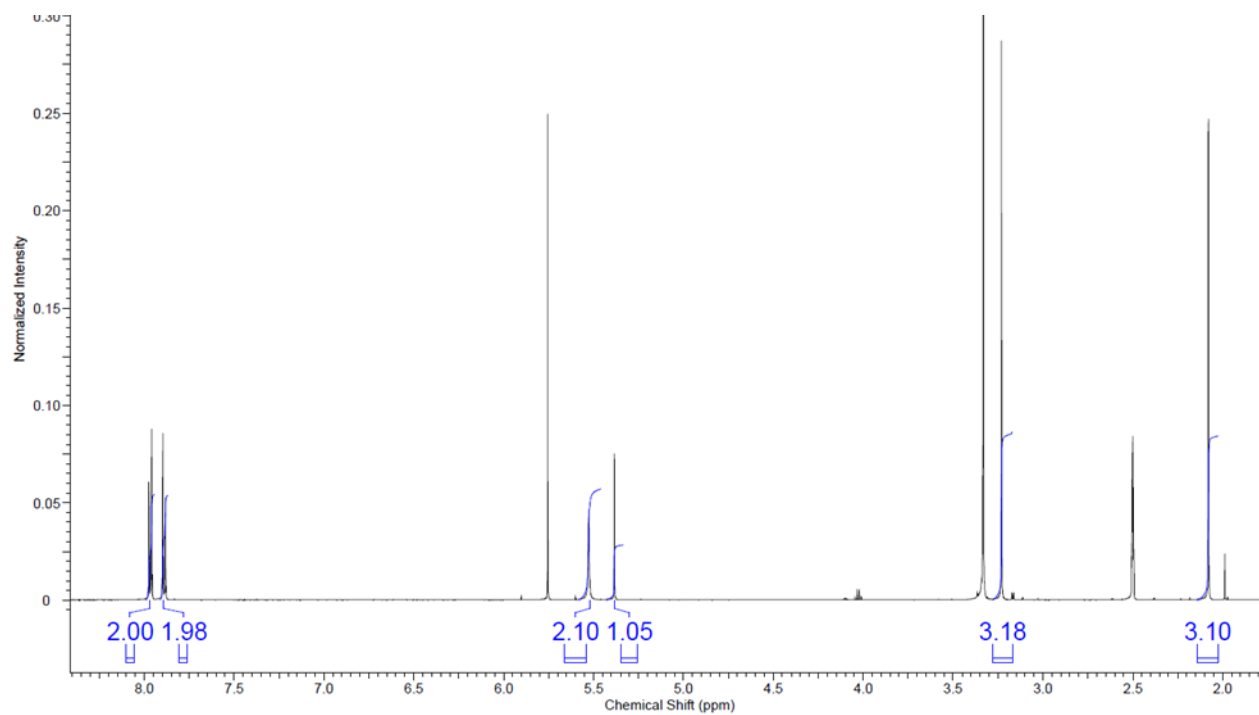


Figure 11. ^1H NMR spectrum of the aminopyrazole (precursor to azide) **6**.

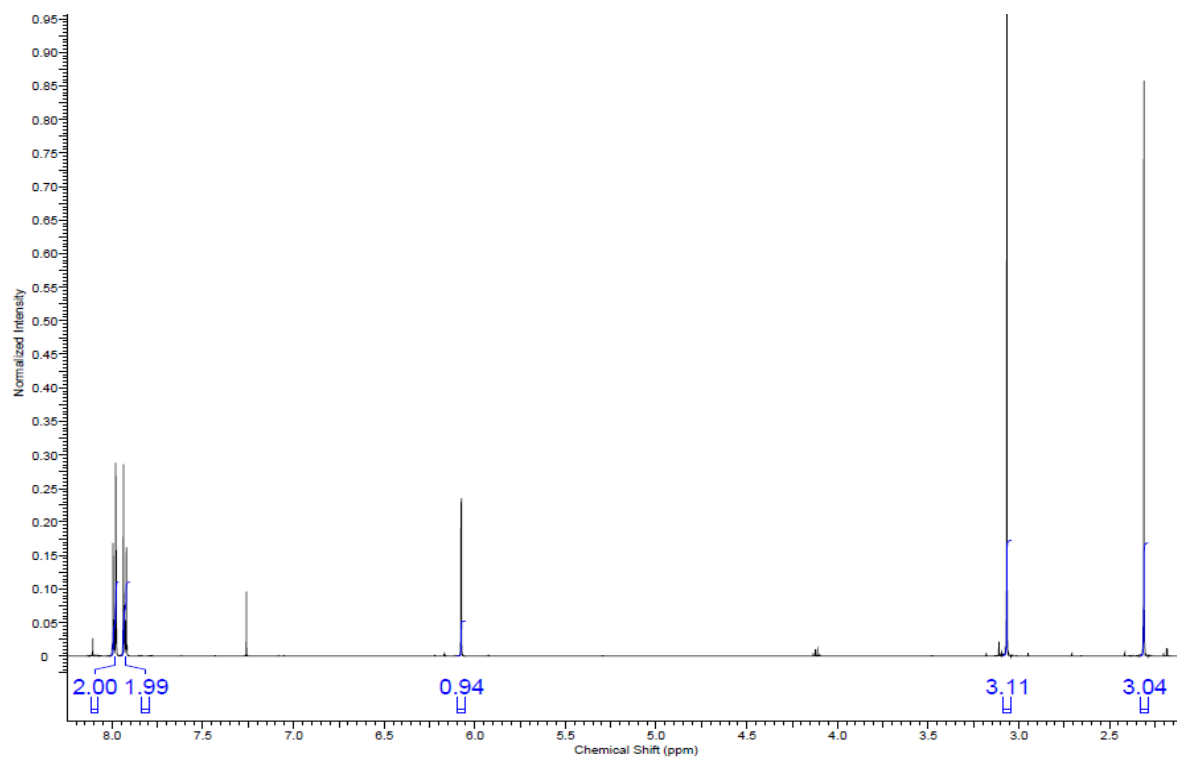


Figure 12. ^1H NMR spectrum of the azide (CuAAC reagent) **1**.

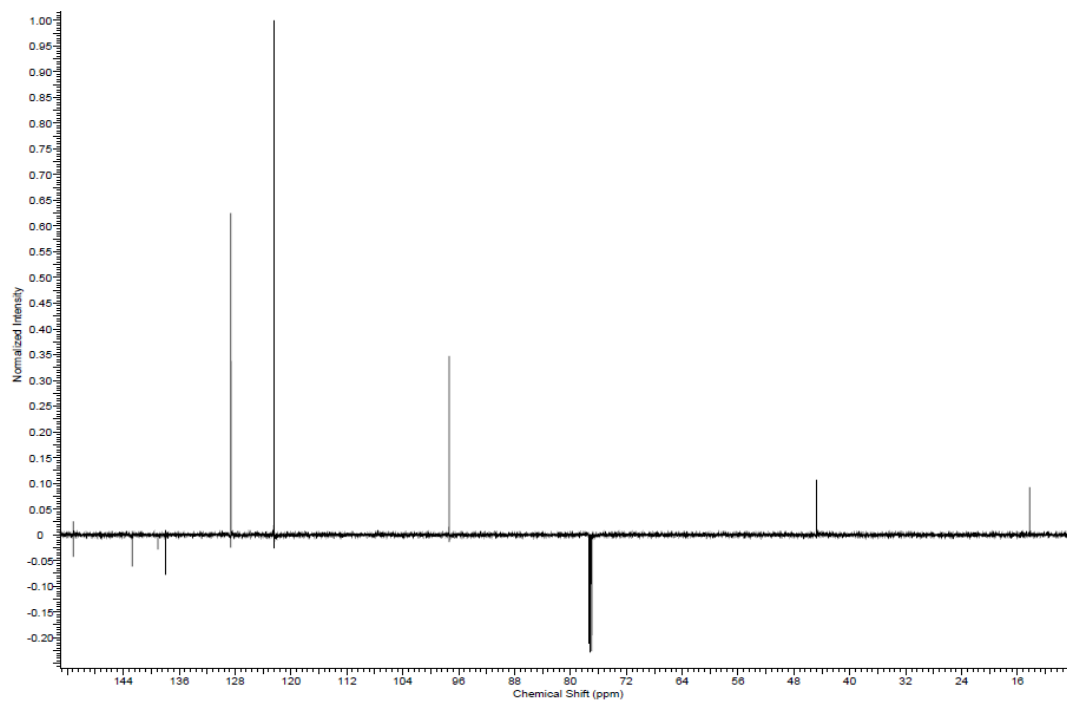


Figure 13. ^{13}C NMR spectrum of the azide (CuAAC reagent) **1**.

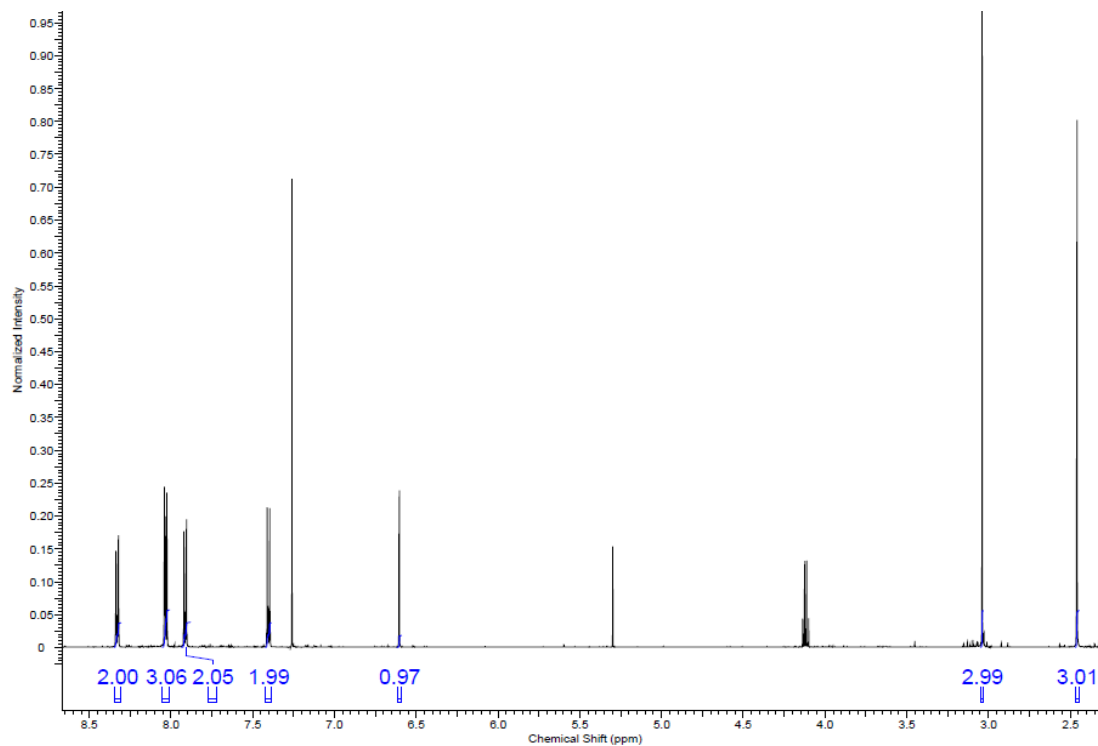


Figure 14. ^1H NMR spectrum of the nitro-triacoxib radiolabelling precursor **7**.

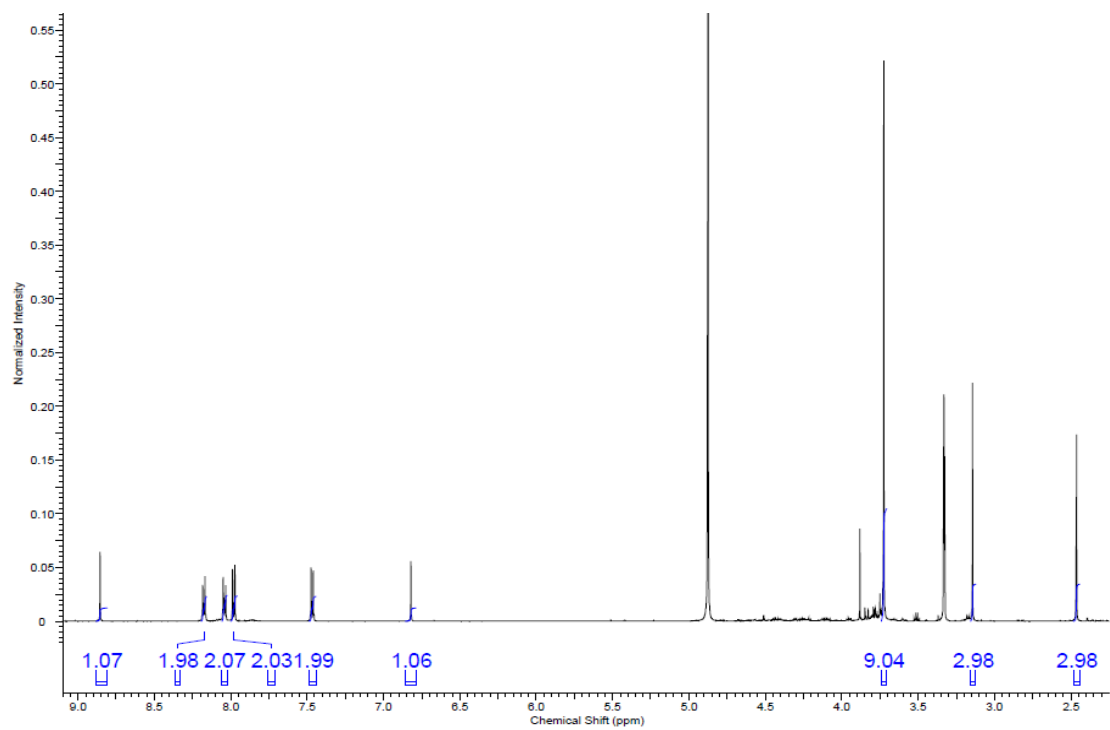


Figure 15. ^1H NMR spectrum of the trimethyl anilinium triacoxib radiolabelling precursor **9**.

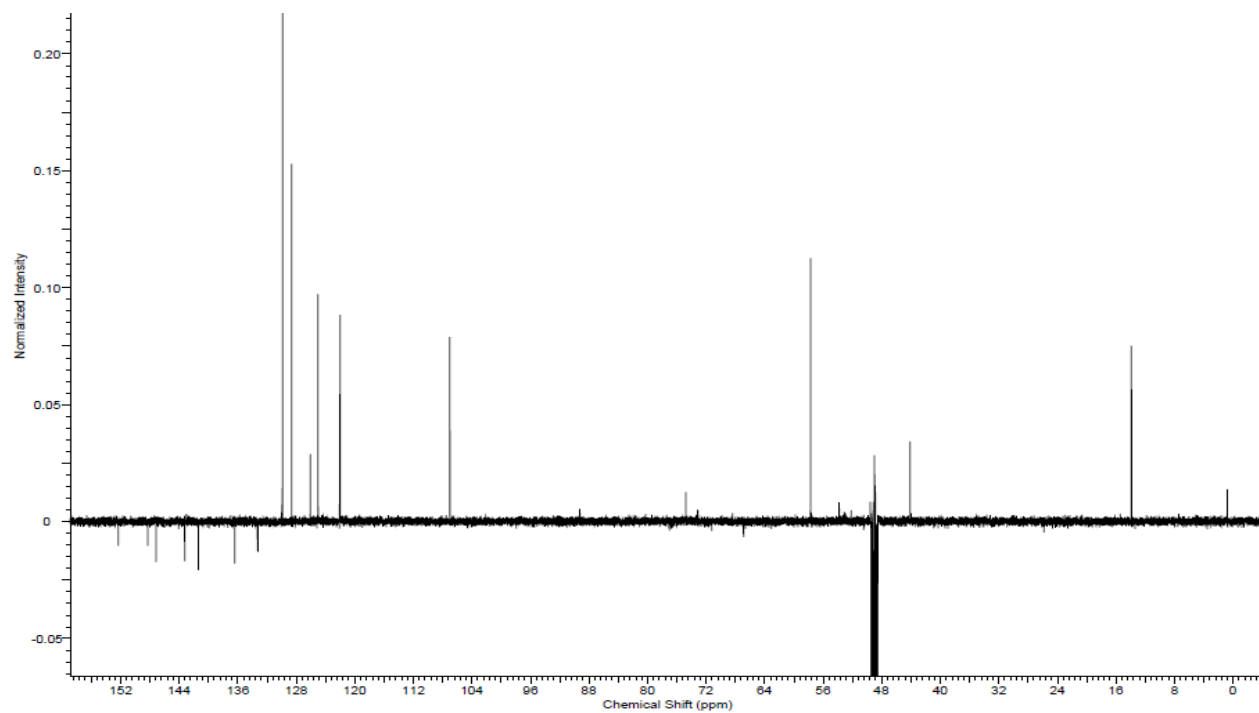


Figure 16. ^{13}C NMR spectrum of the trimethyl anilinium triacoxib radiolabelling precursor **9**.

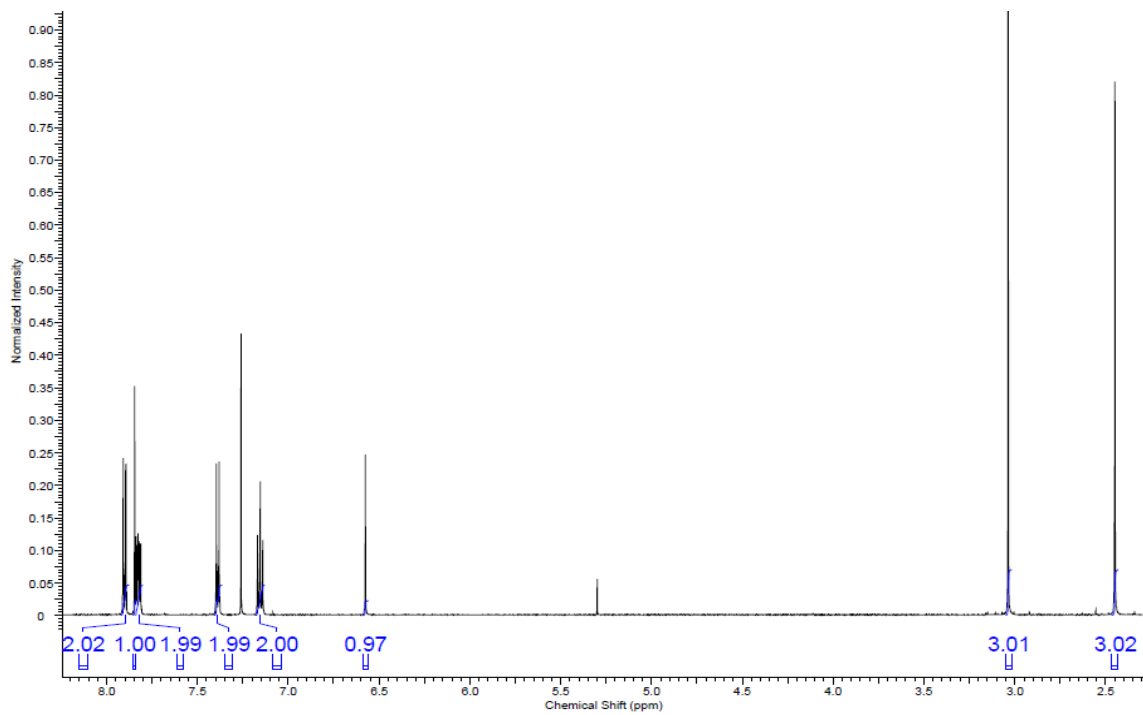


Figure 17. ^1H NMR spectrum of the [^{19}F]triacoxib non-radioactive standard **4**.

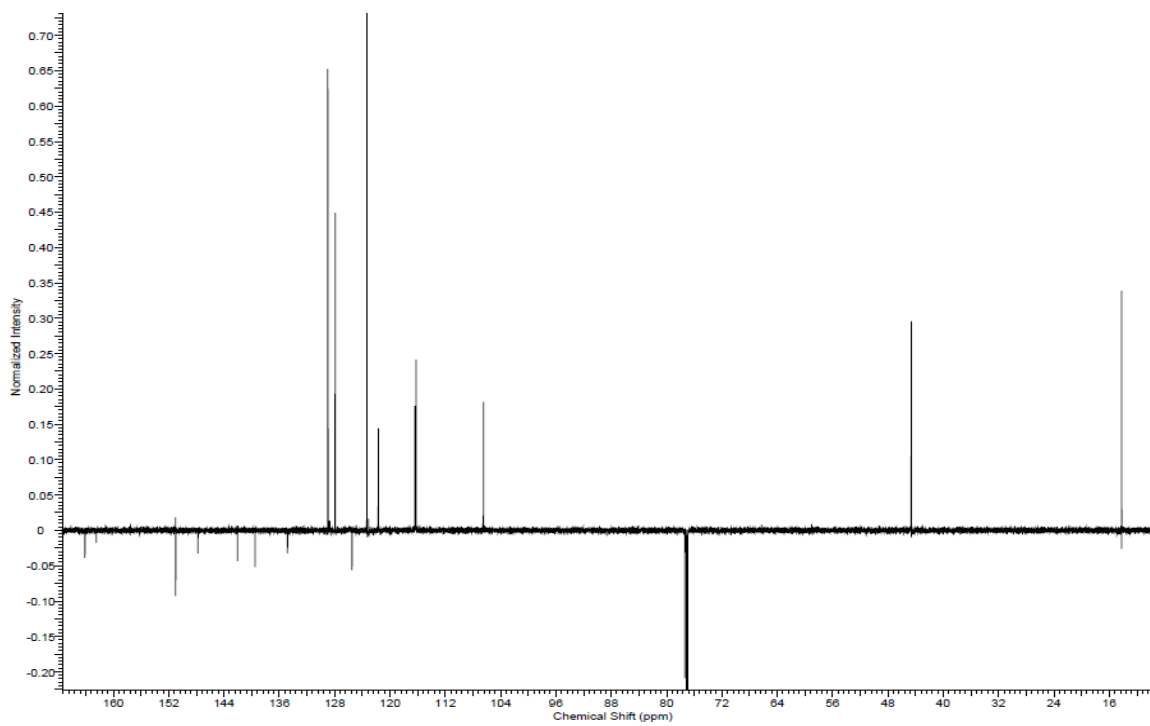


Figure 18. ^{13}C NMR spectrum of the [^{19}F]triacoxib non-radioactive standard **4**.

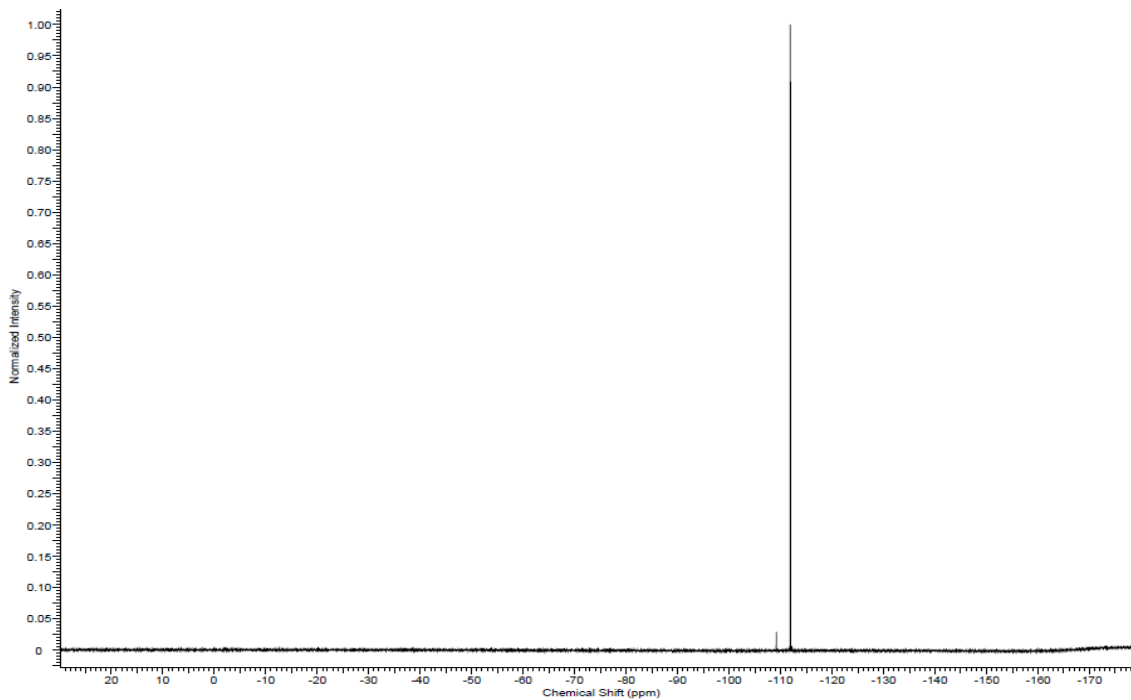


Figure 19. ^{19}F NMR spectrum of the ^{19}F triacoxib non-radioactive standard **4**.

2.6.7. HPLC traces

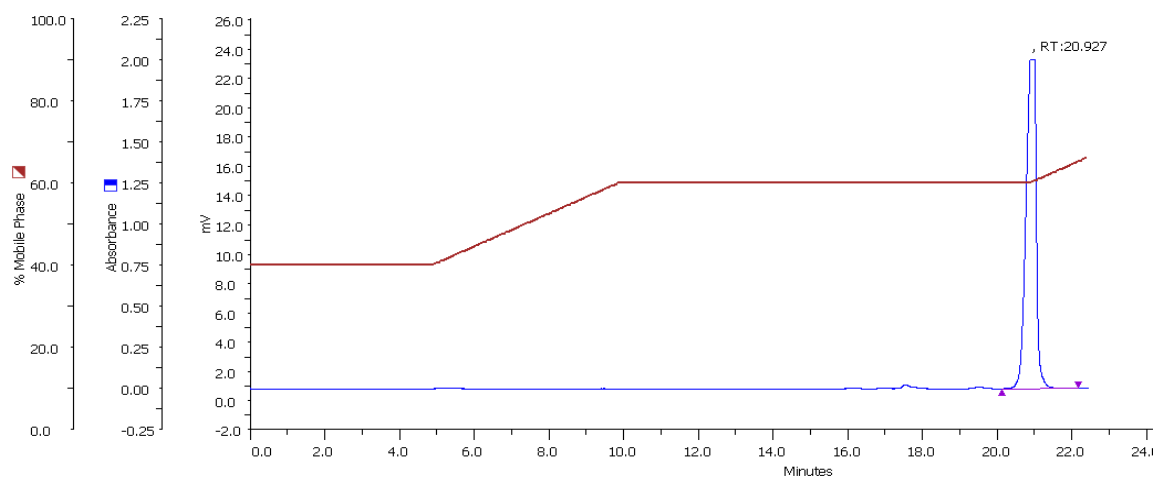


Figure 20. HPLC trace of the ^{19}F triacoxib non-radioactive standard **4**, blue represents the UV-detector signal.

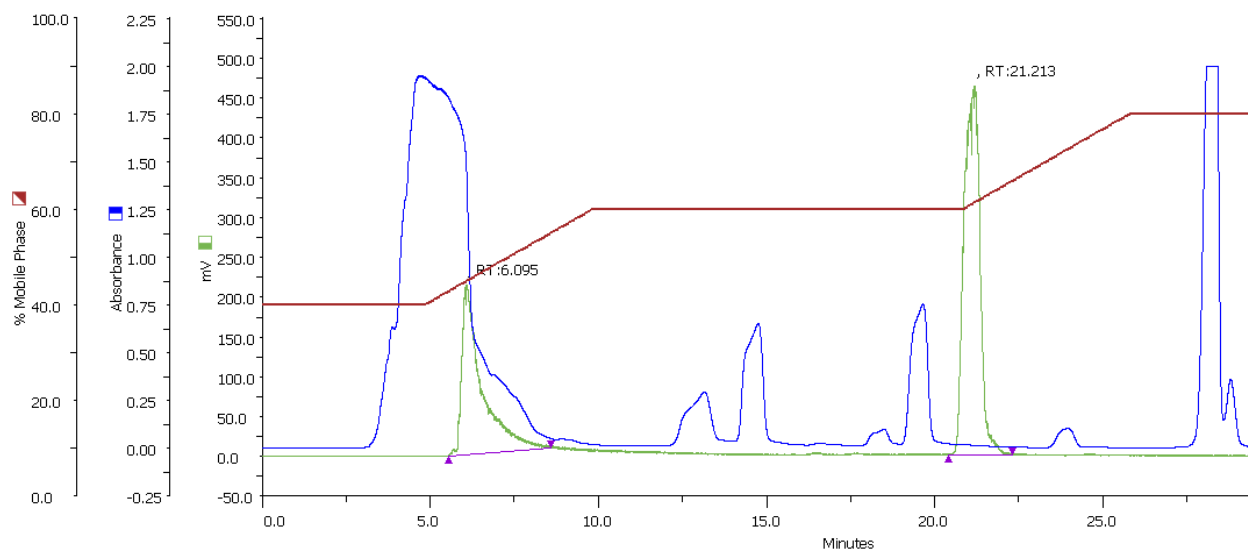


Figure 21. HPLC trace of the [^{18}F]triacoxib crude reaction mixture ($[^{18}\text{F}]\mathbf{4}$), blue represents the UV-detecter signal and green the radio-detecter signal.

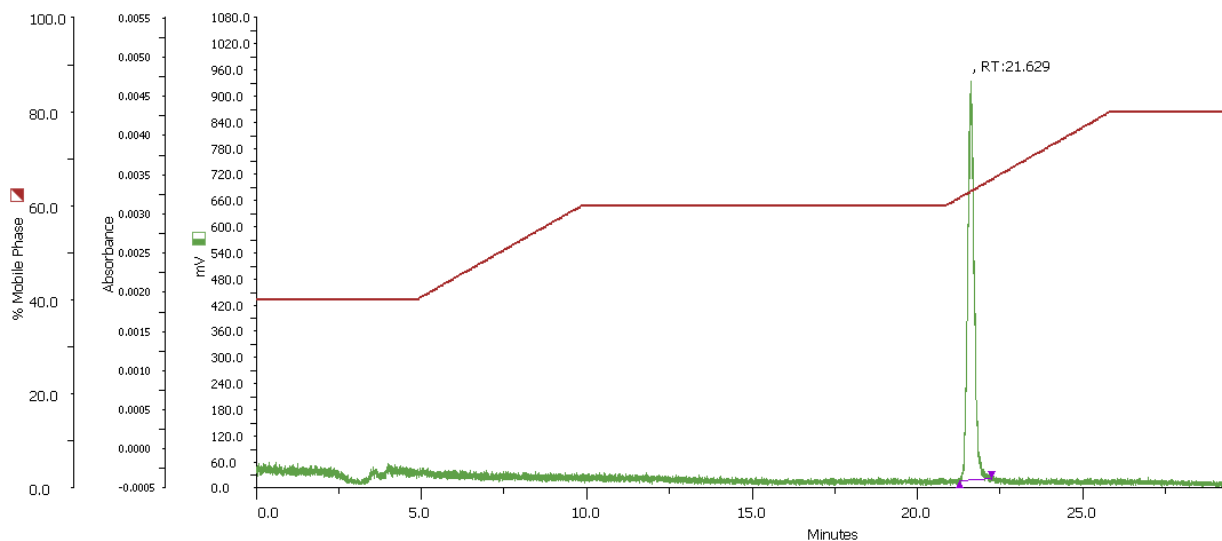


Figure 22. HPLC trace of the purified [^{18}F]triacoxib radiotracer ($[^{18}\text{F}]\mathbf{4}$), green the radio-detecter signal.

2.6.8. Radio-TLC traces

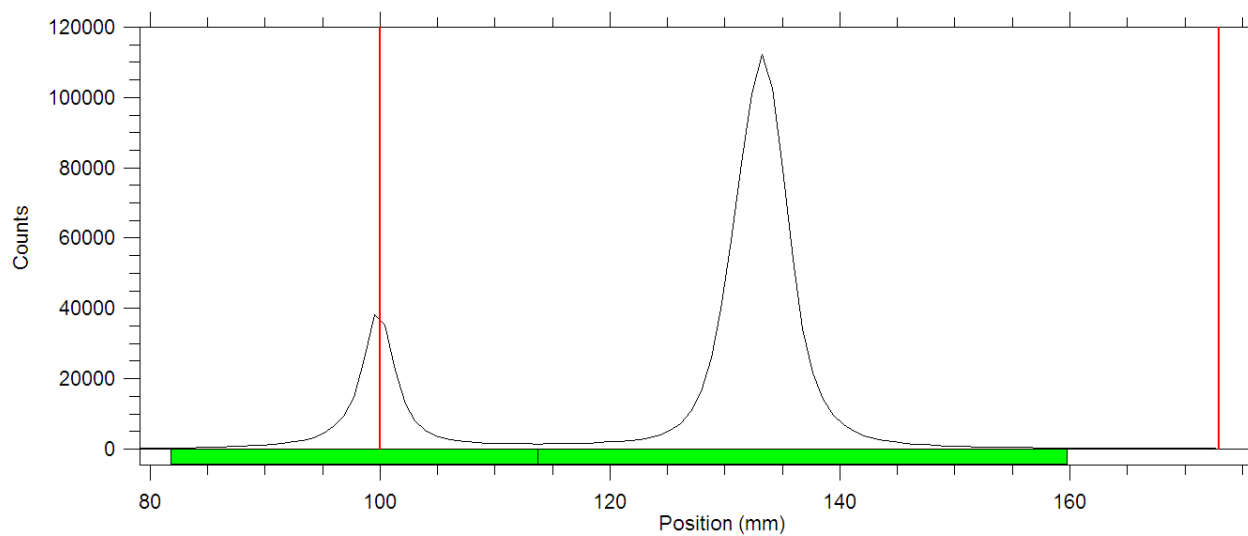


Figure 23. Radio-TLC trace of the [^{18}F]triacoxib crude reaction mixture ([^{18}F]4).

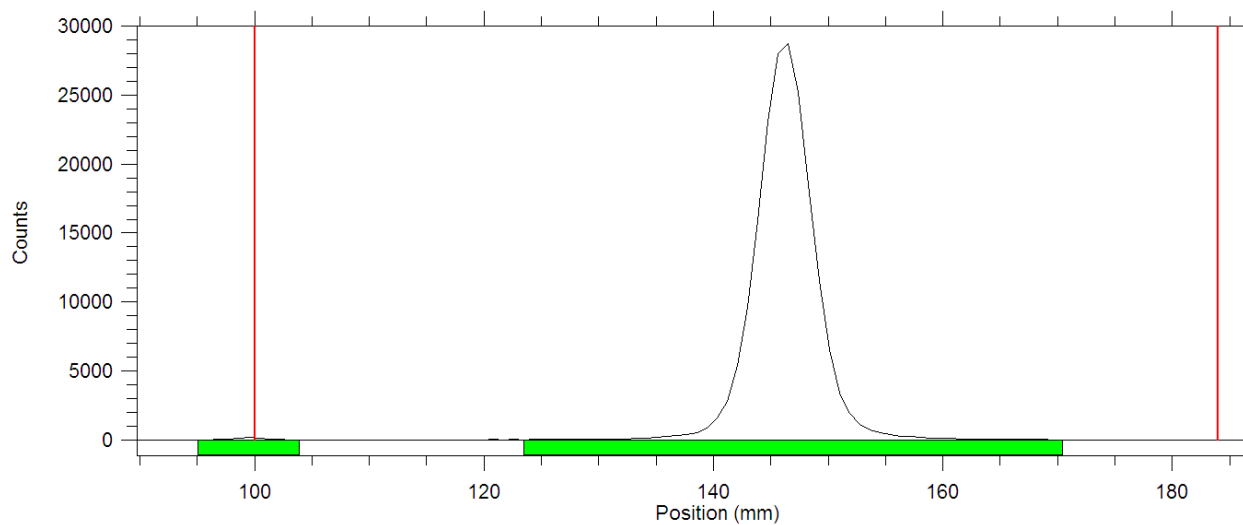


Figure 24. Radio-TLC trace of the purified [^{18}F]triacoxib radiotracer ([^{18}F]4).

2.7. REFERENCES

- (1) Liu, Y.; Sun, H.; Hu, M.; Zhang, Y.; Chen, S.; Tighe, S.; Zhu, Y. The Role of Cyclooxygenase-2 in Colorectal Carcinogenesis. *Clin. Colorectal Cancer* **2017**, *16* (3), 165–172. <https://doi.org/10.1016/j.clcc.2016.09.012>.
- (2) Garg, R.; Blando, J. M.; Perez, C. J.; Lal, P.; Feldman, M. D.; Smyth, E. M.; Ricciotti, E.; Grosser, T.; Benavides, F.; Kazanietz, M. G. COX-2 Mediates pro-Tumorigenic Effects of PKC ϵ in Prostate Cancer. *Oncogene* **2018**, *37* (34), 4735–4749. <https://doi.org/10.1038/s41388-018-0318-9>.
- (3) Bos, P. D.; Zhang, X. H. F.; Nadal, C.; Shu, W.; Gomis, R. R.; Nguyen, D. X.; Minn, A. J.; Van De Vijver, M. J.; Gerald, W. L.; Foekens, J. A.; Massagué, J. Genes That Mediate Breast Cancer Metastasis to the Brain. *Nature* **2009**, *459* (7249), 1005–1009. <https://doi.org/10.1038/nature08021>.
- (4) Ren, R.; Charles, P. C.; Zhang, C.; Wu, Y.; Wang, H.; Patterson, C. Gene Expression Profiles Identify a Role for Cyclooxygenase 2-Dependent Prostanoid Generation in BMP6-Induced Angiogenic Responses. *Blood* **2007**, *109* (7), 2847–2853. <https://doi.org/10.1182/blood-2006-08-039743>.
- (5) Tsujii, M.; Kawano, S.; Tsuji, S.; Sawaoka, H.; Hori, M.; DuBois, R. N. Cyclooxygenase Regulates Angiogenesis Induced by Colon Cancer Cells. *Cell* **1998**, *93* (5), 705–716. [https://doi.org/10.1016/S0092-8674\(00\)81433-6](https://doi.org/10.1016/S0092-8674(00)81433-6).
- (6) Li, W.; Mao, Z.; Fan, X.; Cui, L.; Wang, X. Cyclooxygenase 2 Promoted the Tumorigenicity of Pancreatic Cancer Cells. *Tumor Biol.* **2014**, *35* (3), 2271–2278. <https://doi.org/10.1007/s13277-013-1301-2>.
- (7) Secchiero, P.; Barbarotto, E.; Gonelli, A.; Tiribelli, M.; Zerbinati, C.; Celeghini, C.;

- Agostinelli, C.; Pileri, S. A.; Zauli, G. Potential Pathogenetic Implications of Cyclooxygenase-2 Overexpression in B Chronic Lymphoid Leukemia Cells. *Am. J. Pathol.* **2005**, *167* (6), 1599–1607. <https://doi.org/10.1080/00102202.2010.498676>.
- (8) Bell, E.; Ponthan, F.; Whitworth, C.; Tweddle, D. A.; Lunec, J.; Redfern, C. P. F. COX2 Expression in Neuroblastoma Increases Tumorigenicity but Does Not Affect Cell Death in Response to the COX2 Inhibitor Celecoxib. *Clin. Exp. Metastasis* **2014**, *31* (6), 651–659. <https://doi.org/10.1007/s10585-014-9656-3>.
- (9) Méric, J. B.; Rottey, S.; Olausson, K.; Soria, J. C.; Khayat, D.; Rixe, O.; Spano, J. P. Cyclooxygenase-2 as a Target for Anticancer Drug Development. *Crit. Rev. Oncol. Hematol.* **2006**, *59* (1), 51–64. <https://doi.org/10.1016/j.critrevonc.2006.01.003>.
- (10) Tsujii, M.; DuBois, R. N. Alterations in Cellular Adhesion and Apoptosis in Epithelial Cells Overexpressing Prostaglandin Endoperoxide Synthase 2. *Cell* **1995**, *83* (3), 493–501. [https://doi.org/10.1016/0092-8674\(95\)90127-2](https://doi.org/10.1016/0092-8674(95)90127-2).
- (11) Valesini, G. Selective Cyclooxygenase-2 Inhibition: Biological and Clinical Effects. *Isr. Med. Assoc. J.* **2000**, *2* (11), 841–847.
- (12) Smith, W. L.; DeWitt, D. L.; Garavito, R. M. Cyclooxygenases : Structural, Cellular, and Molecular Biology. *Annu. Rev. Biochem.* **2000**, *69* (1), 145–182. <https://doi.org/10.1146/annurev.biochem.69.1.145>.
- (13) Anderson, R. J.; Berl, T.; McDonald, K. M.; Schrier, R. W. Prostaglandins: Effects on Blood Pressure, Renal Blood Flow, Sodium and Water Excretion. *Kidney Int.* **1976**, *10* (3), 205–215. <https://doi.org/10.1038/ki.1976.99>.
- (14) Adegboyega, P. A.; Ololade, O. Immunohistochemical Expression of Cyclooxygenase-2 in Normal Kidneys. *Appl. Immunohistochem. Mol. Morphol.* **2004**, *12* (1), 71–74.

<https://doi.org/10.1097/00129039-200403000-00013>.

- (15) Willoughby, D. A.; Moore, A. R.; Colville-Nash, P. R. COX-1, COX-2, and COX-3 and the Future Treatment of Chronic Inflammatory Disease. *Lancet* **2000**, *355* (9204), 646–648. [https://doi.org/10.1016/S0140-6736\(99\)12031-2](https://doi.org/10.1016/S0140-6736(99)12031-2).
- (16) Chandrasekharan, N. V.; Dai, H.; Roos, K. L. T.; Evanson, N. K.; Tomsik, J.; Elton, T. S.; Simmons, D. L. COX-3, a Cyclooxygenase-1 Variant Inhibited by Acetaminophen and Other Analgesic/Antipyretic Drugs: Cloning, Structure, and Expression. *Proc. Natl. Acad. Sci.* **2002**, *99* (21), 13926–13931. <https://doi.org/10.1073/pnas.162468699>.
- (17) Crofford, L. J.; Tan, B.; McCarthy, C. J.; Hla, T. Involvement of Nuclear Factor KB in the Regulation of Cyclooxygenase-2 Expression by Interleukin-1 in Rheumatoid Synoviocytes. *Arthritis Rheum.* **1997**, *40* (2), 226–236. <https://doi.org/10.1002/art.1780400207>.
- (18) Tsirka, S. E.; Rogove, A. D.; Strickland, S. Neuronal Cell Death and TPA. *Nature* **1996**, *384* (6605), 123–124.
- (19) Dubois, R. N.; Abramson, S. B.; Crofford, L.; Gupta, R. A.; Simon, L. S.; Van De Putte, L. B.; Lipsky, P. E. Cyclooxygenase in Biology and Disease. *FASEB J.* **1998**, *12* (12), 1063–1073. <https://doi.org/9737710>.
- (20) Zhang, J.; Ding, E. L.; Song, Y. Adverse Effects of Cyclooxygenase 2 Inhibitors on Renal and Arrhythmia Events. *J. Am. Med. Assoc.* **2006**, *296* (13), 1619–1632. <https://doi.org/10.1001/jama.296.13.jrv60015>.
- (21) Davies, N. M.; Jamali, F. COX-2 Selective Inhibitors Cardiac Toxicity: Getting to the Heart of the Matter. *J. Pharm. Pharm. Sci.* **2004**, *7* (3), 332–336.
- (22) Gupta, G. P.; Nguyen, D. X.; Chiang, A. C.; Bos, P. D.; Kim, J. Y.; Nadal, C.; Gomis, R. R.; Manova-Todorova, K.; Massagué, J. Mediators of Vascular Remodelling Co-Opted for

- Sequential Steps in Lung Metastasis. *Nature* **2007**, *446* (7137), 765–770.
<https://doi.org/10.1038/nature05760>.
- (23) Johnsen, J. I.; Lindskog, M.; Ponthan, F.; Pettersen, I.; Elfman, L.; Orrego, A.; Sveinbjornsson, B.; Kogner, P. Cyclooxygenase-2 Is Expressed in Neuroblastoma , and Nonsteroidal Anti-Inflammatory Drugs Induce Apoptosis and Inhibit Tumor Growth *in Vivo*. **2004**, 7210–7215.
- (24) Ghosh, N.; Chaki, R.; Mandal, V.; Mandal, S. C. COX-2 as a Target for Cancer Chemotherapy. *Pharmacol. Reports* **2010**, *62* (2), 233–244. [https://doi.org/10.1016/S1734-1140\(10\)70262-0](https://doi.org/10.1016/S1734-1140(10)70262-0).
- (25) Inoue, H.; Taba, Y.; Miwa, Y.; Yokota, C.; Miyagi, M.; Sasaguri, T. Transcriptional and Posttranscriptional Regulation of Cyclooxygenase-2 Expression by Fluid Shear Stress in Vascular Endothelial Cells. *Arterioscler. Thromb. Vasc. Biol.* **2002**, *22* (9), 1415–1420. <https://doi.org/10.1161/01.ATV.0000028816.13582.13>.
- (26) Hendriks, R. J.; van der Leest, M. M. G.; Dijkstra, S.; Barentsz, J. O.; Van Criekinge, W.; Hulsbergen-van de Kaa, C. A.; Schalken, J. A.; Mulders, P. F. A.; van Oort, I. M. A Urinary Biomarker-Based Risk Score Correlates with Multiparametric MRI for Prostate Cancer Detection. *Prostate* **2017**, *77* (14), 1401–1407. <https://doi.org/10.1002/pros.23401>.
- (27) Laube, M.; Kniess, T.; Pietzsch, J. Radiolabeled COX-2 Inhibitors for Non-Invasive Visualization of COX-2 Expression and Activity - A Critical Update. *Molecules* **2013**, *18* (6), 6311–6355. <https://doi.org/10.3390/molecules18066311>.
- (28) Zhang, Q.; Han, Z.; Tao, J.; Zhang, W.; Li, P.; Tang, L.; Gu, Y. A Novel Near-Infrared Fluorescent Probe for Monitoring Cyclooxygenase-2 in Inflammation and Tumor. *J. Biophotonics* **2018**, *11* (6), 1–9. <https://doi.org/10.1002/jbio.201700339>.

- (29) Tietz, O.; Wuest, M.; Marshall, A.; Glubrecht, D.; Hamann, I.; Wang, M.; Bergman, C.; Way, J. D.; Wuest, F. PET Imaging of Cyclooxygenase-2 (COX-2) in a Pre-Clinical Colorectal Cancer Model. *EJNMMI Res.* **2016**, *6* (1). <https://doi.org/10.1186/s13550-016-0192-9>.
- (30) McCarthy, T. J.; Sheriff, A. U.; Graneto, M. J.; Talley, J. J.; Welch, M. J. Radiosynthesis, *in Vitro* Validation, and *in Vivo* Evaluation of ¹⁸F-Labeled COX-1 and COX-2 Inhibitors. *J. Nucl. Med.* **2002**, *43* (1), 117–124.
- (31) Kaur, J.; Tietz, O.; Bhardwaj, A.; Marshall, A.; Way, J.; Wuest, M.; Wuest, F. Design, Synthesis, and Evaluation of an ¹⁸F-Labeled Radiotracer Based on Celecoxib-NBD for Positron Emission Tomography (PET) Imaging of Cyclooxygenase-2 (COX-2). *ChemMedChem* **2015**, *10* (10), 1635–1640. <https://doi.org/10.1002/cmdc.201500287>.
- (32) Uddin, M. J.; Crews, B. C.; Ghebreselasie, K.; Huda, I.; Kingsley, P. J.; Ansari, M. S.; Tantawy, M. N.; Reese, J.; Marnett, L. J. Fluorinated COX-2 Inhibitors as Agents in PET Imaging of Inflammation and Cancer. *Cancer Prev. Res.* **2011**, *4* (10), 1536–1545. <https://doi.org/10.1158/1940-6207.CAPR-11-0120>.
- (33) Uddin, M. J.; Crews, B. C.; Ghebreselasie, K.; Tantawy, M. N.; Marnett, L. J. [¹²³I]-Celecoxib Analogues as SPECT Tracers of Cyclooxygenase-2 in Inflammation. *ACS Med. Chem. Lett.* **2011**, *2* (2), 160–164. <https://doi.org/10.1021/ml100232q>.
- (34) Schuller, H. M.; Kabalka, G.; Smith, G.; Mereddy, A.; Akula, M.; Cekanova, M. Detection of Overexpressed COX-2 in Precancerous Lesions of Hamster Pancreas and Lungs by Molecular Imaging: Implications for Early Diagnosis and Prevention. *ChemMedChem* **2006**, *1* (6), 603–610. <https://doi.org/10.1002/cmdc.200500032>.
- (35) Prabhakaran, J.; Majo, V. J.; Simpson, N. R.; Van Heertum, R. L.; Mann, J. J.; Kumar, J. S.

- D. Synthesis of [11C]Celecoxib: A Potential PET Probe for Imaging COX-2 Expression. *J. Label. Compd. Radiopharm.* **2005**, *48* (12), 887–895. <https://doi.org/10.1002/jlcr.1002>.
- (36) De Vries, E. F. J.; Van Waarde, A.; Buursma, A. R.; Vaalburg, W. Synthesis and *in Vivo* Evaluation of 18F-Desbromo-Dup-697 as a PET Tracer for Cyclooxygenase-2 Expression. *J. Nucl. Med.* **2003**, *44* (10), 1700–1706.
- (37) Wuest, F.; Aileen, H.; Metz, P. Synthesis of 18 F-Labelled Cyclooxygenase-2 (COX-2) Inhibitors. **2005**, *2*, 503–507.
- (38) Wuest, F.; Kniess, T.; Bergmann, R.; Pietzsch, J. Synthesis and Evaluation *in Vitro* and *in Vivo* of a 11C-Labeled Cyclooxygenase-2 (COX-2) Inhibitor. *Bioorganic Med. Chem.* **2008**, *16* (16), 7662–7670. <https://doi.org/10.1016/j.bmc.2008.07.016>.
- (39) Kuge, Y.; Katada, Y.; Shimonaka, S.; Temma, T.; Kimura, H.; Kiyono, Y.; Yokota, C.; Minematsu, K.; Seki, K. I.; Tamaki, N.; Ohkura, K.; Saji, H. Synthesis and Evaluation of Radioiodinated Cyclooxygenase-2 Inhibitors as Potential SPECT Tracers for Cyclooxygenase-2 Expression. *Nucl. Med. Biol.* **2006**, *33* (1), 21–27. <https://doi.org/10.1016/j.nucmedbio.2005.10.004>.
- (40) Bhardwaj, A.; Kaur, J.; Wuest, M.; Wuest, F. *In Situ* Click Chemistry Generation of Cyclooxygenase-2 Inhibitors. *Nat. Commun.* **2017**, *8* (1), 1–13. <https://doi.org/10.1038/s41467-016-0009-6>.
- (41) Rostovtsev, V. V.; Green, L. G.; Fokin, V. V.; Sharpless, K. B. A Stepwise Huisgen Cycloaddition Process: Copper(I)-Catalyzed Regioselective “Ligation” of Azides and Terminal Alkynes. *Angew. Chemie* **2002**, *41* (14), 2596–2599. <https://doi.org/10.1021/jo011148j>.
- (42) Zischler, J.; Kolks, N.; Modemann, D.; Neumaier, B.; Zlatopolskiy, B. D. Alcohol-

- Enhanced Cu-Mediated Radiofluorination. *Chem. - A Eur. J.* **2017**, *23* (14), 3251–3256.
<https://doi.org/10.1002/chem.201604633>.
- (43) Wilson, A. A.; Jin, L.; Garcia, A.; Dasilva, J. N.; Houle, S. An Admonition When Measuring the Lipophilicity of Radiotracers Using Counting Techniques. **2001**, *54*, 203–208.
- (44) Bhardwaj, A.; Kaur, J.; Bergman, C.; Wuest, F. In-Situ Click Chemistry for the Design and Synthesis of Highly Potent Radiotracers for PET Imaging of Cyclooxygenase-2. In *The 22nd International Symposium on Radiopharmaceutical Sciences (ISRS 2017)*; Dresden, Germany, 2017; p S 483. <https://doi.org/10.1002/jlcr.3508>.
- (45) Frost, S. C.; McKenna, R. *Physiological Functions of the Alpha Class of Carbonic Anhydrases*; 2014; Vol. 75. https://doi.org/10.1007/978-94-007-7359-2_2.
- (46) Weber, A.; Casini, A.; Heine, A.; Kuhn, D.; Supuran, C. T.; Scozzafava, A.; Klebe, G. Unexpected Nanomolar Inhibition of Carbonic Anhydrase by COX-2-Selective Celecoxib: New Pharmacological Opportunities Due to Related Binding Site Recognition. *J. Med. Chem.* **2004**, *47* (3), 550–557. <https://doi.org/10.1021/jm030912m>.
- (47) Brooks, A.; Topczewski, J.; Ichiishi, N.; Sanford, M.; Scott, P. Late-Stage [¹⁸F]Fluorination: New Solutions to Old Problems. *Chem. Sci.* **2014**, *5* (12), 4545–4553. <https://doi.org/10.1039/C4SC02099E>.
- (48) Hanif, R.; Pittas, A.; Feng, Y.; Koutsos, M. I.; Qiao, L.; Staiano-Coico, L.; Shiff, S. I.; Rigas, B. Effects of Nonsteroidal Anti-Inflammatory Drugs on Proliferation and on Induction of Apoptosis in Colon Cancer Cells by a Prostaglandin-Independent Pathway. *Biochem. Pharmacol.* **1996**, *52* (2), 237–245.
- (49) Elder, D. J. E.; Halton, D. E.; Hague, A.; Paraskeva, C. Induction of Apoptotic Cell Death in Human Colorectal Carcinoma Cell Lines by a Cyclooxygenase-2 (COX-2)-Selective

- Nonsteroidal Anti-Inflammatory Drug: Independence from COX-2 Protein Expression. *Clin. Cancer Res.* **1997**, *3*, 1679–1683.
- (50) Rigas, B.; Shiff, S. J. Is Inhibition of Cyclooxygenase Required for the Chemopreventive Effect of NSAIDs in Colon Cancer? A Model Reconciling the Current Contradiction. *Med. Hypotheses* **2000**, *54* (2), 210–215. <https://doi.org/10.1054/mehy.1999.0023>.
- (51) Grösch, S.; Maier, T. J.; Schiffmann, S.; Geisslinger, G. Cyclooxygenase-2 (COX-2) - Independent Anticarcinogenic Effects of Selective COX-2 Inhibitors. *J. Natl. Cancer Inst.* **2006**, *98* (11), 736–747. <https://doi.org/10.1093/jnci/djj206>.
- (52) Assefnia, S.; Dakshanamurthy, S.; Guidry Auvil, J. M.; Hampel, C.; Anastasiadis, P. Z.; Kallakury, B.; Uren, A.; Foley, D. W.; Brown, M. L.; Shapiro, L.; Brenner, M.; Haigh, D.; Byers, S. W. Cadherin-11 in Poor Prognosis Malignancies and Rheumatoid Arthritis: Common Target, Common Therapies. *Oncotarget* **2014**, *5* (6), 1458–1474. <https://doi.org/10.18632/oncotarget.1538>.
- (53) Thaher, B. A.; Koch, P.; Schattel, V.; Laufer, S. Role of the Hydrogen Bonding Heteroatom-Lys53 Interaction between the P38r Mitogen-Activated Protein (MAP) Kinase and Pyridinyl-Substituted 5-Membered Heterocyclic Ring Inhibitors. *J. Med. Chem.* **2009**, *52*, 2613–2617. <https://doi.org/10.1007/BF02886547>.
- (54) Kazmi, F.; Hensley, T.; Pope, C.; Funk, R. S.; Loewen, G. J.; Buckley, D. B.; Parkinson, A. Lysosomal Sequestration (Trapping) of Lipophilic Amine (Cationic Amphiphilic) Drugs in Immortalized Human Hepatocytes (Fa2N-4 Cells). *Drug Metab. Dispos.* **2013**, *41* (4), 897–905. <https://doi.org/10.1124/dmd.112.050054>.
- (55) Banks, W. A. Characteristics of Compounds That Cross the Blood-Brain Barrier. *BMC Neurol.* **2009**, *9* (SUPPL. 1), 5–9. <https://doi.org/10.1186/1471-2377-9-S1-S3>.

- (56) Kumar, J. S. D.; Zanderigo, F.; Prabhakaran, J.; Rubin-Falcone, H.; Parsey, R. V.; Mann, J. J. *In Vivo* Evaluation of [11C]TMI, a COX-2 Selective PET Tracer, in Baboons. *Bioorganic Med. Chem. Lett.* **2018**, *28* (23–24), 3592–3595. <https://doi.org/10.1016/j.bmcl.2018.10.049>.
- (57) Lebedev, A.; Jiao, J.; Lee, J.; Yang, F.; Allison, N.; Herschman, H.; Sadeghi, S. Radiochemistry on Electrodes: Synthesis of An18F-Labelled and *in Vivo* Stable COX-2 Inhibitor. *PLoS One* **2017**, *12* (5), 1–18. <https://doi.org/10.1371/journal.pone.0176606>.
- (58) Prabhakaran, J.; Underwood, M.; Zanderigo, F.; Simpson, N. R.; Cooper, A. R.; Matthew, J.; Rubin-Falcone, H.; Parsey, R. V.; Mann, J. J.; Dileep Kumar, J. S. Radiosynthesis and *in Vivo* Evaluation of [11C]MOV as a PET Imaging Agent for COX-2. *Bioorganic Med. Chem. Lett.* **2018**, *28* (14), 2432–2435. <https://doi.org/10.1016/j.bmcl.2018.06.015>.
- (59) Zhang, F.; Hao, G.; Shao, M.; Nham, K.; An, Y.; Wang, Q.; Zhu, Y.; Kusminski, C. M.; Hassan, G.; Gupta, R. K.; Zhai, Q.; Sun, X.; Scherer, P. E.; Oz, O. K. An Adipose Tissue Atlas: An Image-Guided Identification of Human-like BAT and Beige Depots in Rodents. *Cell Metab.* **2018**, *27* (1), 252–262.e3. <https://doi.org/10.1016/j.cmet.2017.12.004>.
- (60) Enerbäck, S. Clinical Implications of Basic Research The Origins of Brown Adipose Tissue. *N. Engl. J. Med.* **2009**, 2021–2023.
- (61) Himmelsbach, M.; Varesio, E.; Hopfgartner, G. Liquid Extraction Surface Analysis (LESA) of Hydrophobic Tlc Plates Coupled to Chip-Based Nanoelectrospray Highresolution Mass Spectrometry. *Chimia (Aarau).* **2014**, *68* (3), 150–154. <https://doi.org/10.2533/chimia.2014.150>.
- (62) Farmer, S. R. Molecular Determinants of Brown Adipocyte Formation and Function. *Genes Dev.* **2008**, *22* (10), 1269–1275. <https://doi.org/10.1101/gad.1681308>.

(63) Eskildsen, J.; Wenzel Tornoe, C. Pyrazolopyridines Useful in the Treatment of the Central Nervous System. WO 2013/004617 A1, 2013.

CHAPTER 3

***In vivo* imaging of autotaxin in thyroid and breast tumor models using [¹⁸F]PRIMATX**

***In vivo* imaging of autotaxin in thyroid and breast tumor models using [¹⁸F]PRIMATX**

Marcus Litchfield, Melinda Wuest, Guanmin Meng, Emmanuelle Briard, Yves P.

Auberson, Todd McMullen, David Brindley, Frank Wuest

In preparation for submission...

Abstract:

Autotaxin (ATX) is a secreted enzyme responsible for producing lysophosphatidic acid (LPA). The ATX/LPA signaling axis is normally activated in wound healing and other physiological processes, but its activity is hijacked and upregulated in the progression and persistence of chronic inflammatory diseases, including cancer. As ATX inhibitors are now progressing to clinical testing, innovative diagnostic tools such as positron emission tomography (PET) are needed for the exact and accurate measurement of ATX expression *in vivo*. Recently, radiotracer [¹⁸F]PRIMATX was developed and tested for PET imaging of ATX *in vivo* in a murine melanoma model. The goal of the present work was to further validate [¹⁸F]PRIMATX by analyzing its *in vivo* metabolic stability and suitability for PET imaging of ATX expressed in human 8305C thyroid tumor model and in adipose tissue adjacent to murine breast 4T1 tumors. [¹⁸F]PRIMATX displayed favorable metabolic stability (65% intact radiotracer after 60 min p.i.) and provided sufficient tumor-to-muscle contrast in both tumor models (4T1: $SUV_{60min} = 0.81 \pm 0.05$; 8305C: $SUV_{60min} = 0.61 \pm 0.02$). Radiotracer uptake in 8305C tumors could be blocked *in vivo* by 12 and 8% after 30 and 60 min, respectively.

Keywords: ¹⁸F, positron emission tomography (PET), autotaxin (ATX), PRIMATX, lysophosphatidic acid (LPA), molecular imaging

3.1. INTRODUCTION

Ectonucleotide pyrophosphatase/phosphodiesterase 2 (ENPP2), more commonly referred to as autotaxin (ATX), is a secreted phosphodiesterase initially discovered through its lysophospholipase D activity.^{1,2} ATX catalyses the hydrolysis of extracellular lysophosphatidylcholine (LPC) into choline and lysophosphatidic acid (LPA), a lipid mediator which exerts effects on at least six different G protein-coupled receptors (GPCRs): LPAR₁₋₆.³ LPA receptors stimulate various downstream signaling pathways inducing cell proliferation, migration, and survival; thus, healthy levels of ATX expression are seen in various physiological processes such as nervous system development, blood vessel formation, and wound healing.³⁻⁶

Aberrant expression of ATX plays a major role in several chronic inflammatory diseases including rheumatoid arthritis, hepatitis, and fibrosis; and it is among the 40 most upregulated genes in highly metastatic cancer.^{3,7-10} Its role in inflammatory diseases revolves around its complex pro-inflammatory signalling which causes it to both upregulate the production of and be upregulated by inflammatory cytokines.^{3,11-19} This occurs through the recruitment and activation of various immune cells and pro-fibrotic fibroblasts, among many others, which establish chronic inflammatory micro-environments that lead to fibrosis and/or cancer. ATX's contribution to metastasis was initially discovered in melanoma cells where it acted as an autocrine motility factor, a function which is now thought to be achieved through integrin binding.²⁰⁻²² The interaction between ATX and integrin ($\beta 1$ and $\beta 3$) localizes LPA expression close to LPARs on the cell surface, allowing for persistent LPA signalling and its subsequent effects including extracellular matrix remodeling and cell migration.^{20,21,23,24} Although ATX is expressed by melanoma and thyroid cancer cells, breast tumor cells do not express ATX directly, rather, surrounding adipose

tissue of the mammary fat pad increases ATX production and expression in response to secreted pro-inflammatory mediators derived from LPA signaling within the tumor.^{13,22,25}

The crucial role of ATX in inflammatory diseases has, over time, become conclusively evident. Thus, the ATX/LPA signaling axis has become recognized as an important biomarker and drug target for the treatment of chronic inflammatory diseases, including cancer.^{8,25}

Over the past 15 years several small molecule ATX inhibitors have been developed, and although none are yet FDA approved, one compound (GLPG1690) has progressed to phase III clinical trials for the treatment of idiopathic pulmonary fibrosis (IPF).²⁶ With the development and clinical testing of ATX inhibitors there is an emerging need for non-invasive imaging of ATX. Molecular imaging techniques, like positron emission tomography (PET), could be valuable tools for ATX detection and quantification *in vivo* to assess and monitor therapies targeting the ATX/LPA axis in patients with chronic inflammatory diseases.

Cyclooxygenase-2 (COX-2), a down-stream component of the ATX/LPA signalling pathway, is another key regulator of inflammatory processes.^{7,27-29} In the last two decades, COX-2 has emerged as crucial biomarker and drug target in chronic inflammatory diseases, including cancer.³⁰

Numerous selective COX-2 inhibitors have been developed and COX-2 expression and function in cancer have been linked with the stage of the disease.³¹ This correlation is most manifested in colorectal cancer. The link between COX-2 expression and cancer has stimulated the development of COX-2 imaging probes using a variety of small molecule inhibitors in combination with various imaging modalities.³²⁻³⁶ Thus, ATX and COX-2 represent both valuable biomarkers for targeted molecular imaging of pathological inflammation *in vivo*. However, COX-2 and ATX differ in the cellular location of their expression with important consequences for the design *in vivo* imaging probes. The intracellular expression of COX-2 dictates COX-2 imaging probes must pass cellular

membranes through passive diffusion to reach COX-2 which is mainly located in the inner membrane of the endoplasmic reticulum.³⁴ This differs from ATX, a secreted enzyme that either binds to integrins expressed on the cell surface, or floats freely in the intercellular space. Thus, the need for a radiotracer to possess high lipophilicity, which is mandatory for sufficient passive cellular membrane transport, becomes less important while properties like high *in vivo* stability become more important.^{20,24,37} An ideal molecular imaging probe for ATX should be stable *in vivo* throughout the time course of the ATX imaging experiment and it should possess adequate lipophilicity to make transient associations with biomolecules during the biodistribution and targeting process. Most importantly, the radiotracer should demonstrate a high level of specificity in binding to the target.³⁷⁻³⁹

Recent efforts have resulted in the development and initial testing of [¹⁸F]PRIMATX, an ¹⁸F-labeled derivative based on a benzyl-methyl-tetrazole autotaxin inhibitor.^{38,39} Radiotracer [¹⁸F]PRIMATX was assessed in a B16F10 murine melanoma tumor model, where it showed ~4.4 %ID/g tumor uptake.³⁹ While this first *in vivo* analysis resulted in encouraging data, additional testing, especially using different tumor models, is necessary for the full validation of [¹⁸F]PRIMATX as a reliable and versatile *in vivo* ATX PET imaging probe. The goal of the present study was to analyze both the *in vivo* metabolic stability and imaging performance of [¹⁸F]PRIMATX in a murine breast cancer and human thyroid tumor model.

3.2. MATERIALS AND METHODS

3.2.1. General

All chemicals, reagents, and solvents for synthesis and analysis were analytical grade. Chromafix (30-PS-HCO₃, Macherey-Nagel) cartridges were purchased from ABX. All other chemicals and

solvents were purchased from Sigma Aldrich. All solvents were dried and/or distilled prior to utilization. Thin-layer chromatography (TLC) was carried out using HF254 silica gel. Radio-TLC analysis was performed on a Bioscan radio-TLC reader and Winscan analysis software. High-performance liquid chromatography (HPLC) purification and analysis were performed using a Luna 5 μm Carbon-18 (C-18) column on a Gilson 322 Pump module fitted with a 171 Diode Array and a radioactivity detector. The following elution profile was used: 0-5 min, isocratic elution with 40% $\text{CH}_3\text{CN}/\text{H}_2\text{O}$; 5-10 min 40% $\text{CH}_3\text{CN}/\text{H}_2\text{O}$ to 60% $\text{CH}_3\text{CN}/\text{H}_2\text{O}$; 10-21 min isocratic elution with 60% $\text{CH}_3\text{CN}/\text{H}_2\text{O}$; 21-26 min 60% $\text{CH}_3\text{CN}/\text{H}_2\text{O}$ to 80% $\text{CH}_3\text{CN}/\text{H}_2\text{O}$; 26-35 min isocratic elution with 80% $\text{CH}_3\text{CN}/\text{H}_2\text{O}$.

^1H -NMR and ^{13}C -NMR spectra were recorded on an Agilent/Varian Inova two-channel 400 MHz spectrometer, an Agilent/Varian Inova four-channel 500 MHz spectrometer, and an Agilent/Varian VNMRS three-channel 600 MHz spectrometer. Chemical shifts are given in ppm referenced to internal standards (s = singlet, singlet, d = doublet). High-resolution mass spectrometry (HR-MS) was carried out on an Agilent Technologies 6220 oaTOF.

3.2.2. Radiochemistry

^{18}F Fluoride was produced by the $^{18}\text{O}(\text{p},\text{n})^{18}\text{F}$ nuclear reaction through proton irradiation of enriched (98%) ^{18}O water (3.0 ml, Rotem, Germany) using a TR19/9 cyclotron (Advanced Cyclotron Systems, Inc., Richmond, BC, Canada).

The synthesis of (*R,E*)-3-(4-chloro-2-((5-methyl-2*H*-tetrazol-2-yl)methyl)phenyl)-1-(4-((5-(2- ^{18}F)fluoroethoxy)pyridine-2-yl)methyl)-2-methylpiperazin-1-yl)prop-2-en-1-one, or ^{18}F PRIMATX, was performed using nucleophilic radio-fluorination methods. Potassium Kryptofix ($\text{K}_2\text{CO}_3/\text{K}_{222}$) was used to elute no-carrier-added ^{18}F fluoride off of a QMA (Waters Sep-Pak QMA plus Light) cartridge into a drying vial which was dried under nitrogen gas at 95

°C. Dried ^{18}F Fluoride was resuspended in Acetonitrile (~0.3 mL) and was transferred to a new reaction vial containing (R,E)-2-((6-((4-(3-(4-chloro-2-((5-methyl-2H-tetrazol-2-yl)methyl)phenyl)acryloyl)-3-methylpiperazin-1-yl)methyl)pyridin-3-yl)oxy)ethyl-4-methylbenzenesulfonate **1** (3 mg, 4.5 μmol). The whole mixture was reacted at 85 °C for 5 min under nitrogen to produce the ^{18}F PRIMATX, ^{18}F **2**. HPLC purification with a Luna 5 μm Carbon-18 (C-18) was used to isolate the radioactive compound ^{18}F PRIMATX eluting at a retention time of 18 min (in 60% acetonitrile: 40% water), in radiochemical yields of $25 \pm 6.7\%$ ($n = 9$). The molar activity exceeded 55 GBq/ μmol (see graph 2 in supplemental material). Normal-phase radio-TLC (14% MeOH in DCM, $R_f = 0.55$) using a Bioscan radio-TLC reader and Winscan analysis software was performed to verify radiochemical purity greater than 98%. The HPLC solvent was removed under vacuum and the compound was resuspended in a solution of 5% ethanol in saline.

3.2.3. Determination of lipophilicity

The shake-flask method was used to determine the lipophilicity of ^{18}F PRIMATX.⁴⁰ The partition coefficient of ^{18}F PRIMATX was measured using *n*-octanol as the organic phase and PBS (pH 7.4) as the aqueous phase. 500 μL of each phase were added to a LoBind Eppendorf tube, to which <1 MBq of ^{18}F PRIMATX was added, and the mixture was shaken vigorously for 5 min. The mixture was then centrifuged at 2000 rpm for 2 min to allow the layers to separate.

Aliquots of 100 μL were removed from each phase, and the amount of ^{18}F PRIMATX present in each phase was measured by a Wizard gamma counter. Experiments were performed in triplicate, and $\log D_{7.4}$ values were calculated.

3.2.4. Animal models

All animal experiments were performed according to guidelines from the Canadian Council on Animal Care (CCAC) and approved by the local animal care committee (Cross Cancer Institute, University of Alberta).

PET experiments were performed using 4T1 mammary tumor-bearing female BALB/c mice (Charles River Laboratories, Saint Constant, Quebec, Canada) or 8305C thyroid tumor-bearing male NSG mice (Dr. Lynn Postovit, Dept. of Oncology, University of Alberta). Female BALB/c mice and male NSG were housed under standard conditions with free access to standard food and tap water. 4T1 cells (20,000 in 100 μ L PBS/Matrigel [50/50]) were injected into the 2nd inguinal left mammary fat pad of female BALB/c mice, and 8305C cells (5×10^6 cells in 200 μ L of PBS) were injected subcutaneously into the upper left flank of male NSG mice. After 10-12 (4T1 tumors) or 18 to 21 (8305C tumors) days growth, tumors were suitable for all *in vivo* experiments.

3.2.5. Immunohistochemistry

Tumor tissues were fixed in 10% formalin and immunohistochemistry was performed on 5- μ m paraffin-embedded tumor sections using the Specific HRP/DAB Detection Kit (ab64261) from Abcam (Toronto, ON, Canada) according to the manufacturer's instructions. Antigen retrieval was performed by microwave heating using Tris-EDTA buffer (10 mM Tris, 1 mM EDTA, pH 9.0) in a pressure cooker for 20 min. Primary antibody against ATX (1 mg/ml, 1:1000 dilution) was a gift from Dr. Tim Clair (Laboratory of Pathology, NIH, Bethesda, MD, USA). Images were acquired using a Zeiss Axioskop 2 imaging system (Carl Zeiss Canada, Toronto, ON, Canada). At least 6 images were taken to get an average value for each sample.

3.2.6. Radiometabolite analysis

The radiotracer solution containing ~25-30 MBq [¹⁸F]PRIMATX in 150-180 μL saline (~5 % EtOH) was injected intravenously into normal female BALB/c mice under isoflurane anesthesia. Blood samples (20–40 μL) were collected from a tail vein catheter at 5, 15, 30 and 60 min p.i.. Plasma was separated from blood cells by centrifugation (5 min, 13,000×g) followed by plasma protein precipitation using 100 μL methanol and a second centrifugation step (5 min, 13,000×g). Supernatants were analyzed by radio thin-layer chromatography (radio-TLC) and radioactivity in all blood compartments was determined using a WIZARD2 Automatic gamma counter (Perkin Elmer; Waltham, MA, USA). TLCs were developed in 14% MeOH in DCM and analyzed using a BAS-5000 reader. [¹⁸F]PRIMATX had an R_f value of ~0.55 in this solvent system. Experiments were done in triplicate. All data are presented as means ± SEM from 3 experiments.

3.2.7. PET imaging

4T1 mammary tumor-bearing female BALB/c mice or 8305C thyroid tumor-bearing male NSG mice were immobilized in prone position into the center field of view of an Inveon® PET/CT scanner (Siemens Preclinical Solutions, Knoxville, TN, USA) with isoflurane anesthesia in 40% oxygen/60% nitrogen (gas flow= 1 mL/min). The body temperature was kept constant at 37°C for the entire experiment. For PET experiments, 3–8 MBq of [¹⁸F]PRIMATX in ~150 μL of solution (5% EtOH/saline) was administered intravenously as a bolus injection into the tail vein via a preplaced catheter. PET data was collected in 3D list mode over 60 min. Dynamic list mode data were sorted into sinograms with 54 time frames (10x2 s, 8x5 s, 6x10 s, 6x20 s, 8x60 s, 10x120 s, 5x300 s). Frames were reconstructed using Ordered Subset Expectation Maximization (OSEM) or maximum a posteriori (MAP) reconstruction modes.

No correction for partial volume effects was performed. Image files were further processed using ROVER v2.0.51 software (ABX GmbH, Radeberg, Germany). Masks defining 3D regions of interest (ROI) were set and defined by 50% thresholding. For blocking experiments, either 500 µg or 40 mg ATX inhibitor AE-32-NZ70 (provided by Novartis) per animal (corresponding to 14 and 100 mg/kg or dose) in 70 or 190 µL saline/DMSO 50% was injected intraperitoneally 10 or 30 min prior to radiotracer administration. Mean standardized uptake values [$SUV_{mean} = (\text{activity/mL tissue})/(\text{injected activity/body weight}), \text{mL/g}$] were calculated for each region of interest (ROI) with a threshold defined at 50% of radioactivity uptake. The time-activity curves (TACs) were generated using GraphPad Prism 4.0 (GraphPad Software, La Jolla, CA, USA). All semi-quantified PET data are presented as means \pm SEM from n experiments.

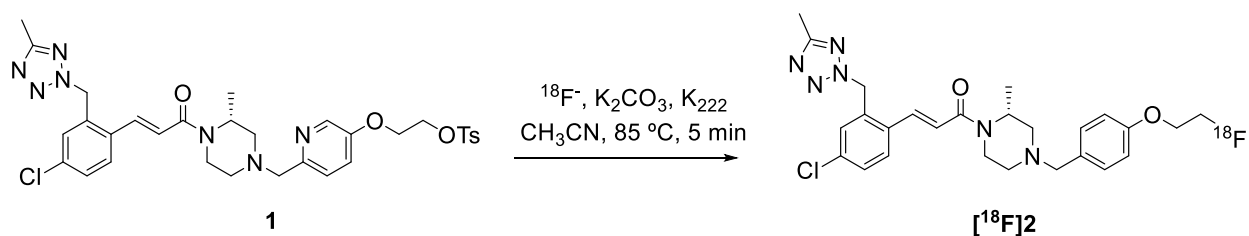
3.2.8. Statistical analysis

All *in vivo* data are expressed as means \pm SEM. Graphs were constructed using Graph- Pad Prism 5.0 (GraphPad Software). Where applicable, statistical differences were tested using unpaired Student's t-test or ANOVA with a post hoc test and were considered significant for $P < 0.05$.

3.3. RESULTS

3.3.1. Radiochemistry

Synthesis of [^{18}F](R,E)-3-(4-Chloro-2-((5-methyl-2H-tetrazol-2-yl)-methyl)phenyl)-1-(4-((5-(2-fluoroethoxy)pyridin-2-yl)methyl)-2-methylpiperazin-1-yl)prop-2-en-1-one ([^{18}F]2) was accomplished using nucleophilic radiofluorination chemistry starting from the tosylate precursor **1** (Scheme 4).



Scheme 4. Radiofluorination of labelling precursor to produce radiotracer [^{18}F]PRIMATX [^{18}F]2.

Reaction of no-carrier-added [^{18}F]fluoride with the tosylate precursor **1** in acetonitrile at $85\text{ }^\circ\text{C}$ for 5 min afforded radiotracer [^{18}F]2 ([^{18}F]PRIMATX) in radiochemical yields of $25 \pm 6.7\%$ ($n = 9$). Total synthesis time was 70-80 min, including HPLC purification, and the molar activity exceeded $55\text{ GBq}/\mu\text{mol}$ (Graph 2).

3.3.2. Lipophilicity

The lipophilicity of [^{18}F]PRIMATX was determined to be $\text{LogD}_{7.4} = 2.45$ using the shake-flask method ($n = 3$).⁴⁰

3.3.3. Radiometabolite analysis

Radiometabolic analysis of radiotracer [^{18}F]PRIMATX in normal BALB/c mice revealed favorable metabolic stability of the radiotracer over 60 min p.i. (Figure 25). Levels of intact [^{18}F]PRIMATX decreased from 98% at 5 min p.i. to ~65% at 60 min p.i.

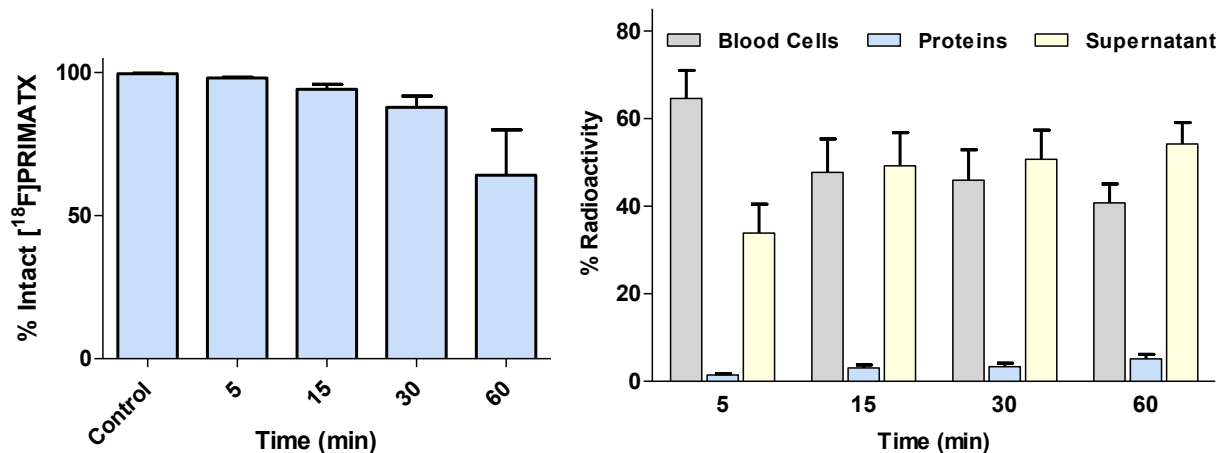


Figure 25. Left) *In vivo* stability of [¹⁸F]PRIMATX in the blood of BALBc mice over 60 min as measured by radio-TLC. Data normalized as percent of intact radiotracer and shown as mean ± SEM from n = 3 experiments. **Right)** Radioactivity distribution in mouse blood compartments over 60 min p.i.. Data normalized as percent of total radioactivity removed at each time point and shown as mean ± SEM from n = 3 experiments.

Blood compartment analysis showed decreasing radioactivity levels in blood cells (from 65% at 5 min to 40% at 60 min), while increasing radioactivity amounts were detected in plasma proteins (1.5% at 5 min to ~5% at 60 min) and in the supernatant (from ~34% at 5 min to ~54% at 60 min) over time.

3.3.4. PET imaging in 4T1 murine breast tumor-bearing mice

Representative PET images in 4T1 murine tumor-bearing mice at 60 min p.i. of [^{18}F]PRIMATX and respective TACs of tumor and muscle uptake over time are shown in Figure 26.

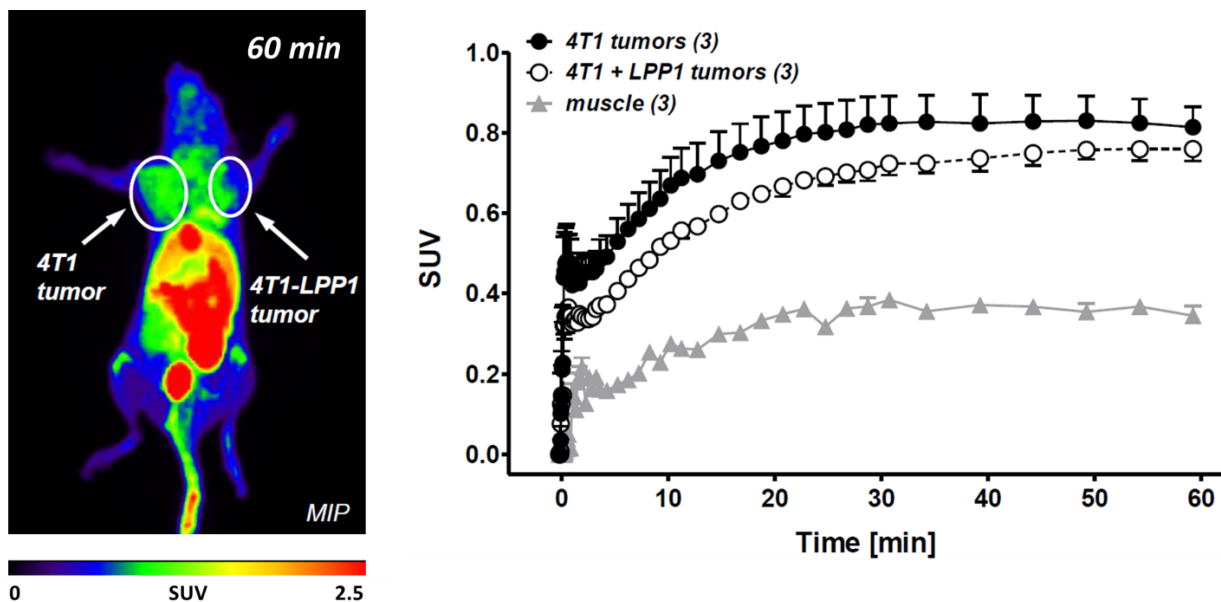


Figure 26. PET image (MIP) of a 4T1 and 4T1-LPP1 tumor-bearing BALB/c mouse 60 min p.i. of [^{18}F]PRIMATX (**left**). Time-activity curves for tumor and muscle uptake of [^{18}F]PRIMATX over 60 min p.i. (**right**). Data are shown as mean \pm SEM from $n = 3$ dynamic PET experiments.

This model was seeded with both 4T1 and 4T1-LPP1 tumor cells. LPP1 (an LPA degrading enzyme) expressing tumors were expected to be of a smaller size due to decreased LPA-related pro-inflammatory signaling. Accumulation of radiotracer [^{18}F]PRIMATX in the region of 4T1 tumors was clearly detectable. Radioactivity uptake in the tumor increased until 30 min, reaching a $\text{SUV}_{30\text{min}}$ of 0.82 ± 0.07 , plateauing over the remaining time course to reach a $\text{SUV}_{60\text{min}}$ of 0.81 ± 0.05 ($n = 3$). Muscle uptake of [^{18}F]PRIMATX followed a similar profile with no washout of radioactivity up to 60 min p.i.: $\text{SUV}_{60\text{min}}$ of 0.34 ± 0.02 ($n = 3$). Radiotracer uptake was also

detected in the mouse brain. [¹⁸F]PRIMATX displayed a combined hepatobiliary and renal clearance pattern as seen by radioactivity accumulation in the liver, gallbladder, intestinal tract, kidneys, and urinary bladder.

3.3.5. Immunohistochemical ATX staining in 8305C human thyroid cancer tissue

Verification of aberrant ATX expression in thyroid tissue through immunohistochemical staining is shown in Figure 27.

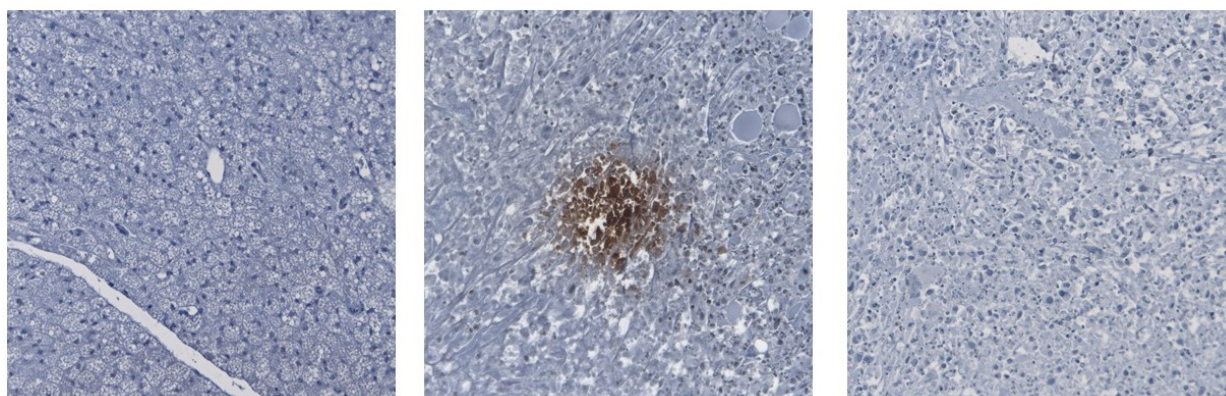


Figure 27. Anti-ATX immunohistochemical (IHC) staining in benign thyroid tissue (**left**) and 8305C human thyroid cancer tissue (**middle**), with IgG control in the 8305C thyroid cancer tissue (**right**). Images displayed at 200x magnification.

Benign thyroid tissue showed no ATX staining (left), whereas, the 8305C thyroid tumor tissue showed ATX staining (middle). Secondary antibody control staining with IgG in the 8305C human thyroid cancer tissue was also negative (right).

3.3.6. PET imaging and in vivo blocking in human thyroid 8305C tumor-bearing mice

Representative PET images of 8305C human thyroid tumor-bearing mice at 30 min p.i. of [¹⁸F]PRIMATX and respective time-activity curves (TACs) of tumor and muscle uptake, tumor-

to-muscle ratio (T/M), as well as *in vivo* blocking, using highly potent ATX inhibitor (*E*)-1-(4-(5-methyl-1,3,4-oxadiazol-2-yl)piperidin-1-yl)-3-(2-((5-methyl-2H-tetrazol-2-yl)-methyl)-4-(trifluoromethyl)phenyl)prop-2-en-1-one^[37,38] are shown in Figure 28.

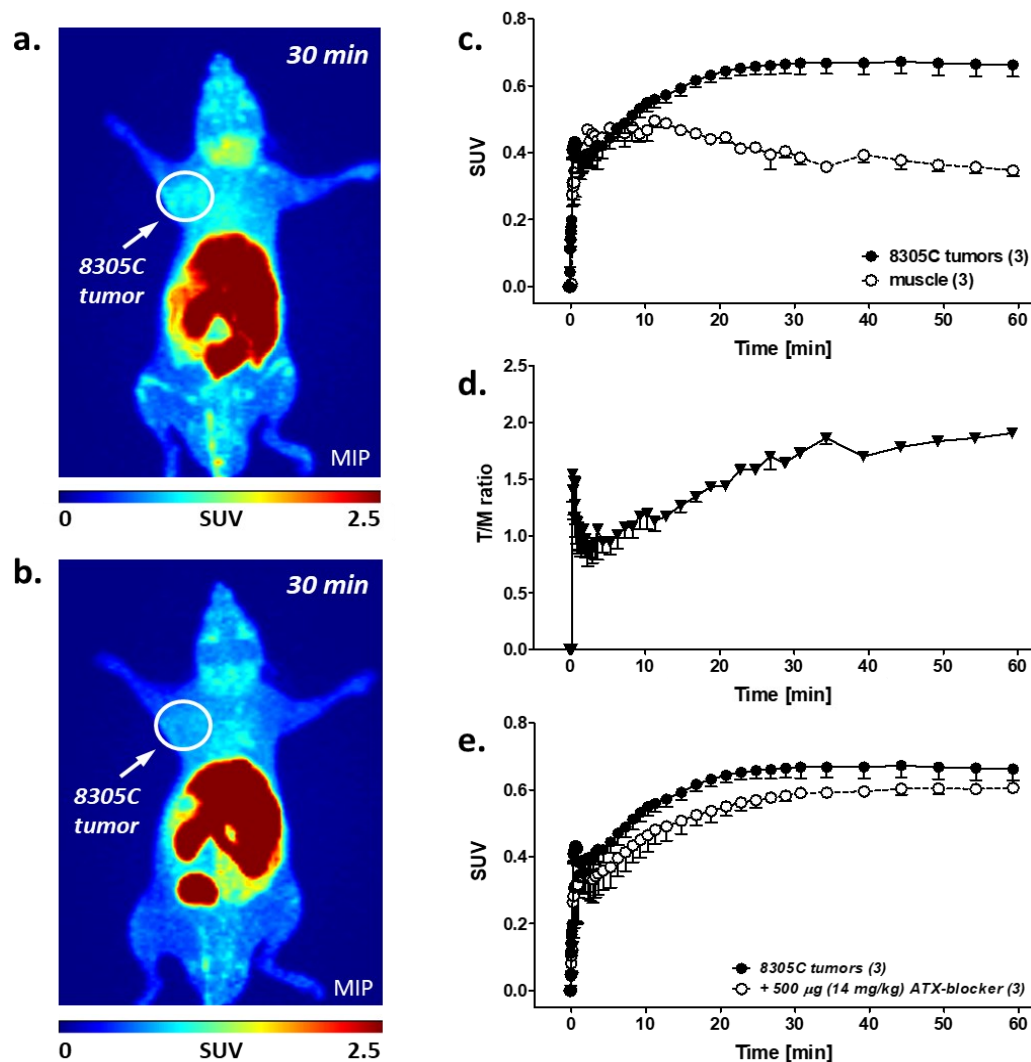


Figure 28. PET images (MIP) of 8305C tumor-bearing NSG mice 30 min after injection of [¹⁸F]PRIMATX in the absence (a) and presence (b) of blocking agent (ATX inhibitor) in the same mouse. Time-activity curves over 60 min p.i. depicting the tumor and muscle uptake (c) and the tumor-to-muscle (T/M) ratio (d), in the absence of ATX inhibitor. [¹⁸F]PRIMATX radiotracer uptake in the tumor over the time course of 60 min in the absence and presence of ATX inhibitor

(*E*)-1-(4-(5-methyl-1,3,4-oxadiazol-2-yl)piperidin-1-yl)-3-(2-((5-methyl-2H-tetrazol-2-yl)-methyl)-4-(trifluoromethyl)phenyl)prop-2-en-1-one (14 mg/kg i.p. injected 15 min before radiotracer administration) (**e**). Data are shown as mean \pm SEM from $n = 3$ dynamic PET experiments each.

As shown in the PET images in Figure 28a and b, blocking effect in the presence of 14 mg/kg of ATX inhibitor (*E*)-1-(4-(5-methyl-1,3,4-oxadiazol-2-yl)piperidin-1-yl)-3-(2-((5-methyl-2H-tetrazol-2-yl)-methyl)-4-(trifluoromethyl)phenyl)prop-2-en-1-one was clearly detectable at 30 min p.i.. However, the trend in reduced radioactivity accumulation in the tumor tissue under blocking conditions was statistically not significant: control $SUV_{30min} = 0.67 \pm 0.03$ versus blocked (14 mg/kg inhibitor) $SUV_{30min} = 0.59 \pm 0.01$ ($p=0.0885$; both $n = 3$), TAC-derived data, respectively (28e). As indicated in the image-derived TACs, radioactivity uptake in the tumor reached maximum levels at 30 min p.i. without further change, remaining constant until 60 min ($SUV_{60min} = 0.66 \pm 0.04$; 28c). Muscle uptake of radioactivity was characterized by a continuous washout after 10 min p.i. reaching a final SUV_{60min} of 0.35 ± 0.02 . Calculation of tumor-to-muscle ratios (T/M; 28d) resulted in an overall increase of radioactivity contrast in the tumor tissue over time representing favorable accumulation and retention of radiotracer [^{18}F]PRIMATX in the tumor. TACs representing blocking conditions versus baseline conditions of tumor uptake are shown in 28e (additional blocking conditions are presented in supplemental information - Figure 31). As described above, using 14 mg/kg ATX inhibitor reduced SUV_{30min} by 12% but this effect was statistically not significant. Interestingly, increasing the blocking dose to 100 mg/kg, administered 30 min before radiotracer administration did not result in more intense blocking effects at 30 min p.i.: $SUV_{30min} = 0.58 \pm 0.05$ ($n=3$; Figure 28). The blocking effect was also rather small (Δ 8%) at

60 min p.i.: SUV_{60min} 0.66 ± 0.04 (control) *versus* blocking conditions (14 mg/kg inhibitor) SUV_{60min} 0.61 ± 0.02 (p>0.05; both n=3).

3.3.7. Blocking effect on radiotracer brain and joint uptake and clearance profile

Figure 29 summarizes generated TACs from different uptake and clearance organs in the absence and presence of blocking compound (500 µg per mouse; 14 mg/kg) after injection of radiotracer [¹⁸F]PRIMATX.

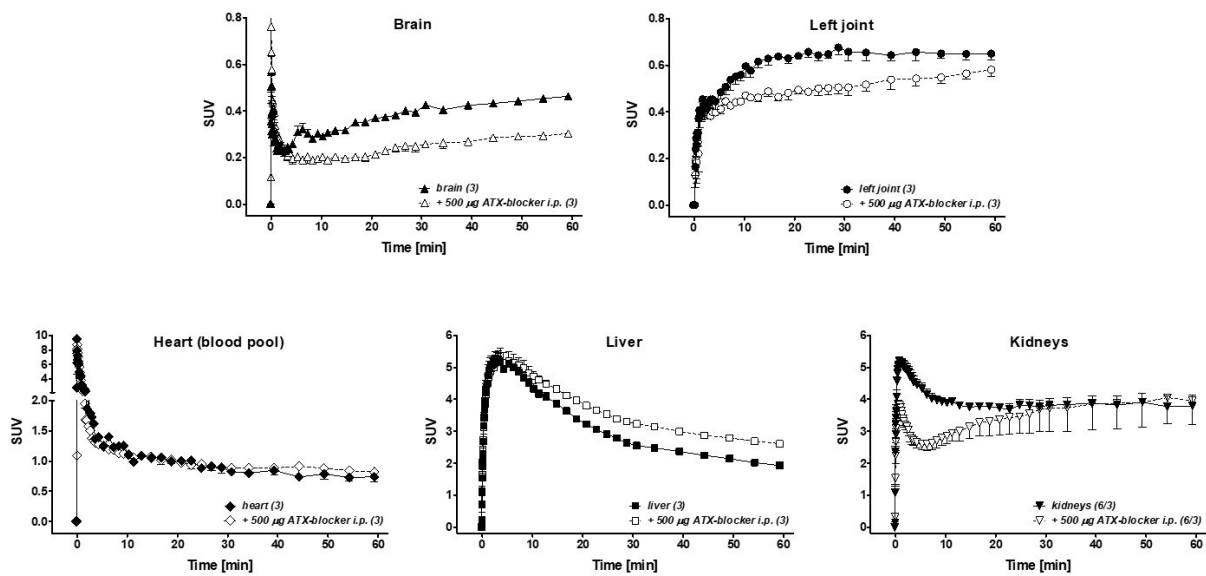


Figure 29. PET image derived TACs representing [¹⁸F]PRIMATX uptake in the brain and left joints (**top**) as well as clearance organs: blood pool (heart), liver, and kidneys (**bottom**), in the absence (control) and presence of ATX inhibitor (14 mg/kg injected i.p. 15 min before the radiotracer) over the time course of 60 min in 8305C thyroid tumor-bearing NSG mice. Data are shown as mean ± SEM from *n* = 3 experiments each.

Radiotracer [¹⁸F]PRIMATX showed substantial uptake in the brain and joints in 8305C thyroid tumor-bearing mice reaching SUV_{60min} of 0.46 ± 0.014 in the brain and 0.65 ± 0.02 in the joints (both *n* = 3). Under blocking conditions, brain uptake was significantly reduced by 34% amounting

to $SUV_{60min,blocked} = 0.303 \pm 0.01$ ($n = 3$; $p < 0.001$). In the joints, blocking was only significant after 30 min reaching Δ of 23% with SUV_{30min} 0.51 ± 0.03 (blocked) *versus* 0.66 ± 0.04 (control; $n = 3$; $p < 0.05$). However, after 60 min this effect was less pronounced, which was similar to the observations in the 8305C thyroid tumor tissue. Blocking effects in brain and joints were clearly visible in the PET images as shown in Figure 28. Blood clearance, as analyzed over the heart region, was not affected by the blocking compound. Both clearance pathways (hepatobiliary and renal) were detectable for radiotracer [^{18}F]PRIMATX. While liver clearance decreased over time, kidneys showed some tendency to retain radioactivity after initial clearance. Presence of ATX blocking compound increased liver clearance levels over the 60 min time course and decreased kidney clearance initially. However, kidney levels approximated baseline levels after 30 min, which lasted throughout the 60 min time course of the PET imaging experiment (see Figure 29, bottom).

3.4. DISCUSSION

ATX is an inflammation and cancer biomarker which has gained great research interest over the last two decades. First ATX inhibitors (GLPG1690) have entered clinical trials for the treatment of idiopathic pulmonary fibrosis. However, very few reports have discussed the development of ATX imaging probes. In 2013, Madan *et al.* and Echelon Biosciences introduced the first, and to date only, ATX fluorescence imaging probe, ATX-red-2. ATX-red-2 was used for the quantification of ATX activity in a murine melanoma model after treatment with different concentrations of carbamoylphosphonates.^{41,42} In 2019, Briard *et al.* introduced the first ^{18}F -labeled radiotracer for the PET imaging of ATX, [^{18}F]PRIMATX.³⁹

The reported radiosynthesis of [¹⁸F]PRIMATX involved nucleophilic radiofluorination chemistry using tosylate **1** as the labeling precursor to introduce n.c.a. [¹⁸F]fluoride.³⁹ Reaction of tosylate precursor **1** in DMSO (0.7 mL) at 140 °C for 10 min afforded radiotracer [¹⁸F]PRIMATX in radiochemical yields of 15%. The goal of the present study was to improve the radiosynthesis of [¹⁸F]PRIMATX starting from tosylate **1** by optimizing the reaction conditions using higher concentrations of **1** (15 μmol/mL *versus* 4.3 μmol/mL). We also varied from the reported method by performing the radiosynthesis in acetonitrile (0.3 mL) at 85 °C for 5 min, and achieved a radiochemical yield of 25 ± 6.7% in a total synthesis time of 70-80 min, including HPLC purification. The molar activity was calculated to be 55 GBq/μmol. Notable, when radiochemical yields were plotted by date, the reaction showed a downward trend in yield over time, suggesting the precursor compound was mildly prone to degradation when stored at 4 °C. Lipophilicity (Log $D_{pH=7.4}$) determination using octanol and PBS resulted in a value of 2.45, slightly lower than the reported value of 3.0.³⁹ *In vivo* metabolic stability analyses revealed about 65% of [¹⁸F]PRIMATX radiotracer was intact after 60 min p.i. in mice. This data correlates with a calculated metabolic half-life of about 1.4 hours for the radiotracer, which is twice as high as the recently reported metabolic half-life of 0.7 hours, though this difference may be due to the use of two different model species (female BALBc mice vs male Sprague-Dawley rats).³⁹

ATX, as a secreted protein with a propensity for integrin binding, would likely be found either associated with cells/cell components, especially T-lymphocytes or platelets, or free-floating.^{12,24,43} This suggests that the bulk of the radioactivity detected may be from the blood cell or protein fractions.

High blood cell and protein binding should especially be seen when induced expression of ATX leads to high levels of circulating protein, as is purported in inflammatory diseases. However, as

the featured BALB/c mice only had constitutive plasma ATX levels, this profile would seem less likely, and indeed was not seen. Looking at trends in radioactivity distribution between the various blood compartments, most of the activity within the first 5 min was associated with the blood cells, but in less than 15 min this activity was reduced from 65 to 48%, while activity amounts in the plasma supernatant fraction increased. The changes in activity levels within each blood compartment fraction likely reflect other contributing processes, apart from ATX binding, such as radiotracer degradation, non-specific interactions resultant from [¹⁸F]PRIMATX's high lipophilicity (including lysosomal trapping⁴⁴), or off-target binding associations, though to date, there are no reported examples of off-target binding by [¹⁸F]PRIMATX.

After the initial *in vivo* PET imaging validation of [¹⁸F]PRIMATX in a subcutaneous murine melanoma model was reported, we investigated the *in vivo* profile of radiotracer [¹⁸F]PRIMATX in an orthotopic murine breast cancer model (4T1). While ATX is directly produced by the reported melanoma cancer cells, its expression in the orthotopic 4T1 breast cancer model occurs in the surrounding adipose tissue and not in the 4T1 cancer cells themselves.^{13,45} Using the orthotopic 4T1 breast cancer model allowed for the validation of [¹⁸F]PRIMATX PET imaging in cancer models with a different ATX source, which acts as a measure of its versatility. We used a second 4T1 tumor in this orthotopic murine breast cancer model, with increased LPP1 expression. LPP1, or lipid phosphate phosphatase 1, is an LPA degrading enzyme which reduces local LPA levels, which in turn results in less ATX/LPA signaling and reduced ATX expression and tumor growth. The comparison of tumor uptake profiles of [¹⁸F]PRIMATX in 4T1 murine breast cancer models (with and without LPP1) with the reported murine melanoma model suggest a similar uptake pattern between the two models with lower radiotracer uptake in the LPP1 tumors.³⁹

In addition to a syngeneic mammary 4T1 tumor model, uptake of [¹⁸F]PRIMATX was also analyzed in a 8305C human thyroid tumor model. Presence of ATX expression in the tumor tissue was verified through immunohistochemical staining.

Tumor uptake levels were similar to those seen in the 4T1 tumor, however, including a better non-target muscle tissue washout of radioactivity over time which led to a progressively better tumor-to-muscle ratio in the thyroid cancer model.

Specific uptake of the [¹⁸F]PRIMATX radiotracer into ATX expressing 8305C thyroid tumors was confirmed by *in vivo* blocking studies using ATX inhibitor (*E*)-1-(4-(5-methyl-1,3,4-oxadiazol-2-yl)piperidin-1-yl)-3-(2-((5-methyl-2H-tetrazol-2-yl)-methyl)-4-(trifluoro-methyl)phenyl)prop-2-en-1-one (14 mg/kg) leading to ~12% reduction in tumor uptake at 30 min p.i.. This reduction in uptake was comparatively less than the ~60% reduction reported in the melanoma model³⁹, but this result may be attributed to the different *in vivo* models. The immunohistochemistry suggests a clustered expression of ATX in 8305C tumors with a high degree of heterogeneity throughout the tumor tissue. The found heterogeneous ATX distribution may be different in recently studied B6D2F1 mice with B16F10 melanoma tumors.^[38] Interestingly, ~34% blocking of [¹⁸F]PRIMATX brain uptake was observed in the 8305C thyroid cancer NSG mice, a value which was comparable to the observed ~38% blocking effect reported for the melanoma model. The inhibitor used in the melanoma model was a 3-methyl-1,2,4-triazole, while a 5-methyl-1,3,4-oxadiazole was used in the present study. However, as ATX mRNA transcripts have been detected in different regions of human and mouse brain,⁴⁶ the observed specific and significant blocking of [¹⁸F]PRIMATX in mouse brain in the present study points toward a functional presence of ATX in the brain which could be detected with ATX imaging probe [¹⁸F]PRIMATX. Brain uptake properties of radiotracer [¹⁸F]PRIMATX could be useful for future studies related to PET imaging of neuroinflammation.

Clearance of radiotracer [^{18}F]PRIMATX occurred by both hepatobiliary and renal elimination routes with ~50% contribution of each pathway as indicated by the generated TACs of the liver and kidneys. Addition of the blocking compound during PET imaging experiments with [^{18}F]PRIMATX resulted in a reduction of early radiotracer uptake into the kidneys, but an increase in liver uptake and therefore slightly favored the hepatobiliary pathway. Interestingly, clearance of [^{18}F]PRIMATX from the kidney was not completed after 60 min p.i. which would be indicative of a prolonged blood pool circulation of the radiotracer. This would also explain the somewhat higher residual radioactivity levels in the heart (=blood pool).

Radiotracer accumulation in the joints was also detected at a level similar to radioactivity levels observed in the 8305C thyroid tumors. Radiotracer uptake in the joints showed a ~23% reduction under blocking conditions, indicating the presence of ATX in the joints. While upregulation of ATX in synovial fluid under inflammatory conditions such as rheumatoid arthritis is well documented, the present xenograft tumor model was unlikely to induce inflammatory condition in the cartilage.¹¹ Instead, baseline levels of ATX expressed in chondrocytes, a previously reported observation, were presumably detected with the radiotracer [^{18}F]PRIMATX.^{11,47}

Among the most interesting findings of the present study was the substantial brain uptake of radiotracer [^{18}F]PRIMATX. This confirms the ready passage of radiotracer [^{18}F]PRIMATX through the blood-brain-barrier and makes it a promising candidate for PET imaging of ATX in neuroinflammatory diseases, including neuroblastomas, gliomas and multiple sclerosis.⁴⁸⁻⁵⁰

3.5. CONCLUSION

Despite the lack of full blood pool clearance (including kidney retention after 60 min which contributes to high background signal), PET imaging of ATX in cancer with radiotracer

[¹⁸F]PRIMATX is feasible as demonstrated with orthotopic 4T1 breast and subcutaneous 8305C thyroid cancer models. Brain uptake of [¹⁸F]PRIMATX was high and could be blocked. This makes radiotracer [¹⁸F]PRIMATX an interesting candidate for PET imaging of neuroinflammation. Overall, [¹⁸F]PRIMATX is a highly promising radiotracer for PET imaging of ATX *in vivo*.

Acknowledgments

The authors would like to thank Dave Clendening and Blake Lazurko from the Edmonton PET centre for radionuclide production. Furthermore, the authors thank other members of the Wuest research lab including Cody Bergman for helping with the establishment of HPLC purification conditions and Daniel Krysz for assistance and training in data processing and figure preparation. The authors also thank Jennifer Dufour (Wuest research lab) for cell culture and help with 8305C tumor cell injections as well animal handling, Xiaogyn Tang (Department of Biochemistry, University of Alberta) for injecting the orthotopic 4T1 tumor model, Dr. Tim Clair (Laboratory of Pathology, NIH, Bethesda, MD, USA) for his gift of the primary antibody against ATX, Dan McGinn (Vivarium of the Cross Cancer Institute, Edmonton, Alberta, Canada) for supporting the animal work, and Dr. Hans-Soenke Jans (Department of Oncology, University of Alberta) for technical support of the preclinical PET imaging facility.

Author Contributions

Experimental planning: ML, MW, GM, DB and FW. Radiosynthesis: ML. Animal experiments including imaging and image data analysis: MW. IHC: GM. EB and YPA synthesized and provided the precursor. TM provided the thyroid tumor cell line. DB provided the breast tumor cell line. Figures preparation ML, MW, and GM. Manuscript writing: ML, MW, and FW.

3.6. SUPPLEMENTAL INFORMATION

3.6.1. Baseline PET imaging with 8305C thyroid tumors – proof of concept

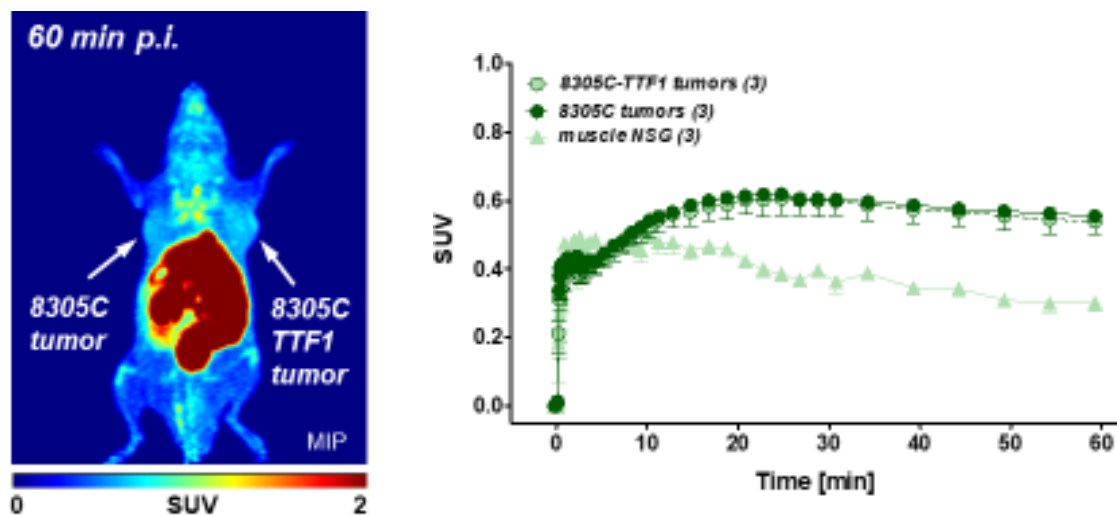


Figure 30. Left) PET image (MIP) of a 8305c and 8305c-TTF1 tumor-bearing NSG mouse 60 min after injection of [^{18}F]PRIMATX. Right) Time-activity curves for tumor and muscle uptake of [^{18}F]PRIMATX over 60 min. p.i.. Data shown are mean \pm SEM from $n = 3$ dynamic PET experiments.

Radiotracer uptake was analyzed in 8305c human thyroid tumors with contralateral muscle as reference tissue. Accumulation of radiotracer [^{18}F]PRIMATX in ATX expressing 8305c tumors was detectable. Radioactivity uptake in the tumor increased until about 25 min, reaching a $\text{SUV}_{25\text{min}} = 0.62 \pm 0.01$, and slightly decreased until 60 min p.i., $\text{SUV}_{60\text{min}} = 0.56 \pm 0.02$ ($n = 3$). Muscle uptake of [^{18}F]PRIMATX, however, demonstrated clear wash out from 10 min, $\text{SUV}_{10\text{min}} = 0.50 \pm 0.02$, to 60 min p.i., $\text{SUV}_{60\text{min}} = 0.30 \pm 0.03$ ($n = 3$).

Notable in this model was the presence of another thyroid tumor placed bilaterally which had upregulated expression of thyroid transcription factor 1 (TTF1), an immunohistochemical marker

of metastasis, a variation which has been shown to possess only little effect on tumor growth or ATX expression.

3.6.2. Radiotracer uptake under baseline vs two blocking conditions

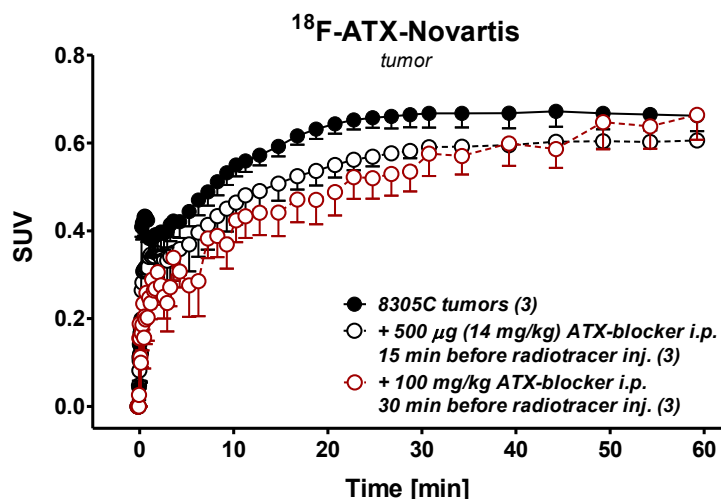
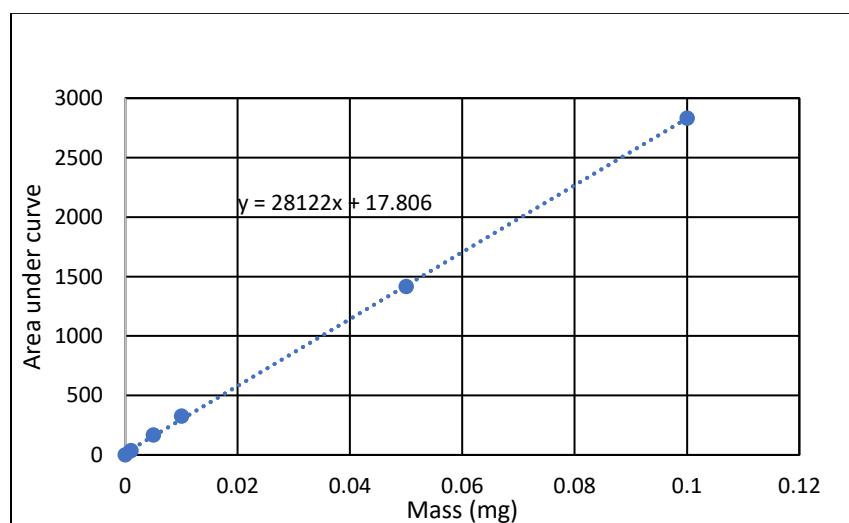


Figure 31. [¹⁸F]PRIMATX radiotracer uptake in the thyroid tumor over the time course of 60 min in the absence and presence of blocking (14 mg/kg i.p. injected or 100 mg/kg i.p. injected 15 min or 30 min, respectively, before radiotracer administration) with a structurally distinct ATX ligand. Data are shown as mean ± SEM from n = 3 dynamic PET experiments each.

Observed blocking results from the PET image-derived TACs show that the 100 mg/kg blocking conditions resulted no further inhibition at 30 min p.i. ($SUV_{30min} = 0.58 \pm 0.05$) than the 14 mg/kg condition ($SUV_{30min} = 0.59 \pm 0.01$).

3.6.3. Molar activity calculations

Molar activity was assessed through the establishment of an HPLC standard curve using varying masses of non-radioactive PRIMATX. For each HPLC run using predetermined masses of $[^{19}\text{F}]$ PRIMATX, corresponding areas under the UV elution peak were recorded. Plotting these data on a graph produced a line equation unique to PRIMATX. During $[^{18}\text{F}]$ PRIMATX HPLC purifications where radioactive mass could not be directly measured, the value of the area under the UV elution peak corresponding to $[^{18}\text{F}]$ PRIMATX was recorded and inserted as the y-component into the $[^{19}\text{F}]$ PRIMATX line equation. The resultant x-value gave the mass of $[^{18}\text{F}]$ PRIMATX present in the elution peak. Thus, dividing the eluted activity by the moles of $[^{18}\text{F}]$ PRIMATX present in the peak gave the molar activity of $[^{18}\text{F}]$ PRIMATX. Supplemental information - graph 2, below, shows the plotted values of the area under the UV peaks versus the mass of non-radioactive PRIMATX injected in the HPLC. Thus, with the line equation $y = 28122x + 17.806$ and a UV peak integration value of 50.18 for a peak where 0.124 GBq were collected, the molar activity of $[^{18}\text{F}]$ PRIMATX in our runs reached 56 GBq/ μmol .



Graph 2. Area under the UV peak versus mass injected to establish an HPLC standard curve.

3.6.4. HPLC traces

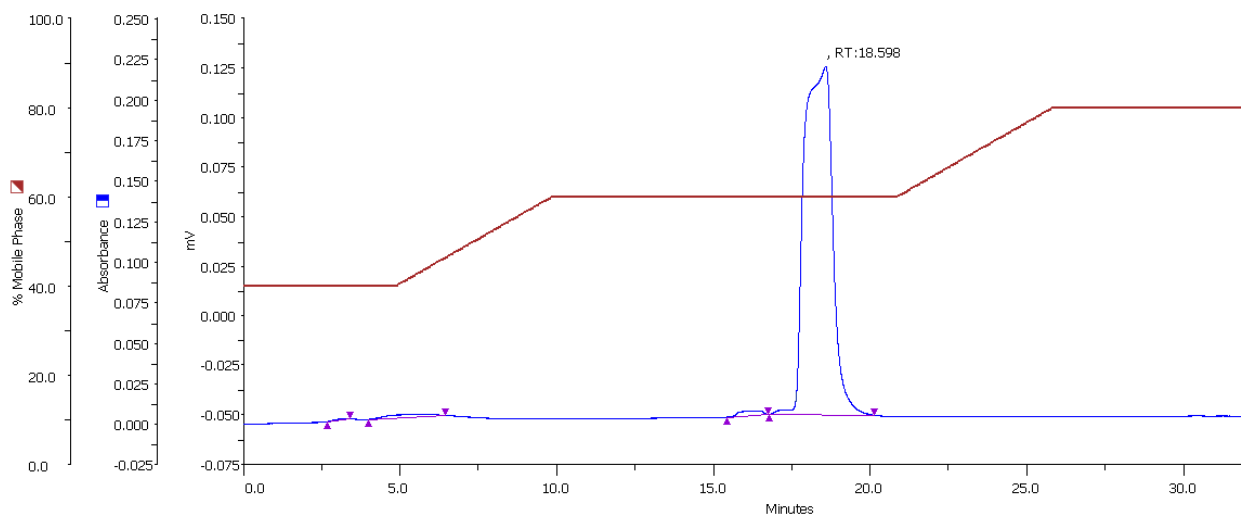


Figure 32. HPLC trace of the $[^{19}\text{F}]$ PRIMATX non-radioactive standard, blue represents the UV-detector signal.

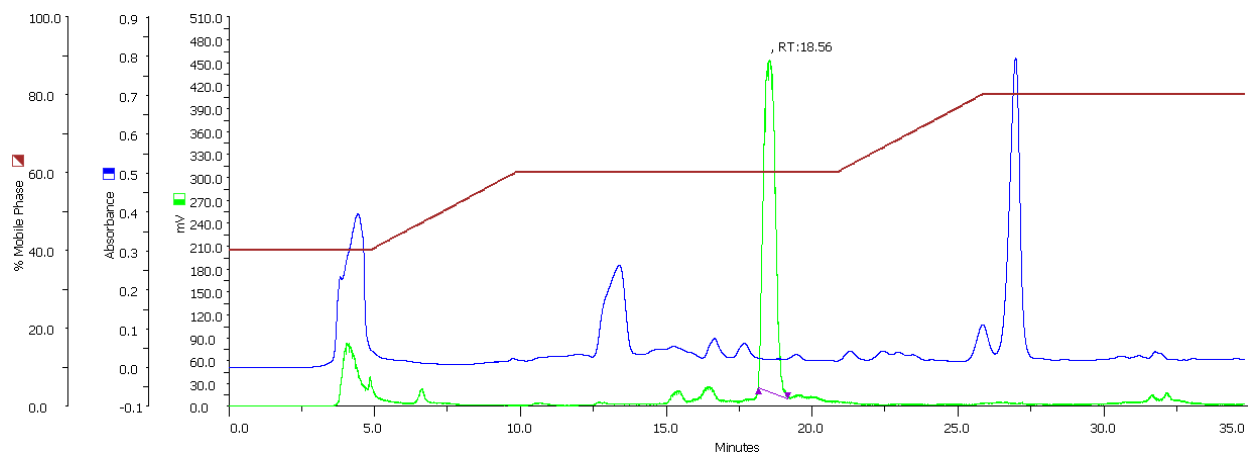


Figure 33. HPLC trace of the $[^{18}\text{F}]$ PRIMATX crude reaction mixture, blue represents the UV-detector signal and green the radio-detector signal.

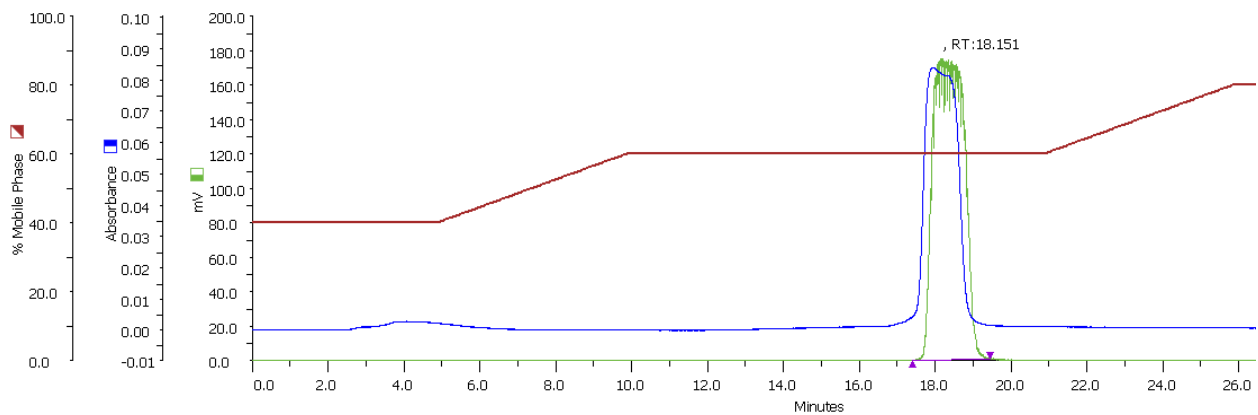


Figure 34. HPLC trace of the purified [^{18}F]PRIMATX radiotracer co-injected with the [^{19}F]PRIMATX non-radioactive standard. Blue represents the UV-detector signal and green, the radio-detector signal.

3.6.5. Radio-TLC traces

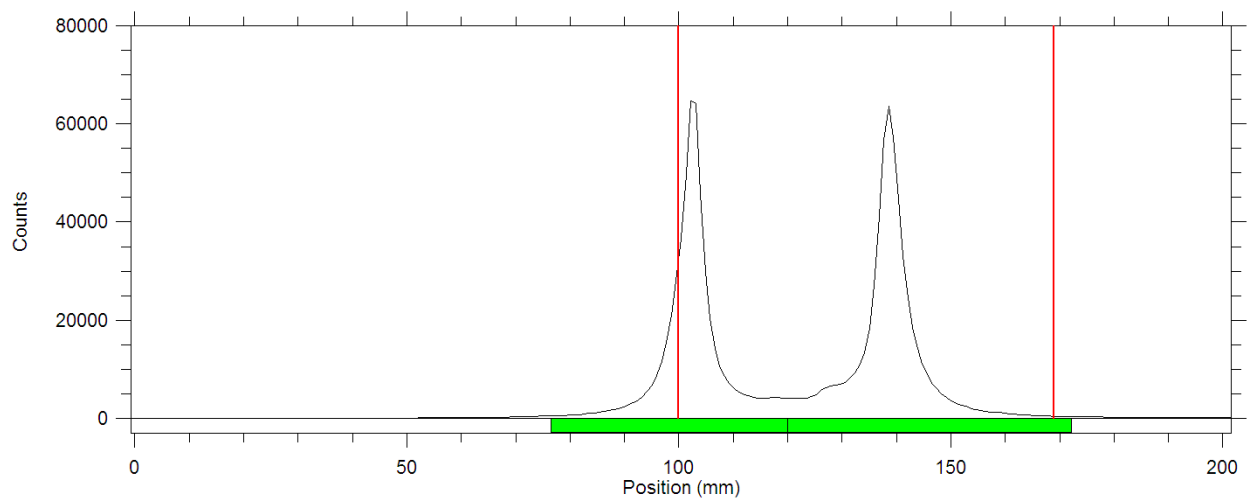


Figure 35. Radio-TLC trace of the [^{18}F]PRIMATX crude reaction mixture.

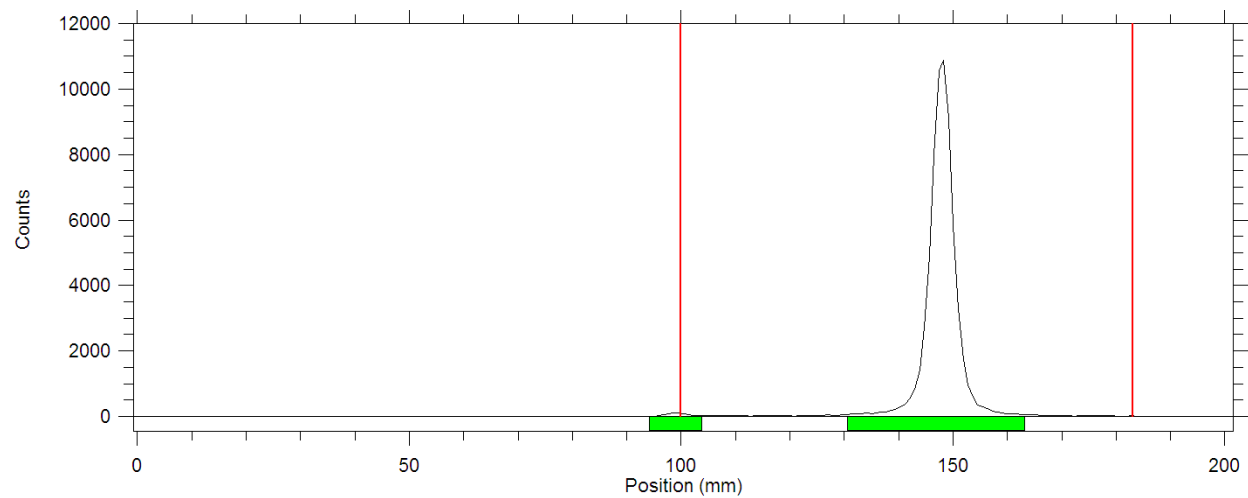


Figure 36. Radio-TLC trace of the purified [^{18}F]PRIMATX radiotracer.

3.7. REFERENCES

- (1) Akira, T.; Kengo, H.; Kenji, F.; Hiroaki, T. Involvement of Lysophospholipase D in the Production of Lysophosphatidic Acid in Rat Plasma. *Biochim. Biophys. Acta (BBA)/Lipids Lipid Metab.* **1986**, *875* (1), 31–38. [https://doi.org/10.1016/0005-2760\(86\)90007-X](https://doi.org/10.1016/0005-2760(86)90007-X).
- (2) Stefan, C.; Jansen, S.; Bollen, M. NPP-Type Ectophosphodiesterases: Unity in Diversity. *Trends Biochem. Sci.* **2005**, *30* (10), 542–550. <https://doi.org/10.1016/j.tibs.2005.08.005>.
- (3) Benesch, M. G. K.; Ko, Y. M.; McMullen, T. P. W.; Brindley, D. N. Autotaxin in the Crosshairs: Taking Aim at Cancer and Other Inflammatory Conditions. *FEBS Lett.* **2014**, *588* (16), 2712–2727. <https://doi.org/10.1016/j.febslet.2014.02.009>.
- (4) Ishii, I.; Fukushima, N.; Ye, X.; Chun, J. Lysophospholipid Receptors: Signaling and Biology. *Annu. Rev. Biochem.* **2004**, *73* (1), 321–354. <https://doi.org/10.1146/annurev.biochem.73.011303.073731>.
- (5) Tanaka, M.; Okudaira, S.; Kishi, Y.; Ohkawa, R.; Iseki, S.; Ota, M.; Noji, S.; Yatomi, Y.; Aoki, J.; Arai, H. Autotaxin Stabilizes Blood Vessels and Is Required for Embryonic Vasculature by Producing Lysophosphatidic Acid. *J. Biol. Chem.* **2006**, *281* (35), 25822–25830. <https://doi.org/10.1074/jbc.M605142200>.
- (6) Lee, H.; Goetzl, E. J.; Songzhu, A. Lysophosphatidic Acid and Sphingosine 1-Phosphate Stimulate Endothelial Cell Wound Healing. *Am. J. Physiol. - Cell Physiol.* **2000**, *278* (3 47-3), 612–618.
- (7) Nochi, H.; Tomura, H.; Tobo, M.; Tanaka, N.; Sato, K.; Shinozaki, T.; Kobayashi, T.; Takagishi, K.; Ohta, H.; Okajima, F.; Tamoto, K. Stimulatory Role of Lysophosphatidic Acid in Cyclooxygenase-2 Induction by Synovial Fluid of Patients with Rheumatoid Arthritis in Fibroblast-like Synovial Cells. *J. Immunol.* **2008**, *181* (7), 511–5119.

<https://doi.org/10.4049/jimmunol.181.7.5111>.

- (8) Orosa, B.; García, S.; Martínez, P.; González, A.; Gómez-Reino, J. J.; Conde, C. Lysophosphatidic Acid Receptor Inhibition as a New Multipronged Treatment for Rheumatoid Arthritis. *Ann. Rheum. Dis.* **2014**, *73* (1), 298–305. <https://doi.org/10.1136/annrheumdis-2012-202832>.
- (9) Vial, C.; Zúñiga, L. M.; Cabello-Verrugio, C.; Cañón, P.; Fadic, R.; Brandan, E. Skeletal Muscle Cells Express the Profibrotic Cytokine Connective Tissue Growth Factor (CTGF/CCN2), Which Induces Their Dedifferentiation. *J. Cell. Physiol.* **2008**, *215* (2), 410–421. <https://doi.org/10.1002/jcp.21324>.
- (10) Euer, N.; Schwirzke, M.; Evtimova, V.; Burtscher, H.; Jarsch, M.; Tarin, D.; Weidle, U. H. Identification of Genes Associated with Metastasis of Mammary Carcinoma in Metastatic versus Non-Metastatic Cell Lines. *Anticancer Res.* **2002**, *22* (2A), 733–740.
- (11) Nikitopoulou, I.; Oikonomou, N.; Karouzakis, E.; Sevastou, I.; Nikolaidou-Katsaridou, N.; Zhao, Z.; Mersinias, V.; Armaka, M.; Xu, Y.; Masu, M.; Mills, G. B.; Gay, S.; Kollias, G.; Aidinis, V. Autotaxin Expression from Synovial Fibroblasts Is Essential for the Pathogenesis of Modeled Arthritis. *J. Exp. Med.* **2012**, *209* (5), 925–933. <https://doi.org/10.1084/jem.20112012>.
- (12) Knowlden, S.; Georas, S. The Autotaxin-LPA Axis Emerges as a Novel Regulator of Lymphocyte Homing and Inflammation. *J. Immunol.* **2014**, *192* (3), 851–857. <https://doi.org/10.1038/mp.2011.182.doi>.
- (13) Benesch, M. G. K.; Tang, X.; Dewald, J.; Dong, W. F.; Mackey, J. R.; Hemmings, D. G.; McMullen, T. P. W.; Brindley, D. N. Tumor-Induced Inflammation in Mammary Adipose Tissue Stimulates a Vicious Cycle of Autotaxin Expression and Breast Cancer Progression.

- FASEB J.* **2015**, *29* (9), 3990–4000. <https://doi.org/10.1096/fj.15-274480>.
- (14) Ikeda, H.; Yatomi, Y. Autotaxin in Liver Fibrosis. *Clin. Chim. Acta* **2012**, *413* (23–24), 1817–1821. <https://doi.org/10.1016/j.cca.2012.07.014>.
- (15) Kanaoka, M.; Yamaguchi, Y.; Komitsu, N.; Feghali-Bostwick, C. A.; Ogawa, M.; Arima, K.; Izuhara, K.; Aihara, M. Pro-Fibrotic Phenotype of Human Skin Fibroblasts Induced by Periostin via Modulating TGF- β Signaling. *J. Dermatol. Sci.* **2018**, *90* (2), 199–208. <https://doi.org/10.1016/j.jdermsci.2018.02.001>.
- (16) Coussens, L. M.; Werb, Z. Inflammation and Cancer. *Nature* **2002**, *420* (December), 406–415. <https://doi.org/10.1016/B978-0-12-374279-7.17002-X>.
- (17) Gun, S. Y.; Lee, S. W. L.; Sieow, J. L.; Wong, S. C. Targeting Immune Cells for Cancer Therapy. *Redox Biol.* **2019**, No. March, 101174. <https://doi.org/10.1016/j.redox.2019.101174>.
- (18) Hussain, S. P.; Hofseth, L. J.; Harris, C. C. Radical Causes of Cancer. *Nat. Rev. Cancer* **2003**, *3* (4), 276–285. <https://doi.org/10.1038/nrc1046>.
- (19) Hanahan, D.; Weinberg, R. A. Hallmarks of Cancer: The next Generation. *Cell* **2011**, *144* (5), 646–674. <https://doi.org/10.1016/j.cell.2011.02.013>.
- (20) Hausmann, J.; Kamtekar, S.; Christodoulou, E.; Day, J. E.; Wu, T.; Fulkerson, Z.; Albers, H. M. H. G.; Van Meeteren, L. A.; Houben, A. J. S.; Van Zeijl, L.; Jansen, S.; Andries, M.; Hall, T.; Pegg, L. E.; Benson, T. E.; Kasiem, M.; Harlos, K.; Kooi, C. W. V.; Smyth, S. S.; Ovaa, H.; Bollen, M.; Morris, A. J.; Moolenaar, W. H.; Perrakis, A. Structural Basis of Substrate Discrimination and Integrin Binding by Autotaxin. *Nat. Struct. Mol. Biol.* **2011**, *18* (2), 198–205. <https://doi.org/10.1038/nsmb.1980>.
- (21) Wu, T.; Kooi, C. Vander; Shah, P.; Charnigo, R.; Huang, C.; Smyth, S. S.; Morris, A. J.

- Integrin-Mediated Cell Surface Recruitment of Autotaxin Promotes Persistent Directional Cell Migration. *FASEB J.* **2014**, *28* (2), 861–870. <https://doi.org/10.1096/fj.13-232868>.
- (22) Stracke, M. L.; Krutzsch, H. C.; Unsworth, E. J.; Arestad, A.; Cioce, V.; Schiffmann, E.; Liotta, L. A. Identification, Purification, and Partial Sequence Analysis of Autotaxin, a Novel Motility-Stimulating Protein. *J. Biol. Chem.* **1992**, *267* (4), 2524–2529.
- (23) Leblanc, R.; Sahay, D.; Houssin, A.; Machuca-Gayet, I.; Peyruchaud, O. Autotaxin- β Interaction with the Cell Surface via Syndecan-4 Impacts on Cancer Cell Proliferation and Metastasis. *Oncotarget* **2018**, *9* (69), 33170–33185. <https://doi.org/10.18632/oncotarget.26039>.
- (24) Fulkerson, Z.; Wu, T.; Sunkara, M.; Kooi, C. Vander; Morris, A. J.; Smyth, S. S. Binding of Autotaxin to Integrins Localizes Lysophosphatidic Acid Production to Platelets and Mammalian Cells. *J. Biol. Chem.* **2011**, *286* (40), 34654–34663. <https://doi.org/10.1074/jbc.M111.276725>.
- (25) Benesch, M. G. K.; Ko, Y. M.; Tang, X.; Dewald, J.; Lopez-Campistrous, A.; Zhao, Y. Y.; Lai, R.; Curtis, J. M.; Brindley, D. N.; McMullen, T. P. W. Autotaxin Is an Inflammatory Mediator and Therapeutic Target in Thyroid Cancer. *Endocr. Relat. Cancer* **2015**, *22* (4), 593–607. <https://doi.org/10.1530/ERC-15-0045>.
- (26) Desroy, N.; Housseman, C.; Bock, X.; Joncour, A.; Bienvenu, N.; Cherel, L.; Labeguere, V.; Rondet, E.; Peixoto, C.; Grassot, J. M.; Picolet, O.; Annoot, D.; Triballeau, N.; Monjardet, A.; Wakselman, E.; Roncoroni, V.; Le Tallec, S.; Blanque, R.; Cottreaux, C.; Vandervoort, N.; Christophe, T.; Mollat, P.; Lamers, M.; Auberval, M.; Hrvacic, B.; Ralic, J.; Oste, L.; Van der Aar, E.; Brys, R.; Heckmann, B. Discovery of 2-[[2-Ethyl-6-[4-[2-(3-Hydroxyazetididin-1-Yl)-2-Oxoethyl]Piperazin-1-Yl]-8-Methylimidazo[1,2-a]Pyridin-3-

- Yl]Methylamino]-4-(4-Fluorophenyl)Thiazole-5-Carbonitrile (GLPG1690), a First-in-Class Autotaxin Inhibitor Undergoing Clinical Evaluation . *J. Med. Chem.* **2017**, *60* (9), 3580–3590. <https://doi.org/10.1021/acs.jmedchem.7b00032>.
- (27) Ye, X.; Hama, K.; Contos, J. J. A.; Anliker, B.; Inoue, A.; Skinner, M. K.; Suzuki, H.; Amane, T.; Kennedy, G.; Arai, H.; Aoki, J.; Chun, J. LPA3-Mediated Lysophosphatitic Acid Signalling in Embryo Implantation and Spacing. *Lett. to Nat.* **2005**, *435* (May), 104–108.
- (28) Aikawa, S.; Kano, K.; Inoue, A.; Wang, J.; Saigusa, D.; Nagamatsu, T.; Hirota, Y.; Fujii, T.; Tsuchiya, S.; Taketomi, Y. Autotaxin – Lysophosphatidic Acid – LPA 3 Signaling at the Embryo-Epithelial Boundary Controls Decidualization Pathways. **2017**, *36* (14), 2146–2160. <https://doi.org/10.15252/emj.201696290>.
- (29) Dubois, R. N.; Abramson, S. B.; Crofford, L.; Gupta, R. A.; Simon, L. S.; Van De Putte, L. B.; Lipsky, P. E. Cyclooxygenase in Biology and Disease. *FASEB J.* **1998**, *12* (12), 1063–1073. <https://doi.org/9737710>.
- (30) Ghosh, N.; Chaki, R.; Mandal, V.; Mandal, S. C. COX-2 as a Target for Cancer Chemotherapy. *Pharmacol. Reports* **2010**, *62* (2), 233–244. [https://doi.org/10.1016/S1734-1140\(10\)70262-0](https://doi.org/10.1016/S1734-1140(10)70262-0).
- (31) Wang, S.; Gao, H.; Zuo, J.; Gao, Z. Cyclooxygenase-2 Expression Correlates with Development, Progression, Metastasis, and Prognosis of Osteosarcoma: A Meta-Analysis and Trial Sequential Analysis. *FEBS Open Bio* **2019**, *9* (2), 226–240. <https://doi.org/10.1002/2211-5463.12560>.
- (32) Zhang, Q.; Han, Z.; Tao, J.; Zhang, W.; Li, P.; Tang, L.; Gu, Y. A Novel Near-Infrared Fluorescent Probe for Monitoring Cyclooxygenase-2 in Inflammation and Tumor. *J.*

- Biophotonics* **2018**, *11* (6), 1–9. <https://doi.org/10.1002/jbio.201700339>.
- (33) Tietz, O.; Kaur, J.; Bhardwaj, A.; Wuest, F. R. Pyrimidine-Based Fluorescent COX-2 Inhibitors: Synthesis and Biological Evaluation. *Org. Biomol. Chem.* **2016**, *14* (30), 7250–7257. <https://doi.org/10.1039/C6OB00493H>.
- (34) Tietz, O.; Wuest, M.; Marshall, A.; Glubrecht, D.; Hamann, I.; Wang, M.; Bergman, C.; Way, J. D.; Wuest, F. PET Imaging of Cyclooxygenase-2 (COX-2) in a Pre-Clinical Colorectal Cancer Model. *EJNMMI Res.* **2016**, *6* (1). <https://doi.org/10.1186/s13550-016-0192-9>.
- (35) Uddin, M. J.; Crews, B. C.; Ghebreselasie, K.; Huda, I.; Kingsley, P. J.; Ansari, M. S.; Tantawy, M. N.; Reese, J.; Marnett, L. J. Fluorinated COX-2 Inhibitors as Agents in PET Imaging of Inflammation and Cancer. *Cancer Prev. Res.* **2011**, *4* (10), 1536–1545. <https://doi.org/10.1158/1940-6207.CAPR-11-0120>.
- (36) Uddin, M. J.; Crews, B. C.; Ghebreselasie, K.; Tantawy, M. N.; Marnett, L. J. [123I]-Celecoxib Analogues as SPECT Tracers of Cyclooxygenase-2 in Inflammation. *ACS Med. Chem. Lett.* **2011**, *2* (2), 160–164. <https://doi.org/10.1021/ml100232q>.
- (37) Joncour, A.; Desroy, N.; Housseman, C.; Bock, X.; Bienvenu, N.; Cherel, L.; Labeguere, V.; Peixoto, C.; Annoot, D.; Lepissier, L.; Heiermann, J.; Hengeveld, W. J.; Pilzak, G.; Monjardet, A.; Wakselman, E.; Roncoroni, V.; Le Tallec, S.; Galien, R.; David, C.; Vandervoort, N.; Christophe, T.; Conrath, K.; Jans, M.; Wohlkonig, A.; Soror, S.; Steyaert, J.; Touitou, R.; Fleury, D.; Vercheval, L.; Mollat, P.; Triballeau, N.; Van Der Aar, E.; Brys, R.; Heckmann, B. Discovery, Structure-Activity Relationship, and Binding Mode of an Imidazo[1,2-a]Pyridine Series of Autotaxin Inhibitors. *J. Med. Chem.* **2017**, *60* (17), 7371–7392. <https://doi.org/10.1021/acs.jmedchem.7b00647>.

- (38) Rosse, G. Benzyl-Methyl-Tetrazole Ligands of Autotaxin for PET Imaging Techniques and Diagnostic. *ACS Med. Chem. Lett.* **2016**, *7* (12), 1016–1017. <https://doi.org/10.1021/acsmedchemlett.6b00408>.
- (39) Briard, E.; Joshi, A. D.; Shanmukhappa, S.; Ilovich, O.; Auberson, Y. P. [18 F]PRIMATX, a New Positron Emission Tomography Tracer for Imaging of Autotaxin in Lung Tissue and Tumor-bearing Mice. *ChemMedChem* **2019**, *14* (16), 1493–1502. <https://doi.org/10.1002/cmdc.201900297>.
- (40) Wilson, A. A.; Jin, L.; Garcia, A.; Dasilva, J. N.; Houle, S. An Admonition When Measuring the Lipophilicity of Radiotracers Using Counting Techniques. **2001**, *54*, 203–208.
- (41) Madan, D.; Ferguson, C. G.; Lee, W. Y.; Prestwich, G. D.; Testa, C. A. Non-Invasive Imaging of Tumors by Monitoring Autotaxin Activity Using an Enzyme-Activated near-Infrared Fluorogenic Substrate. *PLoS One* **2013**, *8* (11). <https://doi.org/10.1371/journal.pone.0079065>.
- (42) Reich, R.; Hoffman, A.; Suresh, R. R.; Shai, O.; Frant, J.; Maresca, A.; Supuran, C. T.; Breuer, E. Carbamoylphosphonates Inhibit Autotaxin and Metastasis Formation *in Vivo*. *J. Enzyme Inhib. Med. Chem.* **2015**, *30* (5), 767–772. <https://doi.org/10.3109/14756366.2014.968146>.
- (43) Leblanc, R.; Houssin, A.; Peyruchaud, O. Platelets, Autotaxin and Lysophosphatidic Acid Signalling: Win-Win Factors for Cancer Metastasis. *Br. J. Pharmacol.* **2018**, *175* (15), 3100–3110. <https://doi.org/10.1111/bph.14362>.
- (44) Kazmi, F.; Hensley, T.; Pope, C.; Funk, R. S.; Loewen, G. J.; Buckley, D. B.; Parkinson, A. Lysosomal Sequestration (Trapping) of Lipophilic Amine (Cationic Amphiphilic) Drugs in Immortalized Human Hepatocytes (Fa2N-4 Cells). *Drug Metab. Dispos.* **2013**, *41* (4), 897–

905. <https://doi.org/10.1124/dmd.112.050054>.
- (45) Schmid, R.; Wolf, K.; Robering, J. W.; Strauß, S.; Strissel, P. L.; Strick, R.; Rübner, M.; Fasching, P. A.; Horch, R. E.; Kremer, A. E.; Boos, A. M.; Weigand, A. ADSCs and Adipocytes Are the Main Producers in the Autotaxin-Lysophosphatidic Acid Axis of Breast Cancer and Healthy Mammary Tissue *in Vitro*. *BMC Cancer* **2018**, *18* (1), 1–11. <https://doi.org/10.1186/s12885-018-5166-z>.
- (46) Giganti, A.; Rodriguez, M.; Fould, B.; Moulharat, N.; Coge, F.; Chomarat, P.; Galizzi, J. P.; Valet, P.; Saulnier-Blache, J. S.; Boutin, J. A.; Ferry, G. Murine and Human Autotaxin α , β , and γ Isoforms: Gene Organization, Tissue Distribution, and Biochemical Characterization. *J. Biol. Chem.* **2008**, *283* (12), 7776–7789. <https://doi.org/10.1074/jbc.M708705200>.
- (47) Nishioka, T.; Arima, N.; Kano, K.; Hama, K.; Itai, E.; Yukiura, H.; Kise, R.; Inoue, A.; Kim, S. H.; Solnica-Krezel, L.; Moolenaar, W. H.; Chun, J.; Aoki, J. ATX-LPA 1 Axis Contributes to Proliferation of Chondrocytes by Regulating Fibronectin Assembly Leading to Proper Cartilage Formation. *Sci. Rep.* **2016**, *6* (March), 1–15. <https://doi.org/10.1038/srep23433>.
- (48) Kawagoe, H.; Stracke, M. L.; Nakamura, H.; Sano, K. Expression and Transcriptional Regulation of the PD-1 α /Autotaxin Gene in Neuroblastoma. *Cancer Res.* **1997**, *57* (12), 2516–2521.
- (49) Hoelzinger, D. B.; Nakada, M.; Demuth, T.; Rosensteel, T.; Reavie, L. B.; Berens, M. E. Autotaxin: A Secreted Autocrine/Paracrine Factor That Promotes Glioma Invasion. *J. Neurooncol.* **2008**, *86* (3), 297–309. <https://doi.org/10.1007/s11060-007-9480-6>.
- (50) Herr, D. R.; Chew, W. S.; Satish, R. L.; Ong, W.-Y. Pleotropic Roles of Autotaxin in the

Nervous System Present Opportunities for the Development of Novel Therapeutics for Neurological Diseases. *Mol. Neurobiol.* **2019**. [https://doi.org/10.1007/s12035-019-01719-](https://doi.org/10.1007/s12035-019-01719-1)

1.

CHAPTER 4

***In vivo* imaging of autotaxin in a thyroid tumor model using [¹⁸F]F-GLPG1690**

4.1. INTRODUCTION

GLPG1690, a small molecule autotaxin (ATX) inhibitor mentioned in the introduction and in chapter 3, is actively undergoing clinical trials as its efficacy and safety profile are being tested.¹ As GLPG1690 is the only ATX inhibitor even remotely close to being approved by the FDA, it would be ideal for any attempt at molecular imaging of ATX to be made using this inhibitor. This alone makes it an ideal choice to be converted into a molecular probe. However, it has also been suggested that because GLPG1690 binds ATX using both the hydrophobic pocket and the hydrophobic channel, and does not interact with the zinc ions at the active site, it may have an advantage over other ATX inhibitors.² Thus, with the goal of developing a non-invasive *in vivo* ATX PET imaging assay, we set out to convert GLPG1690 into a molecular probe and validate its imaging capabilities *in vivo*.

4.2. MATERIALS AND METHODS

4.2.1. General

All chemicals, reagents, and solvents for synthesis and analysis were analytical grade. Chromafix (30-PS-HCO₃, Macherey-Nagel) cartridges were purchased from ABX. All other chemicals and solvents were purchased from Sigma Aldrich. All solvents were dried and/or distilled prior to utilization. Thin-layer chromatography (TLC) was carried out using HF254 silica gel. Radio-TLC analysis was performed on a Bioscan radio-TLC reader and Winscan analysis software. High-performance liquid chromatography (HPLC) purification and analysis were performed using a Luna 5 μ m Carbon-18 (C-18) column on a Gilson 322 Pump module fitted with a 171 Diode Array and a radioactivity detector. The following elution profile was used: 0-5 min, isocratic elution with 40% CH₃CN/H₂O; 5-12 min 40% CH₃CN/H₂O to 70% CH₃CN/H₂O; 12-21 min isocratic elution

with 70% CH₃CN/H₂O; 21-26 min 70% CH₃CN/H₂O to 80% CH₃CN/H₂O; 26-35 min isocratic elution with 80% CH₃CN/H₂O.

¹H-NMR and ¹³C-NMR spectra were recorded on an Agilent/Varian Inova two-channel 400 MHz spectrometer, an Agilent/Varian Inova four-channel 500 MHz spectrometer, and an Agilent/Varian VNMRS three-channel 600 MHz spectrometer. Chemical shifts are given in ppm referenced to internal standards (s = singlet, d = doublet). High-resolution mass spectrometry (HR-MS) was carried out on an Agilent Technologies 6220 oaTOF.

4.2.2. Chemistry

1-(2-(4-(3-((5-cyano-4-(4-fluorophenyl)thiazol-2-yl)(methyl)amino)-2-ethyl-8-methylimidazo[1,2-a]pyridin-6-yl)piperazin-1-yl)acetyl)azetidin-3-yl 4-nitrobenzenesulfonate **2**.

Labeling precursor **2** for radiofluorination reaction was prepared through the addition of a nosylate leaving group as per the literature.³ 2-[[2-Ethyl-6-[4-[2-(3-hydroxyazetidin-1-yl)-2-oxoethyl]-piperazin-1-yl]-8-methylimidazo[1,2-a]pyridin-3-yl]-methylamino]-4-(4-fluorophenyl)thiazole-5-carbonitril **1** (0.15 mmol) was dissolved in dry methylene chloride (DCM) in a 5 mL round bottom flask (RBF). 4-nitrobenzenesulfonyl chloride (nosyl chloride; 0.167 mmol) and triethyl amine (TEA; 0.466 mmol) were added to the RBF and the reaction was stirred for 12 hours hours, extracted with a 0.1N NaOH solution, and purified by column chromatography (0-15% Methanol in DCM) to give 1-(2-(4-(3-((5-cyano-4-(4-fluorophenyl)thiazol-2-yl)(methyl)amino)-2-ethyl-8-methylimidazo[1,2-a]pyridin-6-yl)piperazin-1-yl)acetyl)azetidin-3-yl 4-nitrobenzenesulfonate, **2**, in 92% yield as a reddish-brown solid. ¹H-NMR (CDCl₃, 600 MHz): δ 1.34 (t, J = 7.5 Hz, 3H, CH₂CH₃), 2.62 (s, 3H, NCH₃), 2.65 (t, 4H, (CH₂)₂ of piperazine), 2.76 (qd, J = 7.5 Hz, 2H, CH₂CH₃), 3.07 (m, 4H, (CH₂)₂ of piperazine), 3.11 (d, J = 1.5 Hz, 2H, NCOCH₂N), 3.63 (s, 3H, CH₃ of imidazo-pyridine), 4.04 (m, 1H, from azetidine CH₂), 4.29 (m, 1H, from azetidine CH₂),

4.41 (m, 1H, from azetidine CH_2), 4.61 (m, 1H, from azetidine CH_2), 5.15 (m, 1H, CHO of azetidine), 6.99 (d, $J = 3.8$ Hz, 2H, Ar- H), 7.19 (td, $J = 8.7$ Hz, 1.9 Hz, 2H, Ar- H), 8.12 (dd, $J = 8.7$ Hz, 5.7 Hz, 2H, Ar- H), 8.18 (m, 2H, Ar- H), 8.43 (dd, $J = 9$ Hz, 4.5 Hz, 1H, Ar- H); HR-MS analysis, calculated for $\text{C}_{36}\text{H}_{36}\text{FN}_9\text{O}_6\text{S}_2$ $[\text{M} + \text{H}]^+$ m/z 774.2287, found 774.2283.

2-((2-ethyl-6-(4-(2-(3-fluoroazetidin-1-yl)-2-oxoethyl)piperazin-1-yl)-8-methylimidazo[1,2-a]pyridin-3-yl)(methyl)amino)-4-(4-fluorophenyl)thiazole-5-carbonitrile **3**. Non-radioactive standard **3** was prepared through the replacement of the hydroxyl group with a fluorine using diethylaminosulfur trifluoride (DAST) as per the literature.⁴ 2-[[2-Ethyl-6-[4-[2-(3-hydroxyazetidin-1-yl)-2-oxoethyl]-piperazin-1-yl]-8-methylimidazo[1,2-a]pyridin-3-yl]-methylamino]-4-(4-fluorophenyl)thiazole-5-carbonitril **1** (0.068 mmol) was added to 1.86 mL of dry DCM in a 5 mL RBF and stirred at 0°C until fully dissolved. DAST (0.102 mmol) was then added to the RBF and reaction was stirred at 0°C for 1 hour, extracted with NaCO_3 and purified by column chromatography (0-15% Methanol in DCM) to give 2-((2-ethyl-6-(4-(2-(3-fluoroazetidin-1-yl)-2-oxoethyl)piperazin-1-yl)-8-methylimidazo[1,2-a]pyridin-3-yl)(methyl)amino)-4-(4-fluorophenyl)thiazole-5-carbonitrile, **3**, in 60% yield as a reddish solid. $^1\text{H-NMR}$ (CDCl_3 , 600 MHz): δ 1.34 (t, $J = 7.7$ Hz, 3H, CH_2CH_3), 2.61 (s, 3H, NCH_3), 2.68 (t, $J = 4.5$ Hz, 4H, $(\text{CH}_2)_2$ of piperazine), 2.76 (qd, $J = 7.6$ Hz, 2.1 Hz, 2H, CH_2CH_3), 3.09 (t, $J = 4.9$ Hz, 4H, $(\text{CH}_2)_2$ of piperazine), 3.13 (m, 2H, NCOCH_2N), 3.62 (s, 3H, CH_3 of imidazo-pyridine), 4.15 (m, 1H, from azetidine CH_2), 4.34 (m, 2H, from azetidine CH_2), 4.52 (m, 1H, from azetidine CH_2), 5.24-5.38 (m, $J_F = 56.8$ Hz, 1H, CHF of azetidine), 6.99 (s, 2H, Ar- H), 7.19 (m, 2H, Ar- H), 8.18 (m, 2H, Ar- H); HR-MS analysis, calculated for $\text{C}_{30}\text{H}_{32}\text{F}_2\text{N}_8\text{NaOS}$ $[\text{M} + \text{Na}]^+$ m/z 613.228, found 613.228.

4.2.3. Radiochemistry

[¹⁸F]Fluoride was produced by the ¹⁸O(p,n)¹⁸F nuclear reaction through proton irradiation of enriched (98%) ¹⁸O water (3.0 ml, Rotem, Germany) using a TR19/9 cyclotron (Advanced Cyclotron Systems, Inc., Richmond, BC, Canada).

The synthesis of 2-((2-ethyl-6-(4-(2-(3-(fluoro-¹⁸F)azetidin-1-yl)-2-oxoethyl)piperazin-1-yl)-8-methylimidazo[1,2-a]pyridin-3-yl)(methyl)amino)-4-(4-fluorophenyl)thiazole-5-carbonitrile

[¹⁸F]**3**, or [¹⁸F]F-GLPG1690, was performed using nucleophilic radio-fluorination methods.

Potassium Kryptofix (K₂CO₃/K₂₂₂) was used to elute no-carrier-added [¹⁸F]fluoride off of a QMA (Waters Sep-Pak QMA plus Light) cartridge into a drying vial which was dried under nitrogen gas at 95 °C. Dried ¹⁸[F]Fluoride was resuspended in Acetonitrile (~0.1 mL) and was transferred to a

new reaction vial containing 1-(2-(4-(3-((5-cyano-4-(4-fluorophenyl)thiazol-2-yl)(methyl)amino)-2-ethyl-8-methylimidazo[1,2-a]pyridin-6-yl)piperazin-1-yl)acetyl)azetidin-3-yl 4-nitrobenzenesulfonate **2** (3 mg, 3.9 μmol) in t-BuOH (0.25 mL). The whole mixture was reacted at 125 °C for 5 min under nitrogen to produce [¹⁸F]F-GLPG1690, or [¹⁸F]**3**. HPLC purification with a Luna 5 μm Carbon-18 (C-18) was used to isolate the radioactive compound [¹⁸F]F-GLPG1690 eluting at a retention time of 20.2 min (in 70% acetonitrile: 30% water), in radiochemical yields of 30 ± 5% (n = 2). Normal-phase radio-TLC (14% MeOH in DCM, R_f = ~0.7) using a Bioscan radio-TLC reader and Winscan analysis software was performed to verify radiochemical purity greater than 92%.

The HPLC solvent was removed under vacuum and the compound was resuspended in a solution of 5% ethanol in saline.

4.2.4. Animal model

All animal experiments were performed according to guidelines from the Canadian Council on Animal Care (CCAC) and approved by the local animal care committee (Cross Cancer Institute, University of Alberta).

PET experiments were performed using 8305C thyroid tumor-bearing male NSG mice (Dr. Lynn Postovit, Dept. of Oncology, University of Alberta). Male NSG mice were housed under standard conditions with free access to standard food and tap water. 8305C cells (5×10^6 cells in 200 μ L of PBS) were injected subcutaneously into the upper left flank of male NSG mice. After 18 to 21 (8305C tumors) days growth, tumors were suitable for all *in vivo* experiments.

4.2.5. PET imaging

8305C thyroid tumor-bearing male NSG mice were immobilized in prone position into the center field of view of an Inveon® PET/CT scanner (Siemens Preclinical Solutions, Knoxville, TN, USA) with isoflurane anesthesia in 40% oxygen/60% nitrogen (gas flow= 1 mL/min). The body temperature was kept constant at 37°C for the entire experiment. For PET experiments, 3–8 MBq of [¹⁸F]F-GLPG1690 in ~150 μ L of solution (5% EtOH/saline) was administered intravenously as a bolus injection into the tail vein via a preplaced catheter. PET data was collected in 3D list mode over 60 min. Dynamic list mode data were sorted into sinograms with 54 time frames (10x2 s, 8x5 s, 6x10 s, 6x20 s, 8x60 s, 10x120 s, 5x300 s). Frames were reconstructed using Ordered Subset Expectation Maximization (OSEM) or maximum a posteriori (MAP) reconstruction modes.

No correction for partial volume effects was performed. Image files were further processed using ROVER v2.0.51 software (ABX GmbH, Radeberg, Germany). Masks defining 3D regions of interest (ROI) were set and defined by 50% thresholding. Mean standardized uptake values [$SUV_{mean} = (\text{activity/mL tissue})/(\text{injected activity/body weight}), \text{mL/g}$] were calculated for each

region of interest (ROI) with a threshold defined at 50% of radioactivity uptake. The time-activity curves (TACs) were generated using GraphPad Prism 4.0 (GraphPad Software, La Jolla, CA, USA). All semi-quantified PET data are presented as means \pm SEM from n experiments.

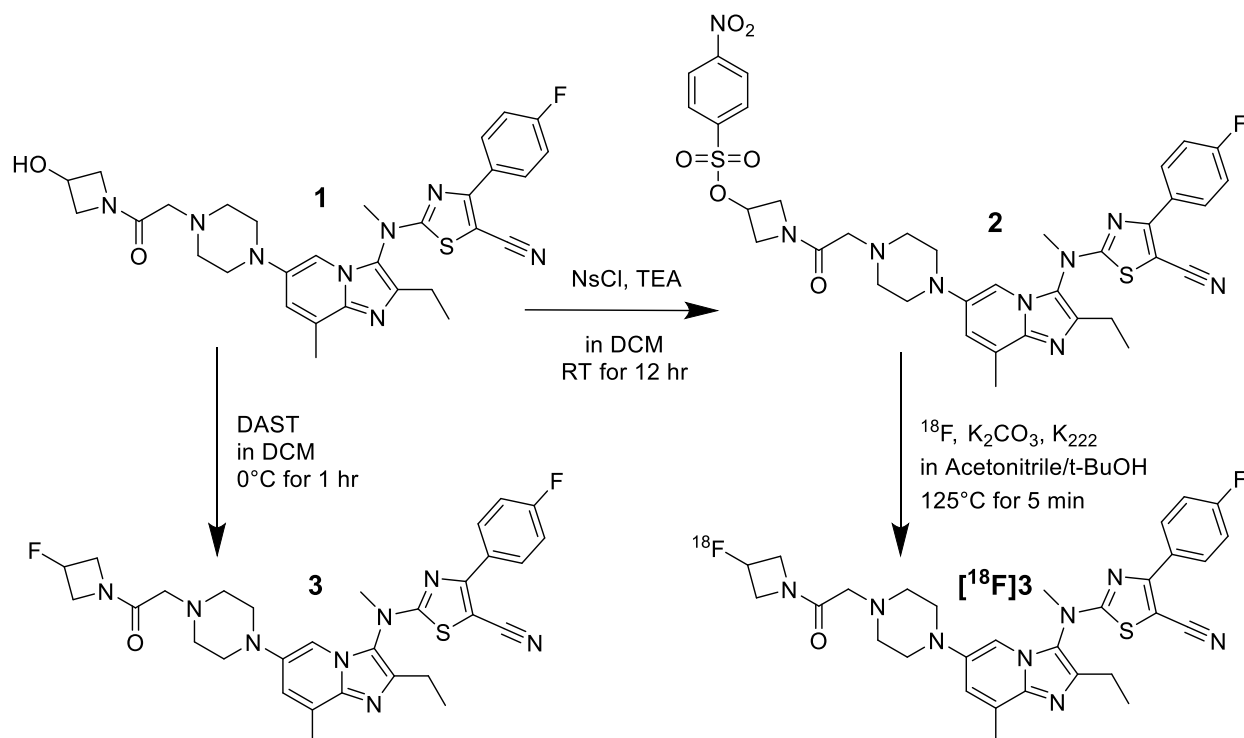
4.2.6. Statistical analysis

All *in vitro* and *in vivo* data are expressed as means \pm SEM. Graphs were constructed using GraphPad Prism 5.0 (GraphPad Software). Where applicable, statistical differences were tested using unpaired Student's t-test and were considered significant for $P < 0.05$.

4.3. RESULTS

4.3.1. Chemistry

The synthesis of reference compound **3** and radiochemical precursor **2** is given in Scheme 5.



Scheme 5. Fluorination of GLPG1690 by DAST to produce non-radioactive standard (**left arrow**). Replacement of a hydroxy group with a nosylate leaving group to produce the labelling precursor (**middle arrow**). Radiofluorination of nosylated precursor to produce radiotracer $[^{18}\text{F}]\text{F}$ -GLPG1690 $[^{18}\text{F}]\text{3}$.

Reference compound 2-((2-ethyl-6-(4-(2-(3-fluoroazetidin-1-yl)-2-oxoethyl)piperazin-1-yl)-8-methylimidazo[1,2-a]pyridin-3-yl)(methylamino)-4-(4-fluorophenyl)thiazole-5-carbonitrile **3** was prepared in 60% chemical yield starting from 2-[[2-Ethyl-6-[4-[2-(3-hydroxyazetidin-1-yl)-2-oxoethyl]-piperazin-1-yl]-8-methylimidazo[1,2-a]pyridin-3-yl]-methylamino]-4-(4-

fluorophenyl)thiazole-5-carbonitril **1** through the use of DAST according to published procedures.⁴ The labelling precursor 1-(2-(4-(3-((5-cyano-4-(4-fluorophenyl)thiazol-2-yl)(methyl)amino)-2-ethyl-8-methylimidazo[1,2-a]pyridin-6-yl)piperazin-1-yl)acetyl)azetidin-3-yl 4-nitrobenzenesulfonate **2** was synthesized with a yield of 92% through the conversion of the alcohol of **1** to a nosyl chloride by published methods.³

4.3.2. Radiochemistry

Synthesis of 2-((2-ethyl-6-(4-(2-(3-(fluoro-¹⁸F)azetidin-1-yl)-2-oxoethyl)piperazin-1-yl)-8-methylimidazo[1,2-a]pyridin-3-yl)(methyl)amino)-4-(4-fluorophenyl)thiazole-5-carbonitrile [¹⁸F]**3** ([¹⁸F]F-GLPG1690) was accomplished using nucleophilic radio-fluorination chemistry, as seen in scheme 5. Reaction of no-carrier-added [¹⁸F]fluoride with nosylate-carrying precursor **2** in t-BuOH and acetonitrile at 125 °C for 5 min afforded radiotracer [¹⁸F]F-GLPG1690 in radiochemical yields of 30 ± 5% (*n* = 2). The total synthesis time was 60 minutes including HPLC purification.

4.3.3. PET imaging in human thyroid 8305C tumor-bearing mice

A representative MIP PET image of 8305C tumor-bearing mice at 60 min p.i. of [^{18}F]F-GLPG1690 and the respective time-activity curves of tumor and muscle uptake over time are shown in Figure 37.

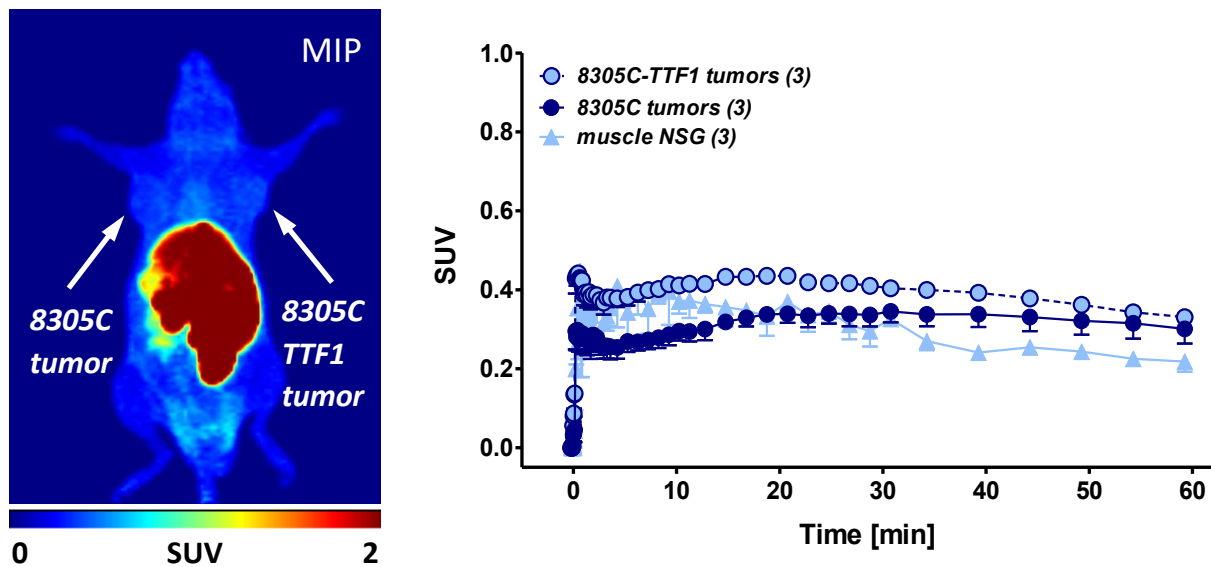


Figure 37. PET image (maximum- intensity projection - MIP) of a 8305C and 8305C-TTF1 tumor-bearing NSG mouse 60 min p.i. of [^{18}F]F-GLPG1690 (**left**). Time-activity curves for tumor and muscle uptake of [^{18}F]F-GLPG1690 over 60 min p.i. (**right**). Data are shown as mean \pm SEM from $n = 3$ dynamic PET experiments.

The uptake of [^{18}F]F-GLPG1690 was analyzed in 8305C tumors and left femoris muscles as reference tissue. Accumulation of the radiotracer in ATX producing tumors was not clearly visible. The uptake of radiotracer into the tumor was relatively low, only reaching a $\text{SUV}_{60\text{min}} = 0.31 \pm 0.04$ ($n = 3$) with a muscle uptake reaching a $\text{SUV}_{60\text{min}} = 0.22 \pm 0.04$ ($n = 3$). Clearance of [^{18}F]F-GLPG1690 was mainly observed through the hepatobiliary pathway.

4.4. DISCUSSION

The development of molecular probes targeting ATX *in vivo* is a relatively new field, with just two published structures to consider. One, a near-IR fluorescent probe called AR-2, made up of a fluorophore linked to a quencher by a lipid and choline linker, the other, an ^{18}F -labelled small molecule inhibitor of ATX, called [^{18}F]PRIMATX, developed for PET imaging by Novartis.^{5,6} Although the fluorescent probe has been available for several years, it has seen very little subsequent use in the literature.⁷ Whether this is due to its performance *in vivo*, its inherent depth limitations, or some other factor, is unknown. [^{18}F]PRIMATX, on the other hand, is relatively new but already showing some promise in the imaging of ATX in melanoma tumors.⁶ Despite the initial promising results, [^{18}F]PRIMATX is relatively untested and a need still exists for the development of additional molecular probes to detect ATX *in vivo*.

The goal of this work was to develop and validate an alternative PET radiotracer, [^{18}F]F-GLPG1690, which could selectively and reliably determine ATX expression levels in and around thyroid tumors. The original compound GLPG1690, developed by Galapagos NV, is in phase III clinical trials for the treatment of idiopathic pulmonary fibrosis and may be available on the market within the next few years.¹ The conceivable market availability of this ATX inhibitor makes GLPG1690 an attractive option for use as a PET radiotracer.

In deciding how to radiolabel the GLPG1690 molecule, there seemed 2 apparent options: replace the existing fluorine from the *p*-fluorophenyl group or replace the hydroxyl from the 3-hydroxyazetidine moiety. In the end, replacement of the hydroxyl made more immediate sense given that we possessed a limited mass with which to work and that this route was the more straight-forward of the two. Therefore, we converted the model compound into a radiolabelling precursor by replacing the hydroxyl with a 4-nitrobenzenesulfonate (nosylate) leaving group.

Subsequent nucleophilic radiofluorination with no-carrier-added [^{18}F]fluoride produced the radiotracer [^{18}F]F-GLPG1690 in decay-corrected yields of 30%.

As ATX is a secreted enzyme, suitable *in vitro* work for the validation of [^{18}F]F-GLPG1690 was not apparent. Thus, we proceeded to the pre-clinical *in vivo* PET imaging of 8305C human thyroid cancer as the next step in validating the radiotracer. Despite the greatly up-regulated ATX levels present in the intercellular area of thyroid tumors, [^{18}F]F-GLPG1690 was not readily taken up over the 60 min time course. Relatively similar radiotracer uptake was seen in both tumors and reference muscle, making it difficult to distinguish the tumor from the surrounding tissue. The vast majority of uptake was seen in organs related to the radiotracer's hepatobiliary clearance profile, such as the intestines.

When compared to the uptake and image quality achieved by [^{18}F]PRIMATX in melanoma tumors, [^{18}F]F-GLPG1690 clearly appears to be inferior, to the point where one may question whether it still binds ATX after the modifications made to its structure.⁶ It may be that the conversion of the hydroxyl to a fluorine altered its binding affinity such that stable binding is no longer favorable. This may be supported by docking studies of GLPG1690 bound to ATX published by Desroy et al, 2017.¹ While the hydrophobic pocket is represented as hydrophobic in the computer-derived docking image, the so-called hydrophobic channel seems to contain a large quantity of hydrophilic surfaces, especially deeper into the channel where the hydroxyl group customarily sits. It may be that the loss of the hydroxyl, followed by the gain of the much less hydrophilic fluorine resulted in the loss of an important hydrophilic interaction. Notably, the referenced docking studies do not show the hydroxy group as participating in hydrogen bonding with any amino acids located in the channel.

Given that the structural change made to GLPG1690 seems to have led to a lack of ATX binding, as demonstrated by PET imaging, it may reasonably be suggested that replacing the fluorine of the *p*-fluorophenyl moiety would be a better approach to creating a functional radiotracer and the logic next step in this work.

4.5. CONCLUSION

We have discussed the development and initial validation of [¹⁸F]F-GLPG1690 for the *in vivo* PET imaging of ATX. [¹⁸F]F-GLPG1690, a derivative of the GLPG1690 small molecule ATX inhibitor, did not successfully image ATX expression in the 8305C human thyroid tumor, showing little difference between radiotracer uptake in the tumor vs the muscle. A redesign of the GLPG1690-based radiotracer is likely to be necessary in order to achieve *in vivo* ATX detection comparable to [¹⁸F]PRIMATX.

Acknowledgements

The authors would like to thank Dave Clendening and Blake Lazurko from the Edmonton PET centre for radionuclide production. Furthermore, the authors thank other members of the Wuest research lab including Cody Bergman for helping with the establishment of HPLC purification conditions. The authors also thank Jennifer Dufour (Wuest research lab) for her help with 8305C tumor cell injections as well animal handling, Dan McGinn (Vivarium of the Cross Cancer Institute, Edmonton, Alberta, Canada) for supporting the animal work, and Dr. Hans-Soenke Jans (Department of Oncology, University of Alberta) for technical support of the preclinical PET imaging facility.

Author Contributions

Experimental planning: Marcus Litchfield (ML), Melinda Wuest (MW), and Frank Wuest (FW).

Radiosynthesis: ML. Animal experiments including imaging and image data analysis: MW. Todd

McMullen (TM) provided the thyroid tumor cell line. Figures preparation ML and MW. Chapter

writing: ML, MW, and FW.

4.6. SUPPLEMENTAL INFORMATION

4.6.1. NMR spectra

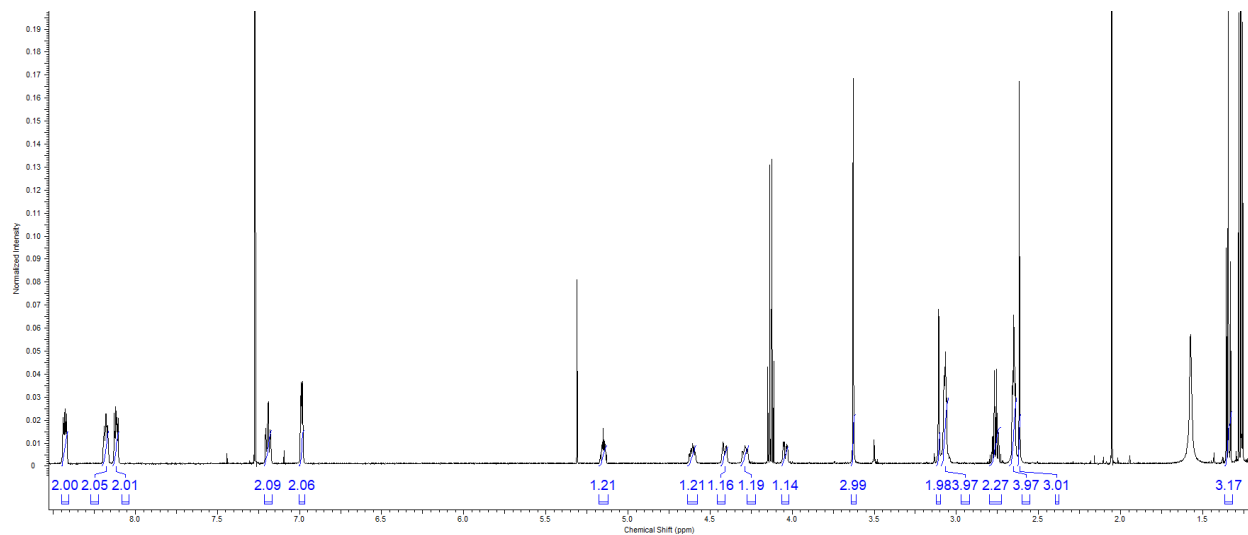


Figure 38. ¹H NMR spectrum of the nosylated GLPG1690 radiolabelling precursor (**2**).

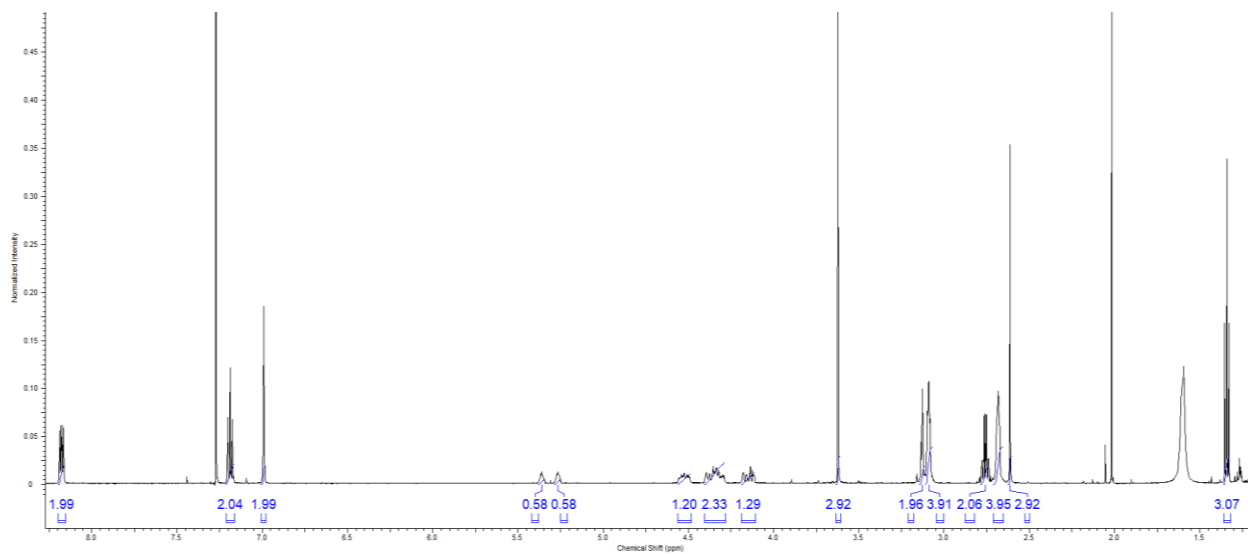


Figure 39. ¹H NMR spectrum of the fluorinated GLPG1690 non-radioactive standard (**3**).

4.6.2. HPLC traces

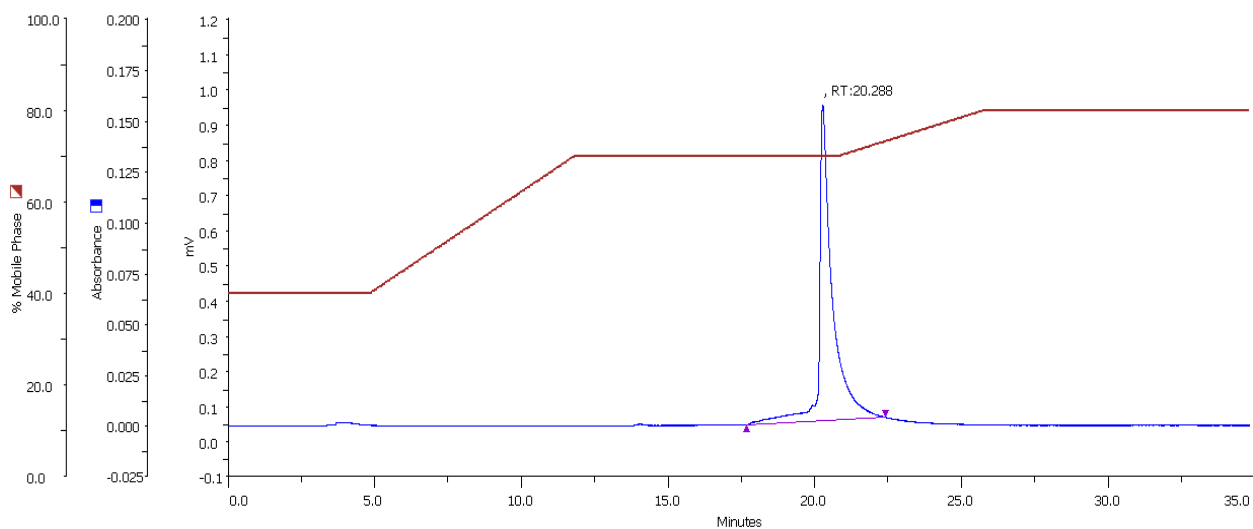


Figure 40. HPLC trace of the $[^{19}\text{F}]\text{F-GLPG1690}$ non-radioactive standard, blue represents the UV-detector signal.

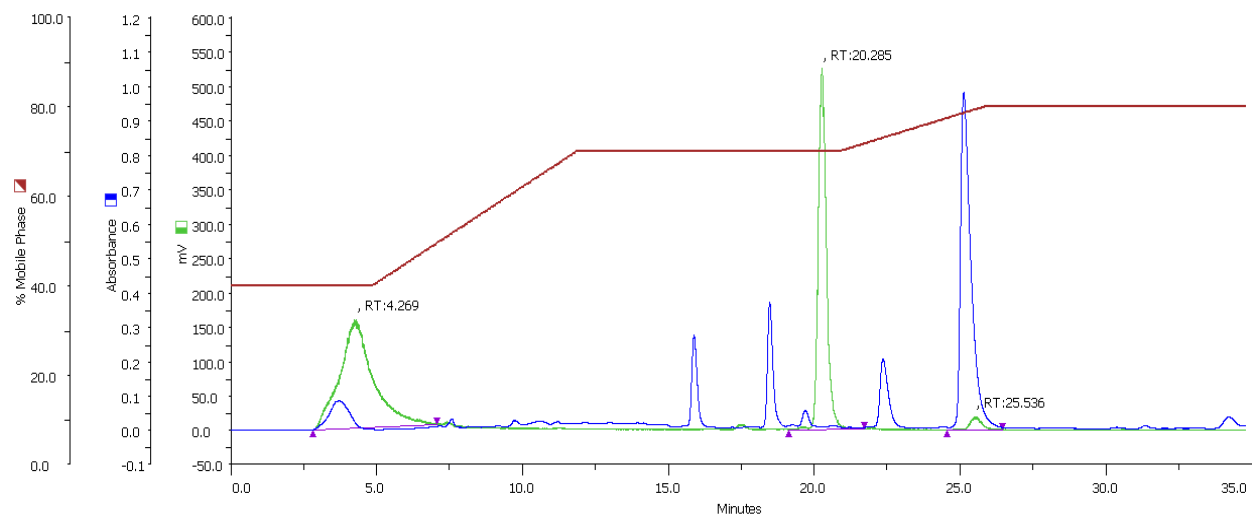


Figure 41. HPLC trace of the $[^{18}\text{F}]\text{F-GLPG1690}$ crude reaction mixture, blue represents the UV-detector signal and green the radio-detector signal.

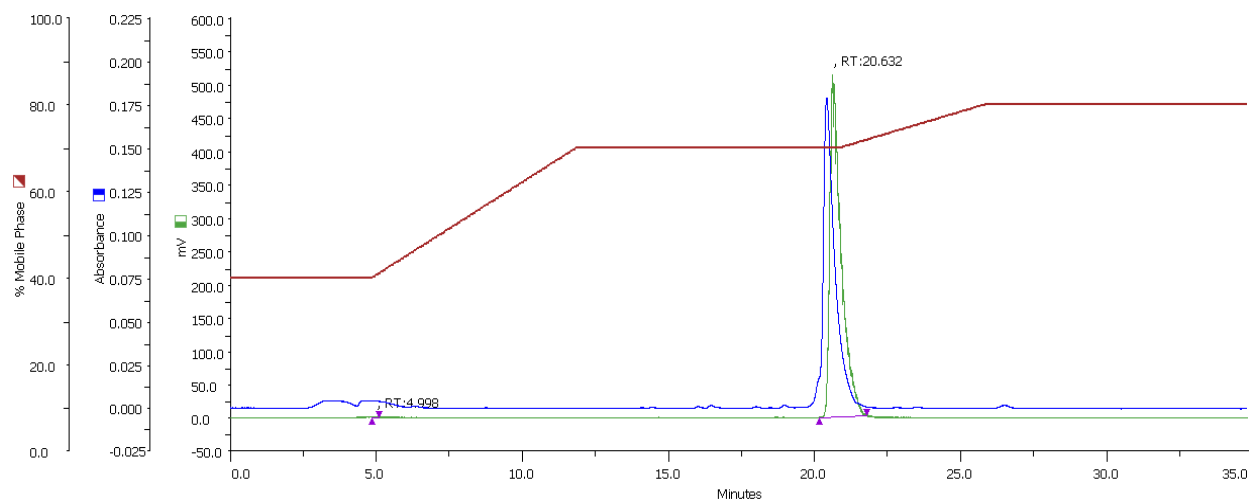


Figure 42. HPLC trace of the purified [^{18}F]F-GLPG1690 radiotracer co-injected with the [^{19}F]F-GLPG1690 non-radioactive standard. Blue represents the UV-detector signal and green, the radio-detector signal

4.6.3. Radio-TLC traces

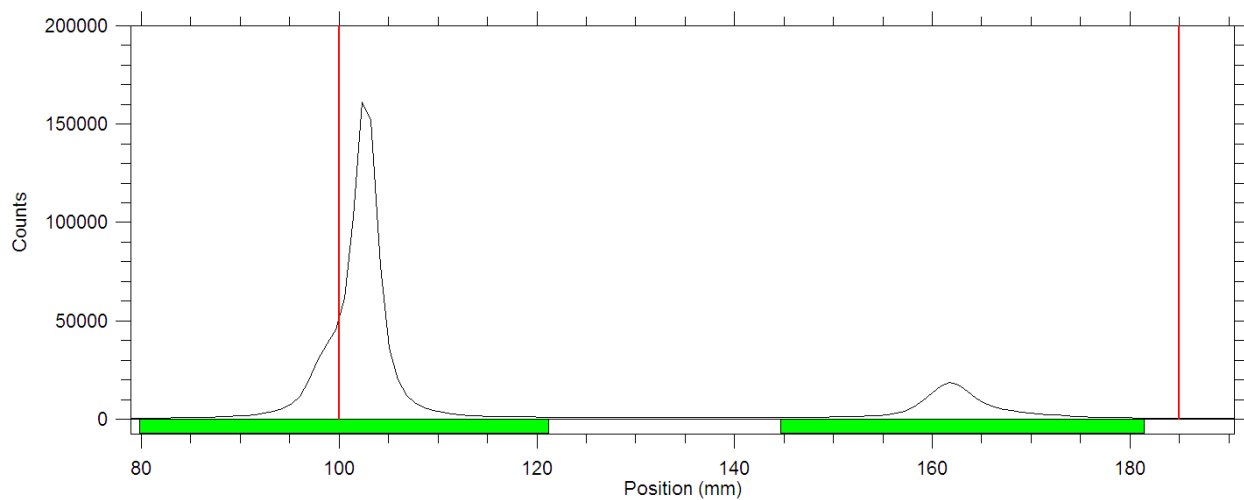


Figure 43. Radio-TLC trace of the $[^{18}\text{F}]$ -GLPG1690 crude reaction mixture.

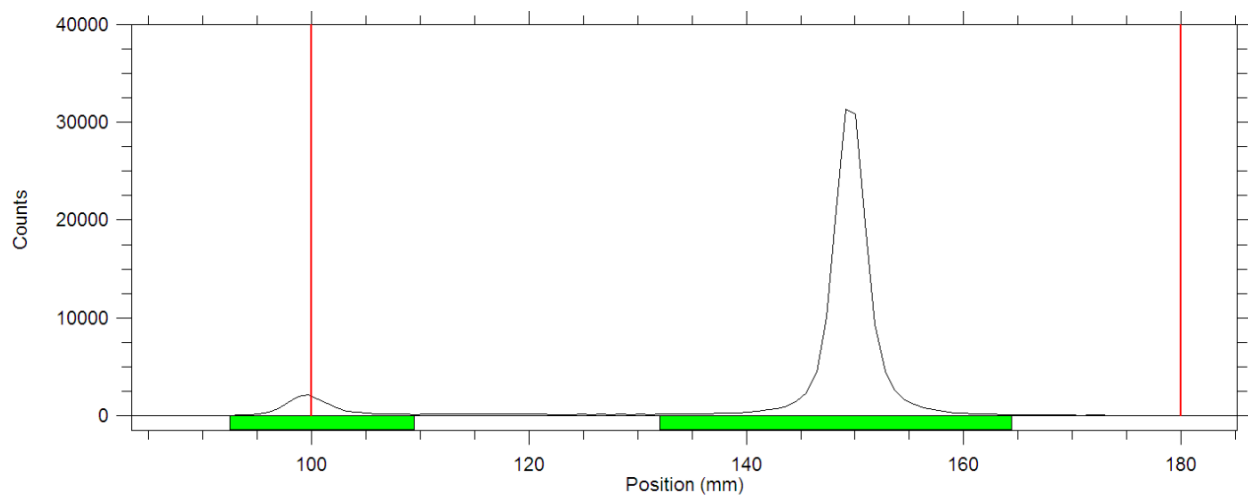


Figure 44. Radio-TLC trace of the purified $[^{18}\text{F}]$ -GLPG1690 radiotracer.

4.7. REFERENCES

- (1) Desroy, N.; Housseman, C.; Bock, X.; Joncour, A.; Bienvenu, N.; Cherel, L.; Labeguere, V.; Rondet, E.; Peixoto, C.; Grassot, J. M.; Picolet, O.; Annoot, D.; Triballeau, N.; Monjardet, A.; Wakselman, E.; Roncoroni, V.; Le Tallec, S.; Blanque, R.; Cottereaux, C.; Vandervoort, N.; Christophe, T.; Mollat, P.; Lamers, M.; Auberval, M.; Hrvacic, B.; Ralic, J.; Oste, L.; Van der Aar, E.; Brys, R.; Heckmann, B. Discovery of 2-[[2-Ethyl-6-[4-[2-(3-Hydroxyazetidino-1-yl)-2-oxoethyl]piperazin-1-yl]-8-methylimidazo[1,2-a]pyridin-3-yl]methylamino]-4-(4-fluorophenyl)thiazole-5-carbonitrile (GLPG1690), a First-in-Class Autotaxin Inhibitor Undergoing Clinical Evaluation. *J. Med. Chem.* **2017**, *60* (9), 3580–3590. <https://doi.org/10.1021/acs.jmedchem.7b00032>.
- (2) Joncour, A.; Desroy, N.; Housseman, C.; Bock, X.; Bienvenu, N.; Cherel, L.; Labeguere, V.; Peixoto, C.; Annoot, D.; Lepissier, L.; Heiermann, J.; Hengeveld, W. J.; Pilzak, G.; Monjardet, A.; Wakselman, E.; Roncoroni, V.; Le Tallec, S.; Galien, R.; David, C.; Vandervoort, N.; Christophe, T.; Conrath, K.; Jans, M.; Wohlkonig, A.; Soror, S.; Steyaert, J.; Toutilou, R.; Fleury, D.; Vercheval, L.; Mollat, P.; Triballeau, N.; Van Der Aar, E.; Brys, R.; Heckmann, B. Discovery, Structure-Activity Relationship, and Binding Mode of an Imidazo[1,2-a]pyridine Series of Autotaxin Inhibitors. *J. Med. Chem.* **2017**, *60* (17), 7371–7392. <https://doi.org/10.1021/acs.jmedchem.7b00647>.
- (3) Zhang, L.; Villalobos, A.; Beck, E. M.; Bocan, T.; Chappie, T. A.; Chen, L.; Grimwood, S.; Heck, S. D.; Helal, C. J.; Hou, X.; Humphrey, J. M.; Lu, J.; Skaddan, M. B.; McCarthy, T. J.; Verhoest, P. R.; Wager, T. T.; Zasadny, K. Design and Selection Parameters to Accelerate the Discovery of Novel Central Nervous System Positron Emission Tomography (PET) Ligands and Their Application in the Development of a Novel Phosphodiesterase 2A

- PET Ligand. *J. Med. Chem.* **2013**, *56* (11), 4568–4579. <https://doi.org/10.1021/jm400312y>.
- (4) Wüst, F.; Müller, M.; Bergmann, R. Synthesis of 4-([¹⁸F]Fluoromethyl)-2-Chlorophenylisothiocyanate: A Novel Bifunctional ¹⁸F-Labeling Agent. *Radiochim. Acta* **2004**, *92* (4–6), 349–353. <https://doi.org/10.1524/ract.92.4.349.35590>.
- (5) Madan, D.; Ferguson, C. G.; Lee, W. Y.; Prestwich, G. D.; Testa, C. A. Non-Invasive Imaging of Tumors by Monitoring Autotaxin Activity Using an Enzyme-Activated near-Infrared Fluorogenic Substrate. *PLoS One* **2013**, *8* (11). <https://doi.org/10.1371/journal.pone.0079065>.
- (6) Briard, E.; Joshi, A. D.; Shanmukhappa, S.; Ilovich, O.; Auberson, Y. P. [¹⁸F]PRIMATX, a New Positron Emission Tomography Tracer for Imaging of Autotaxin in Lung Tissue and Tumor-bearing Mice. *ChemMedChem* **2019**, *14* (16), 1493–1502. <https://doi.org/10.1002/cmdc.201900297>.
- (7) Reich, R.; Hoffman, A.; Suresh, R. R.; Shai, O.; Frant, J.; Maresca, A.; Supuran, C. T.; Breuer, E. Carbamoylphosphonates Inhibit Autotaxin and Metastasis Formation *in Vivo*. *J. Enzyme Inhib. Med. Chem.* **2015**, *30* (5), 767–772. <https://doi.org/10.3109/14756366.2014.968146>.

CHAPTER 5

Discussion, Conclusions, and Future Directions

5.1. DISCUSSION

This project may be summarized as the development and/or validation of molecular probes for the *in vivo* PET imaging of inflammation-related enzymes. Inflammatory cells, through the contribution of bio-active molecules within the tumor micro-environment, have been implicated in the enabling of several cancer hallmarks, from genomic instability and mutation to promoting invasion and metastasis.¹⁻³ Cross-talk between immune and tumor cells is achieved in part through the lipid mediators produced by inflammatory enzymes COX-2 and ATX. Tumors which contain high levels of these enzymes are more likely to be highly proliferative and metastatic than their low expression level counterparts.⁴⁻⁶ Thus, COX-2 and ATX have emerged as therapeutic targets, with some reports suggesting adjuvant inhibition therapy is already proving beneficial.⁶⁻¹¹ However, in order to tailor a therapeutic intervention to the needs of each patient, a robust non-invasive method of measuring individual COX-2 or ATX expression levels must be developed. The results of my project suggest that *in vivo* PET imaging of COX-2 and ATX protein expression levels is a reasonable means of fulfilling this goal.

Although dozens of COX-2-detecting molecular probes have been developed, no definitive tracer has been widely accepted.^{12,13} Issues relating to specificity, lipophilicity, or stability plague these molecular probes and a need for novel probes is ongoing. Our approach to this problem was unique in that our probe had been selectively assembled through *in situ* click chemistry at the COX-2 active site.^{14,15} This meant that in addition to preparing what should be a highly selective PET radiotracer, we were also able to test the claim that products of *in situ* click chemistry have specificity on par with antibodies.¹⁶

As outlined by our hypothesis, we set out to develop a novel COX-2 molecular probe which would allow for the *in vivo* detection and monitoring of COX-2 expression in chronic inflammatory

diseases, including cancer. The objectives of the triacoxib study were to 1) develop a synthesis method which would allow us to obtain the radiotracer; 2) measure the *in vitro* uptake of radioactivity into COX-2 expressing cells under control and blocking conditions, 3) measure the radiotracer's lipophilicity, blood distribution, and metabolic stability, 4) measure the uptake of radioactivity into COX-2 expressing tumors *in vivo* under control and blocking conditions, and 4) verify that the radiotracer was localizing to areas of COX-2 expression. The results obtained from each of these objectives have led to the following conclusions: i) [¹⁸F]triacoxib could be produced in high yields through late-stage copper-mediated radiofluorination chemistry using a boropinacol ester leaving group; ii) uptake into HCA-7 cells was COX-2 mediated; iii) it has a moderate lipophilicity which contributes to its pharmacokinetics and distribution profile; iv) it is resistant to metabolic degradation; v) it associates with plasma supernatant and blood cells relatively equally, though its association with plasma proteins is minimal; vi) [¹⁸F]triacoxib localizes to COX-2 producing HCA-7 tumors *in vivo* and its uptake is in part COX-2 mediated; vii) the radiotracer colocalizes with COX-2 inside the tumor; and viii) it is capable of crossing the BBB.

[¹⁸F]Triacoxib has similar potency ($IC_{50} = 0.09 \mu M$) relative to previously developed COX-2 radiotracer [¹⁸F]mono-fluorinated celecoxib ($IC_{50} = 0.07 \mu M$) and [¹⁸F]pyricoxib ($IC_{50} = 7$ nM).^{12,13} All three of these compounds diffuse passively into the cells. *In vitro* uptake of [¹⁸F]triacoxib into HCA-7 cells demonstrated very similar relative uptake patterns compared to [¹⁸F]pyricoxib, especially under 0.1 mM celecoxib inhibition.¹³ However, a major difference in the *in vitro* uptake values between them was seen in the overall activity taken up into the cells; while [¹⁸F]triacoxib inhibition studies had uptake values of 2-6% radioactivity/mg protein, [¹⁸F]pyricoxib showed uptake in the range of 140-410% activity/mg protein. During *in vivo* uptake, [¹⁸F]triacoxib produced tumor images similar in quality to [¹⁸F]pyricoxib, one of the most

advanced COX-2 radiotracers yet produced, however, the non-tumor related uptake distribution showed some variation. [¹⁸F]triacoxib showed heavy uptake into hepatobiliary clearance organs and brown adipose tissue deposits. While [¹⁸F]pyricoxib showed liver uptake, it also showed heavy lung uptake not seen in [¹⁸F]triacoxib. As both [¹⁸F]triacoxib and [¹⁸F]pyricoxib are composed of structural motifs or pharmacophores similar or identical to those in celecoxib and pyricoxib, it is not surprising that they may share some or many off-target binding relationships or clearance patterns with them and with each other.

[¹⁸F]Triacoxib and [¹⁸F]pyricoxib differ significantly in their lipophilicity (1.70 vs 3.37, respectively), which may have contributed to the relative time it took for distribution of the radiotracer, and the fact that baseline *in vivo* imaging in both tracers were completed at different time points.¹³ At 1 hour post injection [¹⁸F]triacoxib tumor uptake was just about to plateau, however, this same point wasn't reached by [¹⁸F]pyricoxib until about 4 hours post injection. Finally, the *in vivo* metabolic stability of these compounds appears to have been different as well; [¹⁸F]pyricoxib remained 60% intact after 2 hours while [¹⁸F]triacoxib was still 90% intact, but only at the 1 hour time point. After a close comparison of their respective performances, it can be seen that despite their differences in design and lipophilicity, their ability to produce images was similarly strong, both being relatively better than the majority of COX-2 imaging probes which came before them.^{12,13,17,18}

The main finding of the triacoxib project was that the radiotracer shows a mix of COX-2 specific and non-specific binding and uptake. Although the *in situ* derived COX-2 inhibitor was proposed to have superior specificity, perhaps similar to that of an antibody, this did not appear to be the case, and indeed off-target binding seemed to occur, at least to some degree. While [¹⁸F]triacoxib was able to perform its target function of visualizing COX-2, our findings suggest that its

performance and drawbacks are relatively similar to those of previous COX-2 imaging agents such as [¹⁸F]mono-fluorinated celecoxib, [¹¹C]MOV, and [¹⁸F]pyricoxib, and included *in vivo* instability, a lack of true specificity, and the occurrence of non-specific binding.^{12,13,18} However, one consideration of why signal may be seen in non-cancerous regions of our mouse model is that despite the long-established understanding that COX-2 expression is inducible, baseline levels (much smaller) of COX-2 are indeed expressed.¹⁹⁻²² Constitutive COX-2 expression independent of inflammation has been found in many tissues including mammary, brain, nasal polyp, renal medulla, thymus, stomach, ileum, and colon, and in peripheral blood cells. It may be that uptake of our radiotracer is seen in non-tumor locations is in part due to baseline COX-2 expression, though notably, our NIH-III mouse model lacks a thymus.

Regarding the progression of [¹⁸F]triacoxib to clinical imaging, there are some characteristics of our mouse model which would likely lead to differences in pre-clinical and clinical imaging. For example, our mouse's immunodeficiency is a requirement for the growth of a xenograft tumor, but it is likely that the human patients imaged will have some or most components of a working immune system. One aspect of tumor-related inflammation, as discussed in the introduction, is the infiltration of tumors with neutrophils, macrophages, and other immune cells which express COX-2. The lack of heterogeneity in our mouse tumor model may also mean that other (direct or indirect) contributors to COX-2 production, such as fibroblasts, vascular cells, endothelial cells, adipocytes, and others, are not present for pre-clinical imaging, but may be present in a clinical setting. This may mean that imaging in human tumors could be more successful, but that remains to be established. Conversely, the subcutaneous injection of our HCA-7 tumor cells resulted in a colon adenocarcinoma growing in the flank of our mouse. Obviously, this is unlikely in a clinical setting, and the real location of a colon carcinoma would likely be adjacent to the colon. As the colon

showed high levels of activity, whether because of baseline COX-2 production or because of the hepatobiliary clearance, observing the tumor in an orthotopic location may be more complicated. Again, the true impact of this potential problem may not be evident until a first in human trial is performed.

The ATX PET imaging project was rather unique because when it began there were no ATX PET imaging probes published, just the fluorescent probe.²³ Only in 2019 were the PRIMATX probe results published.²⁴ Additionally, as a relatively new focus among those who develop drugs to treat ATX-related diseases, there were no FDA approved medications; thus, few inhibitors were commercially available. All of this meant that the field of ATX molecular probes was and still is in need of contributions.

As outlined by our hypothesis, we set out to validate a novel ATX molecular probe which would allow for the *in vivo* detection and monitoring of ATX expression in chronic inflammatory diseases, including cancer. The objectives of the PRIMATX study were to: 1) modify an existing synthesis and isolate the [¹⁸F]PRIMATX radiotracer; 2) measure the radiotracer's lipophilicity, blood distribution, and metabolic stability, 3) measure the uptake of radioactivity into ATX expressing orthotopic breast tumors *in vivo*; 4) confirm the expression of ATX in thyroid tumors; 5) measure the uptake of radioactivity into thyroid tumors *in vivo* under control and blocking conditions. The results obtained from these objectives have led to the following conclusions: i) the radiotracer could be synthesized using conventional nucleophilic radiofluorination chemistry and isolated for subsequent use; ii) radiotracer lipophilicity was moderate which contributed to its pharmacokinetic profile and biodistribution; iii) it was moderately prone to metabolic degradation; iv) while it started out associating with blood cells, [¹⁸F]PRIMATX shifts to associate with plasma supernatant; v) [¹⁸F]PRIMATX localizes to ATX-producing areas surrounding breast tumors; vi)

ATX is produced in thyroid tumors; vii) [^{18}F]PRIMATX localizes to ATX-producing thyroid tumors and its uptake is partially blocked by ATX inhibition; viii) ATX mediated uptake of [^{18}F]PRIMATX occurs in the brain and joints.

The main finding of the [^{18}F]PRIMATX project was that ATX producing tumor micro-environments could be successfully imaged, though the visualization capabilities are perhaps better in some models than others. This is in agreement with the recently published [^{18}F]PRIMATX imaging results, and suggests that the potential exists for successful ATX imaging of tumors with varying origins.²⁴

Just as was the case for our [^{18}F]triacoxib imaging, the immunodeficient mice we used were necessary but likely resulted in less ATX production than might occur in a immunocompetent (or mostly immunocompetent) human patients. In the NSG mice used for our thyroid tumor model, for example, there is a diminished ability to produce many pro- and anti-inflammatory cytokines. Since cytokines are important to the production of a chronic inflammatory state and to the production of ATX, their absence in the model differentiates it from what we may expect in a clinical situation. Once again, these differences (along with the presence of a differentiated tumor and cells which either directly express or support the expression of ATX) may bode well for clinical translation because they lead to increased inflammation and biomarker production in prospective human patients. This may especially be the case for 4T1 tumors, which despite not directly producing ATX, were still visible with ATX imaging. It is likely that after the re-introduction of ATX promoting stromal cells, an increased presence of ATX will result in enhanced visualization by PET imaging. As with the colon cancer model, the thyroid cancer model was also established through subcutaneous injection resulting in a tumor growing in our mouse flank. However, in the case of an orthotopic thyroid tumor imaged by [^{18}F]PRIMATX, relatively

little uptake was detected in the thyroid region. When translated to the clinic this may be beneficial because of the simplicity in spotting a signal without significant background interference.

The GLPG1690 project also had great potential. As the drug nearest to being approved for treatment of an ATX-driven disease, GLPG1690 was an ideal candidate to be converted into a radiotracer. The objectives of the [¹⁸F]F-GLPG1690 study were to: 1) develop a radiofluorination route and isolate the radiotracer, and 2) measure the uptake of radioactivity into thyroid tumors *in vivo*. The results obtained based on these objectives have led to the conclusions that: i) the radiotracer could be synthesized in acceptable yields using conventional nucleophilic radiofluorination chemistry and isolated for subsequent use, and ii) [¹⁸F]F-GLPG1690 shows minimal localization to ATX-expressing thyroid tumors *in vivo*.

GLPG1690 presented a challenge in that we possessed very little of the compound. Thus, of the two potential radiofluorination methods, we chose to use the more straightforward, with idea that if it under performed we could obtain additional compound and use the other method. This was likely the wrong decision as it modified the structure in a way that seems to have reduced its association with ATX.

The PRIMATX and GLPG1690 projects presented together provide a worthwhile comparison. The [¹⁸F]F-GLPG1690 radiotracer's failure to image ATX provides a lower extreme or baseline with which to compare the [¹⁸F]PRIMATX imaging results, especially since they were tested in the same thyroid tumor model. It would seem that this failure simply functions to validate the [¹⁸F]PRIMATX radiotracer further. Overall, this project has achieved what it set out to do and has resulted in the development and/or validation of novel PET molecular probes for the *in vivo* detection of COX-2 and ATX. The findings of our work support the potential for clinical use of

molecular imaging tools targeting inflammatory biomarkers in the development of personalized therapeutic strategies.

5.2. CONCLUSIONS

We have reported the development of [^{18}F]triacoxib and its validation in the *in vivo* PET imaging of COX-2 expressing colon cancer cells. [^{18}F]Triacoxib is unique in that it is, to the knowledge of this author, the first *in situ* click-derived inhibitor to be converted into a radiotracer. The high potency and specificity of [^{18}F]triacoxib contributes to its ability to image COX-2 *in vivo*. The imaging capability of the [^{18}F]triacoxib PET radiotracer is on par with some of the best COX-2 PET imaging agents yet introduced, however, for multiple reasons [^{18}F]triacoxib still demonstrates significant non-specific binding which represents a stumbling block on the way to clinical translation.

We have also reported on the validation of [^{18}F]PRIMATX in the *in vivo* PET imaging of ATX in both ATX-negative breast and ATX-positive thyroid tumor models. As [^{18}F]PRIMATX is the first reported PET radiotracer targeting ATX, no meaningful comparisons to published tracers can be made. However, [^{18}F]PRIMATX vastly outperformed the 1st generation GLPG1690 PET radiotracer, which showed no tumor association. Due to its ability to cross the BBB, [^{18}F]PRIMATX has emerged as a promising radiotracer for the imaging of several prospective inflammatory disorders, especially neuroinflammatory disorders, expressing ATX.

5.3. FUTURE DIRECTIONS

With the completion of each portion of this Master project, new potential directions became increasingly apparent. It is clear that several aspects of this work need additional testing of some form, and it is my hope that due consideration be given to each of the featured radiotracers.

Beginning on a smaller scale, I think that the claim - that [¹⁸F]triacoxib underwent COX-2 specific uptake into the tumor - could be bolstered through a PET imaging and biodistribution analysis of [¹⁸F]triacoxib in a COX-2-negative colorectal cancer model. However, establishing this model may be challenging. Previously, the HCT-116 cells, which are COX-2 negative *in vitro*, were used to establish a tumor *in vivo*, however, after confounding biodistribution results stating no difference in uptake vs a COX-2 positive tumor, it was found that the tumor was in fact producing COX-2.¹³ Thus, although a cell line may not show COX-2 activity *in vitro*, that's no guarantee of its *in vivo* activity. However, if it were possible to establish a COX-2 negative tumor model, or even a model of significantly reduced COX-2 expression which could be combined with a COX-2 inhibitor, it would go a long way toward eliminating concerns about incomplete COX-2 blocking within the tumor during PET imaging.

In order to support and bolster previously obtained uptake results, [¹⁸F]triacoxib should have its PET imaging capabilities tested in additional COX-2 positive tumors such as prostate cancer or neuroblastoma.^{25,26} This would allow for a greater understanding of how generalizable [¹⁸F]triacoxib can be in imaging COX-2 expressing tumors.

On a larger scale, there are several (especially neuro)inflammatory diseases which have been reported to express COX-2 or its most common metabolite PGE₂, including rheumatoid arthritis (RA), amyotrophic lateral sclerosis (ALS), Alzheimer's disease, Parkinson's disease, and multiple sclerosis (MS).²⁷⁻³⁰ The prevalent expression of COX-2 in these diseases suggests they are all

potential applications for [¹⁸F]triacoxib imaging. MS, in particular, is an apt choice to be a future disease model as its current means of diagnosis and monitoring require multiple tests, exams, and scans which rely on the accumulation of anatomic changes (lesions) to be visually confirmed.³¹

Molecular imaging of inflammatory enzymes could allow for earlier detection, monitoring of disease progression, or assessment of treatment response, resulting in more personalized care.

The first work that should be done with [¹⁸F]PRIMATX should be aimed at confirming the results that we have thus-far obtained. One logical step in achieving this goal is to perform a biodistribution analysis in both the breast and thyroid tumor models under control and blocking conditions. Special care should be taken to analyze the ATX content in the tumor vs the surrounding adipose/muscle tissue, which may call for an autoradiographic analysis of excised tissue, including tissue from the margins. This could provide a visual demonstration of the disparity in ATX levels between those respective tissues, while simultaneously confirming reports of the origin of ATX in those models. In both the biodistribution and the autoradiography experiments, the brain, due to its confirmed ATX expression and response to blocking, could be used as a positive control, demonstrating the uptake pattern that may be expected from other ATX positive tissues.

[¹⁸F]PRIMATX should be thoroughly tested across various tumor models, including ATX-positive tumors (neuroblastoma, glioma, liver, lymphoma) and ATX-negative tumors (additional breast cancer models, lung, ovarian), in order to better define its limitations and uses. [¹⁸F]PRIMATX, as suggested by its brain uptake and subsequent specific inhibition, appears well-suited for imaging neuroinflammation. Increased ATX levels reported in a variety of inflammatory diseases, such as neuroblastoma, glioma, RA, Alzheimer's, traumatic brain injury, liver fibrosis, and IPF suggest several possible molecular imaging applications for [¹⁸F]PRIMATX.³²⁻³⁶ While there is some

doubt regarding the role of ATX in MS, its generally accepted that high ATX and LPA levels are found in CNS of MS patients, suggesting that imaging ATX in MS may also be possible.

The next step for [¹⁸F]F-GLPG1690 seems fairly conclusive: redesign. As discussed, our approach to radiolabeling, despite being more straightforward, involved changing an important chemical moiety used for binding to ATX. This action was conceivably responsible for the resultant loss of binding potential seen in our first imaging attempt. A redesign where we replace the existing fluorine with ¹⁸F-fluorine may be a more successful avenue toward imaging ATX with GLPG1690 because it allows us to keep the true molecule. This would likely be advantageous for obtaining permission to use it in the clinic as well, since chemically it's identical to a compound which, by then, may already be approved. This should be done before any further imaging is attempted.

Finally, while it wasn't in the direct purview of this work, evidence suggesting a signalling relationship between ATX and COX-2 initially emerged in 2005, and has slowly been building until now.³⁷⁻³⁹ This relationship should be explored to a greater extent. Specifically, the question of why cell lines expressing ATX do not all express COX-2, and vice versa, should be elucidated. In order to address this question, it would likely be important to probe the expression of both enzymes in a variety of cell lines/tumors. This would likely be made easier if the COX-2- and ATX-targeting molecular probes discussed above were utilized.

5.4. REFERENCES

- (1) Hussain, S. P.; Hofseth, L. J.; Harris, C. C. Radical Causes of Cancer. *Nat. Rev. Cancer* **2003**, *3* (4), 276–285. <https://doi.org/10.1038/nrc1046>.
- (2) Chio, I. I. C.; Tuveson, D. A. ROS in Cancer: The Burning Question. *Trends Mol. Med.* **2017**, *23* (5), 411–429. <https://doi.org/10.1016/j.molmed.2017.03.004>.
- (3) Hanahan, D.; Weinberg, R. A. Hallmarks of Cancer: The next Generation. *Cell* **2011**, *144* (5), 646–674. <https://doi.org/10.1016/j.cell.2011.02.013>.
- (4) Euer, N.; Schwirzke, M.; Evtimova, V.; Burtscher, H.; Jarsch, M.; Tarin, D.; Weidle, U. H. Identification of Genes Associated with Metastasis of Mammary Carcinoma in Metastatic versus Non-Metastatic Cell Lines. *Anticancer Res.* **2002**, *22* (2A), 733–740.
- (5) Bos, P. D.; Zhang, X. H. F.; Nadal, C.; Shu, W.; Gomis, R. R.; Nguyen, D. X.; Minn, A. J.; Van De Vijver, M. J.; Gerald, W. L.; Foekens, J. A.; Massagué, J. Genes That Mediate Breast Cancer Metastasis to the Brain. *Nature* **2009**, *459* (7249), 1005–1009. <https://doi.org/10.1038/nature08021>.
- (6) Li, W.; Mao, Z.; Fan, X.; Cui, L.; Wang, X. Cyclooxygenase 2 Promoted the Tumorigenicity of Pancreatic Cancer Cells. *Tumor Biol.* **2014**, *35* (3), 2271–2278. <https://doi.org/10.1007/s13277-013-1301-2>.
- (7) Barbayianni, E.; Kaffe, E.; Aidinis, V.; Kokotos, G. Autotaxin, a Secreted Lysophospholipase D, as a Promising Therapeutic Target in Chronic Inflammation and Cancer. *Prog. Lipid Res.* **2015**, *58*, 76–96. <https://doi.org/10.1016/j.plipres.2015.02.001>.
- (8) Benesch, M. G. K.; Ko, Y. M.; Tang, X.; Dewald, J.; Lopez-Campistrous, A.; Zhao, Y. Y.; Lai, R.; Curtis, J. M.; Brindley, D. N.; McMullen, T. P. W. Autotaxin Is an Inflammatory Mediator and Therapeutic Target in Thyroid Cancer. *Endocr. Relat. Cancer* **2015**, *22* (4),

- 593–607. <https://doi.org/10.1530/ERC-15-0045>.
- (9) Willoughby, D. A.; Moore, A. R.; Colville-Nash, P. R. COX-1, COX-2, and COX-3 and the Future Treatment of Chronic Inflammatory Disease. *Lancet* **2000**, *355* (9204), 646–648. [https://doi.org/10.1016/S0140-6736\(99\)12031-2](https://doi.org/10.1016/S0140-6736(99)12031-2).
- (10) Benesch, M. G. K.; Macintyre, I. T. K.; McMullen, T. P. W.; Brindley, D. N. Coming of Age for Autotaxin and Lysophosphatidate Signaling: Clinical Applications for Preventing, Detecting and Targeting Tumor-Promoting Inflammation. *Cancers (Basel)*. **2018**, *10* (3). <https://doi.org/10.3390/cancers10030073>.
- (11) Grösch, S.; Maier, T. J.; Schiffmann, S.; Geisslinger, G. Cyclooxygenase-2 (COX-2) - Independent Anticarcinogenic Effects of Selective COX-2 Inhibitors. *J. Natl. Cancer Inst.* **2006**, *98* (11), 736–747. <https://doi.org/10.1093/jnci/djj206>.
- (12) Uddin, M. J.; Crews, B. C.; Ghebreselasie, K.; Huda, I.; Kingsley, P. J.; Ansari, M. S.; Tantawy, M. N.; Reese, J.; Marnett, L. J. Fluorinated COX-2 Inhibitors as Agents in PET Imaging of Inflammation and Cancer. *Cancer Prev. Res.* **2011**, *4* (10), 1536–1545. <https://doi.org/10.1158/1940-6207.CAPR-11-0120>.
- (13) Tietz, O.; Wuest, M.; Marshall, A.; Glubrecht, D.; Hamann, I.; Wang, M.; Bergman, C.; Way, J. D.; Wuest, F. PET Imaging of Cyclooxygenase-2 (COX-2) in a Pre-Clinical Colorectal Cancer Model. *EJNMMI Res.* **2016**, *6* (1). <https://doi.org/10.1186/s13550-016-0192-9>.
- (14) Sharpless, K. B.; Manetsch, R. *In Situ* Click Chemistry: A Powerful Means for Lead Discovery. *Expert Opin. Drug Discov.* **2006**, *1* (6), 525–538. <https://doi.org/10.1517/17460441.1.6.525>.
- (15) Bhardwaj, A.; Kaur, J.; Wuest, M.; Wuest, F. *In Situ* Click Chemistry Generation of

- Cyclooxygenase-2 Inhibitors. *Nat. Commun.* **2017**, 8 (1), 1–13. <https://doi.org/10.1038/s41467-016-0009-6>.
- (16) Millward, S. W.; Agnew, H. D.; Lai, B.; Lee, S. S.; Lim, J.; Nag, A.; Pitram, S.; Rohde, R.; Heath, J. R. *In Situ* Click Chemistry: From Small Molecule Discovery to Synthetic Antibodies. *Integr. Biol.* **2013**, 235 (1), 87–95. <https://doi.org/10.1038/jid.2014.371>.
- (17) Uddin, M. J.; Crews, B. C.; Ghebreselasie, K.; Tantawy, M. N.; Marnett, L. J. [123I]-Celecoxib Analogues as SPECT Tracers of Cyclooxygenase-2 in Inflammation. *ACS Med. Chem. Lett.* **2011**, 2 (2), 160–164. <https://doi.org/10.1021/ml100232q>.
- (18) Prabhakaran, J.; Underwood, M.; Zanderigo, F.; Simpson, N. R.; Cooper, A. R.; Matthew, J.; Rubin-Falcone, H.; Parsey, R. V.; Mann, J. J.; Dileep Kumar, J. S. Radiosynthesis and *in Vivo* Evaluation of [11C]MOV as a PET Imaging Agent for COX-2. *Bioorganic Med. Chem. Lett.* **2018**, 28 (14), 2432–2435. <https://doi.org/10.1016/j.bmcl.2018.06.015>.
- (19) Fornetti, J.; Jindal, S.; Middleton, K. A.; Borges, V. F.; Schedin, P. Physiological COX-2 Expression in Breast Epithelium Associates with COX-2 Levels in Ductal Carcinoma *in Situ* and Invasive Breast Cancer in Young Women. *Am. J. Pathol.* **2014**, 184 (4), 1219–1229. <https://doi.org/10.1016/j.ajpath.2013.12.026>.
- (20) Pujols, L.; Benitez, P.; Alobid, I.; Martinez-Antón, A.; Roca-Ferrer, J.; Mullol, J.; Picado, C. Glucocorticoid Therapy Increases COX-2 Gene Expression in Nasal Polyps *in Vivo*. *Eur. Respir. J.* **2009**, 33 (3), 502–508. <https://doi.org/10.1183/09031936.00017408>.
- (21) Almendingen, K.; Brevik, A.; Nymoén, D. A.; Hilmarsen, H. T.; Andresen, P. A.; Andersen, L. F.; Vatn, M. Modulation of COX-2 Expression in Peripheral Blood Cells by Increased Intake of Fruit and Vegetables? *Eur. J. Clin. Nutr.* **2005**, 59 (4), 597–602. <https://doi.org/10.1038/sj.ejcn.1602110>.

- (22) Kirkby, N. S.; Chan, M. V.; Zaiss, A. K.; Garcia-Vaz, E.; Jiao, J.; Berglund, L. M.; Verdu, E. F.; Ahmetaj-Shala, B.; Wallace, J. L.; Herschman, H. R.; Gomez, M. F.; Mitchell, J. A. Systematic Study of Constitutive Cyclooxygenase-2 Expression: Role of NF-KB and NFAT Transcriptional Pathways. *Proc. Natl. Acad. Sci. U. S. A.* **2016**, *113* (2), 434–439. <https://doi.org/10.1073/pnas.1517642113>.
- (23) Madan, D.; Ferguson, C. G.; Lee, W. Y.; Prestwich, G. D.; Testa, C. A. Non-Invasive Imaging of Tumors by Monitoring Autotaxin Activity Using an Enzyme-Activated near-Infrared Fluorogenic Substrate. *PLoS One* **2013**, *8* (11). <https://doi.org/10.1371/journal.pone.0079065>.
- (24) Briard, E.; Joshi, A. D.; Shanmukhappa, S.; Ilovich, O.; Auberson, Y. P. [18 F]PRIMATX, a New Positron Emission Tomography Tracer for Imaging of Autotaxin in Lung Tissue and Tumor-bearing Mice. *ChemMedChem* **2019**, *14* (16), 1493–1502. <https://doi.org/10.1002/cmdc.201900297>.
- (25) Garg, R.; Blando, J. M.; Perez, C. J.; Lal, P.; Feldman, M. D.; Smyth, E. M.; Ricciotti, E.; Grosser, T.; Benavides, F.; Kazanietz, M. G. COX-2 Mediates pro-Tumorigenic Effects of PKC ϵ in Prostate Cancer. *Oncogene* **2018**, *37* (34), 4735–4749. <https://doi.org/10.1038/s41388-018-0318-9>.
- (26) Johnsen, J. I.; Lindskog, M.; Ponthan, F.; Pettersen, I.; Elfman, L.; Orrego, A.; Sveinbjornsson, B.; Kogner, P. Cyclooxygenase-2 Is Expressed in Neuroblastoma , and Nonsteroidal Anti-Inflammatory Drugs Induce Apoptosis and Inhibit Tumor Growth *in Vivo*. **2004**, 7210–7215.
- (27) Peng, A.; Lu, X.; Huang, J.; He, M.; Xu, J.; Huang, H.; Chen, Q. Rheumatoid Arthritis Synovial Fibroblasts Promote TREM-1 Expression in Monocytes via COX-2/PGE₂

- Pathway. *Arthritis Res. Ther.* **2019**, *21* (1), 1–11. <https://doi.org/10.1186/s13075-019-1954-3>.
- (28) Graves, M. C.; Fiala, M.; Dinglasan, L. A. V.; Liu, N. Q.; Sayre, J.; Chiappelli, F.; van Kooten, C.; Vinters, H. V. Inflammation in Amyotrophic Lateral Sclerosis Spinal Cord and Brain Is Mediated by Activated Macrophages, Mast Cells and t Cells. *Amyotroph. Lateral Scler. Other Mot. Neuron Disord.* **2004**, *5* (4), 213–219. <https://doi.org/10.1080/14660820410020286>.
- (29) Minghetti, L. Cyclooxygenase-2 (COX-2) in Inflammatory and Degenerative Brain Diseases. *J. Neuropathol. Exp. Neurol.* **2004**, *63* (9), 901–910. <https://doi.org/10.1093/jnen/63.9.901>.
- (30) Rose, J. W.; Hill, K. E.; Watt, H. E.; Carlson, N. G. Inflammatory Cell Expression of Cyclooxygenase-2 in the Multiple Sclerosis Lesion. *J. Neuroimmunol.* **2004**, *149* (1–2), 40–49. <https://doi.org/10.1016/j.jneuroim.2003.12.021>.
- (31) Arrambide, G.; Tintore, M. Diagnosis of Multiple Sclerosis: What Is Changing? *Expert Rev. Neurother.* **2019**, *00* (00), 1–4. <https://doi.org/10.1080/14737175.2020.1691530>.
- (32) Hoelzinger, D. B.; Nakada, M.; Demuth, T.; Rosensteel, T.; Reavie, L. B.; Berens, M. E. Autotaxin: A Secreted Autocrine/Paracrine Factor That Promotes Glioma Invasion. *J. Neurooncol.* **2008**, *86* (3), 297–309. <https://doi.org/10.1007/s11060-007-9480-6>.
- (33) Ninou, I.; Magkrioti, C.; Aidinis, V. Autotaxin in Pathophysiology and Pulmonary Fibrosis. *Front. Med.* **2018**, *5* (JUN), 1–11. <https://doi.org/10.3389/fmed.2018.00180>.
- (34) Herr, D. R.; Chew, W. S.; Satish, R. L.; Ong, W.-Y. Pleotropic Roles of Autotaxin in the Nervous System Present Opportunities for the Development of Novel Therapeutics for Neurological Diseases. *Mol. Neurobiol.* **2019**. <https://doi.org/10.1007/s12035-019-01719->

- 1.
- (35) Ikeda, H.; Yatomi, Y. Autotaxin in Liver Fibrosis. *Clin. Chim. Acta* **2012**, *413* (23–24), 1817–1821. <https://doi.org/10.1016/j.cca.2012.07.014>.
- (36) Orosa, B.; García, S.; Martínez, P.; González, A.; Gómez-Reino, J. J.; Conde, C. Lysophosphatidic Acid Receptor Inhibition as a New Multipronged Treatment for Rheumatoid Arthritis. *Ann. Rheum. Dis.* **2014**, *73* (1), 298–305. <https://doi.org/10.1136/annrheumdis-2012-202832>.
- (37) Ye, X.; Hama, K.; Contos, J. J. A.; Anliker, B.; Inoue, A.; Skinner, M. K.; Suzuki, H.; Amane, T.; Kennedy, G.; Arai, H.; Aoki, J.; Chun, J. LPA3-Mediated Lysophosphatidic Acid Signalling in Embryo Implantation and Spacing. *Lett. to Nat.* **2005**, *435* (May), 104–108.
- (38) Aikawa, S.; Kano, K.; Inoue, A.; Wang, J.; Saigusa, D.; Nagamatsu, T.; Hirota, Y.; Fujii, T.; Tsuchiya, S.; Taketomi, Y. Autotaxin – Lysophosphatidic Acid – LPA 3 Signaling at the Embryo-Epithelial Boundary Controls Decidualization Pathways. **2017**, *36* (14), 2146–2160. <https://doi.org/10.15252/emj.201696290>.
- (39) Nochi, H.; Tomura, H.; Tobo, M.; Tanaka, N.; Sato, K.; Shinozaki, T.; Kobayashi, T.; Takagishi, K.; Ohta, H.; Okajima, F.; Tamoto, K. Stimulatory Role of Lysophosphatidic Acid in Cyclooxygenase-2 Induction by Synovial Fluid of Patients with Rheumatoid Arthritis in Fibroblast-like Synovial Cells. *J. Immunol.* **2008**, *181* (7), 511–5119. <https://doi.org/10.4049/jimmunol.181.7.5111>.

Bibliography

Chapter 1

- (1) Chiba, T.; Marusawa, H.; Ushijima, T. Inflammation-Associated Cancer Development in Digestive Organs: Mechanisms and Roles for Genetic and Epigenetic Modulation. *Gastroenterology* **2012**, *143* (3), 550–563. <https://doi.org/10.1053/j.gastro.2012.07.009>.
- (2) Hanahan, D.; Weinberg, R. A. Hallmarks of Cancer: The next Generation. *Cell* **2011**, *144* (5), 646–674. <https://doi.org/10.1016/j.cell.2011.02.013>.
- (3) Hanahan, D.; Weinberg, R. The Hallmarks of Cancer. *Cell* **2000**, *100*, 57–70.
- (4) Serhan, C. N.; Krishnamoorthy, S.; Recchiuti, A.; Chiang, N. Novel Anti-Inflammatory-pro-Resolving Mediators and Their Receptors. *Curr. Top. Med. Chem.* **2011**, *11* (6), 629–647. <https://doi.org/10.2174/1568026611109060629>.
- (5) Robbins, S. L. *Basic Pathology*; Kumar, V., Abbas, A. K., Aster, J. C., Eds.; Elsevier, 2015.
- (6) Harada, A.; Sekido, N.; Akahoshi, T.; Wada, T.; Mukaida, N.; Matsushima, K. Essential Involvement of Interleukin-8 (IL-8) in Acute Inflammation. *J. Leukoc. Biol.* **1994**, *56* (5), 559–564. <https://doi.org/10.1002/jlb.56.5.559>.
- (7) Kumar, K. P.; Nicholls, A. J.; Wong, C. H. Y. Partners in Crime: Neutrophils and Monocytes/Macrophages in Inflammation and Disease. *Cell Tissue Res.* **2018**, *371* (3), 551–565. <https://doi.org/10.1007/s00441-017-2753-2>.
- (8) Serhan, C. N.; Chiang, N.; Dalli, J.; Levy, B. D. Lipid Mediators in the Resolution of Inflammation. *Cold Spring Harb. Perspect. Biol.* **2015**, *7* (2). <https://doi.org/10.1101/cshperspect.a016311>.
- (9) Marwick, J. A.; Mills, R.; Kay, O.; Michail, K.; Stephen, J.; Rossi, A. G.; Dransfield, I.; Hirani, N. Neutrophils Induce Macrophage Anti-Inflammatory Reprogramming by

- Suppressing NF-KB Activation Article. *Cell Death Dis.* **2018**, *9* (6).
<https://doi.org/10.1038/s41419-018-0710-y>.
- (10) Nakanishi, M.; Rosenberg, D. W. Multifaceted Roles of PGE₂ in Inflammation and Cancer. *Semin. Immunopathol.* **2013**, *35* (2), 123–137. <https://doi.org/10.1007/s00281-012-0342-8>.
- (11) Serhan, C. N. The Resolution of Inflammation: The Devil in the Flask and in the Details. *FASEB J.* **2011**, *25* (5), 1441–1448. <https://doi.org/10.1096/fj.11-0502ufm>.
- (12) Levy, B. D.; Clish, C. B.; Schmidt, B.; Gronert, K.; Serhan, C. N. Lipid Mediator Class Switching during Acute Inflammation: Signals in Resolution. *Nat. Immunol.* **2001**, *2* (7), 612–619. <https://doi.org/10.1038/89759>.
- (13) Godson, C.; Mitchell, S.; Harvey, K.; Petasis, N. A.; Hogg, N.; Brady, H. R. Cutting Edge: Lipoxins Rapidly Stimulate Nonphlogistic Phagocytosis of Apoptotic Neutrophils by Monocyte-Derived Macrophages. *J. Immunol.* **2000**, *164* (4), 1663–1667.
<https://doi.org/10.4049/jimmunol.164.4.1663>.
- (14) Serhan, C. N.; Levy, B. D. Resolvins in Inflammation: Emergence of the pro-Resolving Superfamily of Mediators Protection versus Uncontrolled Inflammation: First Responders and Resolution. *J Clin Invest* **2018**, *128* (7), 2657–2669. <https://doi.org/10.1172/JCI97943>.
- (15) Pastar, I.; Stojadinovic, O.; Yin, N. C.; Ramirez, H.; Nusbaum, A. G.; Sawaya, A.; Patel, S. B.; Khalid, L.; Isseroff, R. R.; Tomic-Canic, M. Epithelialization in Wound Healing: A Comprehensive Review. *Adv. Wound Care* **2014**, *3* (7), 445–464.
<https://doi.org/10.1089/wound.2013.0473>.
- (16) Monteiro, H. P.; Rodrigues, E. G.; Amorim Reis, A. K. C.; Longo, L. S.; Ogata, F. T.; Moretti, A. I. S.; da Costa, P. E.; Teodoro, A. C. S.; Toledo, M. S.; Stern, A. Nitric Oxide

- and Interactions with Reactive Oxygen Species in the Development of Melanoma, Breast, and Colon Cancer: A Redox Signaling Perspective. *Nitric Oxide* **2019**, *89* (October 2018), 1–13. <https://doi.org/10.1016/j.niox.2019.04.009>.
- (17) Hodge, D. R.; Hurt, E. M.; Farrar, W. L. The Role of IL-6 and STAT3 in Inflammation and Cancer. *Eur. J. Cancer* **2005**, *41* (16), 2502–2512. <https://doi.org/10.1016/j.ejca.2005.08.016>.
- (18) Fisher, D. T.; Appenheimer, M. M.; Evans, S. S. The Two Faces of IL-6 in the Tumor Microenvironment. *Semin. Immunol.* **2014**, *26* (1), 38–47. <https://doi.org/10.1038/jid.2014.371>.
- (19) Landskron, G.; De La Fuente, M.; Thuwajit, P.; Thuwajit, C.; Hermoso, M. A. Chronic Inflammation and Cytokines in the Tumor Microenvironment. *J. Immunol. Res.* **2014**, *2014*. <https://doi.org/10.1155/2014/149185>.
- (20) Chen, L.; Shi, Y.; Zhu, X.; Guo, W.; Zhang, M.; Che, Y.; Tang, L.; Yang, X.; You, Q.; Liu, Z. IL-10 Secreted by Cancer-Associated Macrophages Regulates Proliferation and Invasion in Gastric Cancer Cells via c-Met/STAT3 Signaling. *Oncol. Rep.* **2019**, *42* (2), 595–604. <https://doi.org/10.3892/or.2019.7206>.
- (21) Fabre, J.; Giustiniani, J.; Garbar, C.; Antonicelli, F.; Merrouche, Y.; Bensussan, A.; Bagot, M.; Al-Dacak, R. Targeting the Tumor Microenvironment: The Protumor Effects of IL-17 Related to Cancer Type. *Int. J. Mol. Sci.* **2016**, *17* (9). <https://doi.org/10.3390/ijms17091433>.
- (22) Qian, B. Z.; Pollard, J. W. Macrophage Diversity Enhances Tumor Progression and Metastasis. *Cell* **2010**, *141* (1), 39–51. <https://doi.org/10.1016/j.cell.2010.03.014>.
- (23) DeNardo, D. G.; Barreto, J. B.; Andreu, P.; Vasquez, L.; Tawfik, D.; Kolhatkar, N.;

- Coussens, L. M. CD4+ T Cells Regulate Pulmonary Metastasis of Mammary Carcinomas by Enhancing Protumor Properties of Macrophages. *Cancer Cell* **2009**, *16* (2), 91–102. <https://doi.org/10.1016/j.ccr.2009.06.018>.
- (24) Ugel, S.; De Sanctis, F.; Mandruzzato, S.; Bronte, V. Tumor-Induced Myeloid Deviation: When Myeloid-Derived Suppressor Cells Meet Tumor-Associated Macrophages. *J. Clin. Invest.* **2015**, *125* (9), 3365–3376. <https://doi.org/10.1172/JCI80006>.
- (25) Wendt, M. K.; Allington, T. M.; Schiemann, W. P. Mechanisms of the Epithelial-Mesenchymal Transition by TGF- β . *Futur. Oncol.* **2009**, *5* (8), 1145–1168. <https://doi.org/10.2217/fon.09.90>.
- (26) Gao, D.; Joshi, N.; Choi, H.; Ryu, S.; Hahn, M.; Catena, R.; Sadik, H.; Argani, P.; Wagner, P.; Vahdat, L. T.; Port, J. L.; Stiles, B.; Sukumar, S.; Altorki, N. K.; Raffii, S.; Mittal, V. Myeloid Progenitor Cells in the Premetastatic Lung Promote Metastases by Inducing Mesenchymal to Epithelial Transition. *Cancer Res.* **2012**, *72* (6), 1384–1394. <https://doi.org/10.1158/0008-5472.CAN-11-2905>.
- (27) Krys, D.; Hamann, I.; Wuest, M.; Wuest, F. Effect of Hypoxia on Human Equilibrative Nucleoside Transporters HENT1 and HENT2 in Breast Cancer. *FASEB J.* **2019**, *33* (12), 13837–13851. <https://doi.org/10.1096/fj.201900870RR>.
- (28) Brown, J. M. Tumor Hypoxia in Cancer Therapy. *Methods Enzymol.* **2007**, *435*. [https://doi.org/10.1016/S0076-6879\(07\)35015-5](https://doi.org/10.1016/S0076-6879(07)35015-5).
- (29) Belotti, D.; Paganoni, P.; Manenti, L.; Garofalo, A.; Marchini, S.; Taraboletti, G.; Giavazzi, R. Matrix Metalloproteinases (MMP9 and MMP2) Induce the Release of Vascular Endothelial Growth Factor (VEGF) by Ovarian Carcinoma Cells: Implications for Ascites Formation. *Cancer Res.* **2003**, *63* (17), 5224–5229.

- (30) Hawinkels, L. J. A. C.; Zuidwijk, K.; Verspaget, H. W.; de Jonge-Muller, E. S. M.; Duijn, W. van; Ferreira, V.; Fontijn, R. D.; David, G.; Hommes, D. W.; Lamers, C. B. H. W.; Sier, C. F. M. VEGF Release by MMP-9 Mediated Heparan Sulphate Cleavage Induces Colorectal Cancer Angiogenesis. *Eur. J. Cancer* **2008**, *44* (13), 1904–1913. <https://doi.org/10.1016/j.ejca.2008.06.031>.
- (31) Wang, X.; Lin, Y. Tumor Necrosis Factor and Cancer, Buddies or Foes? *Acta Pharmacol. Sin.* **2008**, *29* (11), 1275–1288. <https://doi.org/10.1111/j.1745-7254.2008.00889.x>.
- (32) DeNardo, D. G.; Andreu, P.; Coussens, L. M. Interactions between Lymphocytes and Myeloid Cells Regulate Pro-versus Anti-Tumor Immunity. *Cancer Metastasis Rev.* **2010**, *29* (2), 309–316. <https://doi.org/10.1007/s10555-010-9223-6>.
- (33) Gonzalez, H.; Hagerling, C.; Werb, Z. Roles of the Immune System in Cancer: From Tumor Initiation to Metastatic Progression. *Genes Dev.* **2018**, *32* (19–20), 1267–1284. <https://doi.org/10.1101/GAD.314617.118>.
- (34) Taylor, A.; Verhagen, J.; Blaser, K.; Akdis, M.; Akdis, C. A. Mechanisms of Immune Suppression by Interleukin-10 and Transforming Growth Factor- β : The Role of T Regulatory Cells. *Immunology* **2006**, *117* (4), 433–442. <https://doi.org/10.1111/j.1365-2567.2006.02321.x>.
- (35) Gun, S. Y.; Lee, S. W. L.; Sieow, J. L.; Wong, S. C. Targeting Immune Cells for Cancer Therapy. *Redox Biol.* **2019**, No. March, 101174. <https://doi.org/10.1016/j.redox.2019.101174>.
- (36) Tesi, R. J. MDSC; the Most Important Cell You Have Never Heard Of. *Trends Pharmacol. Sci.* **2019**, *40* (1), 4–7. <https://doi.org/10.1016/j.tips.2018.10.008>.
- (37) Ma, P.; Beatty, P. L.; McKolanis, J.; Brand, R.; Schoen, R. E.; Finn, O. J. Circulating

- Myeloid Derived Suppressor Cells (MDSC) That Accumulate in Premalignancy Share Phenotypic and Functional Characteristics with MDSC in Cancer. *Front. Immunol.* **2019**, *10* (JUN). <https://doi.org/10.3389/fimmu.2019.01401>.
- (38) Dvorak, H. Tumors: Wounds That Do Not Heal. *N. Engl. J. Med.* **1986**, *315* (26), 1650–1659.
- (39) Hussain, S. P.; Hofseth, L. J.; Harris, C. C. Radical Causes of Cancer. *Nat. Rev. Cancer* **2003**, *3* (4), 276–285. <https://doi.org/10.1038/nrc1046>.
- (40) Chio, I. I. C.; Tuveson, D. A. ROS in Cancer: The Burning Question. *Trends Mol. Med.* **2017**, *23* (5), 411–429. <https://doi.org/10.1016/j.molmed.2017.03.004>.
- (41) Ayala, A.; Munoz, M. F.; Arguelles, S. Lipid Peroxidation: Production, Metabolism, and Signaling Mechanisms of Malondialdehyde and 4-Hydroxy-2-Nonenal. *Oxid. Med. Cell. Longev.* **2014**, *2014*, 360438. https://doi.org/10.1007/978-3-211-33303-7_2.
- (42) Seyfried, T. N.; Huysentruyt, L. c. On the Origin of Cancer Metastasis. *Crit. Rev. Oncol.* **2013**, *18* (1–2), 43–73. [https://doi.org/10.1002/1097-0142\(195205\)5:3<581::AID-CNCR2820050319>3.0.CO;2-Q](https://doi.org/10.1002/1097-0142(195205)5:3<581::AID-CNCR2820050319>3.0.CO;2-Q).
- (43) Johnsen, J. I.; Lindskog, M.; Ponthan, F.; Pettersen, I.; Elfman, L.; Orrego, A.; Sveinbjornsson, B.; Kogner, P. Cyclooxygenase-2 Is Expressed in Neuroblastoma , and Nonsteroidal Anti-Inflammatory Drugs Induce Apoptosis and Inhibit Tumor Growth *in Vivo*. **2004**, 7210–7215.
- (44) Gupta, G. P.; Nguyen, D. X.; Chiang, A. C.; Bos, P. D.; Kim, J. Y.; Nadal, C.; Gomis, R. R.; Manova-Todorova, K.; Massagué, J. Mediators of Vascular Remodelling Co-Opted for Sequential Steps in Lung Metastasis. *Nature* **2007**, *446* (7137), 765–770. <https://doi.org/10.1038/nature05760>.

- (45) Stracke, M. L.; Krutzsch, H. C.; Unsworth, E. J.; Arestad, A.; Cioce, V.; Schiffmann, E.; Liotta, L. A. Identification, Purification, and Partial Sequence Analysis of Autotaxin, a Novel Motility-Stimulating Protein. *J. Biol. Chem.* **1992**, *267* (4), 2524–2529.
- (46) Benesch, M. G. K.; Tang, X.; Dewald, J.; Dong, W. F.; Mackey, J. R.; Hemmings, D. G.; McMullen, T. P. W.; Brindley, D. N. Tumor-Induced Inflammation in Mammary Adipose Tissue Stimulates a Vicious Cycle of Autotaxin Expression and Breast Cancer Progression. *FASEB J.* **2015**, *29* (9), 3990–4000. <https://doi.org/10.1096/fj.15-274480>.
- (47) Benesch, M. G. K.; Ko, Y. M.; Tang, X.; Dewald, J.; Lopez-Campistrous, A.; Zhao, Y. Y.; Lai, R.; Curtis, J. M.; Brindley, D. N.; McMullen, T. P. W. Autotaxin Is an Inflammatory Mediator and Therapeutic Target in Thyroid Cancer. *Endocr. Relat. Cancer* **2015**, *22* (4), 593–607. <https://doi.org/10.1530/ERC-15-0045>.
- (48) Hemmings, D. G.; Brindley, D. N. Signalling by Lysophosphatidate and Its Health Implications. *Essays Biochem.* **2020**, *Ahead of P* (May), 1–17.
- (49) Yang, T.; Du, Y. Distinct Roles of Central and Peripheral Prostaglandin e 2 and EP Subtypes in Blood Pressure Regulation. *Am. J. Hypertens.* **2012**, *25* (10), 1042–1049. <https://doi.org/10.1038/ajh.2012.67>.
- (50) Loynes, C. A.; Lee, J. A.; Robertson, A. L.; Steel, M. J. G.; Ellett, F.; Feng, Y.; Levy, B. D.; Whyte, M. K. B.; Renshaw, S. A. PGE₂ Production at Sites of Tissue Injury Promotes an Anti-Inflammatory Neutrophil Phenotype and Determines the Outcome of Inflammation Resolution *in Vivo*. *Sci. Adv.* **2018**, *4* (9). <https://doi.org/10.1126/sciadv.aar8320>.
- (51) Chen, C. Lipids: COX-2's New Role in Inflammation. *Nat. Chem. Biol.* **2010**, *6* (6), 401–402. <https://doi.org/10.1038/nchembio.375>.

- (52) Ricciotti, E.; A, G.; Fitzgerald. [Eicosanoid Neuroinflammation] Prostaglandins and Inflammation. *Arter. Thromb Vasc Biol.* **2011**, *31* (5), 986–1000.
<https://doi.org/10.1161/ATVBAHA.110.207449>.Prostaglandins.
- (53) Xia, D.; Wang, D.; Kim, S. H.; Katoh, H.; Dubois, R. N. Prostaglandin E 2 Promotes Intestinal Tumor Growth via DNA Methylation. *Nat. Med.* **2012**, *18* (2), 224–226.
<https://doi.org/10.1038/nm.2608>.
- (54) Dubois, R. N.; Abramson, S. B.; Crofford, L.; Gupta, R. A.; Simon, L. S.; Van De Putte, L. B.; Lipsky, P. E. Cyclooxygenase in Biology and Disease. *FASEB J.* **1998**, *12* (12), 1063–1073. <https://doi.org/9737710>.
- (55) Garg, R.; Blando, J. M.; Perez, C. J.; Lal, P.; Feldman, M. D.; Smyth, E. M.; Ricciotti, E.; Grosser, T.; Benavides, F.; Kazanietz, M. G. COX-2 Mediates pro-Tumorigenic Effects of PKC ϵ in Prostate Cancer. *Oncogene* **2018**, *37* (34), 4735–4749.
<https://doi.org/10.1038/s41388-018-0318-9>.
- (56) Ghosh, N.; Chaki, R.; Mandal, V.; Mandal, S. C. COX-2 as a Target for Cancer Chemotherapy. *Pharmacol. Reports* **2010**, *62* (2), 233–244.
[https://doi.org/10.1016/S1734-1140\(10\)70262-0](https://doi.org/10.1016/S1734-1140(10)70262-0).
- (57) Hood, W. F.; Gierse, J. K.; Isakson, P. C.; Kiefer, J. R.; Kurumbail, R. G.; Seibert, K.; Monahan, J. B. Characterization of Celecoxib and Valdecoxib Binding to Cyclooxygenase. *Mol. Pharmacol.* **2003**, *63* (4), 870–877.
<https://doi.org/10.1124/mol.63.4.870>.
- (58) Gao, Y.; Zhang, H.; Luo, L.; Lin, J.; Li, D.; Zheng, S.; Huang, H.; Yan, S.; Yang, J.; Hao, Y.; Li, H.; Gao Smith, F.; Jin, S. Resolvin D1 Improves the Resolution of Inflammation via Activating NF-KB P50/P50–Mediated Cyclooxygenase-2 Expression in Acute

- Respiratory Distress Syndrome. *J. Immunol.* **2017**, *199* (6), 2043–2054.
<https://doi.org/10.4049/jimmunol.1700315>.
- (59) Lucido, M. J.; Orlando, B. J.; Vecchio, A. J.; Malkowski, M. G. The Crystal Structure of Aspirin Acetylated Human Cyclooxygenase-2: Insight into the Formation of Products with Reversed Stereochemistry. *Biochemistry* **2016**, *55* (8), 1226–1238.
<https://doi.org/10.1021/acs.biochem.5b01378>.THE.
- (60) Laube, M.; Kniess, T.; Pietzsch, J. Radiolabeled COX-2 Inhibitors for Non-Invasive Visualization of COX-2 Expression and Activity - A Critical Update. *Molecules* **2013**, *18* (6), 6311–6355. <https://doi.org/10.3390/molecules18066311>.
- (61) Jansen, S.; Stefan, C.; Creemers, J. W. M.; Waelkens, E.; Van Eynde, A.; Stalmans, W.; Bollen, M. Proteolytic Maturation and Activation of Autotaxin (NPP2), a Secreted Metastasis-Enhancing Lysophospholipase D. *J. Cell Sci.* **2005**, *118* (14), 3081–3089.
<https://doi.org/10.1242/jcs.02438>.
- (62) Ninou, I.; Magkrioti, C.; Aidinis, V. Autotaxin in Pathophysiology and Pulmonary Fibrosis. *Front. Med.* **2018**, *5* (JUN), 1–11. <https://doi.org/10.3389/fmed.2018.00180>.
- (63) Im, D. S. Pharmacological Tools for Lysophospholipid GPCRs: Development of Agonists and Antagonists for LPA and S1P Receptors. *Acta Pharmacol. Sin.* **2010**, *31* (9), 1213–1222. <https://doi.org/10.1038/aps.2010.135>.
- (64) Ishii, I.; Fukushima, N.; Ye, X.; Chun, J. Lysophospholipid Receptors: Signaling and Biology. *Annu. Rev. Biochem.* **2004**, *73* (1), 321–354.
<https://doi.org/10.1146/annurev.biochem.73.011303.073731>.
- (65) An, S.; Bleu, T.; Hallmark, O. G.; Goetzl, E. J. Characterization of a Novel Subtype of Human G Protein-Coupled Receptor for Lysophosphatidic Acid. *J. Biol. Chem.* **1998**, *273*

- (14), 7906–7910. <https://doi.org/10.1074/jbc.273.14.7906>.
- (66) Lee, H.; Goetzl, E. J.; Songzhu, A. Lysophosphatidic Acid and Sphingosine 1-Phosphate Stimulate Endothelial Cell Wound Healing. *Am. J. Physiol. - Cell Physiol.* **2000**, *278* (3 47-3), 612–618.
- (67) Benesch, M. G. K.; Tang, X.; Brindley, D. N. Autotaxin and Breast Cancer : Towards Overcoming Treatment Barriers and Sequelae. **2020**, 1–18.
- (68) Balazs, L.; Okolicany, J.; Ferrebee, M.; Tolley, B.; Tigyi, G. Topical Application of the Phospholipid Growth Factor Lysophosphatidic Acid Promotes Wound Healing *in Vivo*. *Am. J. Physiol. - Regul. Integr. Comp. Physiol.* **2001**, *280* (2 49-2), 466–472. <https://doi.org/10.1152/ajpregu.2001.280.2.r466>.
- (69) Benesch, M. G. K.; Macintyre, I. T. K.; McMullen, T. P. W.; Brindley, D. N. Coming of Age for Autotaxin and Lysophosphatidate Signaling: Clinical Applications for Preventing, Detecting and Targeting Tumor-Promoting Inflammation. *Cancers (Basel)*. **2018**, *10* (3). <https://doi.org/10.3390/cancers10030073>.
- (70) Benesch, M. G. K.; Zhao, Y. Y.; Curtis, J. M.; McMullen, T. P. W.; Brindley, D. N. Regulation of Autotaxin Expression and Secretion by Lysophosphatidate and Sphingosine 1-Phosphate. *J. Lipid Res.* **2015**, *56* (6), 1134–1144. <https://doi.org/10.1194/jlr.M057661>.
- (71) Ray, R.; Rai, V. Lysophosphatidic Acid Converts Monocytes into Macrophages in Both Mice and Humans. *Blood* **2017**, *129* (9), 1177–1183. <https://doi.org/10.1182/blood-2016-10-743757>.
- (72) Knowlden, S.; Georas, S. The Autotaxin-LPA Axis Emerges as a Novel Regulator of Lymphocyte Homing and Inflammation. *J. Immunol.* **2014**, *192* (3), 851–857. <https://doi.org/10.1038/mp.2011.182.doi>.

- (73) Euer, N.; Schwirzke, M.; Evtimova, V.; Burtscher, H.; Jarsch, M.; Tarin, D.; Weidle, U. H. Identification of Genes Associated with Metastasis of Mammary Carcinoma in Metastatic versus Non-Metastatic Cell Lines. *Anticancer Res.* **2002**, *22* (2A), 733–740.
- (74) Wu, T.; Kooi, C. Vander; Shah, P.; Charnigo, R.; Huang, C.; Smyth, S. S.; Morris, A. J. Integrin-Mediated Cell Surface Recruitment of Autotaxin Promotes Persistent Directional Cell Migration. *FASEB J.* **2014**, *28* (2), 861–870. <https://doi.org/10.1096/fj.13-232868>.
- (75) Barbayianni, E.; Kaffe, E.; Aidinis, V.; Kokotos, G. Autotaxin, a Secreted Lysophospholipase D, as a Promising Therapeutic Target in Chronic Inflammation and Cancer. *Prog. Lipid Res.* **2015**, *58*, 76–96. <https://doi.org/10.1016/j.plipres.2015.02.001>.
- (76) Benesch, M. G. K.; Ko, Y. M.; McMullen, T. P. W.; Brindley, D. N. Autotaxin in the Crosshairs: Taking Aim at Cancer and Other Inflammatory Conditions. *FEBS Lett.* **2014**, *588* (16), 2712–2727. <https://doi.org/10.1016/j.febslet.2014.02.009>.
- (77) Auberson, Y. P.; Briard, E.; Oberhauser, B.; Legrand, D. WO 2016/116875 A1, 2016.
- (78) Desroy, N.; Housseman, C.; Bock, X.; Joncour, A.; Bienvenu, N.; Cherel, L.; Labeguere, V.; Rondet, E.; Peixoto, C.; Grassot, J. M.; Picolet, O.; Annoot, D.; Triballeau, N.; Monjardet, A.; Wakselman, E.; Roncoroni, V.; Le Tallec, S.; Blaque, R.; Cottreaux, C.; Vandervoort, N.; Christophe, T.; Mollat, P.; Lamers, M.; Auberval, M.; Hrvacic, B.; Ralic, J.; Oste, L.; Van der Aar, E.; Brys, R.; Heckmann, B. Discovery of 2-[[2-Ethyl-6-[4-[2-(3-Hydroxyazetidino-1-Yl)-2-Oxoethyl]Piperazin-1-Yl]-8-Methylimidazo[1,2-a]Pyridin-3-Yl]Methylamino]-4-(4-Fluorophenyl)Thiazole-5-Carbonitrile (GLPG1690), a First-in-Class Autotaxin Inhibitor Undergoing Clinical Evaluation. *J. Med. Chem.* **2017**, *60* (9), 3580–3590. <https://doi.org/10.1021/acs.jmedchem.7b00032>.
- (79) Shah, P.; Cheasty, A.; Foxton, C.; Raynham, T.; Farooq, M.; Gutierrez, I. F.; Lejeune, A.;

- Pritchard, M.; Turnbull, A.; Pang, L.; Owen, P.; Boyd, S.; Stowell, A.; Jordan, A.; Hamilton, N. M.; Hitchin, J. R.; Stockley, M.; MacDonald, E.; Quesada, M. J.; Trivier, E.; Skeete, J.; Ovaa, H.; Moolenaar, W. H.; Ryder, H. Discovery of Potent Inhibitors of the Lysophospholipase Autotaxin. *Bioorganic Med. Chem. Lett.* **2016**, *26* (22), 5403–5410. <https://doi.org/10.1016/j.bmcl.2016.10.036>.
- (80) Madan, D.; Ferguson, C. G.; Lee, W. Y.; Prestwich, G. D.; Testa, C. A. Non-Invasive Imaging of Tumors by Monitoring Autotaxin Activity Using an Enzyme-Activated near-Infrared Fluorogenic Substrate. *PLoS One* **2013**, *8* (11). <https://doi.org/10.1371/journal.pone.0079065>.
- (81) Briard, E.; Joshi, A. D.; Shanmukhappa, S.; Ilovich, O.; Auberson, Y. P. [¹⁸F]PRIMATX, a New Positron Emission Tomography Tracer for Imaging of Autotaxin in Lung Tissue and Tumor-bearing Mice. *ChemMedChem* **2019**, *14* (16), 1493–1502. <https://doi.org/10.1002/cmdc.201900297>.
- (82) Ye, X.; Hama, K.; Contos, J. J. A.; Anliker, B.; Inoue, A.; Skinner, M. K.; Suzuki, H.; Amane, T.; Kennedy, G.; Arai, H.; Aoki, J.; Chun, J. LPA3-Mediated Lysophosphatitic Acid Signalling in Embryo Implantation and Spacing. *Lett. to Nat.* **2005**, *435* (May), 104–108.
- (83) Aikawa, S.; Kano, K.; Inoue, A.; Wang, J.; Saigusa, D.; Nagamatsu, T.; Hirota, Y.; Fujii, T.; Tsuchiya, S.; Taketomi, Y. Autotaxin – Lysophosphatidic Acid – LPA 3 Signaling at the Embryo-Epithelial Boundary Controls Decidualization Pathways. **2017**, *36* (14), 2146–2160. <https://doi.org/10.15252/emj.201696290>.
- (84) Nochi, H.; Tomura, H.; Tobo, M.; Tanaka, N.; Sato, K.; Shinozaki, T.; Kobayashi, T.; Takagishi, K.; Ohta, H.; Okajima, F.; Tamoto, K. Stimulatory Role of Lysophosphatidic

Acid in Cyclooxygenase-2 Induction by Synovial Fluid of Patients with Rheumatoid Arthritis in Fibroblast-like Synovial Cells. *J. Immunol.* **2008**, *181* (7), 511–5119.

<https://doi.org/10.4049/jimmunol.181.7.5111>.

(85) Das, B. K. *Positron Emission Tomography*; 2015.

<https://doi.org/10.1002/9781444303254.ch133>.

(86) Bailey, D. L.; Townsend, D. W.; Valk, P. E.; Maisey, M. N. *Positron Emission Tomography Basic Sciences*; Springer-Verlag: London, 2005.

<https://doi.org/10.1016/B978-0-12-385157-4.00203-7>.

(87) Alam, I. S.; Arshad, M. A.; Nguyen, Q. D.; Aboagye, E. O. Radiopharmaceuticals as Probes to Characterize Tumour Tissue. *Eur. J. Nucl. Med. Mol. Imaging* **2015**, *42* (4), 537–561. <https://doi.org/10.1007/s00259-014-2984-3>.

Chapter 2

- 1) Liu, Y.; Sun, H.; Hu, M.; Zhang, Y.; Chen, S.; Tighe, S.; Zhu, Y. The Role of Cyclooxygenase-2 in Colorectal Carcinogenesis. *Clin. Colorectal Cancer* **2017**, *16* (3), 165–172. <https://doi.org/10.1016/j.clcc.2016.09.012>.
- (2) Garg, R.; Blando, J. M.; Perez, C. J.; Lal, P.; Feldman, M. D.; Smyth, E. M.; Ricciotti, E.; Grosser, T.; Benavides, F.; Kazanietz, M. G. COX-2 Mediates pro-Tumorigenic Effects of PKC ϵ in Prostate Cancer. *Oncogene* **2018**, *37* (34), 4735–4749. <https://doi.org/10.1038/s41388-018-0318-9>.
- (3) Bos, P. D.; Zhang, X. H. F.; Nadal, C.; Shu, W.; Gomis, R. R.; Nguyen, D. X.; Minn, A. J.; Van De Vijver, M. J.; Gerald, W. L.; Foekens, J. A.; Massagué, J. Genes That Mediate Breast Cancer Metastasis to the Brain. *Nature* **2009**, *459* (7249), 1005–1009. <https://doi.org/10.1038/nature08021>.
- (4) Ren, R.; Charles, P. C.; Zhang, C.; Wu, Y.; Wang, H.; Patterson, C. Gene Expression Profiles Identify a Role for Cyclooxygenase 2-Dependent Prostanoid Generation in BMP6-Induced Angiogenic Responses. *Blood* **2007**, *109* (7), 2847–2853. <https://doi.org/10.1182/blood-2006-08-039743>.
- (5) Tsujii, M.; Kawano, S.; Tsuji, S.; Sawaoka, H.; Hori, M.; DuBois, R. N. Cyclooxygenase Regulates Angiogenesis Induced by Colon Cancer Cells. *Cell* **1998**, *93* (5), 705–716. [https://doi.org/10.1016/S0092-8674\(00\)81433-6](https://doi.org/10.1016/S0092-8674(00)81433-6).
- (6) Li, W.; Mao, Z.; Fan, X.; Cui, L.; Wang, X. Cyclooxygenase 2 Promoted the Tumorigenicity of Pancreatic Cancer Cells. *Tumor Biol.* **2014**, *35* (3), 2271–2278. <https://doi.org/10.1007/s13277-013-1301-2>.
- (7) Secchiero, P.; Barbarotto, E.; Gonelli, A.; Tiribelli, M.; Zerbinati, C.; Celeghini, C.;

- Agostinelli, C.; Pileri, S. A.; Zauli, G. Potential Pathogenetic Implications of Cyclooxygenase-2 Overexpression in B Chronic Lymphoid Leukemia Cells. *Am. J. Pathol.* **2005**, *167* (6), 1599–1607. <https://doi.org/10.1080/00102202.2010.498676>.
- (8) Bell, E.; Ponthan, F.; Whitworth, C.; Tweddle, D. A.; Lunec, J.; Redfern, C. P. F. COX2 Expression in Neuroblastoma Increases Tumorigenicity but Does Not Affect Cell Death in Response to the COX2 Inhibitor Celecoxib. *Clin. Exp. Metastasis* **2014**, *31* (6), 651–659. <https://doi.org/10.1007/s10585-014-9656-3>.
- (9) Méric, J. B.; Rottey, S.; Olausson, K.; Soria, J. C.; Khayat, D.; Rixe, O.; Spano, J. P. Cyclooxygenase-2 as a Target for Anticancer Drug Development. *Crit. Rev. Oncol. Hematol.* **2006**, *59* (1), 51–64. <https://doi.org/10.1016/j.critrevonc.2006.01.003>.
- (10) Tsujii, M.; DuBois, R. N. Alterations in Cellular Adhesion and Apoptosis in Epithelial Cells Overexpressing Prostaglandin Endoperoxide Synthase 2. *Cell* **1995**, *83* (3), 493–501. [https://doi.org/10.1016/0092-8674\(95\)90127-2](https://doi.org/10.1016/0092-8674(95)90127-2).
- (11) Valesini, G. Selective Cyclooxygenase-2 Inhibition: Biological and Clinical Effects. *Isr. Med. Assoc. J.* **2000**, *2* (11), 841–847.
- (12) Smith, W. L.; DeWitt, D. L.; Garavito, R. M. Cyclooxygenases : Structural, Cellular, and Molecular Biology. *Annu. Rev. Biochem.* **2000**, *69* (1), 145–182. <https://doi.org/10.1146/annurev.biochem.69.1.145>.
- (13) Anderson, R. J.; Berl, T.; McDonald, K. M.; Schrier, R. W. Prostaglandins: Effects on Blood Pressure, Renal Blood Flow, Sodium and Water Excretion. *Kidney Int.* **1976**, *10* (3), 205–215. <https://doi.org/10.1038/ki.1976.99>.
- (14) Adegboyega, P. A.; Ololade, O. Immunohistochemical Expression of Cyclooxygenase-2 in Normal Kidneys. *Appl. Immunohistochem. Mol. Morphol.* **2004**, *12* (1), 71–74.

<https://doi.org/10.1097/00129039-200403000-00013>.

- (15) Willoughby, D. A.; Moore, A. R.; Colville-Nash, P. R. COX-1, COX-2, and COX-3 and the Future Treatment of Chronic Inflammatory Disease. *Lancet* **2000**, *355* (9204), 646–648. [https://doi.org/10.1016/S0140-6736\(99\)12031-2](https://doi.org/10.1016/S0140-6736(99)12031-2).
- (16) Chandrasekharan, N. V.; Dai, H.; Roos, K. L. T.; Evanson, N. K.; Tomsik, J.; Elton, T. S.; Simmons, D. L. COX-3, a Cyclooxygenase-1 Variant Inhibited by Acetaminophen and Other Analgesic/Antipyretic Drugs: Cloning, Structure, and Expression. *Proc. Natl. Acad. Sci.* **2002**, *99* (21), 13926–13931. <https://doi.org/10.1073/pnas.162468699>.
- (17) Crofford, L. J.; Tan, B.; McCarthy, C. J.; Hla, T. Involvement of Nuclear Factor KB in the Regulation of Cyclooxygenase-2 Expression by Interleukin-1 in Rheumatoid Synoviocytes. *Arthritis Rheum.* **1997**, *40* (2), 226–236. <https://doi.org/10.1002/art.1780400207>.
- (18) Tsirka, S. E.; Rogove, A. D.; Strickland, S. Neuronal Cell Death and TPA. *Nature* **1996**, *384* (6605), 123–124.
- (19) Dubois, R. N.; Abramson, S. B.; Crofford, L.; Gupta, R. A.; Simon, L. S.; Van De Putte, L. B.; Lipsky, P. E. Cyclooxygenase in Biology and Disease. *FASEB J.* **1998**, *12* (12), 1063–1073. <https://doi.org/9737710>.
- (20) Zhang, J.; Ding, E. L.; Song, Y. Adverse Effects of Cyclooxygenase 2 Inhibitors on Renal and Arrhythmia Events. *J. Am. Med. Assoc.* **2006**, *296* (13), 1619–1632. <https://doi.org/10.1001/jama.296.13.jrv60015>.
- (21) Davies, N. M.; Jamali, F. COX-2 Selective Inhibitors Cardiac Toxicity: Getting to the Heart of the Matter. *J. Pharm. Pharm. Sci.* **2004**, *7* (3), 332–336.
- (22) Gupta, G. P.; Nguyen, D. X.; Chiang, A. C.; Bos, P. D.; Kim, J. Y.; Nadal, C.; Gomis, R. R.; Manova-Todorova, K.; Massagué, J. Mediators of Vascular Remodelling Co-Opted for

- Sequential Steps in Lung Metastasis. *Nature* **2007**, *446* (7137), 765–770.
<https://doi.org/10.1038/nature05760>.
- (23) Johnsen, J. I.; Lindskog, M.; Ponthan, F.; Pettersen, I.; Elfman, L.; Orrego, A.; Sveinbjornsson, B.; Kogner, P. Cyclooxygenase-2 Is Expressed in Neuroblastoma , and Nonsteroidal Anti-Inflammatory Drugs Induce Apoptosis and Inhibit Tumor Growth *in Vivo*. **2004**, 7210–7215.
- (24) Ghosh, N.; Chaki, R.; Mandal, V.; Mandal, S. C. COX-2 as a Target for Cancer Chemotherapy. *Pharmacol. Reports* **2010**, *62* (2), 233–244. [https://doi.org/10.1016/S1734-1140\(10\)70262-0](https://doi.org/10.1016/S1734-1140(10)70262-0).
- (25) Inoue, H.; Taba, Y.; Miwa, Y.; Yokota, C.; Miyagi, M.; Sasaguri, T. Transcriptional and Posttranscriptional Regulation of Cyclooxygenase-2 Expression by Fluid Shear Stress in Vascular Endothelial Cells. *Arterioscler. Thromb. Vasc. Biol.* **2002**, *22* (9), 1415–1420. <https://doi.org/10.1161/01.ATV.0000028816.13582.13>.
- (26) Hendriks, R. J.; van der Leest, M. M. G.; Dijkstra, S.; Barentsz, J. O.; Van Criekinge, W.; Hulsbergen-van de Kaa, C. A.; Schalken, J. A.; Mulders, P. F. A.; van Oort, I. M. A Urinary Biomarker-Based Risk Score Correlates with Multiparametric MRI for Prostate Cancer Detection. *Prostate* **2017**, *77* (14), 1401–1407. <https://doi.org/10.1002/pros.23401>.
- (27) Laube, M.; Kniess, T.; Pietzsch, J. Radiolabeled COX-2 Inhibitors for Non-Invasive Visualization of COX-2 Expression and Activity - A Critical Update. *Molecules* **2013**, *18* (6), 6311–6355. <https://doi.org/10.3390/molecules18066311>.
- (28) Zhang, Q.; Han, Z.; Tao, J.; Zhang, W.; Li, P.; Tang, L.; Gu, Y. A Novel Near-Infrared Fluorescent Probe for Monitoring Cyclooxygenase-2 in Inflammation and Tumor. *J. Biophotonics* **2018**, *11* (6), 1–9. <https://doi.org/10.1002/jbio.201700339>.

- (29) Tietz, O.; Wuest, M.; Marshall, A.; Glubrecht, D.; Hamann, I.; Wang, M.; Bergman, C.; Way, J. D.; Wuest, F. PET Imaging of Cyclooxygenase-2 (COX-2) in a Pre-Clinical Colorectal Cancer Model. *EJNMMI Res.* **2016**, *6* (1). <https://doi.org/10.1186/s13550-016-0192-9>.
- (30) McCarthy, T. J.; Sheriff, A. U.; Graneto, M. J.; Talley, J. J.; Welch, M. J. Radiosynthesis, *in Vitro* Validation, and *in Vivo* Evaluation of ^{18}F -Labeled COX-1 and COX-2 Inhibitors. *J. Nucl. Med.* **2002**, *43* (1), 117–124.
- (31) Kaur, J.; Tietz, O.; Bhardwaj, A.; Marshall, A.; Way, J.; Wuest, M.; Wuest, F. Design, Synthesis, and Evaluation of an ^{18}F -Labeled Radiotracer Based on Celecoxib-NBD for Positron Emission Tomography (PET) Imaging of Cyclooxygenase-2 (COX-2). *ChemMedChem* **2015**, *10* (10), 1635–1640. <https://doi.org/10.1002/cmdc.201500287>.
- (32) Uddin, M. J.; Crews, B. C.; Ghebreselasie, K.; Huda, I.; Kingsley, P. J.; Ansari, M. S.; Tantawy, M. N.; Reese, J.; Marnett, L. J. Fluorinated COX-2 Inhibitors as Agents in PET Imaging of Inflammation and Cancer. *Cancer Prev. Res.* **2011**, *4* (10), 1536–1545. <https://doi.org/10.1158/1940-6207.CAPR-11-0120>.
- (33) Uddin, M. J.; Crews, B. C.; Ghebreselasie, K.; Tantawy, M. N.; Marnett, L. J. [^{123}I]-Celecoxib Analogues as SPECT Tracers of Cyclooxygenase-2 in Inflammation. *ACS Med. Chem. Lett.* **2011**, *2* (2), 160–164. <https://doi.org/10.1021/ml100232q>.
- (34) Schuller, H. M.; Kabalka, G.; Smith, G.; Mereddy, A.; Akula, M.; Cekanova, M. Detection of Overexpressed COX-2 in Precancerous Lesions of Hamster Pancreas and Lungs by Molecular Imaging: Implications for Early Diagnosis and Prevention. *ChemMedChem* **2006**, *1* (6), 603–610. <https://doi.org/10.1002/cmdc.200500032>.
- (35) Prabhakaran, J.; Majo, V. J.; Simpson, N. R.; Van Heertum, R. L.; Mann, J. J.; Kumar, J. S.

- D. Synthesis of [¹¹C]Celecoxib: A Potential PET Probe for Imaging COX-2 Expression. *J. Label. Compd. Radiopharm.* **2005**, *48* (12), 887–895. <https://doi.org/10.1002/jlcr.1002>.
- (36) De Vries, E. F. J.; Van Waarde, A.; Buursma, A. R.; Vaalburg, W. Synthesis and *in Vivo* Evaluation of ¹⁸F-Desbromo-Dup-697 as a PET Tracer for Cyclooxygenase-2 Expression. *J. Nucl. Med.* **2003**, *44* (10), 1700–1706.
- (37) Wuest, F.; Aileen, H.; Metz, P. Synthesis of ¹⁸F-Labelled Cyclooxygenase-2 (COX-2) Inhibitors. **2005**, *2*, 503–507.
- (38) Wuest, F.; Kniess, T.; Bergmann, R.; Pietzsch, J. Synthesis and Evaluation *in Vitro* and *in Vivo* of a ¹¹C-Labeled Cyclooxygenase-2 (COX-2) Inhibitor. *Bioorganic Med. Chem.* **2008**, *16* (16), 7662–7670. <https://doi.org/10.1016/j.bmc.2008.07.016>.
- (39) Kuge, Y.; Katada, Y.; Shimonaka, S.; Temma, T.; Kimura, H.; Kiyono, Y.; Yokota, C.; Minematsu, K.; Seki, K. I.; Tamaki, N.; Ohkura, K.; Saji, H. Synthesis and Evaluation of Radioiodinated Cyclooxygenase-2 Inhibitors as Potential SPECT Tracers for Cyclooxygenase-2 Expression. *Nucl. Med. Biol.* **2006**, *33* (1), 21–27. <https://doi.org/10.1016/j.nucmedbio.2005.10.004>.
- (40) Bhardwaj, A.; Kaur, J.; Wuest, M.; Wuest, F. *In Situ* Click Chemistry Generation of Cyclooxygenase-2 Inhibitors. *Nat. Commun.* **2017**, *8* (1), 1–13. <https://doi.org/10.1038/s41467-016-0009-6>.
- (41) Rostovtsev, V. V.; Green, L. G.; Fokin, V. V.; Sharpless, K. B. A Stepwise Huisgen Cycloaddition Process: Copper(I)-Catalyzed Regioselective “Ligation” of Azides and Terminal Alkynes. *Angew. Chemie* **2002**, *41* (14), 2596–2599. <https://doi.org/10.1021/jo011148j>.
- (42) Zischler, J.; Kolks, N.; Modemann, D.; Neumaier, B.; Zlatopolskiy, B. D. Alcohol-

- Enhanced Cu-Mediated Radiofluorination. *Chem. - A Eur. J.* **2017**, *23* (14), 3251–3256.
<https://doi.org/10.1002/chem.201604633>.
- (43) Wilson, A. A.; Jin, L.; Garcia, A.; Dasilva, J. N.; Houle, S. An Admonition When Measuring the Lipophilicity of Radiotracers Using Counting Techniques. **2001**, *54*, 203–208.
- (44) Bhardwaj, A.; Kaur, J.; Bergman, C.; Wuest, F. In-Situ Click Chemistry for the Design and Synthesis of Highly Potent Radiotracers for PET Imaging of Cyclooxygenase-2. In *The 22nd International Symposium on Radiopharmaceutical Sciences (ISRS 2017)*; Dresden, Germany, 2017; p S 483. <https://doi.org/10.1002/jlcr.3508>.
- (45) Frost, S. C.; McKenna, R. *Physiological Functions of the Alpha Class of Carbonic Anhydrases*; 2014; Vol. 75. https://doi.org/10.1007/978-94-007-7359-2_2.
- (46) Weber, A.; Casini, A.; Heine, A.; Kuhn, D.; Supuran, C. T.; Scozzafava, A.; Klebe, G. Unexpected Nanomolar Inhibition of Carbonic Anhydrase by COX-2-Selective Celecoxib: New Pharmacological Opportunities Due to Related Binding Site Recognition. *J. Med. Chem.* **2004**, *47* (3), 550–557. <https://doi.org/10.1021/jm030912m>.
- (47) Brooks, A.; Topczewski, J.; Ichiishi, N.; Sanford, M.; Scott, P. Late-Stage [¹⁸F]Fluorination: New Solutions to Old Problems. *Chem. Sci.* **2014**, *5* (12), 4545–4553. <https://doi.org/10.1039/C4SC02099E>.
- (48) Hanif, R.; Pittas, A.; Feng, Y.; Koutsos, M. I.; Qiao, L.; Staiano-Coico, L.; Shiff, S. I.; Rigas, B. Effects of Nonsteroidal Anti-Inflammatory Drugs on Proliferation and on Induction of Apoptosis in Colon Cancer Cells by a Prostaglandin-Independent Pathway. *Biochem. Pharmacol.* **1996**, *52* (2), 237–245.
- (49) Elder, D. J. E.; Halton, D. E.; Hague, A.; Paraskeva, C. Induction of Apoptotic Cell Death in Human Colorectal Carcinoma Cell Lines by a Cyclooxygenase-2 (COX-2)-Selective

- Nonsteroidal Anti-Inflammatory Drug: Independence from COX-2 Protein Expression. *Clin. Cancer Res.* **1997**, *3*, 1679–1683.
- (50) Rigas, B.; Shiff, S. J. Is Inhibition of Cyclooxygenase Required for the Chemopreventive Effect of NSAIDs in Colon Cancer? A Model Reconciling the Current Contradiction. *Med. Hypotheses* **2000**, *54* (2), 210–215. <https://doi.org/10.1054/mehy.1999.0023>.
- (51) Grösch, S.; Maier, T. J.; Schiffmann, S.; Geisslinger, G. Cyclooxygenase-2 (COX-2) - Independent Anticarcinogenic Effects of Selective COX-2 Inhibitors. *J. Natl. Cancer Inst.* **2006**, *98* (11), 736–747. <https://doi.org/10.1093/jnci/djj206>.
- (52) Assefnia, S.; Dakshanamurthy, S.; Guidry Auvil, J. M.; Hampel, C.; Anastasiadis, P. Z.; Kallakury, B.; Uren, A.; Foley, D. W.; Brown, M. L.; Shapiro, L.; Brenner, M.; Haigh, D.; Byers, S. W. Cadherin-11 in Poor Prognosis Malignancies and Rheumatoid Arthritis: Common Target, Common Therapies. *Oncotarget* **2014**, *5* (6), 1458–1474. <https://doi.org/10.18632/oncotarget.1538>.
- (53) Thaher, B. A.; Koch, P.; Schattel, V.; Laufer, S. Role of the Hydrogen Bonding Heteroatom-Lys53 Interaction between the P38r Mitogen-Activated Protein (MAP) Kinase and Pyridinyl-Substituted 5-Membered Heterocyclic Ring Inhibitors. *J. Med. Chem.* **2009**, *52*, 2613–2617. <https://doi.org/10.1007/BF02886547>.
- (54) Kazmi, F.; Hensley, T.; Pope, C.; Funk, R. S.; Loewen, G. J.; Buckley, D. B.; Parkinson, A. Lysosomal Sequestration (Trapping) of Lipophilic Amine (Cationic Amphiphilic) Drugs in Immortalized Human Hepatocytes (Fa2N-4 Cells). *Drug Metab. Dispos.* **2013**, *41* (4), 897–905. <https://doi.org/10.1124/dmd.112.050054>.
- (55) Banks, W. A. Characteristics of Compounds That Cross the Blood-Brain Barrier. *BMC Neurol.* **2009**, *9* (SUPPL. 1), 5–9. <https://doi.org/10.1186/1471-2377-9-S1-S3>.

- (56) Kumar, J. S. D.; Zanderigo, F.; Prabhakaran, J.; Rubin-Falcone, H.; Parsey, R. V.; Mann, J. J. *In Vivo* Evaluation of [¹¹C]TMI, a COX-2 Selective PET Tracer, in Baboons. *Bioorganic Med. Chem. Lett.* **2018**, *28* (23–24), 3592–3595. <https://doi.org/10.1016/j.bmcl.2018.10.049>.
- (57) Lebedev, A.; Jiao, J.; Lee, J.; Yang, F.; Allison, N.; Herschman, H.; Sadeghi, S. Radiochemistry on Electrodes: Synthesis of An ¹⁸F-Labelled and *in Vivo* Stable COX-2 Inhibitor. *PLoS One* **2017**, *12* (5), 1–18. <https://doi.org/10.1371/journal.pone.0176606>.
- (58) Prabhakaran, J.; Underwood, M.; Zanderigo, F.; Simpson, N. R.; Cooper, A. R.; Matthew, J.; Rubin-Falcone, H.; Parsey, R. V.; Mann, J. J.; Dileep Kumar, J. S. Radiosynthesis and *in Vivo* Evaluation of [¹¹C]MOV as a PET Imaging Agent for COX-2. *Bioorganic Med. Chem. Lett.* **2018**, *28* (14), 2432–2435. <https://doi.org/10.1016/j.bmcl.2018.06.015>.
- (59) Zhang, F.; Hao, G.; Shao, M.; Nham, K.; An, Y.; Wang, Q.; Zhu, Y.; Kusminski, C. M.; Hassan, G.; Gupta, R. K.; Zhai, Q.; Sun, X.; Scherer, P. E.; Oz, O. K. An Adipose Tissue Atlas: An Image-Guided Identification of Human-like BAT and Beige Depots in Rodents. *Cell Metab.* **2018**, *27* (1), 252–262.e3. <https://doi.org/10.1016/j.cmet.2017.12.004>.
- (60) Enerbäck, S. Clinical Implications of Basic Research The Origins of Brown Adipose Tissue. *N. Engl. J. Med.* **2009**, 2021–2023.
- (61) Himmelsbach, M.; Varesio, E.; Hopfgartner, G. Liquid Extraction Surface Analysis (LESA) of Hydrophobic Tlc Plates Coupled to Chip-Based Nanoelectrospray Highresolution Mass Spectrometry. *Chimia (Aarau).* **2014**, *68* (3), 150–154. <https://doi.org/10.2533/chimia.2014.150>.
- (62) Farmer, S. R. Molecular Determinants of Brown Adipocyte Formation and Function. *Genes Dev.* **2008**, *22* (10), 1269–1275. <https://doi.org/10.1101/gad.1681308>.

(63) Eskildsen, J.; Wenzel Tornoe, C. Pyrazolopyridines Useful in the Treatment of the Central Nervous System. WO 2013/004617 A1, 2013.

Chapter 3

- (1) Akira, T.; Kengo, H.; Kenji, F.; Hiroaki, T. Involvement of Lysophospholipase D in the Production of Lysophosphatidic Acid in Rat Plasma. *Biochim. Biophys. Acta (BBA)/Lipids Lipid Metab.* **1986**, *875* (1), 31–38. [https://doi.org/10.1016/0005-2760\(86\)90007-X](https://doi.org/10.1016/0005-2760(86)90007-X).
- (2) Stefan, C.; Jansen, S.; Bollen, M. NPP-Type Ectophosphodiesterases: Unity in Diversity. *Trends Biochem. Sci.* **2005**, *30* (10), 542–550. <https://doi.org/10.1016/j.tibs.2005.08.005>.
- (3) Benesch, M. G. K.; Ko, Y. M.; McMullen, T. P. W.; Brindley, D. N. Autotaxin in the Crosshairs: Taking Aim at Cancer and Other Inflammatory Conditions. *FEBS Lett.* **2014**, *588* (16), 2712–2727. <https://doi.org/10.1016/j.febslet.2014.02.009>.
- (4) Ishii, I.; Fukushima, N.; Ye, X.; Chun, J. Lysophospholipid Receptors: Signaling and Biology. *Annu. Rev. Biochem.* **2004**, *73* (1), 321–354. <https://doi.org/10.1146/annurev.biochem.73.011303.073731>.
- (5) Tanaka, M.; Okudaira, S.; Kishi, Y.; Ohkawa, R.; Iseki, S.; Ota, M.; Noji, S.; Yatomi, Y.; Aoki, J.; Arai, H. Autotaxin Stabilizes Blood Vessels and Is Required for Embryonic Vasculature by Producing Lysophosphatidic Acid. *J. Biol. Chem.* **2006**, *281* (35), 25822–25830. <https://doi.org/10.1074/jbc.M605142200>.
- (6) Lee, H.; Goetzl, E. J.; Songzhu, A. Lysophosphatidic Acid and Sphingosine 1-Phosphate Stimulate Endothelial Cell Wound Healing. *Am. J. Physiol. - Cell Physiol.* **2000**, *278* (3 47-3), 612–618.
- (7) Nochi, H.; Tomura, H.; Tobo, M.; Tanaka, N.; Sato, K.; Shinozaki, T.; Kobayashi, T.; Takagishi, K.; Ohta, H.; Okajima, F.; Tamoto, K. Stimulatory Role of Lysophosphatidic Acid in Cyclooxygenase-2 Induction by Synovial Fluid of Patients with Rheumatoid Arthritis in Fibroblast-like Synovial Cells. *J. Immunol.* **2008**, *181* (7), 511–5119.

<https://doi.org/10.4049/jimmunol.181.7.5111>.

- (8) Orosa, B.; García, S.; Martínez, P.; González, A.; Gómez-Reino, J. J.; Conde, C. Lysophosphatidic Acid Receptor Inhibition as a New Multipronged Treatment for Rheumatoid Arthritis. *Ann. Rheum. Dis.* **2014**, *73* (1), 298–305. <https://doi.org/10.1136/annrheumdis-2012-202832>.
- (9) Vial, C.; Zúñiga, L. M.; Cabello-Verrugio, C.; Cañón, P.; Fadic, R.; Brandan, E. Skeletal Muscle Cells Express the Profibrotic Cytokine Connective Tissue Growth Factor (CTGF/CCN2), Which Induces Their Dedifferentiation. *J. Cell. Physiol.* **2008**, *215* (2), 410–421. <https://doi.org/10.1002/jcp.21324>.
- (10) Euer, N.; Schwirzke, M.; Evtimova, V.; Burtscher, H.; Jarsch, M.; Tarin, D.; Weidle, U. H. Identification of Genes Associated with Metastasis of Mammary Carcinoma in Metastatic versus Non-Metastatic Cell Lines. *Anticancer Res.* **2002**, *22* (2A), 733–740.
- (11) Nikitopoulou, I.; Oikonomou, N.; Karouzakis, E.; Sevastou, I.; Nikolaidou-Katsaridou, N.; Zhao, Z.; Mersinias, V.; Armaka, M.; Xu, Y.; Masu, M.; Mills, G. B.; Gay, S.; Kollias, G.; Aidinis, V. Autotaxin Expression from Synovial Fibroblasts Is Essential for the Pathogenesis of Modeled Arthritis. *J. Exp. Med.* **2012**, *209* (5), 925–933. <https://doi.org/10.1084/jem.20112012>.
- (12) Knowlden, S.; Georas, S. The Autotaxin-LPA Axis Emerges as a Novel Regulator of Lymphocyte Homing and Inflammation. *J. Immunol.* **2014**, *192* (3), 851–857. <https://doi.org/10.1038/mp.2011.182.doi>.
- (13) Benesch, M. G. K.; Tang, X.; Dewald, J.; Dong, W. F.; Mackey, J. R.; Hemmings, D. G.; McMullen, T. P. W.; Brindley, D. N. Tumor-Induced Inflammation in Mammary Adipose Tissue Stimulates a Vicious Cycle of Autotaxin Expression and Breast Cancer Progression.

- FASEB J.* **2015**, *29* (9), 3990–4000. <https://doi.org/10.1096/fj.15-274480>.
- (14) Ikeda, H.; Yatomi, Y. Autotaxin in Liver Fibrosis. *Clin. Chim. Acta* **2012**, *413* (23–24), 1817–1821. <https://doi.org/10.1016/j.cca.2012.07.014>.
- (15) Kanaoka, M.; Yamaguchi, Y.; Komitsu, N.; Feghali-Bostwick, C. A.; Ogawa, M.; Arima, K.; Izuhara, K.; Aihara, M. Pro-Fibrotic Phenotype of Human Skin Fibroblasts Induced by Periostin via Modulating TGF- β Signaling. *J. Dermatol. Sci.* **2018**, *90* (2), 199–208. <https://doi.org/10.1016/j.jdermsci.2018.02.001>.
- (16) Coussens, L. M.; Werb, Z. Inflammation and Cancer. *Nature* **2002**, *420* (December), 406–415. <https://doi.org/10.1016/B978-0-12-374279-7.17002-X>.
- (17) Gun, S. Y.; Lee, S. W. L.; Sieow, J. L.; Wong, S. C. Targeting Immune Cells for Cancer Therapy. *Redox Biol.* **2019**, No. March, 101174. <https://doi.org/10.1016/j.redox.2019.101174>.
- (18) Hussain, S. P.; Hofseth, L. J.; Harris, C. C. Radical Causes of Cancer. *Nat. Rev. Cancer* **2003**, *3* (4), 276–285. <https://doi.org/10.1038/nrc1046>.
- (19) Hanahan, D.; Weinberg, R. A. Hallmarks of Cancer: The next Generation. *Cell* **2011**, *144* (5), 646–674. <https://doi.org/10.1016/j.cell.2011.02.013>.
- (20) Hausmann, J.; Kamtekar, S.; Christodoulou, E.; Day, J. E.; Wu, T.; Fulkerson, Z.; Albers, H. M. H. G.; Van Meeteren, L. A.; Houben, A. J. S.; Van Zeijl, L.; Jansen, S.; Andries, M.; Hall, T.; Pegg, L. E.; Benson, T. E.; Kasiem, M.; Harlos, K.; Kooi, C. W. V.; Smyth, S. S.; Ovaa, H.; Bollen, M.; Morris, A. J.; Moolenaar, W. H.; Perrakis, A. Structural Basis of Substrate Discrimination and Integrin Binding by Autotaxin. *Nat. Struct. Mol. Biol.* **2011**, *18* (2), 198–205. <https://doi.org/10.1038/nsmb.1980>.
- (21) Wu, T.; Kooi, C. Vander; Shah, P.; Charnigo, R.; Huang, C.; Smyth, S. S.; Morris, A. J.

- Integrin-Mediated Cell Surface Recruitment of Autotaxin Promotes Persistent Directional Cell Migration. *FASEB J.* **2014**, *28* (2), 861–870. <https://doi.org/10.1096/fj.13-232868>.
- (22) Stracke, M. L.; Krutzsch, H. C.; Unsworth, E. J.; Arestad, A.; Cioce, V.; Schiffmann, E.; Liotta, L. A. Identification, Purification, and Partial Sequence Analysis of Autotaxin, a Novel Motility-Stimulating Protein. *J. Biol. Chem.* **1992**, *267* (4), 2524–2529.
- (23) Leblanc, R.; Sahay, D.; Houssin, A.; Machuca-Gayet, I.; Peyruchaud, O. Autotaxin- β Interaction with the Cell Surface via Syndecan-4 Impacts on Cancer Cell Proliferation and Metastasis. *Oncotarget* **2018**, *9* (69), 33170–33185. <https://doi.org/10.18632/oncotarget.26039>.
- (24) Fulkerson, Z.; Wu, T.; Sunkara, M.; Kooi, C. Vander; Morris, A. J.; Smyth, S. S. Binding of Autotaxin to Integrins Localizes Lysophosphatidic Acid Production to Platelets and Mammalian Cells. *J. Biol. Chem.* **2011**, *286* (40), 34654–34663. <https://doi.org/10.1074/jbc.M111.276725>.
- (25) Benesch, M. G. K.; Ko, Y. M.; Tang, X.; Dewald, J.; Lopez-Campistrous, A.; Zhao, Y. Y.; Lai, R.; Curtis, J. M.; Brindley, D. N.; McMullen, T. P. W. Autotaxin Is an Inflammatory Mediator and Therapeutic Target in Thyroid Cancer. *Endocr. Relat. Cancer* **2015**, *22* (4), 593–607. <https://doi.org/10.1530/ERC-15-0045>.
- (26) Desroy, N.; Housseman, C.; Bock, X.; Joncour, A.; Bienvenu, N.; Cherel, L.; Labeguere, V.; Rondet, E.; Peixoto, C.; Grassot, J. M.; Picolet, O.; Annoot, D.; Triballeau, N.; Monjardet, A.; Wakselman, E.; Roncoroni, V.; Le Tallec, S.; Blanque, R.; Cottreaux, C.; Vandervoort, N.; Christophe, T.; Mollat, P.; Lamers, M.; Auberval, M.; Hrvacic, B.; Ralic, J.; Oste, L.; Van der Aar, E.; Brys, R.; Heckmann, B. Discovery of 2-[[2-Ethyl-6-[4-[2-(3-Hydroxyazetididin-1-Yl)-2-Oxoethyl]Piperazin-1-Yl]-8-Methylimidazo[1,2-a]Pyridin-3-

- Yl]Methylamino]-4-(4-Fluorophenyl)Thiazole-5-Carbonitrile (GLPG1690), a First-in-Class Autotaxin Inhibitor Undergoing Clinical Evaluation . *J. Med. Chem.* **2017**, *60* (9), 3580–3590. <https://doi.org/10.1021/acs.jmedchem.7b00032>.
- (27) Ye, X.; Hama, K.; Contos, J. J. A.; Anliker, B.; Inoue, A.; Skinner, M. K.; Suzuki, H.; Amane, T.; Kennedy, G.; Arai, H.; Aoki, J.; Chun, J. LPA3-Mediated Lysophosphatitic Acid Signalling in Embryo Implantation and Spacing. *Lett. to Nat.* **2005**, *435* (May), 104–108.
- (28) Aikawa, S.; Kano, K.; Inoue, A.; Wang, J.; Saigusa, D.; Nagamatsu, T.; Hirota, Y.; Fujii, T.; Tsuchiya, S.; Taketomi, Y. Autotaxin – Lysophosphatidic Acid – LPA 3 Signaling at the Embryo-Epithelial Boundary Controls Decidualization Pathways. **2017**, *36* (14), 2146–2160. <https://doi.org/10.15252/emj.201696290>.
- (29) Dubois, R. N.; Abramson, S. B.; Crofford, L.; Gupta, R. A.; Simon, L. S.; Van De Putte, L. B.; Lipsky, P. E. Cyclooxygenase in Biology and Disease. *FASEB J.* **1998**, *12* (12), 1063–1073. <https://doi.org/9737710>.
- (30) Ghosh, N.; Chaki, R.; Mandal, V.; Mandal, S. C. COX-2 as a Target for Cancer Chemotherapy. *Pharmacol. Reports* **2010**, *62* (2), 233–244. [https://doi.org/10.1016/S1734-1140\(10\)70262-0](https://doi.org/10.1016/S1734-1140(10)70262-0).
- (31) Wang, S.; Gao, H.; Zuo, J.; Gao, Z. Cyclooxygenase-2 Expression Correlates with Development, Progression, Metastasis, and Prognosis of Osteosarcoma: A Meta-Analysis and Trial Sequential Analysis. *FEBS Open Bio* **2019**, *9* (2), 226–240. <https://doi.org/10.1002/2211-5463.12560>.
- (32) Zhang, Q.; Han, Z.; Tao, J.; Zhang, W.; Li, P.; Tang, L.; Gu, Y. A Novel Near-Infrared Fluorescent Probe for Monitoring Cyclooxygenase-2 in Inflammation and Tumor. *J.*

- Biophotonics* **2018**, *11* (6), 1–9. <https://doi.org/10.1002/jbio.201700339>.
- (33) Tietz, O.; Kaur, J.; Bhardwaj, A.; Wuest, F. R. Pyrimidine-Based Fluorescent COX-2 Inhibitors: Synthesis and Biological Evaluation. *Org. Biomol. Chem.* **2016**, *14* (30), 7250–7257. <https://doi.org/10.1039/C6OB00493H>.
- (34) Tietz, O.; Wuest, M.; Marshall, A.; Glubrecht, D.; Hamann, I.; Wang, M.; Bergman, C.; Way, J. D.; Wuest, F. PET Imaging of Cyclooxygenase-2 (COX-2) in a Pre-Clinical Colorectal Cancer Model. *EJNMMI Res.* **2016**, *6* (1). <https://doi.org/10.1186/s13550-016-0192-9>.
- (35) Uddin, M. J.; Crews, B. C.; Ghebreselasie, K.; Huda, I.; Kingsley, P. J.; Ansari, M. S.; Tantawy, M. N.; Reese, J.; Marnett, L. J. Fluorinated COX-2 Inhibitors as Agents in PET Imaging of Inflammation and Cancer. *Cancer Prev. Res.* **2011**, *4* (10), 1536–1545. <https://doi.org/10.1158/1940-6207.CAPR-11-0120>.
- (36) Uddin, M. J.; Crews, B. C.; Ghebreselasie, K.; Tantawy, M. N.; Marnett, L. J. [123I]-Celecoxib Analogues as SPECT Tracers of Cyclooxygenase-2 in Inflammation. *ACS Med. Chem. Lett.* **2011**, *2* (2), 160–164. <https://doi.org/10.1021/ml100232q>.
- (37) Joncour, A.; Desroy, N.; Housseman, C.; Bock, X.; Bienvenu, N.; Cherel, L.; Labeguere, V.; Peixoto, C.; Annoot, D.; Lepissier, L.; Heiermann, J.; Hengeveld, W. J.; Pilzak, G.; Monjardet, A.; Wakselman, E.; Roncoroni, V.; Le Tallec, S.; Galien, R.; David, C.; Vandervoort, N.; Christophe, T.; Conrath, K.; Jans, M.; Wohlkonig, A.; Soror, S.; Steyaert, J.; Touitou, R.; Fleury, D.; Vercheval, L.; Mollat, P.; Triballeau, N.; Van Der Aar, E.; Brys, R.; Heckmann, B. Discovery, Structure-Activity Relationship, and Binding Mode of an Imidazo[1,2-a]Pyridine Series of Autotaxin Inhibitors. *J. Med. Chem.* **2017**, *60* (17), 7371–7392. <https://doi.org/10.1021/acs.jmedchem.7b00647>.

- (38) Rosse, G. Benzyl-Methyl-Tetrazole Ligands of Autotaxin for PET Imaging Techniques and Diagnostic. *ACS Med. Chem. Lett.* **2016**, *7* (12), 1016–1017. <https://doi.org/10.1021/acsmedchemlett.6b00408>.
- (39) Briard, E.; Joshi, A. D.; Shanmukhappa, S.; Ilovich, O.; Auberson, Y. P. [¹⁸F]PRIMATX, a New Positron Emission Tomography Tracer for Imaging of Autotaxin in Lung Tissue and Tumor-bearing Mice. *ChemMedChem* **2019**, *14* (16), 1493–1502. <https://doi.org/10.1002/cmdc.201900297>.
- (40) Wilson, A. A.; Jin, L.; Garcia, A.; Dasilva, J. N.; Houle, S. An Admonition When Measuring the Lipophilicity of Radiotracers Using Counting Techniques. **2001**, *54*, 203–208.
- (41) Madan, D.; Ferguson, C. G.; Lee, W. Y.; Prestwich, G. D.; Testa, C. A. Non-Invasive Imaging of Tumors by Monitoring Autotaxin Activity Using an Enzyme-Activated near-Infrared Fluorogenic Substrate. *PLoS One* **2013**, *8* (11). <https://doi.org/10.1371/journal.pone.0079065>.
- (42) Reich, R.; Hoffman, A.; Suresh, R. R.; Shai, O.; Frant, J.; Maresca, A.; Supuran, C. T.; Breuer, E. Carbamoylphosphonates Inhibit Autotaxin and Metastasis Formation *in Vivo*. *J. Enzyme Inhib. Med. Chem.* **2015**, *30* (5), 767–772. <https://doi.org/10.3109/14756366.2014.968146>.
- (43) Leblanc, R.; Houssin, A.; Peyruchaud, O. Platelets, Autotaxin and Lysophosphatidic Acid Signalling: Win-Win Factors for Cancer Metastasis. *Br. J. Pharmacol.* **2018**, *175* (15), 3100–3110. <https://doi.org/10.1111/bph.14362>.
- (44) Kazmi, F.; Hensley, T.; Pope, C.; Funk, R. S.; Loewen, G. J.; Buckley, D. B.; Parkinson, A. Lysosomal Sequestration (Trapping) of Lipophilic Amine (Cationic Amphiphilic) Drugs in Immortalized Human Hepatocytes (Fa2N-4 Cells). *Drug Metab. Dispos.* **2013**, *41* (4), 897–

905. <https://doi.org/10.1124/dmd.112.050054>.
- (45) Schmid, R.; Wolf, K.; Robering, J. W.; Strauß, S.; Strissel, P. L.; Strick, R.; Rübner, M.; Fasching, P. A.; Horch, R. E.; Kremer, A. E.; Boos, A. M.; Weigand, A. ADSCs and Adipocytes Are the Main Producers in the Autotaxin-Lysophosphatidic Acid Axis of Breast Cancer and Healthy Mammary Tissue *in Vitro*. *BMC Cancer* **2018**, *18* (1), 1–11. <https://doi.org/10.1186/s12885-018-5166-z>.
- (46) Giganti, A.; Rodriguez, M.; Fould, B.; Moulharat, N.; Coge, F.; Chomarat, P.; Galizzi, J. P.; Valet, P.; Saulnier-Blache, J. S.; Boutin, J. A.; Ferry, G. Murine and Human Autotaxin α , β , and γ Isoforms: Gene Organization, Tissue Distribution, and Biochemical Characterization. *J. Biol. Chem.* **2008**, *283* (12), 7776–7789. <https://doi.org/10.1074/jbc.M708705200>.
- (47) Nishioka, T.; Arima, N.; Kano, K.; Hama, K.; Itai, E.; Yukiura, H.; Kise, R.; Inoue, A.; Kim, S. H.; Solnica-Krezel, L.; Moolenaar, W. H.; Chun, J.; Aoki, J. ATX-LPA 1 Axis Contributes to Proliferation of Chondrocytes by Regulating Fibronectin Assembly Leading to Proper Cartilage Formation. *Sci. Rep.* **2016**, *6* (March), 1–15. <https://doi.org/10.1038/srep23433>.
- (48) Kawagoe, H.; Stracke, M. L.; Nakamura, H.; Sano, K. Expression and Transcriptional Regulation of the PD-1 α /Autotaxin Gene in Neuroblastoma. *Cancer Res.* **1997**, *57* (12), 2516–2521.
- (49) Hoelzinger, D. B.; Nakada, M.; Demuth, T.; Rosensteel, T.; Reavie, L. B.; Berens, M. E. Autotaxin: A Secreted Autocrine/Paracrine Factor That Promotes Glioma Invasion. *J. Neurooncol.* **2008**, *86* (3), 297–309. <https://doi.org/10.1007/s11060-007-9480-6>.
- (50) Herr, D. R.; Chew, W. S.; Satish, R. L.; Ong, W.-Y. Pleotropic Roles of Autotaxin in the

Nervous System Present Opportunities for the Development of Novel Therapeutics for Neurological Diseases. *Mol. Neurobiol.* **2019**. [https://doi.org/10.1007/s12035-019-01719-](https://doi.org/10.1007/s12035-019-01719-1)

1.

Chapter 4

- (1) Desroy, N.; Housseman, C.; Bock, X.; Joncour, A.; Bienvenu, N.; Cherel, L.; Labeguere, V.; Rondet, E.; Peixoto, C.; Grassot, J. M.; Picolet, O.; Annoot, D.; Triballeau, N.; Monjardet, A.; Wakselman, E.; Roncoroni, V.; Le Tallec, S.; Blanque, R.; Cottereaux, C.; Vandervoort, N.; Christophe, T.; Mollat, P.; Lamers, M.; Auberval, M.; Hrvacic, B.; Ralic, J.; Oste, L.; Van der Aar, E.; Brys, R.; Heckmann, B. Discovery of 2-[[2-Ethyl-6-[4-[2-(3-Hydroxyazetidin-1-Yl)-2-Oxoethyl]Piperazin-1-Yl]-8-Methylimidazo[1,2-a]Pyridin-3-Yl]Methylamino]-4-(4-Fluorophenyl)Thiazole-5-Carbonitrile (GLPG1690), a First-in-Class Autotaxin Inhibitor Undergoing Clinical Evaluation . *J. Med. Chem.* **2017**, *60* (9), 3580–3590. <https://doi.org/10.1021/acs.jmedchem.7b00032>.
- (2) Joncour, A.; Desroy, N.; Housseman, C.; Bock, X.; Bienvenu, N.; Cherel, L.; Labeguere, V.; Peixoto, C.; Annoot, D.; Lepissier, L.; Heiermann, J.; Hengeveld, W. J.; Pilzak, G.; Monjardet, A.; Wakselman, E.; Roncoroni, V.; Le Tallec, S.; Galien, R.; David, C.; Vandervoort, N.; Christophe, T.; Conrath, K.; Jans, M.; Wohlkonig, A.; Soror, S.; Steyaert, J.; Toutilou, R.; Fleury, D.; Vercheval, L.; Mollat, P.; Triballeau, N.; Van Der Aar, E.; Brys, R.; Heckmann, B. Discovery, Structure-Activity Relationship, and Binding Mode of an Imidazo[1,2-a]Pyridine Series of Autotaxin Inhibitors. *J. Med. Chem.* **2017**, *60* (17), 7371–7392. <https://doi.org/10.1021/acs.jmedchem.7b00647>.
- (3) Zhang, L.; Villalobos, A.; Beck, E. M.; Bocan, T.; Chappie, T. A.; Chen, L.; Grimwood, S.; Heck, S. D.; Helal, C. J.; Hou, X.; Humphrey, J. M.; Lu, J.; Skaddan, M. B.; McCarthy, T. J.; Verhoest, P. R.; Wager, T. T.; Zasadny, K. Design and Selection Parameters to Accelerate the Discovery of Novel Central Nervous System Positron Emission Tomography (PET) Ligands and Their Application in the Development of a Novel Phosphodiesterase 2A

- PET Ligand. *J. Med. Chem.* **2013**, *56* (11), 4568–4579. <https://doi.org/10.1021/jm400312y>.
- (4) Wüst, F.; Müller, M.; Bergmann, R. Synthesis of 4-([¹⁸F]Fluoromethyl)-2-Chlorophenylisothiocyanate: A Novel Bifunctional ¹⁸F-Labeling Agent. *Radiochim. Acta* **2004**, *92* (4–6), 349–353. <https://doi.org/10.1524/ract.92.4.349.35590>.
- (5) Madan, D.; Ferguson, C. G.; Lee, W. Y.; Prestwich, G. D.; Testa, C. A. Non-Invasive Imaging of Tumors by Monitoring Autotaxin Activity Using an Enzyme-Activated near-Infrared Fluorogenic Substrate. *PLoS One* **2013**, *8* (11). <https://doi.org/10.1371/journal.pone.0079065>.
- (6) Briard, E.; Joshi, A. D.; Shanmukhappa, S.; Ilovich, O.; Auberson, Y. P. [¹⁸F]PRIMATX, a New Positron Emission Tomography Tracer for Imaging of Autotaxin in Lung Tissue and Tumor-bearing Mice. *ChemMedChem* **2019**, *14* (16), 1493–1502. <https://doi.org/10.1002/cmdc.201900297>.
- (7) Reich, R.; Hoffman, A.; Suresh, R. R.; Shai, O.; Frant, J.; Maresca, A.; Supuran, C. T.; Breuer, E. Carbamoylphosphonates Inhibit Autotaxin and Metastasis Formation *in Vivo*. *J. Enzyme Inhib. Med. Chem.* **2015**, *30* (5), 767–772. <https://doi.org/10.3109/14756366.2014.968146>.

Chapter 5

- (1) Hussain, S. P.; Hofseth, L. J.; Harris, C. C. Radical Causes of Cancer. *Nat. Rev. Cancer* **2003**, *3* (4), 276–285. <https://doi.org/10.1038/nrc1046>.
- (2) Chio, I. I. C.; Tuveson, D. A. ROS in Cancer: The Burning Question. *Trends Mol. Med.* **2017**, *23* (5), 411–429. <https://doi.org/10.1016/j.molmed.2017.03.004>.
- (3) Hanahan, D.; Weinberg, R. A. Hallmarks of Cancer: The next Generation. *Cell* **2011**, *144* (5), 646–674. <https://doi.org/10.1016/j.cell.2011.02.013>.
- (4) Euer, N.; Schwirzke, M.; Evtimova, V.; Burtscher, H.; Jarsch, M.; Tarin, D.; Weidle, U. H. Identification of Genes Associated with Metastasis of Mammary Carcinoma in Metastatic versus Non-Metastatic Cell Lines. *Anticancer Res.* **2002**, *22* (2A), 733–740.
- (5) Bos, P. D.; Zhang, X. H. F.; Nadal, C.; Shu, W.; Gomis, R. R.; Nguyen, D. X.; Minn, A. J.; Van De Vijver, M. J.; Gerald, W. L.; Foekens, J. A.; Massagué, J. Genes That Mediate Breast Cancer Metastasis to the Brain. *Nature* **2009**, *459* (7249), 1005–1009. <https://doi.org/10.1038/nature08021>.
- (6) Li, W.; Mao, Z.; Fan, X.; Cui, L.; Wang, X. Cyclooxygenase 2 Promoted the Tumorigenicity of Pancreatic Cancer Cells. *Tumor Biol.* **2014**, *35* (3), 2271–2278. <https://doi.org/10.1007/s13277-013-1301-2>.
- (7) Barbayianni, E.; Kaffe, E.; Aidinis, V.; Kokotos, G. Autotaxin, a Secreted Lysophospholipase D, as a Promising Therapeutic Target in Chronic Inflammation and Cancer. *Prog. Lipid Res.* **2015**, *58*, 76–96. <https://doi.org/10.1016/j.plipres.2015.02.001>.
- (8) Benesch, M. G. K.; Ko, Y. M.; Tang, X.; Dewald, J.; Lopez-Campistrous, A.; Zhao, Y. Y.; Lai, R.; Curtis, J. M.; Brindley, D. N.; McMullen, T. P. W. Autotaxin Is an Inflammatory Mediator and Therapeutic Target in Thyroid Cancer. *Endocr. Relat. Cancer* **2015**, *22* (4),

- 593–607. <https://doi.org/10.1530/ERC-15-0045>.
- (9) Willoughby, D. A.; Moore, A. R.; Colville-Nash, P. R. COX-1, COX-2, and COX-3 and the Future Treatment of Chronic Inflammatory Disease. *Lancet* **2000**, *355* (9204), 646–648. [https://doi.org/10.1016/S0140-6736\(99\)12031-2](https://doi.org/10.1016/S0140-6736(99)12031-2).
- (10) Benesch, M. G. K.; Macintyre, I. T. K.; McMullen, T. P. W.; Brindley, D. N. Coming of Age for Autotaxin and Lysophosphatidate Signaling: Clinical Applications for Preventing, Detecting and Targeting Tumor-Promoting Inflammation. *Cancers (Basel)*. **2018**, *10* (3). <https://doi.org/10.3390/cancers10030073>.
- (11) Grösch, S.; Maier, T. J.; Schiffmann, S.; Geisslinger, G. Cyclooxygenase-2 (COX-2) - Independent Anticarcinogenic Effects of Selective COX-2 Inhibitors. *J. Natl. Cancer Inst.* **2006**, *98* (11), 736–747. <https://doi.org/10.1093/jnci/djj206>.
- (12) Uddin, M. J.; Crews, B. C.; Ghebreselasie, K.; Huda, I.; Kingsley, P. J.; Ansari, M. S.; Tantawy, M. N.; Reese, J.; Marnett, L. J. Fluorinated COX-2 Inhibitors as Agents in PET Imaging of Inflammation and Cancer. *Cancer Prev. Res.* **2011**, *4* (10), 1536–1545. <https://doi.org/10.1158/1940-6207.CAPR-11-0120>.
- (13) Tietz, O.; Wuest, M.; Marshall, A.; Glubrecht, D.; Hamann, I.; Wang, M.; Bergman, C.; Way, J. D.; Wuest, F. PET Imaging of Cyclooxygenase-2 (COX-2) in a Pre-Clinical Colorectal Cancer Model. *EJNMMI Res.* **2016**, *6* (1). <https://doi.org/10.1186/s13550-016-0192-9>.
- (14) Sharpless, K. B.; Manetsch, R. *In Situ* Click Chemistry: A Powerful Means for Lead Discovery. *Expert Opin. Drug Discov.* **2006**, *1* (6), 525–538. <https://doi.org/10.1517/17460441.1.6.525>.
- (15) Bhardwaj, A.; Kaur, J.; Wuest, M.; Wuest, F. *In Situ* Click Chemistry Generation of

- Cyclooxygenase-2 Inhibitors. *Nat. Commun.* **2017**, 8 (1), 1–13. <https://doi.org/10.1038/s41467-016-0009-6>.
- (16) Millward, S. W.; Agnew, H. D.; Lai, B.; Lee, S. S.; Lim, J.; Nag, A.; Pitram, S.; Rohde, R.; Heath, J. R. *In Situ* Click Chemistry: From Small Molecule Discovery to Synthetic Antibodies. *Integr. Biol.* **2013**, 235 (1), 87–95. <https://doi.org/10.1038/jid.2014.371>.
- (17) Uddin, M. J.; Crews, B. C.; Ghebreselasie, K.; Tantawy, M. N.; Marnett, L. J. [123I]-Celecoxib Analogues as SPECT Tracers of Cyclooxygenase-2 in Inflammation. *ACS Med. Chem. Lett.* **2011**, 2 (2), 160–164. <https://doi.org/10.1021/ml100232q>.
- (18) Prabhakaran, J.; Underwood, M.; Zanderigo, F.; Simpson, N. R.; Cooper, A. R.; Matthew, J.; Rubin-Falcone, H.; Parsey, R. V.; Mann, J. J.; Dileep Kumar, J. S. Radiosynthesis and *in Vivo* Evaluation of [11C]MOV as a PET Imaging Agent for COX-2. *Bioorganic Med. Chem. Lett.* **2018**, 28 (14), 2432–2435. <https://doi.org/10.1016/j.bmcl.2018.06.015>.
- (19) Fornetti, J.; Jindal, S.; Middleton, K. A.; Borges, V. F.; Schedin, P. Physiological COX-2 Expression in Breast Epithelium Associates with COX-2 Levels in Ductal Carcinoma *in Situ* and Invasive Breast Cancer in Young Women. *Am. J. Pathol.* **2014**, 184 (4), 1219–1229. <https://doi.org/10.1016/j.ajpath.2013.12.026>.
- (20) Pujols, L.; Benitez, P.; Alobid, I.; Martinez-Antón, A.; Roca-Ferrer, J.; Mullol, J.; Picado, C. Glucocorticoid Therapy Increases COX-2 Gene Expression in Nasal Polyps *in Vivo*. *Eur. Respir. J.* **2009**, 33 (3), 502–508. <https://doi.org/10.1183/09031936.00017408>.
- (21) Almendingen, K.; Brevik, A.; Nymoén, D. A.; Hilmarsen, H. T.; Andresen, P. A.; Andersen, L. F.; Vatn, M. Modulation of COX-2 Expression in Peripheral Blood Cells by Increased Intake of Fruit and Vegetables? *Eur. J. Clin. Nutr.* **2005**, 59 (4), 597–602. <https://doi.org/10.1038/sj.ejcn.1602110>.

- (22) Kirkby, N. S.; Chan, M. V.; Zaiss, A. K.; Garcia-Vaz, E.; Jiao, J.; Berglund, L. M.; Verdu, E. F.; Ahmetaj-Shala, B.; Wallace, J. L.; Herschman, H. R.; Gomez, M. F.; Mitchell, J. A. Systematic Study of Constitutive Cyclooxygenase-2 Expression: Role of NF-KB and NFAT Transcriptional Pathways. *Proc. Natl. Acad. Sci. U. S. A.* **2016**, *113* (2), 434–439. <https://doi.org/10.1073/pnas.1517642113>.
- (23) Madan, D.; Ferguson, C. G.; Lee, W. Y.; Prestwich, G. D.; Testa, C. A. Non-Invasive Imaging of Tumors by Monitoring Autotaxin Activity Using an Enzyme-Activated near-Infrared Fluorogenic Substrate. *PLoS One* **2013**, *8* (11). <https://doi.org/10.1371/journal.pone.0079065>.
- (24) Briard, E.; Joshi, A. D.; Shanmukhappa, S.; Ilovich, O.; Auberson, Y. P. [18 F]PRIMATX, a New Positron Emission Tomography Tracer for Imaging of Autotaxin in Lung Tissue and Tumor-bearing Mice. *ChemMedChem* **2019**, *14* (16), 1493–1502. <https://doi.org/10.1002/cmdc.201900297>.
- (25) Garg, R.; Blando, J. M.; Perez, C. J.; Lal, P.; Feldman, M. D.; Smyth, E. M.; Ricciotti, E.; Grosser, T.; Benavides, F.; Kazanietz, M. G. COX-2 Mediates pro-Tumorigenic Effects of PKC ϵ in Prostate Cancer. *Oncogene* **2018**, *37* (34), 4735–4749. <https://doi.org/10.1038/s41388-018-0318-9>.
- (26) Johnsen, J. I.; Lindskog, M.; Ponthan, F.; Pettersen, I.; Elfman, L.; Orrego, A.; Sveinbjornsson, B.; Kogner, P. Cyclooxygenase-2 Is Expressed in Neuroblastoma , and Nonsteroidal Anti-Inflammatory Drugs Induce Apoptosis and Inhibit Tumor Growth *in Vivo*. **2004**, 7210–7215.
- (27) Peng, A.; Lu, X.; Huang, J.; He, M.; Xu, J.; Huang, H.; Chen, Q. Rheumatoid Arthritis Synovial Fibroblasts Promote TREM-1 Expression in Monocytes via COX-2/PGE₂

- Pathway. *Arthritis Res. Ther.* **2019**, *21* (1), 1–11. <https://doi.org/10.1186/s13075-019-1954-3>.
- (28) Graves, M. C.; Fiala, M.; Dinglasan, L. A. V.; Liu, N. Q.; Sayre, J.; Chiappelli, F.; van Kooten, C.; Vinters, H. V. Inflammation in Amyotrophic Lateral Sclerosis Spinal Cord and Brain Is Mediated by Activated Macrophages, Mast Cells and T Cells. *Amyotroph. Lateral Scler. Other Mot. Neuron Disord.* **2004**, *5* (4), 213–219. <https://doi.org/10.1080/14660820410020286>.
- (29) Minghetti, L. Cyclooxygenase-2 (COX-2) in Inflammatory and Degenerative Brain Diseases. *J. Neuropathol. Exp. Neurol.* **2004**, *63* (9), 901–910. <https://doi.org/10.1093/jnen/63.9.901>.
- (30) Rose, J. W.; Hill, K. E.; Watt, H. E.; Carlson, N. G. Inflammatory Cell Expression of Cyclooxygenase-2 in the Multiple Sclerosis Lesion. *J. Neuroimmunol.* **2004**, *149* (1–2), 40–49. <https://doi.org/10.1016/j.jneuroim.2003.12.021>.
- (31) Arrambide, G.; Tintore, M. Diagnosis of Multiple Sclerosis: What Is Changing? *Expert Rev. Neurother.* **2019**, *00* (00), 1–4. <https://doi.org/10.1080/14737175.2020.1691530>.
- (32) Hoelzinger, D. B.; Nakada, M.; Demuth, T.; Rosensteel, T.; Reavie, L. B.; Berens, M. E. Autotaxin: A Secreted Autocrine/Paracrine Factor That Promotes Glioma Invasion. *J. Neurooncol.* **2008**, *86* (3), 297–309. <https://doi.org/10.1007/s11060-007-9480-6>.
- (33) Ninou, I.; Magkrioti, C.; Aidinis, V. Autotaxin in Pathophysiology and Pulmonary Fibrosis. *Front. Med.* **2018**, *5* (JUN), 1–11. <https://doi.org/10.3389/fmed.2018.00180>.
- (34) Herr, D. R.; Chew, W. S.; Satish, R. L.; Ong, W.-Y. Pleotropic Roles of Autotaxin in the Nervous System Present Opportunities for the Development of Novel Therapeutics for Neurological Diseases. *Mol. Neurobiol.* **2019**. <https://doi.org/10.1007/s12035-019-01719->

- 1.
- (35) Ikeda, H.; Yatomi, Y. Autotaxin in Liver Fibrosis. *Clin. Chim. Acta* **2012**, *413* (23–24), 1817–1821. <https://doi.org/10.1016/j.cca.2012.07.014>.
- (36) Orosa, B.; García, S.; Martínez, P.; González, A.; Gómez-Reino, J. J.; Conde, C. Lysophosphatidic Acid Receptor Inhibition as a New Multipronged Treatment for Rheumatoid Arthritis. *Ann. Rheum. Dis.* **2014**, *73* (1), 298–305. <https://doi.org/10.1136/annrheumdis-2012-202832>.
- (37) Ye, X.; Hama, K.; Contos, J. J. A.; Anliker, B.; Inoue, A.; Skinner, M. K.; Suzuki, H.; Amane, T.; Kennedy, G.; Arai, H.; Aoki, J.; Chun, J. LPA3-Mediated Lysophosphatidic Acid Signalling in Embryo Implantation and Spacing. *Lett. to Nat.* **2005**, *435* (May), 104–108.
- (38) Aikawa, S.; Kano, K.; Inoue, A.; Wang, J.; Saigusa, D.; Nagamatsu, T.; Hirota, Y.; Fujii, T.; Tsuchiya, S.; Taketomi, Y. Autotaxin – Lysophosphatidic Acid – LPA 3 Signaling at the Embryo-Epithelial Boundary Controls Decidualization Pathways. **2017**, *36* (14), 2146–2160. <https://doi.org/10.15252/emboj.201696290>.
- (39) Nochi, H.; Tomura, H.; Tobo, M.; Tanaka, N.; Sato, K.; Shinozaki, T.; Kobayashi, T.; Takagishi, K.; Ohta, H.; Okajima, F.; Tamoto, K. Stimulatory Role of Lysophosphatidic Acid in Cyclooxygenase-2 Induction by Synovial Fluid of Patients with Rheumatoid Arthritis in Fibroblast-like Synovial Cells. *J. Immunol.* **2008**, *181* (7), 511–5119. <https://doi.org/10.4049/jimmunol.181.7.5111>.